IN-SITU MEASUREMENT OF THE JET ENERGY SCALE AND STUDIES OF JET STRUCTURE AT ATLAS

by

Arthur James Horton

MSc., Simon Fraser University, 2013
BSc., University of Prince Edward Island, 2010

Thesis Submitted in Partial Fulfillment of the
Requirements for the Degree of
Doctor of Philosophy

in the
Department of Physics
Faculty of Science

SIMON FRASER UNIVERSITY
Fall 2017

Approval

Name:	**Arthur James Horton**
Degree:	**Doctor of Philosophy [Physics]**
Title:	**IN-SITU MEASUREMENT OF THE JET ENERGY SCALE AND STUDIES OF JET STRUCTURE AT ATLAS**
Examining Committee:	**Chair:** Dr. Malcolm Kennett Associate Professor
	Dr. Michel Vetterli Senior Supervisor Professor
	Dr. Dugan O'Neil Supervisor Professor
	Dr. Bernd Stelzer Supervisor Associate Professor
	Dr. Sarah Johnson Internal Examiner Senior Lecturer
	Dr. Douglas Bryman External Examiner Professor Department of Physics & Astronomy University of British Columbia
Date Defended:	**December 7th, 2017**

Abstract

This thesis presents results for the determination of the ATLAS jet energy scale (JES) using the Missing E_{T} Projecting Fraction (MPF) method along with studies to better understand and validate the MPF. Hadronic jets are the most commonly observed objects in proton-proton collisions, and are therefore a part of most final states for processes which are studied at the Large Hadron Collider (LHC). The abundance of jets makes a precise knowledge of the JES essential to the success of the ATLAS physics program. This thesis uses the MPF in events where either a photon or a Z boson is produced back-to-back with a jet to provide an uncertainty on the response of the calorimeter which is below 1% for jets between 30 GeV and 1 TeV.

Studies measuring the impact of the underlying event on the MPF's ability to measure the response of the hadronic recoil are also presented, which validate the previously held assumption that the MPF is insensitive to these effects. In addition, studies into the relation between the measured recoil response and the desired jet response are presented. This includes measures of the flow of energy across the jet boundary during the showering process and the effect on the total measured response of low energy/low response particles near the fringe of the recoil. These measurements show up to a 10% difference between the jet response and the recoil response for jets reconstructed with the anti-k_{t} algorithm with midrange size parameters (0.4-0.7). These differences however show little dependence on physics modeling choices (less than 1%), on which the Monte Carlo jet calibration is based. These results put the MPF technique on a firmer ground, and they will reduce future JES uncertainties for jets with energies below 100 GeV.

Keywords: ATLAS; Jet, Jet energy scale

Acknowledgements

I'd like to thank my supervisory committee for their time and patience and all of my fellow grad students over the years who have helped along the way and provided the occasional welcome distraction. I'd also like to thank Bethany Mayne, her support has made this thesis possible.

Table of Contents

List of Tables

List of Figures

Acronyms

ALICE A Large Ion Collider Experiment.

ATLAS A Torroidal LHC ApparatuS.

BIC Binary Cascade Model.

CERN European Organization for Nuclear Research.

CMS Compact Muon Solenoid.

CSC Cathode Strip Chamber.

EM Electromagnetic.

eV electronvolt.

FSR Final State Radiation.

GSC Global Sequential Calibration.

IBL Insertable B-Layer.

ISR Initial State Radiation.

JES Jet Energy Scale.

JVT Jet Vertex Tagger.

L1 Level-1.

LC Local Hadronic Cell Weighting.

LEP Low Energy Parameterization.

LHC Large Hadron Collider.

LHCb LHC-beauty.

MDT Monitored Drift Tubes.

MET Missing Transverse Energy.

MPC Multiwire Proportional Chamber.

MPF Missing E_{T} projection fraction.

PDF Parton Distribution Function.

QCD Quantum Chromodynamics.

QGSM Quark Gluon String Model.

RPC Resistive Plate Chambers.

SCT Semiconductor Tracker.

TGC Thin Gap Chamber.

TRT Transition Radiation Tracker.

Chapter 1

Introduction

1.1 The Standard Model

For the last 50 years particle physicists have very successfully described the short distance interactions of elementary particles using the Standard Model. The Standard Model consists of two quantum field theories: the Electroweak Theory and Quantum Chromodynamics (QCD), which describe the interactions of 12 fundamental spin $\frac{1}{2}$ fermions. While the Standard Model contains no explanation for gravity, dark matter, dark energy, etc. it does remain the most successful model available to describe reality on the smallest distance scales and at the highest energies.

The fermions, listed in Table 1.1, are categorized into three generations of four particles, with each generation being a heavier copy of the previous one. Each generation includes two quarks, particles that have colour charge and are therefore subject to the strong force described by QCD, and two leptons that have no colour charge. The six types (flavours) of quarks are organized into generational pairs, the up (u) and the down (d), the charm (c) and the strange (s), and the top (t) and the bottom (b). Similarly each generation of leptons is composed of one charged lepton, known as the electron (e), the muon (μ), and the tau (τ), and their neutral counterparts the neutrinos ($\nu_{\mathrm{e}}, \nu_{\mu}, \nu_{\tau}$). In addition to each of these matter particles there is a complementary anti-particle, which has the opposite quantum numbers, e.g. charge, to it's regular counterpart and is denoted using an over bar. It is worth noting that the entirety of the periodic table of elements, and therefore all regular matter, require only the first generation of particles to construct. The Standard Model also includes spin-1 bosons which mediate the various forces included in the theory (see Table 1.2).

The electroweak interaction has four force carrying bosons: the photon, the Z, and $\mathrm{W}^{\pm}$. While the electroweak force is unified at high energies, at lower energies the electroweak symmetry is spontaneously broken into the electromagnetic force and the weak force. In the Standard Model this breaking is explained by introducing a new scalar field with a non-zero vacuum expectation value, known as the Higgs field. This breaking into two separate forces also allows the W and Z bosons to acquire their very large observed mass through the

fermion	mass [GeV/c^2]	spin	electric charge	colour charge	generation
charged leptons					
e	5.11 x10^{-4}	$\frac{1}{2}$	-1	no	1
μ	1.06 x10^{-1}	$\frac{1}{2}$	-1	no	2
τ	1.78	$\frac{1}{2}$	-1	no	3
neutral leptons					
ν_e	0	$\frac{1}{2}$	0	no	1
ν_μ	0	$\frac{1}{2}$	0	no	2
ν_τ	0	$\frac{1}{2}$	0	no	3
up-type quarks					
u	2.3 x10^{-3}	$\frac{1}{2}$	$+\frac{2}{3}$	yes	1
c	1.28	$\frac{1}{2}$	$+\frac{2}{3}$	yes	2
t	173.5	$\frac{1}{2}$	$+\frac{2}{3}$	yes	3
down-type quarks					
d	4.8 x10^{-3}	$\frac{1}{2}$	$-\frac{1}{3}$	yes	1
s	9.5 x10^{-2}	$\frac{1}{2}$	$-\frac{1}{3}$	yes	2
b	4.18	$\frac{1}{2}$	$-\frac{1}{3}$	yes	3

Table 1.1: Properties of the known spin-$\frac{1}{2}$ fermions in the Standard Model [1]. The quark masses have been estimated using the $\overline{\text{MS}}$ renormalization scheme at a scale $\mu = 2$ GeV, and while the neutrino masses are non-zero, they are small enough that they are approximated as zero for the purposes of this thesis.

interaction	boson	mass [GeV/c^2]	spin	electric charge	colour charge
force carrying bosons					
electromagnetic	γ (photon)	0	1	0	no
Weak	$W^\pm$	80.39	1	±1	no
	Z	91.19	1	0	no
strong	g (gluon)	0	1	0	yes
non-force carrying bosons					
—	Higgs	125.09	0	0	no

Table 1.2: Properties of known bosons in the Standard Model.

Brout-Englert-Higgs (BEH) mechanism. The large mass of the W and Z bosons also leads to the relatively short range of the weak interaction. This Higgs field also allows the fermions in the Standard Model to obtain mass as well. A measurable consequence of this theory is the presence of a massive spin-0 boson called the Higgs Boson, which was discovered in 2012 at the Large Hadron Collider (LHC).

As previously mentioned, QCD describes the strong force, which affects particles carrying colour charge much like the electric force affects particles carrying an electric charge. Unlike electromagnetism which only has one charge, the electric charge, QCD has three colour charges known as red, green, and blue. Another notable difference between the two interactions is that while the force mediator of the electric force (the photon) has no electric charge itself, this is not the case for the force carriers of the strong interaction (gluons). One important consequence of this difference is that the strength of the strong force does not weaken with increasing distance between the particles in question. This difference means that quarks cannot be found as individual particles but come in bound "colour neutral" states, a phenomenon known as confinement. While these bound states are colour neutral a much weaker residual force still exists, and while it decreases quite rapidly with distance it is this residual force which is responsible for holding protons and neutrons together in the nuclei of atoms.

These bound states of 'valence' quarks also contain an infinite number of quark/anti-quark pairs constantly being created and annihilated (called sea quarks) and gluons, but the overall identity and properties of a given bound state are determined by it's valence quarks. Bound states can have either three valence quarks (or anti-quarks) which are known as the baryons, or a quark/anti-quark pair, called the mesons. Baryons and mesons are collectively known as hadrons. As hinted at above, familiar examples of these bound states include protons (uud) and neutrons (udd). As a result of these complicated bound states the masses of the quarks cannot be measured directly, but must be approximated by measuring the bound states and making certain theoretical assumptions [1].

1.2 Experimental Particle Physics

As the Standard Model is an incomplete theory there is a great amount of interest to better understand physics beyond the scope of the Standard Model. This has lead to a great variety of beyond the Standard Model (BSM) theories, predicting a wide range of new particles and behaviours which would have no explanation within the Standard Model. Tests looking for variations from the Standard Model can be performed under a variety of conditions. One category of experiment involves accelerating stable, or long-lived, particles and bringing them to collision inside of a detector, allowing for the study of the various particles of

[1] The t quark is the exception, as it decays fast enough that no bound states are formed.

the Standard Model that are created in the collisions. The particles being accelerated can be both elementary (electrons for example) or composite (like protons), with the different choices affecting the types of collisions that will be observed. A relevant example of such a detector/accelerator combination is A Torroidal LHC ApparatuS (ATLAS) at the LHC.

The LHC is a machine that straddles the border of Switzerland and France at the European Organization for Nuclear Research (CERN) in Geneva. While it can produce heavy ion collisions, it is best known for its ability to produce higher energy proton-proton collisions than any other accelerator facility in the world. Bringing protons from rest to within a few meters per second of the speed of light is a multi-step process, a description of which can be found in the LHC Design Report [2] while a summary can be found in section 2.1.

ATLAS is a general purpose detector that has been placed in the LHC accelerator ring to observe collisions along with three other detectors. There is another general purpose detector known as the Compact Muon Solenoid (CMS), in addition to two more specialized detectors called LHC-beauty (LHCb) and A Large Ion Collider Experiment (ALICE). Detectors like ATLAS and CMS are designed to be able to accurately measure a wide variety of processes allowing them to more fully explore the collisions provided by the LHC to push the Standard Model to its limit and search for potential new physics beyond the Standard Model. Details on how this is accomplished in ATLAS will be provided in section 2.2.

As the LHC collides protons, and therefore quarks and gluons, the most commonly produced objects in the ATLAS detector are collimated sprays of particles called jets. Jets are the result of an interplay between a high energy colour charged particle being ejected from a collision and the confinement property of the strong force allowing only colour neutral particles to exist. The formation of jets will be discussed in greater detail in Sec. 3.3. This thesis presents detailed studies of a technique for measuring the Jet Energy Scale (JES) *in-situ* using events where jets are produced along with other well measured objects (photons, electrons and muons). This includes studies of how jets are produced and defined, how this determines their structure, and how it influences the jet calibration.

As the LHC is a hadron collider jets are inevitably present in a large number of final states being searched for or studied in ATLAS. As jets are the most abundant object produced in the LHC, an accurate reconstruction of the both the energy and momentum of jets is essential to the success of the physics program at ATLAS, both while performing detailed studies of well known Standard Model processes and in searches for new physics beyond the Standard Model. Currently a large number of physics results are limited by the size of the uncertainty on the JES, one of the most significant components of which is the in-situ calibration. Following this crucial impact of the JES, it is important that its determination be well tested, in particular the assumptions made. The results presented in this thesis reduce the *in-situ* component of the JES uncertainty, especially for jets below 100 GeV, and put the MPF method of measuring the JES on sounder ground.

1.3 Units and Conventions

For the remainder of this thesis it will be worth keeping a few particle physics conventions in mind. The most commonly used is the non-SI unit of energy, the electronvolt (eV), which is the amount of energy a singly-charged particle (an electron for example) gains after being accelerated across a potential of 1 Volt. One eV is the equivalent of 1.602×10^{-19} Joules. Energies relevant to this thesis are typically much larger than a single eV, so giga-electronvolt (GeV, 10^9 eV) and tera-electronvolts (TeV, 10^{12} eV) are more commonly used. Traditionally electronvolts are also used to describe mass and momentum. This is made possible using another particle physics convention which is to set the speed of light c to be unitless and equal to one, allowing mass to be described in terms of eV/c^2 (see tables 1.1 and 1.2), and momentum to be referenced in terms of eV/c. It is standard practice to also set $\hbar$ to be 1.

Another high energy physics convention is to refer to both the particle and its anti-particle by the name of the particle. For this thesis this convention will be used, meaning that unless otherwise specified 'electron' and 'muon' will also refer to positrons and anti-muons.

Chapter 2

Experimental setup

The LHC successfully began circulating its first protons within its 27 km long underground tunnel on the 10th of September 2008. Unfortunately an incident on the 19th of that same month, where a superconducting magnet quench caused 6 tonnes of liquid helium to vent and subsequently expand with violent force, damaged over 50 superconducting magnets which needed to be repaired. On the 23rd of November the following year the first collisions were recorded [3], signalling the beginning of the LHC era at the forefront of the high energy frontier. In the years since the LHC has been consistently pushing to more frequent collisions at higher energies, allowing the experiments along its ring to explore and extend our knowledge of physics at the subatomic level.

This chapter describes the technology that allows these studies to be performed. First a description of the LHC accelerator complex is provided. This is followed by a subdetector-by-subdetector description of the ATLAS experiment, including details on the physics behind the technology used in these detectors.

2.1 The Large Hadron Collider

The components of a particle accelerator can be grouped into two functional categories: rf cavities which use electric fields to accelerate particles, and magnets which are used to control the accelerated particles. Circular accelerators come in two distinct types: cyclotrons which contain the beam usually using a fixed-strength magnetic field but allow for the radius of the charged particles' orbit to increase, and synchrotrons which maintain a fixed radius by increasing the magnetic field strength to compensate for the increasing energy of the accelerating particles. The LHC fits into the second of these categories.

Designing a single synchrotron accelerator to accelerate bunches of protons to the energies attained at the LHC would be a difficult and expensive task. One requirement would be the ability to finely control the field in the superconducting electromagnets used to contain the particle beam in the ring over several orders of magnitude of energy. A much more cost

effective approach involves using existing machines to accomplish at least part of this task, which is the approach used at the LHC.

The LHC acceleration complex begins with a linear accelerator, called linac2, a machine that accelerates protons originating from an ion source to 50 MeV in bunches. These bunches are delivered to the PS booster, a machine that consists of four superimposed synchrotron rings which accelerate protons to 1.4 GeV before they are injected into the next machine, the Proton Synchrotron. The Proton Synchrotron, or PS, is the oldest component of the LHC acceleration facility. It was built in the 1950's and was designed to accelerate up to 10^{10} protons per pulse to 26 GeV.

After the PS, the protons are injected into the Super Proton Synchrotron (SPS), a machine that in 1976 when it was turned on had the ability to accelerate protons to 400 GeV, the second highest energy attainable by an accelerator at that time. The SPS, while in proton/anti-proton collision mode (the so-called Sp$\bar{\text{p}}$S mode) allowed the discovery of both the W and Z bosons by the UA1 and UA2 collaborations. It may be worth noting that it takes several fills of the PS to fill the SPS, and it subsequently takes several fills of the SPS to fully fill the LHC. The SPS is the final pre-injector into the LHC, accelerating the protons up to 450 GeV before they enter the LHC itself.

The LHC is a machine that was designed to use 16 RF cavities to accelerate 2808 bunches, each with 1.15x10^{11} protons, to 7 TeV per proton. These bunches travel the 27 km around the ring of the LHC being held in orbit by 1232 superconducting dipole magnets (8.33 Tesla) which bend the beam, along with a number of additional magnets, mostly quadrupoles, which help focus the beam [4]. The LHC then crosses these counter rotating beams at four points along the beam line (the four experiments listed in 1.2) every 25 ns, with an average of 25 interactions occurring per crossing (up to $\sim$ 52) in 2016.

One measure of the collider's performance is its luminosity, a description of the number of particles per unit area per unit time, which directly relates to the number of collisions per unit time and therefore the probability of obtaining a given final state. The LHC's design luminosity is approximately 20 times the maximum luminosity of its predecessor, the Tevatron (10^{34} cm^{-2}s^{-1} vs. 4 x 10^{32} cm^{-2}s^{-1}), with this design luminosity being surpassed by the end of the 2016 data taking period (1.38 x 10^{34} cm^{-2}s^{-1}).

2.2 The ATLAS Experiment

2.2.1 The ATLAS Coordinate System

The origin of the coordinate system that is used in ATLAS is at the geometric centre of the ATLAS detector. The z-axis is parallel to the beam pipe running counterclockwise along the LHC ring when viewed from above, with the x-axis pointing toward the middle of the ring and the y-axis pointing up. A more common way to describe the coordinates in the x-y plane is to use the azimuthal angle ϕ, where ϕ=0 is defined to be along the positive x-axis

and to increase in the direction of the positive y-axis, along with the radial coordinate r which is the distance of the point from the origin. As the remnants of the collisions will be ejected in all directions a spherical coordinate system is adopted by adding a second angle θ, with the most natural orientation being to define θ=0 along the positive z-axis and increasing in the direction of the x-y plane. In high energy physics however it is often more convenient to speak in terms of rapidity(y) and pseudorapidity(η). This is especially true for a hadron collider like the LHC, which at high energy effectively collides partons. Each parton carries an unknown fraction of the total momentum of the proton. This means that the center of mass frame for each collision is Lorentz boosted along the z axis. This makes the use of θ problematic due to how it transforms from the detector reference frame to the centre of mass reference frame. Rapidity, given by $y = \frac{1}{2}\ln\left[\frac{E+p_z}{E-p_z}\right]$, is much more helpful in this regard as differences in rapidity remain constant under Lorentz boosts. Pseudorapidity, defined as $\eta = -\ln\left[\tan\left(\frac{\theta}{2}\right)\right]$, is a good approximation of rapidity, especially at high energy, and does not require knowledge of the energy and momentum of the particle in question. Pseudorapidity is equal to the rapidity in the case of a massless particle.

2.2.2 ATLAS Detector: Overview

ATLAS is a multipurpose detector, meaning it must be able to simultaneously measure the large number and variety of particles produced in each collision provided by the LHC at a high enough rate to take advantage of the large luminosity required for the physics studies at the LHC. The ATLAS detector is composed of many individual layers, with each layer being designed to measure different properties of the particles. Going from the interaction point outwards these layers are known as the inner detector, the electromagnetic (EM) calorimeter, the hadronic calorimeter, and the muon spectrometer.

2.2.3 ATLAS Hardware: Inner Detector

The inner detector is made up of three subdetectors: the pixel detector, the Semiconductor Tracker (SCT), and the Transition Radiation Tracker (TRT). These three subdetectors are all immersed in a 2 Tesla magnetic field that is supplied by a solenoidal magnet. This magnetic field bends the trajectories of charged particles by an amount that is proportional to their momentum. The main purpose of the inner detector is to make non-destructive measurements of this bending, allowing the momentum of charged particles to be measured. It is also possible to track the trajectories of multiple particles back to a single origin, called a vertex. Vertices along the beam axis may indicate an individual proton-proton collision event, while vertices off of the beam axis may indicate the location where some heavy particle produced in the original collision further decays into lighter secondaries. The TRT also contributes to particle identification by measuring transition radiation (discussed later in this section).

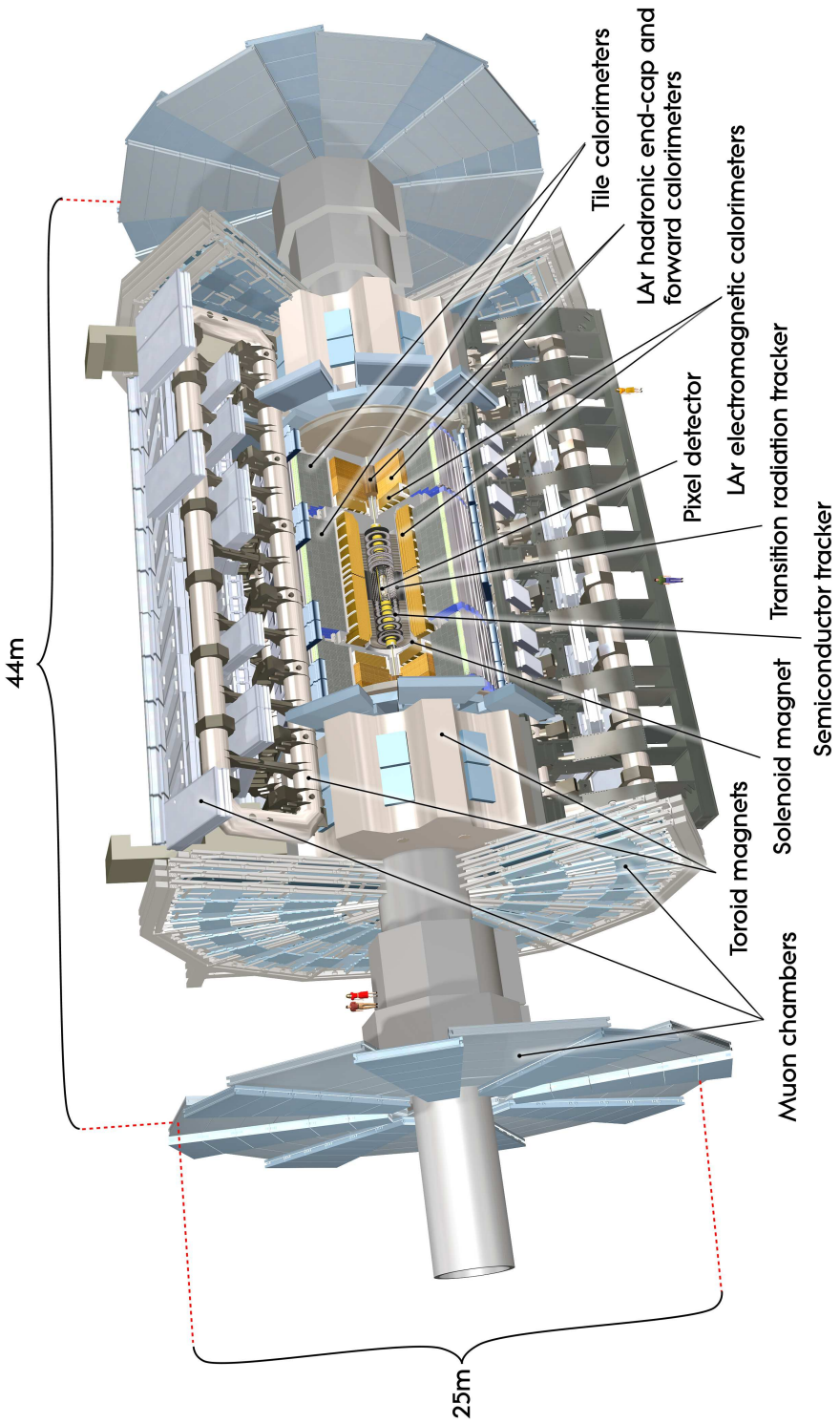

Figure 2.1: Layout of the ATLAS detector showing the location of the various subdetectors. ATLAS Experiment Image: Copyright CERN, [5].

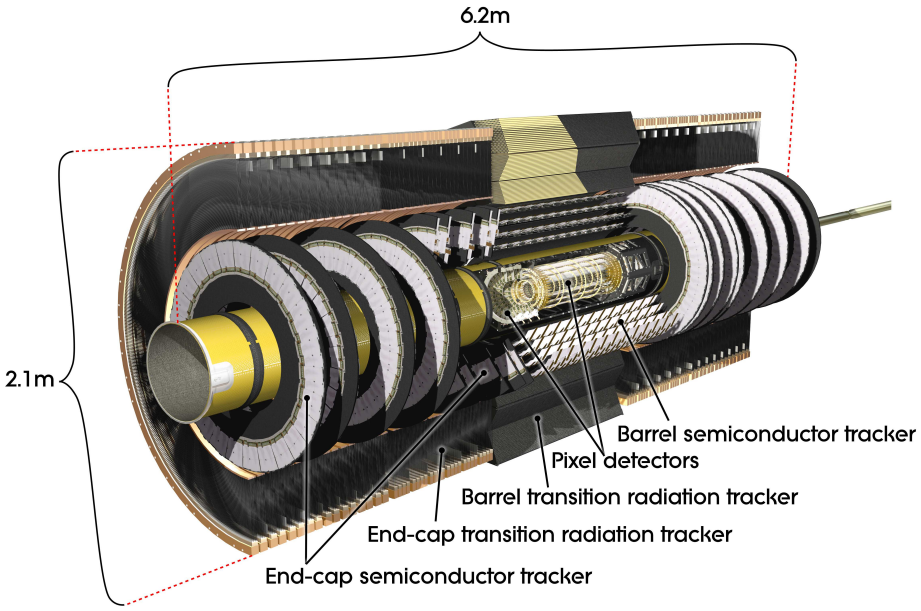

Figure 2.2: Drawing of the various subsystems of the inner detector. ATLAS Experiment Image: Copyright CERN, [6].

These trajectories are measured by a large number of concentric cylindrical detectors (and circular endcap detectors) with well known positions surrounding the interaction point. When a particle passes through these detectors a space-point is measured (a hit). A pattern recognition, or reconstruction, algorithm is then run over all of these hits to recreate the paths the particles have travelled (known as tracks). It is this track reconstruction that leads the inner detector to more colloquially be known as the tracker.

The first two subdetectors of the tracker are both semiconductor detectors, a type of detector that measures the electron-hole pairs that are produced as a charged particle passes through silicon sensors that are segmented into either squares (pixels) or strips. Both are made up of 4 concentric cylinders in the central region, and circular endcap disks further extending the η coverage of the detectors. For the 2011 and 2012 data taking periods the pixel detector consisted of three layers situated a radial distance of 50.5, 88.5 and 122.5 mm from the centre of the beam pipe. The layers are made up of 22, 38 and 52 staves, with each stave containing 6 x 10^5 pixels. This detector is capped at both ends by three endcap disk layers, with each endcap having a further 4.4 x 10^6 pixels. The resolution of a tracking detector is parameterized by $A \oplus B/p_T$, where A is the intrinsic resolution of the detector and B describes the effect of multiple scatterings on the resolution. This setup allowed for an intrinsic resolution of 10 μm in the transverse impact parameter d_0 and 115 μm in the longitudinal impact parameter ($z_0 \sin\theta$) [7], which are measures of the distance from the particle track to the reconstructed vertex.

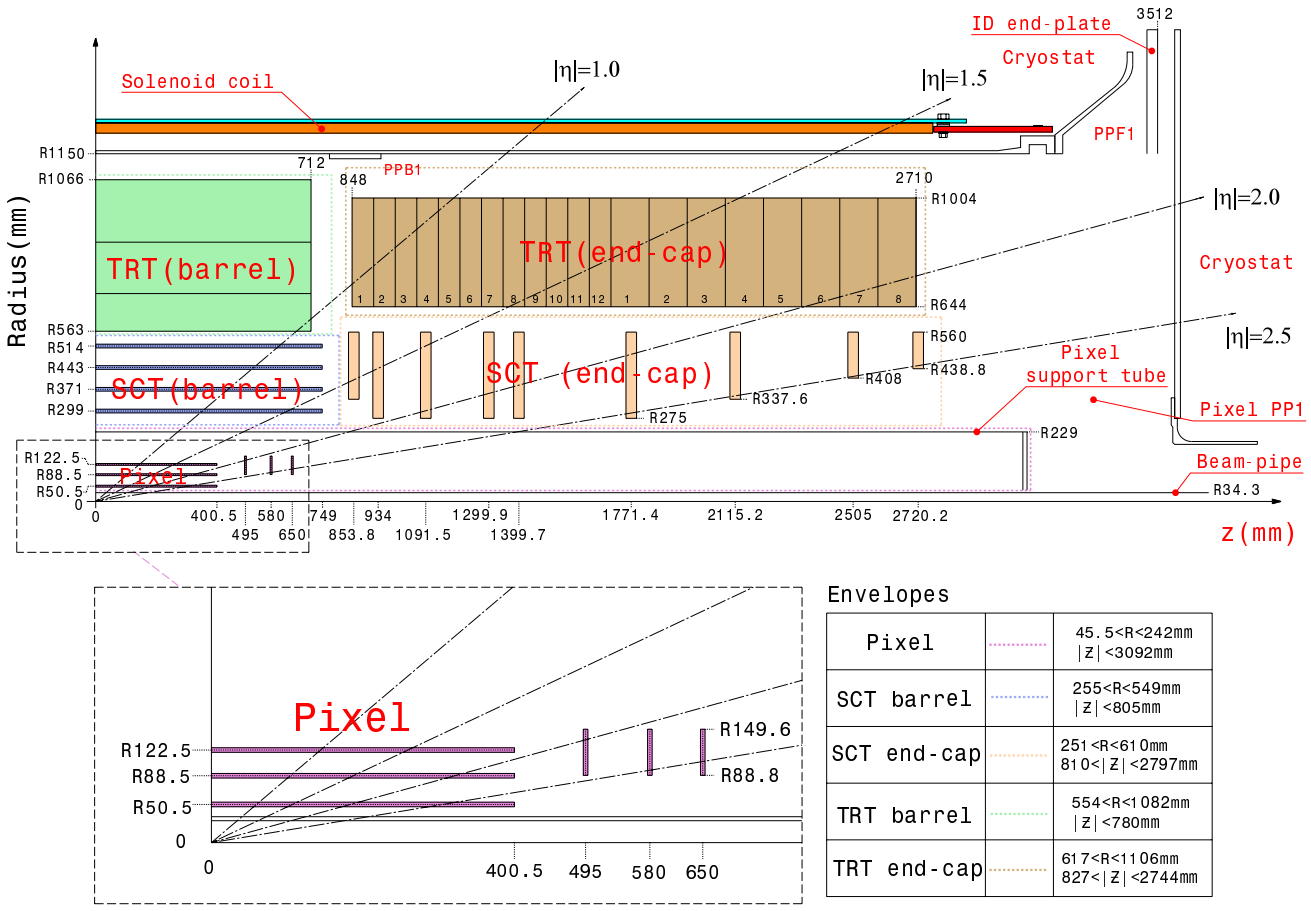

Figure 2.3: Layout and coverage of the ID. Figure from [8]. Note that the IBL is not included.

During the first long shutdown of the LHC a fourth additional layer was added closer to the beam, known as the Insertable B-Layer (IBL). This layer was designed to deal with the high occupancy expected as the luminosity delivered by the LHC increases into 2020 (2-3 x 10^{34} cm^{-2}s^{-1}) [9], and to provide an additional hit near the interaction point to ensure good tracking efficiency as the ID ages. This new layer has 14 staves which are arranged in an overlapping circular pattern 33 mm away from the centre of the beam pipe, adding a further 6x10^{6} individual readout channels to the pixel detector. The IBL improves the intrinsic resolution of the pixel detector by a factor of 1.7 in longitudinal impact parameter and by 1.2 in transverse impact parameter. It also reduces the p_{T} dependence of the resolution by a factor of 1.8 in both directions [10]. One measurement that can be improved by this increased track resolution is b-tagging, which involves using vertices which are displaced from the beam line to identify the remnants of very short lived particles decaying before they reach the tracking system (in this case B mesons). The light jet rejection rate of a b-tagger set to accept 60% of b jets has been shown to increase by nearly a factor of 2 with this improvement in resolution (in the absence of pileup).

As mentioned above the SCT is also a semiconductor detector, consisting of 4088 modules tiling 4 cylinders and two endcaps, with each endcap consisting of 9 layers [11]. In the barrel these modules consist of two inner and two outer sensors with a stereo angle of 40 mrad to provide a position measurement in a complementary direction. The endcap modules use the same strategy, having two sensors glued back-to-back once again with a stereo angle of 40 mrad. The SCT has a nominal resolution of 17 μm in R-ϕ and 580 μm in z.

The final subsystem in the tracker is the TRT which uses up to 73 layers of gas filled "straws" in the barrel and as many as 160 straw planes in the endcaps. Each straw is filled with a mixture of 70% xenon gas (for x-ray absorption), 27% CO_2, and 3% O_2 (for photon quenching and increasing the electron drift velocity respectively). Charged particles ionize the gas mixture as they pass through and the charge is collected by a central gold plated tungsten anode wire within each straw. Each of these 144 cm long straws provides only information in R-ϕ, for which the intrinsic accuracy is 130 μm. In addition to providing position measurements the TRT is also able to detect the low energy transition radiation photons created as the charged particles travel between the gas, the layers within the straw walls, and the inter-straw medium (polypropylene foils or fibres). The amount of radiation emitted during each transition is a function of the Lorentz factor of the particle. By having two detection thresholds for each straw, a low ionization threshold and a high transition radiation threshold, and counting the number of high threshold hits belonging to a given reconstructed track, information about the type of particle creating the track can be obtained. Tracks with a large number of high threshold hits can be assumed to be highly boosted light particles, namely electrons.

2.2.4 ATLAS Hardware: Calorimeter

Calorimeters, in contrast to tracking systems, absorb the energy of incoming particles through destructive processes and produce signals that are proportional to the incoming energy. In addition to pure energy measurements, calorimeters which are segmented into η x ϕ x R cells can also provide information on how the energy from a given particle is deposited, which helps both particle identification and energy calibration. With a large coverage in both η and ϕ one can also determine the location in ϕ where signals may be expected due to the conservation of momentum in the transverse plane but nothing is detected. These imbalances in measured momentum may be interpreted as a miscalibration of the observed energy or as particles having passed through the detector without interacting, such as a neutrino. A detailed description of the operation of calorimeters is presented below.

The ATLAS calorimeter is broken up into three η sections: the central barrel region, the endcaps and the forward calorimeters (FCal). In all three regions the ATLAS calorimeter is split into two well defined primary radial segments, the Electromagnetic (EM) calorimeter, and the hadronic calorimeter. This division is to take advantage of the relatively shallow

showering depth of electromagnetic particles while ensuring that the much deeper hadronic showers are still fully measured. These differences will be further explained in the following sections.

The remainder of this section is divided into four subsections. The first subsection describes particles that result in electromagnetic showers and how electromagnetic showers are propagated. This is followed by a description of the technology used in the EM calorimeters in ATLAS. The same two-stage approach is used to explain hadronic showers and how they are measured in ATLAS.

Electromagnetic Calorimeter

Electromagnetic calorimeters are focused on measuring the energy of photons and electrons, which interact with matter through a variety of processes that are all results of the electromagnetic interaction [12] [13]. The photon for example has four primary processes through which it interacts with matter: Rayleigh scattering, the photoelectric effect, Compton scattering, and pair production. The contribution of each of these processes to the overall energy loss of the photon depends on the energy of the photon.

For low energy photons (less than $\sim$ 100 KeV) the photoelectric effect, where a photon is absorbed by an atom and an electron is emitted, dominates. Due to the strong energy dependence of the cross section for this process (goes as E^{-3}) it is largely suppressed for higher energy photons. Rayleigh scattering, which is the coherent scattering of photons by atomic nuclei and is the second most important process at low energy, also dies out very quickly with increasing photon energies. In most materials for photons with energies between $\mathcal{O}$(10 KeV) to $\mathcal{O}$(10 MeV) the largest contribution to the photon interaction cross section is Compton scattering. In Compton scattering photons scatter from atomic electrons. For even larger energies the dominant interaction mechanism is pair production where a photon, while interacting with the EM field of either an atomic nucleus or an electron, creates an electron/positron pair. Pair production is possible for photons with energies above twice the mass of an electron (2 x 511 KeV), with the cross section growing rapidly before leveling off at higher energies. Figure 2.4 shows the cross-section for these various interaction mechanisms for photons in lead. An important measure of the number of interactions a photon will experience while travelling through a material is the mean distance traveled between each interaction, or the mean free path ($\lambda\,(E)$). By measuring the amount of material present in a given detector in terms of λ one can more readily compare two calorimeters made with different materials.

The primary electromagnetic mechanism by which charged particles (electrons and positrons for example) lose their energy is also energy dependent. Lower energy particles primarily lose energy by ionizing the material they are travelling through (with processes like Møller scattering or Bhabha scattering also contributing). Particles with higher energy tend to lose energy by radiating photons (bremsstrahlung). The energy at which the average

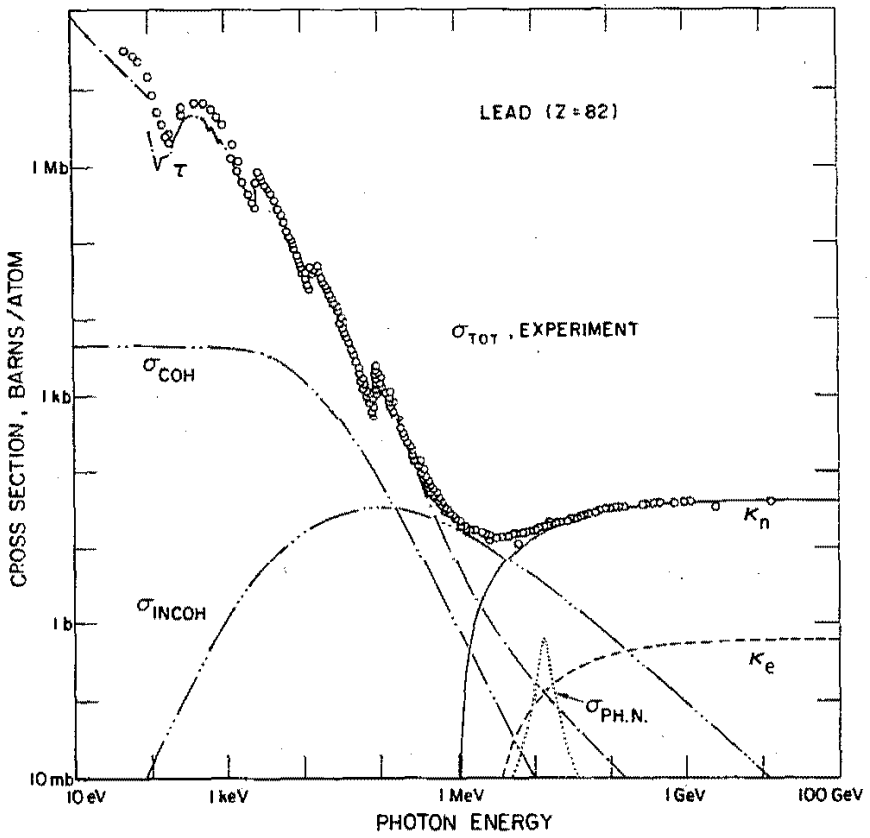

Figure 2.4: Contributions to the photon interaction cross section as a function of the photon energy. τ is the photoelectric effect, σ_{COH} is Rayleigh scattering, σ_{INCOH} is Compton scattering, κ_{n} and κ_{e} are pair production off of atomic nuclei and electrons respectively in lead [14].

energy loss due to ionization is equal to the average energy loss due to bremsstrahlung is called the critical energy ϵ_{C}. The critical energy depends both on the atomic number Z of the material, and more strongly, on the mass of the particle in question. The critical energy is proportional to m^2, meaning that for energies typically reached in experiment the bremsstrahlung component to the energy loss can be insignificant for particles with masses

even as low as 100 MeV (muons and pions for example). While photons are usually discussed in terms of mean free path, electron interactions with matter are characterized by the energy lost per unit distance which is also a function of energy ($-\frac{dE}{dx} = \frac{E}{\chi_0}$). χ_0, known as the radiation length, defines this energy loss rate and is the average distance an electron will travel before radiating a photon.

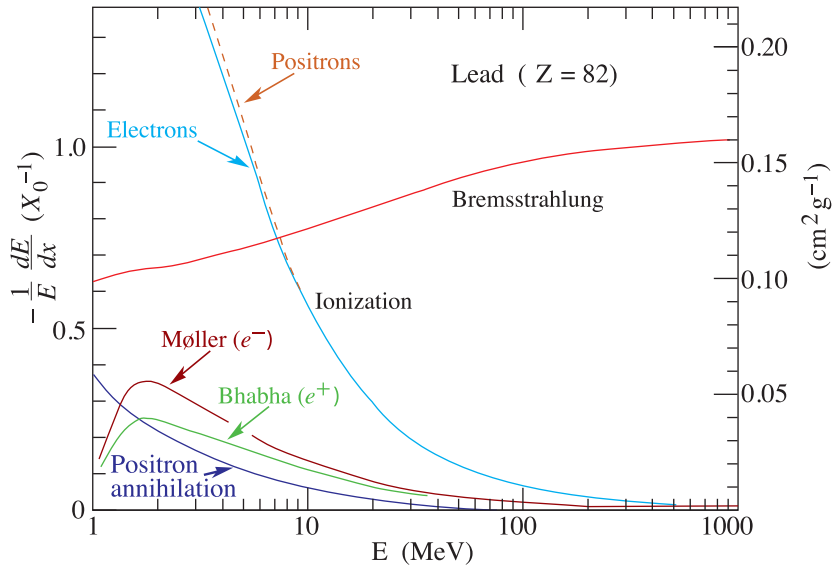

Figure 2.5: Energy loss per radiation length as a function of particle energy for electrons/positrons in lead [1].

The dominant interaction mechanism for high energy photons is pair production, which results in a high energy electron/positron pair, and light high energy charged particles lose energy primarily by emitting photons. With this in mind it is easy to imagine that a single high energy EM particle will lead to a large cascade of lower energy EM particles while travelling through a material. These cascading events (known as electromagnetic showers) tend to remain in a narrow cone around the trajectory of the initiating particle, with the tightness of the cone being independent of the initial energy of the particle (see Molière radius in [12]). Another feature of electromagnetic showers is that, relatively speaking, they do not penetrate very deeply into the material. These are properties that will be useful in identifying EM showers. See Sec. 3.1.

The ATLAS detector makes use of sampling calorimeters. In a sampling calorimeter a dense material used to create the particle shower (absorber) alternates with an active material that measures the energy deposited. While there is a disadvantage to this design with energy deposited in the absorber being invisible to the detector, having the full energy of the particle being deposited in a shorter length of material allows for a reduction in size of any additional detectors beyond the calorimeter. It is also typically cheaper. In both the barrel and endcaps the absorber for the EM calorimeter is lead and the active material is

EM calorimeter		
Longitudinal layers, η coverage		
Presampler	1, $\mid \eta \mid < 1.52$	1, $1.5 < \mid \eta \mid < 1.8$
Calorimeter	3, $\mid \eta \mid < 1.35$ 2, $1.35 < \mid \eta \mid < 1.475$	2, $.1375 < \mid \eta \mid 1.5$ 3, $1.5 < \mid \eta \mid < 2.5$ 2, $2.5 < \mid \eta \mid < 3.2$
FCal		1, $3.1 < \mid \eta \mid < 4.9$
Granularity $\Delta\eta \times \Delta\phi$		
Presampler	0.025 x 0.1, $\mid \eta \mid < 1.52$	0.025 x 0.1, $1.5 < \mid \eta \mid < 1.8$
Calorimeter layer 1	0.003 x 0.1, $\mid \eta \mid < 1.4$ 0.025 x 0.025, $1.4 < \mid \eta \mid < 1.475$	0.05 x 0.1, $1.375 < \mid \eta \mid < 1.425$ 0.025 x 0.1, $1.425 < \mid \eta \mid < 1.5$ 0.003 x 0.1, $1.5 < \mid \eta \mid < 1.8$ 0.004 x 0.1, $1.8 < \mid \eta \mid < 2.0$ 0.006 x 0.1, $2.0 < \mid \eta \mid < 2.4$ 0.025 x 0.1, $2.4 < \mid \eta \mid < 2.5$ 0.1 x 0.1, $2.5 < \mid \eta \mid < 3.2$
Calorimeter layer 2	0.025 x 0.025, $\mid \eta \mid < 1.4$ 0.075 x 0.025, $1.4 < \mid \eta \mid < 1.475$	0.05 x 0.025,$1.375 < \mid \eta \mid < 1.425$ 0.025 x 0.025, $1.425 < \mid \eta \mid < 2.5$ 0.1 x 0.1, $2.5 < \mid \eta \mid < 3.2$
Calorimeter layer 3	0.05 x 0.025, $\mid \eta \mid < 1.35$	0.05 x 0.025, $1.5 < \mid \eta \mid < 2.5$
FCal		0.2 x 0.2, $3.1 < \mid \eta \mid < 4.9$

Table 2.1: Main parameters of the electromagnetic calorimeter system in ATLAS [11]

liquid argon (LAr), while in the forward region a copper/LAr combination is used. When charged particles, both primary and secondary, pass through the active medium the liquid argon is ionized and the charge is collected on kapton electrodes. A breakdown of how the number of sampling layers and the resolution of the EM calorimeter vary with η in the central and endcap regions is shown in Table 2.1.

Hadronic Calorimeter

There are many similarities between EM calorimeters and hadronic calorimeters. Hadronic calorimeters rely on both electromagnetic and nuclear interactions between the particles to be measured and the detector. These interactions produce secondary particles, which go on to have subsequent interactions with the material in the calorimeter. This process, known as a hadronic shower, continues until the secondary particles reach a low enough energy that they are fully absorbed by the material and their energy is measured through ionization. The differences between hadronic and electromagnetic showers are the size of the shower, both in depth and width (with hadronic showers being larger in both dimensions) and the event by event variations of the showers (with hadronic showers being subject to much larger fluctuations because of the large number of available types and the character of nuclear interactions).

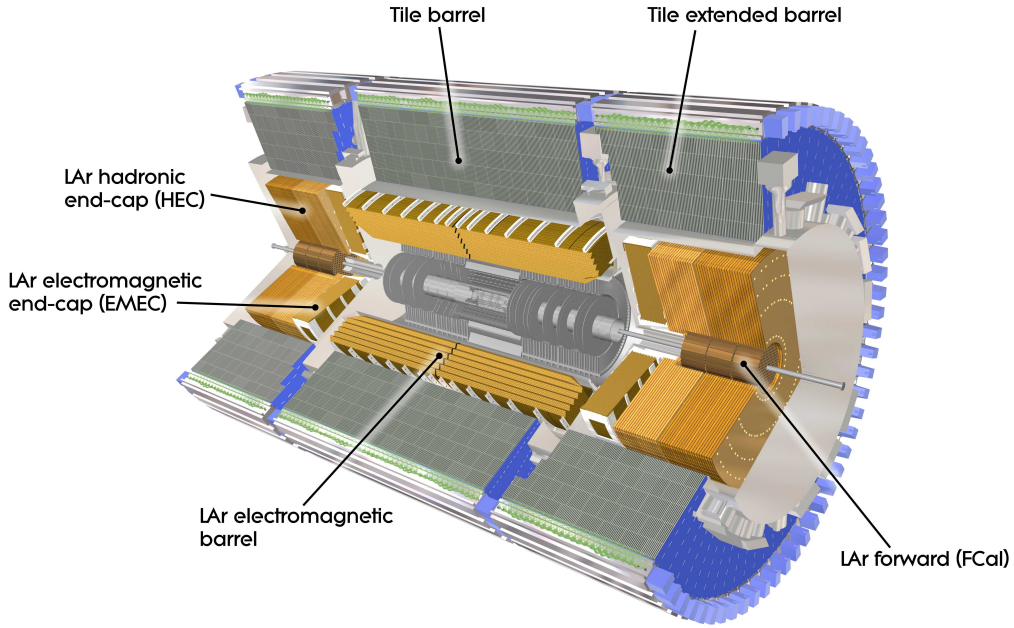

Figure 2.6: Computer generated image showing how the various subsystems of the ATLAS calorimeter are arranged. ATLAS Experiment Image: Copyright CERN, [15].

As the lowest mass charged hadron is over 200 times more massive than the electron ($\pi^{\pm}$ at 140 MeV) it is safe to assume that at energies which will be achieved in the ATLAS detector bremsstrahlung will not be an important energy loss mechanism for hadrons. Ionization and excitation on the other hand are still relevant contributors to the overall energy loss of hadrons. The rate at which energy is lost via these mechanisms for particles which are heavier than an electron is described by the Bethe-Bloch formula,

$$-\frac{\mathrm{d}E}{\mathrm{d}x} = \frac{2CZz^2}{A\beta^2}\left[\ln\left(a\gamma^2\beta^2\right) - \beta^2 - \frac{\delta}{2}\right], \tag{2.1}$$

where C is a constant, z is the charge of the incident particle, Z and A are the atomic number and weight of the material being ionized, β and γ are the velocity and Lorentz factors of the incident particle, δ is a parameter describing density effects, and a depends on the electron mass and the ionization energy of the absorber.

While these particles do interact electromagnetically it is the interactions between the hadrons and the atomic nuclei via the nuclear force (resulting in secondary hadrons) that account for the majority of the energy loss. The average distance between these interactions is much larger than the radiation length which is the cause of the extra penetration depth of these showers compared to EM showers. To get an idea of the difference in length of hadronic and electromagnetic showers one needs only to pick a material, say copper, and

Hadronic calorimeter		
Tile calorimeter		
	Barrel	Extended barrel
Coverage	$\mid \eta \mid < 1.0$	$0.8 < \mid \eta \mid < 1.7$
Number of layers	3	3
Granularity	0.1 x 0.1	0.1 x 0.1
Last layer only	0.2 x 0.1	0.2 x 0.1
Hadronic endcaps		
Coverage	$1.5 < \mid \eta \mid < 3.2$	
Number of layers	4	
Granularity	0.1 x 0.1, $1.5 < \mid \eta \mid < 2.5$	
	0.2 x 0.2, $2.5 < \mid \eta \mid < 3.2$	
Forward calorimeter		
Coverage	$3.1 < \mid \eta \mid < 4.9$	
Number of layers	2	
Granularity	$\approx$ 0.2 x 0.2	

Table 2.2: Main parameters of the hadronic calorimeter system in ATLAS [11].

compare the hadronic interaction length λ_{int} (15 cm in copper) to the radiation length χ_0 in the same material (1.4 cm) [13]. The large width of hadronic showers is caused by large transverse momentum transfer in the nuclear interactions.

While a large fraction of the particles resulting from the nuclear interactions are pions ($\approx$ 90 %), other particles like protons, neutrons, kaons, etc. are also produced. On average the three pion flavours (π^0, π^+, and π^-) are produced with equal frequency, with large variations being possible between any two given interactions. Charged pions interact with matter much differently than their neutral counterparts. Where charged pions have a mean lifetime τ of 2.6 x 10^{-8} s ($c\tau$ = 7.8 m) and tend to have further nuclear interactions before decaying, neutral pions have a much shorter lifetime ($c\tau$ = 25 nm) and quickly decay into a pair of photons which initiate EM showers within the hadronic shower [1]. As a result of this important difference the amount of detectable energy deposited in a calorimeter from a hadronic shower can have a strong dependence on the fraction of neutral pions from the first few interactions.

The fraction of the total energy deposited in the calorimeter by these small EM subshowers (f_{em}) varies as a function of the energy of the particle initiating the shower, increasing from $\approx$ 30% for particles at 10 GeV to $\approx$ 50% for particles at 100 GeV. The rest of the energy can be accounted for as follows: 34% is used to overcome the nuclear binding potential to release protons and neutrons (so-called invisible energy), 10% is in low energy (typically 3 MeV) neutrons which have been released from nuclear spallation reactions, and 56% is deposited via ionizing particles, where 2/3 of that is via protons [13]. Therefore,

a large portion of the non-EM energy is deposited in the calorimeter via low energy free nucleons, not relativistic pions.

The hadronic calorimeter is also a sampling calorimeter. The similarities with the EM calorimeter go even further in that in both the FCal and endcaps the active material for the hadronic calorimeter is LAr, with the absorber in the endcaps being copper and the absorber in the forward region being tungsten. In the barrel the hadronic calorimeter uses steel as the absorber material and plastic scintillator as the active material. The number of sampling layers and the granularity of each of the regions of the hadronic calorimeter are shown in Table. 2.2.

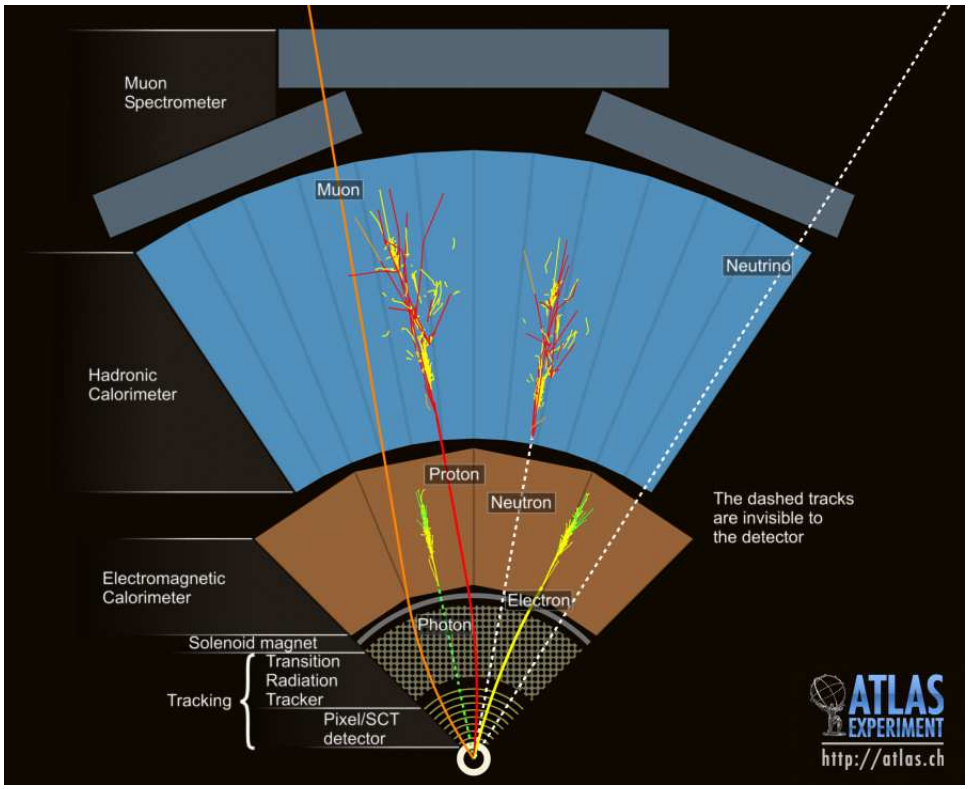

Figure 2.7: Illustration showing how and where various particles interact with the ATLAS detector. Note that while neutrons and protons are shown to only begin interacting in the hadronic calorimeter the showering does in fact begin in the EM calorimeter. The muon track bends in the magnetic field of the ID and deposits small amounts of energy in every detector along it's path. Note that muons are the only charged particles to reach the muon spectrometer [11].

2.2.5 ATLAS Hardware: Muon Spectrometer

Muons are 200 times heavier than electrons, are typically minimum ionizing at the LHC and therefore do not produce electromagnetic showers. Since muons also do not interact via the nuclear force, they do not produce hadronic showers either. Thankfully as they are charge carriers they do interact with the tracking systems in the inner detector, and with the

help of a second tracking system beyond the hadronic calorimeter they are easy to identify as they are the only ionizing particles that regularly pass through the entire calorimeter. The magnetic field for the muon spectrometer is provided by large superconducting air-core toroids, with the field in the central region ($|\eta| < 1.4$) being provided by the barrel toroid and in the forward regions ($1.6 < |\eta| < 2.7$) by two relatively smaller endcap magnets. In the transition regions the magnetic fields are provided by a combination of these three magnets.

In the central barrel region the muon hits are measured in three separate layers (stations) that are arranged in concentric cylinders with radii of about 5, 7.5, and 10 m [16]. These distances are chosen to measure the muons' position as they enter, are at the midpoint, and again as they exit the magnetic field to best measure the deflection of the muons and hence their momentum. The two endcaps consist of four wheels at distances of 7.4, 10.8, 14, and 21.5 m from the interaction point. The additional wheel at 10.8 m is to allow for the full three measurements of the muon trajectory in the region that is uncovered by the outermost wheel (see Fig. 2.8).

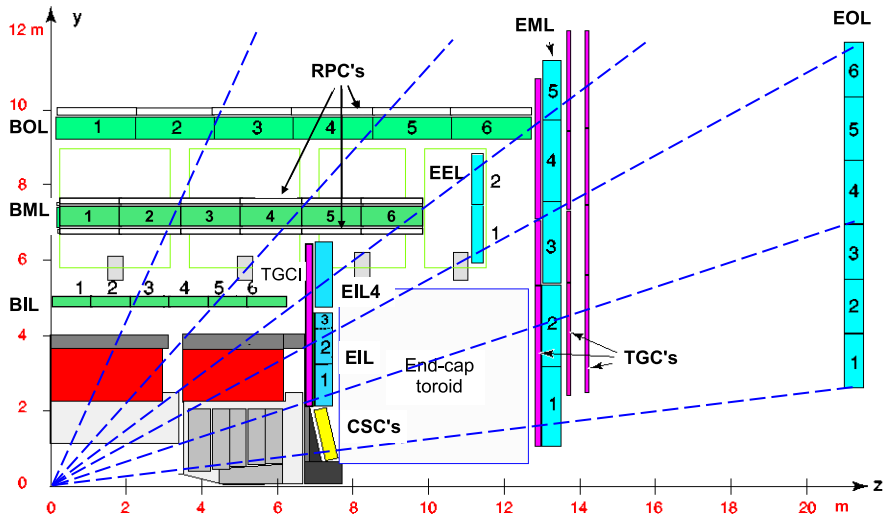

Figure 2.8: Cross-section of the muon system in a plane containing the beam axis (bending plane). The light green and light blue cells are the MDTs, the yellow cell represents the CSCs, the light purple lines are the TGCs and the labeled black lines are the RPC's.

Monitored Drift Tubes (MDT)'s are used to make the position measurements in the outer two layers of the muon spectrometer over the full eta range ($|\eta| < 2.7$), and they are also used in all but the most forward portion of the innermost layer ($|\eta| < 2.0$). MDTs make use of the trail of ionized particles left behind as a charged particle passes through a gas in a similar way to the TRT (see Sec. 2.2.3), where the gas used here is a 93/7 mixture of Ar/CO_2 [11]. The most forward region of the inner most layer of the

endcaps experiences larger particle rates than is generally considered safe for operating MDTs (greater than 150 Hz/cm^2). For this reason this region uses Cathode Strip Chamber (CSC)'s, which have better time and space resolution as well as lower neutron sensitivity. CSC's consist of an array of positively charged anode wires which run perpendicular to a series of negatively charged cathode plates all immersed in an active gas medium (80/20 Ar/CO_2). Charged particles ionize this gas and the electrons/ions are collected on the anodes/cathodes, providing measurements in both directions.

The MS also contains additional detectors to be used for triggering (see Sec. 2.2.6), where these detectors must have a fast enough response to deal with the large collision rates present at the LHC. In the central region ($| \eta | < 1.05$) three layers of Resistive Plate Chambers (RPC) are used (two sandwiching the central station and a third either on the inside or the outside of the third station). RPC's contain no wires and consist of two parallel charged plates surrounding an active gaseous medium (94.7/5/0.3 of $C_2H_2F_4$/Iso-C_4H_{10}/SF_6), where charged particles ionize the gas and the electrons are collected on the anode plate. The forward region ($1.05 < | \eta | < 1.4$) has additional complications with regards to triggering compared to the central region (larger momentum for the given transverse momentum, inhomogeneities in the magnetic field, higher occupancy), motivating the use of Thin Gap Chamber (TGC)'s which are better suited to handle this environment. TGC's consist of a number of parallel anode wires between two cathode plates, immersed in an active gas (55/45 CO_2/n-pentane). Three layers of TGC are used in the forward region, organized around the second muon stations (see Fig. 2.8). TGC's are distinguished from Multiwire Proportional Chamber (MPC)'s (not in ATLAS) by having a wire to cathode distance (1.4 mm in this case) smaller than their wire to wire distance (1.8 mm in this case).

2.2.6 Triggers

During both 2015 and 2016 the LHC used a beam bunch spacing of 25 ns. This resulted in crossing rates of 40 MHz at the centre of the ATLAS detector. With each event potentially taking up to 2 MB to store, recording, storing, and analyzing all of these data can be a problem. Moreover, the large majority of the collisions are elastic collisions or low p_{T} dijet events which are of little interest in this high energy environment. The solution to this problem is to only record a certain fraction of the total number of events that have been produced. This must be done in a way that maximizes the number of rare events of interest recorded while simultaneously removing as many low interest events as possible. The triggering system uses a combination of hardware and software tools to perform this task [17].

The trigger system consists of two parts the first being the Level-1 (L1) trigger. The L1 trigger is hardware based and reduces the number of events to be considered from 40 MHz down to 100 kHz. It uses a coarser object definition than the full event reconstruc-

tion. Selections can still be made based on energy thresholds for given objects, as well as more topological information like particle isolation requirements or a specified range for the invariant mass of a combination of objects.

The second stage of the trigger system, which is implemented in software on a computer farm, is known as the high-level trigger, or HLT. In the HLT some full offline-like unseeded reconstruction algorithms can be run, including topo-clustering (see Sec. 3.3.1) and muon reconstruction. This is not always the case. For example L1 tracking information is used to seed tracks in the HLT to reduce the reconstruction time. The HLT is designed to reduce the event rate from the 100 kHz output of the L1 trigger down to 600 Hz, which can be increased to 1-1.5 kHz at peak luminosities. Events that pass the HLT criteria are recorded on computer tape for subsequent analysis.

While these triggers can be very efficient at selecting relatively rare more "interesting" events to be recorded for future study, not all event topologies desired by the various physics groups in the ATLAS collaboration are infrequent enough that every instance of that event can be stored. In these cases, only a randomly selected, but fixed-fraction, subset of the events is stored for subsequent analysis. This is called prescaling. The true number of events of these types which have actually occurred can then be determined using the random acceptance rate.

Chapter 3

Physics Object Reconstruction

3.1 Electron/Photon

The reconstruction of electrons and photons with the ATLAS detector involves measurements by both the electromagnetic calorimeter and the inner detector. The process begins with a list of clusters found using a sliding window algorithm with a size equal to 3 x 5 cells (η x ϕ) in the second layer of the EM calorimeter. Tracks are also fit in the inner detector, a process which begins by clustering together neighboring cell hits in each layer of the tracking system. Track seeds are then created using sets of three of these clusters and assuming a perfect helical trajectory in a uniform magnetic field. Track seeds can be rejected based on their reconstructed momentum, on impact parameter (how close they come to the interaction point), and on not being near enough to additional clusters [18]. The electron and photon reconstruction algorithms use a modified version of the list of reconstructed tracks, where tracks containing only hits in the TRT are simply copied over and tracks with silicon hits are refit to account for the potentially large radiative energy loss that electrons can experience during their flight [19]. Tracks become associated with a calorimeter cluster if they are close enough in η-ϕ (0.05 x 0.05 with Si, 0.35 x 0.02 without) and pass some quality criteria. Clusters with tracks are candidates for either electrons or photons that have converted to an electron-positron pair, where either both or only one track is reconstructed.

At this stage clusters are expanded to 3 x 7 (5 x 5) in the barrel (endcap). Clusters with two tracks without pixel layer hits or with no single track having more than 4 Si hits are labeled as photon candidates, while clusters with single tracks including pixel hits are labeled as electron candidates. The energy of these larger clusters is used as the input energy of the object for calibration, while the η and ϕ are taken from the track(s) (if present) or the cluster (with no tracks).

3.2 Muons

Muons are reconstructed using information from both the muon spectrometer and the inner detector. Muon reconstruction begins by creating station by station muon track segments which are then fit into a combined track. The fit takes into account the magnetic field from the toroid magnets and a detailed description of the material density throughout the detector. These spectrometer-only muon tracks are then propagated back through the calorimeter (again taking the energy the muons deposit into account) into the inner detector. Here they are combined with tracks left by the muon in the tracking detector that have been reconstructed using the regular all-purpose track reconstruction algorithm.

3.3 Jets

A result of colour confinement (see Sec. 1.1) is that single particles with colour charge cannot be observed. This does not actually eliminate collisions where a large amount of energy is transfered to a single quark or gluon. When these types of collision do occur (they are actually the most common in a p-p collider) what is seen is a large "spray" of hadrons all traveling in roughly the same direction as the original single particle. This spray is created iteratively by quarks radiating gluons, which create quark/anti-quark pairs, which subsequently radiate additional gluons, a process known as parton showering. When the amount of energy per gluon drops below the pair creation threshold a second stage known as hadronization occurs, where gluons undergo one final split and the secondary coloured quarks combine into colour neutral mesons ($q\bar{q}$) or baryons (qqq). Collectively these two stages are known as quark or gluon fragmentation.

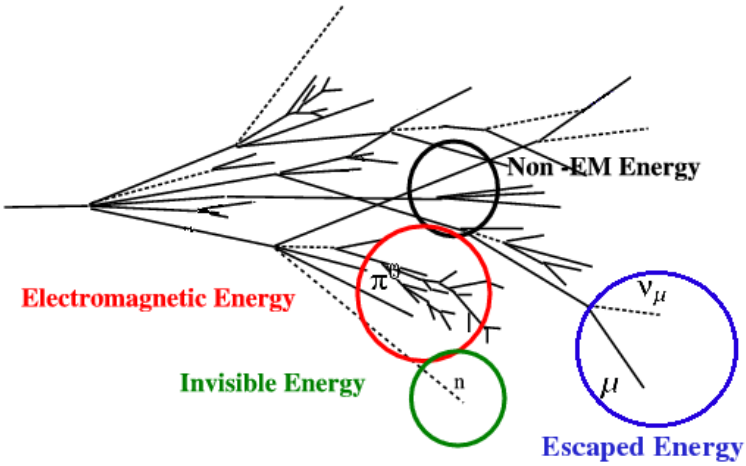

Figure 3.1: Example showing the progression of a calorimeter shower.

It is now worth going into slightly more detail as to why QCD behaves differently than QED, and pointing out a few additional consequences. In quantum field theories calculations are done using series expansions. Each term in the series is scaled by the coupling constant of the force in question raised to some power. In the case of QED the coupling constant is such that terms with the coupling constant to higher orders are quite small and at some point can be ignored, i.e. the series converges. These smaller and smaller terms can be considered corrections to the larger terms, making QED what is known as a perturbative theory. There is an energy dependence to the coupling constant, where it becomes smaller at lower energies as a result of the bare charge of particles being partially screened by a cloud of virtual particles.

With QCD this screening goes the other way, with the apparent colour charge of quarks growing at lower energies. This is because along with the charge screening provided by light quarks there is a larger anti-screening effect provided by the gluons (as they also carry colour charge). This effect is such that at low enough energies the coupling constant becomes larger than one and the series does not converge. This makes QCD non-perturbative leaving only phenomenological models to simulate the behaviour of QCD at low energy. This means that for the simulated samples that are used in this thesis there is both a perturbative QCD portion (parton showering) and a phenomenological portion (hadronization).

As was mentioned in Sec. 2.2.4 the interactions between hadrons and matter tend to lead to wide and deep calorimeter showers[1] that are subject to large fluctuations. The large number of hadrons moving in the same direction combined with this calorimeter showering profile means that accurately measuring the properties of these sprays in the calorimeter can be challenging. The strategy that is generally used is two staged. First, individual particle candidates are constructed followed by a second stage where these particle candidates are combined with nearby particles into groups that are known as jets.

Multiple options are available for each stage. Early on ATLAS has used calorimeter towers (stacks of cells in the calorimeter pointing back to the centre of the inner detector) and "TopoTowers" (towers with additional noise suppression) as inputs to jet finding algorithms, but they are not necessarily a good representation of a single particle. Tracks in the inner detector can also be used to define jets, although using only tracks ignores all neutral particle information obtained by the calorimeter. The most commonly used inputs to jet finding algorithms in ATLAS are topological clusters of calorimeter cells and truth particles[2].

[1]Calorimeter showers are created as particles interact with the material of the calorimeter, and are distinct from the parton showers discussed in the previous paragraph.

[2]In ATLAS truth particles are simulated particles that are stable, which is defined as having a lifetime $c\tau_0$ greater than 10 mm. The list of truth particles does not include particles that are the result of showering in the detector, and for jet building purposes muons and neutrinos are also not included [20].

3.3.1 Topological Clusters

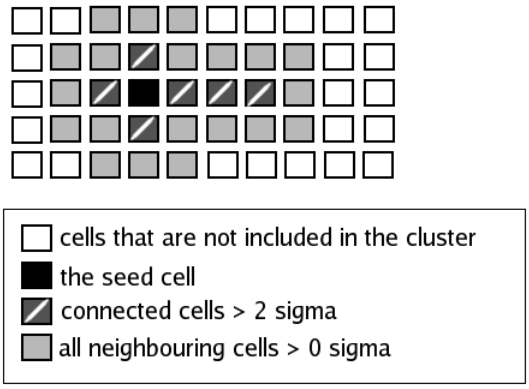

Figure 3.2: Example of the 4-2-0 topo-cluster algorithm showing how cells passing the different thresholds are grouped together.

In the context of high energy physics detectors topological (topo) clustering is an algorithm where individual calorimeter cells are grouped together based on how significant the energy deposited within a given cell is relative to its neighbours and to the expected noise. Topo-clusters can have a wide variety of three-dimensional shapes, which allows them to include a large fraction of the energy deposited by incoming particles while ignoring much of the noise.

Topo-clustering begins by determining the significance of the energy deposited within each cell, which is defined as the absolute value of the measured energy divided by the average expected noise for that cell[3]. All cells above some predetermined threshold t_{seed}, referred to as seeds, are then put into a list of proto-clusters. Next for each seed, cells with an energy above a second threshold, $t_{\text{neighbour}}$, and which are "neighbours" to a proto-cluster are added to that proto-cluster. In this case neighbours consist of the eight neighbours in the same layer of the calorimeter as the seed cell, as well as all cells in adjacent layers which overlap or partially overlap with the cell in question. Neighbours to proto-clusters are iteratively added to proto clusters until there are no longer any neighbour cells above $t_{\text{neighbour}}$. The final stage of cluster building involves adding a single final layer around each proto-cluster of all neighbouring cells above some third threshold, t_{cell} [21]. The thresholds used in topo-clustering are usually reported as $t_{\text{seed}} - t_{\text{neighbour}} - t_{\text{cell}}$; ATLAS uses a 4-2-0 clustering scheme. In addition to 4-2-0, 4-3-0 topo-clusters are also used in ATLAS to reconstruct low p_T electrons, but they are not considered in this thesis.

[3]The average electronic noise expected in each cell is removed from the measured energy, which can lead to negative energy cells/clusters

After all clusters have been fully formed there is an additional stage where clusters are split. This process begins by looking for local maxima within a given cluster, which are defined as a cell having an energy above 500 MeV with at least four neighbours, none of which have a higher energy than the cell in question. Clusters are built surrounding these local maxima ignoring thresholds. Cells at the boundary of these two subclusters have their energy split between the two, where the splitting is determined using the relative energy of the subclusters as well as the distance between the cell to be split and the two proto-cluster centres. This splitting is done to improve both the Jet and the Missing Transverse Energy (MET) (see Sec. 3.4) resolution by allowing each cluster to better represent a single stable particle at truth level.

While topo-clusters do a relatively good job of representing the visible energy deposited in the detector by a single particle they are not perfect. Clustering may leave some visible energy outside of the boundaries of a cluster, energy may be deposited in dead material, or the energy may simply be mis-measured as the response to EM energy of the ATLAS detector (e) is not equal to the response of hadronic energy deposits (h). These are the factors that motivate the second collection of clusters used by ATLAS. This second collection begins with the original (EM scale) clusters and applies a series of cell-by-cell weights based on energy density in an attempt to correct the calorimeter response problem at the cluster level. The weights are one for EM-like deposits (high energy density) and greater than one for hadron-like deposits (low energy density). This calibration scheme is known as the Local Hadronic Cell Weighting (LC) scale. The applied corrections depend on energy-based moments of the cluster. The depth and density of the cluster is used for EM/Had identification for example. The correction also depends on the physical location of the cluster which is used to estimate the energy lost in dead material. This calibration is based on Monte Carlo simulation.

3.3.2 Jet Finding

In order to meaningfully compare experimental results and fixed order QCD calculations jet algorithms must behave in a way that follows certain criteria [22]. Two of these criteria are infrared and collinear safety, which means that the reconstruction should be insensitive to soft and collinear radiation, respectively. Without these criteria the jet topology in simulated events would be very dependent on how the low p_{T}/small angle singularities in the parton splitting functions are handled (i.e. low energy gluons emitted as small angles), making it difficult to compare theory to experiment. These considerations mean that the most straight forward possibility of searching for the area with the largest energy in a given cone (cone jets) may not be the best option (see Fig. 3.3). A group of jet finding algorithms that satisfy these criteria are sequential recombination algorithms, which begin with a series of inputs and (as the name suggests) sequentially combine the inputs following certain criteria into full jets. The motivation for these types of algorithms is to attempt to recapture the nature

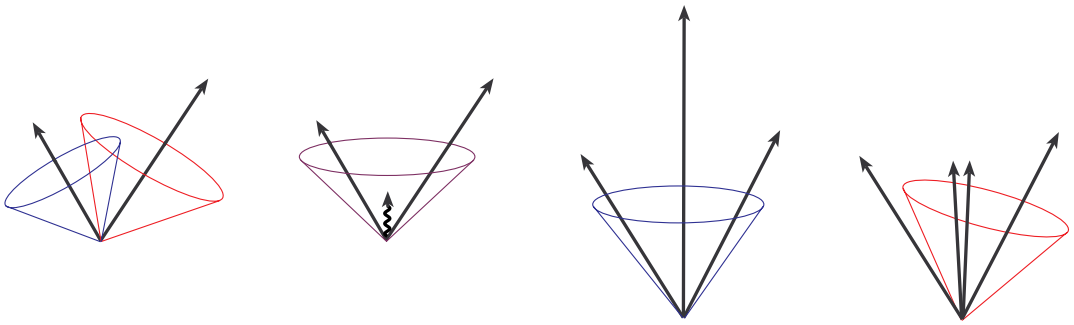

(a) Infrared radiation merging jets.

(b) Collinear radiation changing jet topology.

(c) Jet existence depending on collinear radiation.

Figure 3.3: A few examples of how soft infrared/collinear radiation can affect the reconstructed jet topology of an event. In example *a*) soft infrared radiation causes two potential jets to merge into a single jet. In example *b*) collinear radiation causes the central particle to be lower down the energy-weighted list of jet seeds, changing the jet topology. Example *c*) shows how the presence of collinear radiation has the possibility to lower the reconstructed energy below the jet seed threshold altogether. Figures from [22].

of the parton showering phase. The family of sequential algorithms used in ATLAS is the k_{t} family [23]; specifically k_{t} jets, Cambridge/Aachen jets, and the most commonly used type, anti-k_{t} jets (where k_{t} is the transverse momentum of the jet components). Objects that are used as inputs to these algorithms by ATLAS include tracks, truth particles (in Monte Carlo samples), clusters, etc. These algorithms all begin by constructing a list of proto-jets, which consists of four vectors representing all of the inputs at the desired scale (e.g. EM or LC clusters for calorimeter jets). Next a "distance" in momentum/angle space between every pair of proto-jets is calculated, defined as:

$$d_{ij} = min\left(p_{\mathrm{T},i}^{2n}, p_{\mathrm{T},j}^{2n}\right)\frac{\Delta_{ij}^2}{R^2}, \tag{3.1}$$

where Δ_{ij} is

$$\Delta_{ij} = \sqrt{(\phi_i - \phi_j)^2 + (\eta_i - \eta_j)^2}, \tag{3.2}$$

R is a tunable size parameter, and the parameter n determines the behaviour of the algorithm, with n=1,0,-1 being the k_t, Cambridge/Aachen, and anti-k_t algorithms respectively. Additionally for each proto-jet a distance to the beam pipe is calculated using:

$$d_{iB} = p_{T,i}^{2n}. \tag{3.3}$$

The jet building is then performed by finding the smallest distance parameter. If the smallest distance parameter corresponds to a proto-jet/beam pipe distance this proto-jet is selected as a jet and removed from the list of proto-jets, while if the smallest distance is between a proto-jet pair those proto-jets are combined into a new proto-jet which is added to the list. Various four-momentum combination schemes exist (p_T weighted, p_T^2 weighted) but ATLAS uses a simple addition of the four-vectors of the proto-jets using the FastJet implementation [24].

While the k_t, Cambridge/Aachen, and anti-k_t algorithms are all used in ATLAS they each serve a different purpose. One large difference between the k_t and the anti-k_t algorithms is that the k_t algorithm begins by combining the lowest p_T proto-jets while the anti-k_t begins with larger p_t proto-jets. This means that proto-jets are quite stable in location as they grow in the anti-k_t algorithm, which tends to lead to mostly circular jets. This is not the case for k_t jets, which tend to have a wide variety of final jet shapes (see Fig. 3.4). This k_t growth can lead to some pathological cases where the jet grows well beyond what one would intuitively call a jet.

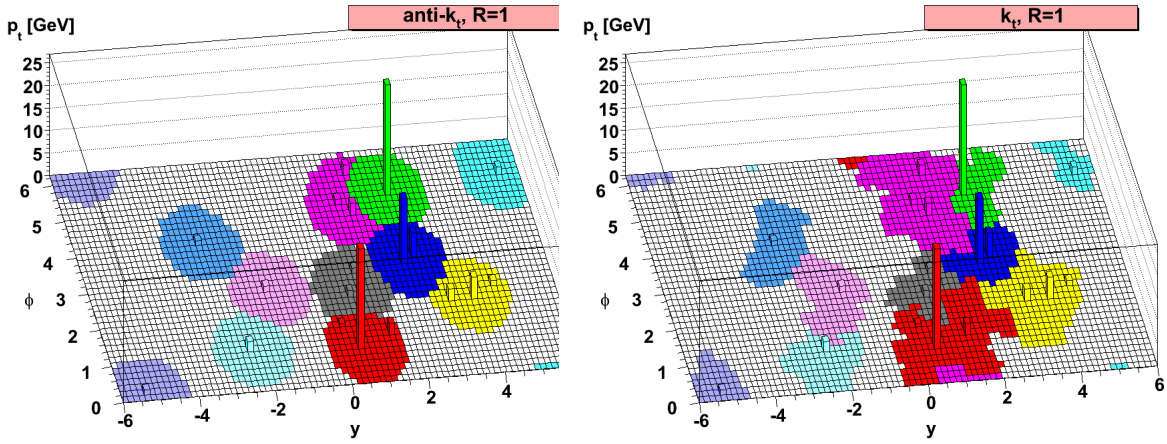

(a) Anti-k_t jets using R=1.0.

(b) k_t jets using R=1.0.

Figure 3.4: Outputs of both the anti-k_t and k_t algorithms for the same event, where both have been run using size parameter R=1.0. Truth particles from an event generated with HERWIG have been used as inputs. Figure from [23].

3.4 Missing Transverse Energy

While large multipurpose detectors like ATLAS do a good job of detecting a wide range of particles they do not and cannot measure 100% of the energy of every particle produced in every collision. Some of this missed energy is from particles interacting with the detector and having a response lower than one. Sometimes the more interesting energy that is undetected comes from particles that do not interact with the detector at all (eg. neutrinos). It is not always straightforward to measure how much energy the calorimeter did not detect. Fortunately in a p-p collider all of the initial momentum of the collision is along the beam line, with the exception of a small (effectively negligible) amount of transverse momentum within the protons themselves. Using the conservation of momentum one can use as a measurement itself an imbalance in momentum along any given axis in the transverse plane and interpret the missing energy that would balance the momentum as a non-interacting particle once the detector has been fully calibrated. This quantity is known as the MET or E_{T}^{miss}.

The MET, like jets, can be constructed using a number of different inputs at various scales. For many analyses in ATLAS the most appropriate MET to use is one where all physics objects are used at their fully calibrated scales. This is done by starting with some base collection (EM clusters, LC clusters, tracks, etc.) then adding calibrated physics objects while removing overlapping base objects to avoid double counting. The final MET is calculated by taking the negative vector sum of the transverse momentum of the remaining base objects and all physics objects. The work described in this thesis uses topo-cluster based MET definitions with only photons, electrons, and muons being replaced by the fully calibrated objects.

Chapter 4

Jet Energy Scale

Recalling from Sec. 3.3 that jets evolve through many different stages (see Fig. 4.1) it becomes clear that to reasonably compare experimental results to theoretical calculations one must decide on a scale at which to make the comparison. This is usually done by bringing all results to the "particle jet" or "truth jet" scale, as described in Sec. 3.3.2. This makes the results detector independent also allowing for cross experiment comparisons. This is accomplished by carefully studying the relationship between the particle scale jet energy and the detector scale jet energy, known as the JES. A successful JES accounts for escaped/invisible energy, algorithm effects, energy from multiple interactions in the same beam crossing (in-time pileup) or adjacent beam crossings (out of-time pileup), etc.

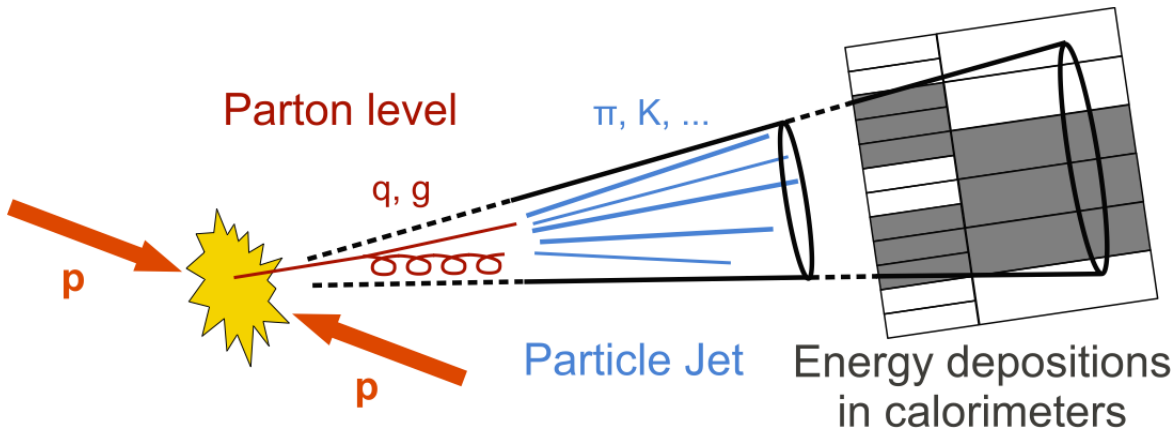

Figure 4.1: A diagram outlining the progression from parton level to a calorimeter jet.

4.1 Jet Energy Scale in ATLAS

Calibrating jets at ATLAS is a multistaged process. During the initial jet reconstruction the jet is set to originate from point (0,0,0) in the ATLAS coordinate system, so the first step is to adjust the jet to originate from the reconstructed vertex using the tracking information.

Next in order to compensate for pileup, energy is subtracted from the jet first using the average energy density observed in that given event multiplied by the active area of the jet. The area of a jet is determined by adding a large number of equally spaced particles with infinitesimally small energy (called ghost particles, see [25]) to the event and rerunning the jet reconstruction algorithm, with the number of these ghost particles which are clustered into a jet being proportional to the area of that jet. This subtraction is followed by two residual corrections, which are applied to completely remove the jet energy's dependence on pileup. One correction is based on the average number of interactions in neighbouring bunch crossings (for out-of-time pileup) and another is based on the actual reconstructed number of interactions in that given event (for in-time pileup). With pileup now removed a Monte Carlo based calibration, which corrects for the average response as a function of energy and pseudorapidity of the jet, is applied.

To improve the energy resolution and reduce the flavour (quark or gluon) dependence of the jets at this stage a series of smaller Monte Carlo based calibration factors are applied. These ideally flatten the dependence of the response on the amount of energy in the first layer of the hadronic calorimeter, the energy in the last layer of the EM calorimeter, the number of charged tracks in the jet, the width of the distribution of the tracks in the jet, and the number of track segments in the muon spectrometer behind the jet. These calibrations are collectively known as the Global Sequential Calibration (GSC) scheme [26].

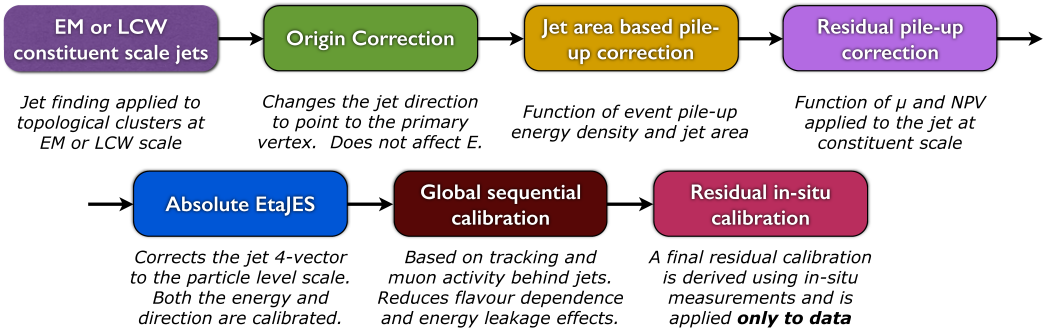

Figure 4.2: A diagram outlining the calibration scheme used by ATLAS to transform the energy from a calorimeter jet back to the energy of the particle level jet.

The last step involves applying final corrections to account for the observed differences in response between the data which have been collected and the Monte Carlo simulations. The response is measured using a series of *in-situ* techniques in both data and Monte Carlo, and the ratio is applied as a final factor to complete the calibration of the data. In general these *in-situ* techniques make use of transverse momentum balance in a system of physics objects that have been produced back-to-back in ϕ. One object, which is well measured, is

labeled as the reference object and the response of the second object is measured relative to it. These studies can be performed in dijet events where the jets land in different η regions, which is done to transfer the jet calibration from one part of the detector to another (so-called eta intercalibration), γ/Z+jet events where the jet response is measured relative to the well-measured boson to give the absolute JES, and multi jet events where one high energy jet is measured relative to several previously calibrated lower energy jets to extend the calibration to energies where the γ/Z+jet cross-section is too small to be useful.

This thesis presents work using both Z+jet and γ+jet events to study the jet energy scale in ATLAS. Only events where the Z decays into either an electron/positron pair or a muon/anti-muon pair are considered. When it comes to measuring the JES these two types of events are similar and complementary. Both offer well-measured objects that are ideally produced back-to-back in ϕ with a single jet, with a significant difference being that the cross section for γ+jet is several orders of magnitude larger. This larger cross section allows for a larger number of high energy γ+jet events, increasing the energy range that can be calibrated. Unfortunately this larger cross section also forces lower energy photon triggers to be prescaled to much lower rates. This prescaling at low energy combined with the large number of low energy dijet events being misidentified as γ+jet events makes Z+jet a much better choice to calibrate the low energy regime.

4.2 Jet Response

The largest component of the JES correction is the absolute response, which describes how the calorimeter responds to both hadronic and electromagnetic energy deposits within the jet. Even for a single incoming hadron there will be some fraction of energy deposited in the calorimeter via EM interactions. This is in part because hadrons have electric charge, but is largely due to hadrons producing particles in the calorimeter that decay electromagnetically ($\pi^0 \rightarrow \gamma\gamma$). The single-particle response (defined as $E^{\text{measured}}/E^{\text{truth}}$) can be written in terms of these two types if energy deposits as follows:

$$r(E) = f_{\text{em}}(E)\, e + [1 - f_{\text{em}}(E)]\, h, \tag{4.1}$$

where e is the response to purely EM energy deposits, h is the response to purely hadronic energy deposits, and f_{em} is the fraction of the total incoming energy that is electromagnetic in nature.

This can be further explored by using a simplistic model of a particle showering within a material. When a hadron interacts with a nucleus several new hadrons are created, with pions being produced in the largest numbers. Thanks to the (slightly broken) isospin symmetry of hadronic interactions each flavour of pion is created with equal probability, so if only pions are produced in a given interaction on average 1/3 of them will be electromagnetically decaying neutral pions. With this model in mind after the first generation of hadrons

is produced 1/3 of the available energy is electromagnetic in nature, deposited by photons resulting from the decay of neutral pions. If the charged pions making up the remaining 2/3 of the original available energy each have enough energy to cause subsequent nuclear interactions, a further $2/9^{\text{ths}}$ of the energy is deposited electromagnetically, and so on. This dependence of the fraction of EM energy on the total energy of the incident particle can be modeled using

$$f_{\text{em}}(E) = 1 - \left(\frac{E}{E_0}\right)^{m-1}. \tag{4.2}$$

Another function that has been used to model the EM fraction with success is

$$f_{\text{em}}(E) = a_0 + a_1 \ln \frac{E}{E_{\text{scale}}}, \tag{4.3}$$

where variations including higher orders of $\ln \frac{E}{E_{\text{scale}}}$ have been used as well, with ATLAS previously including both $\ln\left(\frac{E}{E_{\text{scale}}}\right)^2$ and $\ln\left(\frac{E}{E_{\text{scale}}}\right)^3$ terms into their fit [27] [28]. The response of an entire jet (R_{jet}) can be expressed as

$$R_{\text{jet}}(E) = w_h \, r(w_h \, E) + w_e \, e(w_e \, E) \tag{4.4}$$

along with Eq. 4.1 and either Eq. 4.2 or Eq. 4.3, where w_h and w_e are the fractions of particles in the jet *incident* on the calorimeter that interact hadronically or electromagnetically, respectively. These quantities are solely dependent on the parton shower and hadronization processes and are independent of any subsequent showering within the detector.

4.3 E_{T}^{miss} Projection Fraction Method

The Missing E_{T} projection fraction (MPF) method is an *in-situ* technique for measuring the jet response. It was first developed at the CDF collaboration [29] to help with their η intercalibration, and was also used by the D0 collaboration to extract an absolute jet energy scale [30]. In contrast to the p_{T} balance method, which directly compares the measured energy of the jet to the reference object, the MPF measures the response of the calorimeter to the entire recoiling system which balances the reference object.

The MPF does this using only the measured reference (or probe) energy and the MET, removing the need to explicitly include the measured jet energy in the response measurement which makes it independent of the jet algorithm that was used. It should be noted that the response still depends on the inputs to the jet finding algorithm, and therefore a MET calculated at the appropriate scale must be used. This absence of jet information in the calibration means that to perform a full *in-situ* calibration additional algorithm/jet size related corrections need to be derived. This deficiency is compensated by the fact that the MPF method is much more resilient to initial/final state radiation, which allows for looser

event selection criteria resulting in a relatively larger sample size. Furthermore, the MPF technique is relatively unaffected by pileup. This is because any energy imbalance in the transverse plane will be in a random direction with respect to the hard scattering of interest, meaning that while pileup may affect the measurement for any given event on average the MPF will not be affected.

The MPF takes advantage of the balance between the reference object and the recoiling parton to obtain a measure of the true momentum in the recoil, so the derivation of the MPF response begins with

$$\vec{p}_{\mathrm{T}}^{\,\mathrm{ref}} + \vec{p}_{\mathrm{T}}^{\,\mathrm{recoil}} = 0. \tag{4.5}$$

where $\vec{p}_{\mathrm{T}}$ is the total momentum of a given particle/object projected into the transverse plane. This momentum balance must also be considered at the calorimeter level, which in the simple case of a 2 →2 collision can be written as

$$R_{\mathrm{ref}}\vec{E}_{\mathrm{T}}^{\mathrm{ref}} + R_{\mathrm{recoil}}\vec{E}_{\mathrm{T}}^{\mathrm{recoil}} = -\vec{E}_{\mathrm{T}}^{\mathrm{miss}}, \tag{4.6}$$

where we are using R_{object} to be the response of the calorimeter to that object and in this ideal case any$\vec{E}_{\mathrm{T}}^{\mathrm{miss}}$ is a result of the fact that $R_{\mathrm{ref}} \neq R_{\mathrm{recoil}}$. We have also assumed that the masses of the particles in question are small compared to the energies involved so we approximate $\vec{p} = E\hat{p}$. $\vec{E}_{\mathrm{T}}^{\mathrm{object}}$ is known as the transverse energy of the object which is defined as

$$\vec{E}_{\mathrm{T}} = \frac{E}{\cosh(\eta)}\hat{p}_{\mathrm{T}}. \tag{4.7}$$

In this thesis only well measured objects (from test beam data and *in-situ* techniques) are used as references, so $R_{\mathrm{ref}} \simeq 1$ and small differences are well known and can be propagated to $\vec{E}_{\mathrm{T}}^{\mathrm{miss}}$. By projecting both sides of Eq. 4.6 along the direction of the reference object and using Eq. 4.5 to remove $E_{\mathrm{T}}^{\mathrm{recoil}}$ we obtain

$$E_{\mathrm{T}}^{\mathrm{ref}} - R_{\mathrm{recoil}}E_{\mathrm{T}}^{\mathrm{ref}} = -\vec{E}_{\mathrm{T}}^{\mathrm{miss}} \cdot \hat{p}_{\mathrm{T}}^{\mathrm{ref}}. \tag{4.8}$$

$$R_{\mathrm{recoil}} = 1 + \frac{\vec{E}_{\mathrm{T}}^{\mathrm{miss}} \cdot \hat{p}_{\mathrm{T}}^{\mathrm{ref}}}{E_{\mathrm{T}}^{\mathrm{ref}}}. \tag{4.9}$$

This variable, referred to henceforth as MPF, is used to measure the JES *in-situ*. What exactly the MPF measures can be made more clear by expanding out the MET. In the ideal case where only the reference object and the recoil exist (using Eq. 4.6) we get that the MPF is just the ratio of the measured energy of the recoil to the measured energy of the reference object, so it measures the response of the calorimeter to the particles making up the recoil. In practice the MET includes particles radiated by the partons participating in the hard scattering (before and after the interaction), known as initial and final state radiation (ISR and FSR), as well as the underlying event (all particles in the initial protons

which do not participate in the hard scattering), and pileup. This means that the MET can be written as

$$\vec{E}_{\mathrm{T}}^{\mathrm{miss}} = -\vec{E}_{T}^{\mathrm{ref}} - \sum_{n} \vec{E}_{\mathrm{T}}^{n}, \tag{4.10}$$

where n runs over all energy deposits in the calorimeter that are not related to the reference object. Using this definition of the MET we see that the MPF (as measured) can be written as

$$R_{\mathrm{recoil}} = 1 - \frac{E_{\mathrm{T}}^{\mathrm{ref}} + \hat{p}_{\mathrm{T}}^{\mathrm{ref}} \cdot \sum_{n} \vec{E}_{\mathrm{T}}^{n}}{E_{\mathrm{T}}^{\mathrm{ref}}} = -\frac{\sum_{n} \vec{E}_{\mathrm{T}}^{n} \cdot \hat{p}_{\mathrm{T}}^{\mathrm{ref}}}{E_{\mathrm{T}}^{\mathrm{ref}}}. \tag{4.11}$$

In this form it is much clearer that the MPF is in fact balancing all energy in the event against the reference object. Although at first this may seem like a potentially large problem for the MPF to overcome thankfully this is not the case. Both the pileup, and to a lesser extent the underlying activity, are uncorrelated with the hard scattering. This means that while this extra energy may raise or lower the measured response on an event-by-event basis when measured over a large sample they will average out to zero (to first order). It will be shown in this thesis that the effects of these extra contributions to the MET are small and can for the most part be ignored. As seen in Fig. 4.2 the ATLAS collaboration uses these *in-situ* JES studies as a residual correction to a MC-based calibration.

4.4 Jet Showering

The idealized event topology used to derive the MPF equation ignored the potential effects of a number of subtle issues which have the potential to affect the accuracy of a calibration derived using this method. One of these issues is the assumption that the response of the full hadronic recoil is the same as the response of jet which is reconstructed at the centre of the recoil. While the majority of the energy of the recoil does reside within a narrow core (the jet) there are contributions from a diffuse halo of mostly low energy particles outside of the jet but still related to the recoil. This small amount of energy from lower energy particles has a lower response than the high energy particles in the core, an effect made more significant by the noise suppressing nature of the topo-clustering algorithm.

Another issue is that the MPF is designed to measure the response of the full hadronic recoil in the calorimeter, that does not include a measure of the flow of energy in the calorimeter shower across the boundaries drawn by the jet reconstruction algorithm. This means that not all of the energy within the reconstructed calorimeter jet necessarily originated from particles in the particle/truth jet, and likewise there is no guarantee that all of the energy deposited by particles in the truth jet is reconstructed within the calorimeter jet. While a p_{T}-balance based calibration inherently measures and compensates for any potential flow of energy across the boundaries of the jet (as they are included in the jet reconstruction), an MPF-based calibration (being jet algorithm independent) does not.

These two issues could be covered by a single correction, but that correction would provide no insight into the underlying physics. Instead they will be treated independently as the showering correction, which deals with the flow of energy across the jet boundary and is mostly affected by the low energy nuclear physics modeling, and the topology correction, which deals with the difference between the jet response and the recoil response, and can be affected by both perturbative and non-perturbative QCD modelling. To define these corrections the so-called "true calorimeter response" is introduced. It is defined as

$$R_{\text{true}} = \frac{\sum_{i \in \text{particle jet}} E_i^{\text{measured}}}{\sum_{i \in \text{particle jet}} E_i^{\text{true}}}, \tag{4.12}$$

that is to say the sum of the energy measured in the calorimeter that originates from particles within the particle/truth jet divided by the total energy of the particle jet. Using this definition for the true calorimeter response the topology correction is defined as

$$k_{\text{topo}} = \frac{R_{\text{MPF}}}{R_{\text{true}}} \tag{4.13}$$

This isolates the question relating the full hadronic response to the response of the dense energy core. In addition a "showering" correction can now be defined as

$$S = \frac{R_{\text{true}}}{R_{\text{jet}}}. \tag{4.14}$$

This showering correction solely focuses on the flow of energy across the boundary of the calorimeter jet. The movement of energy across this boundary which necessitates a showering correction is caused by a combination of the physical showering within the calorimeter moving energy outside of the boundary, the difference in position of the reconstructed jet axis at particle level and reconstruction level, and particles being bent out of or into the jet by the magnetic field of the tracking system.

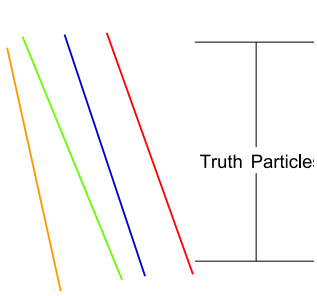

(a) Recoil at particle level

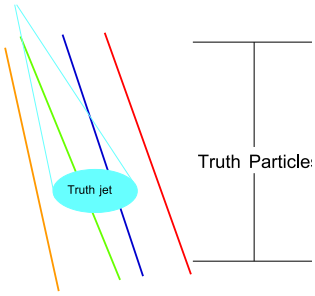

(b) Particle level jet

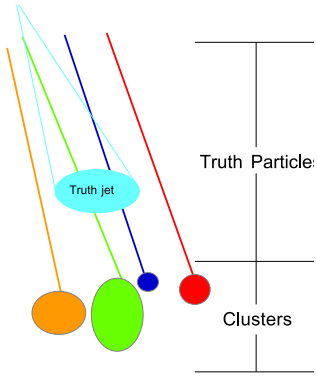

(c) Recoil at the calorimeter level

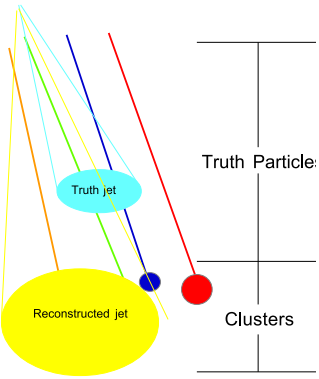

(d) Calorimeter level jet

Figure 4.3: Illustration showing some of the effects motivating the showering correction. In this diagram panel a) is intended to show the full hadronic recoil against some reference object with only four stable particles. Some fraction of these particles are then reconstructed as a truth jet in panel b). While a single particle may create two or more clusters in the calorimeter, and more than one particle can contribute energy to a single cluster, here we have assumed that each coloured particle leads to a single cluster identified with the same colour. The different sizes of these 'clusters' are meant to represent the different responses (and therefore different reconstructed energies) of these particles in panel c). The final panel shows how some energy from particles in the particle jet may not be included in the reconstructed jet, and how some energy in the reconstructed jet may originate from particles outside of the particle jet. In this diagram the showering correction would be calculated as $S = \frac{E^{\text{reco,green}} + E^{\text{reco,blue}}}{E^{\text{reco,green}} + E^{\text{reco,orange}}}$

Chapter 5

Determining the Jet Energy Scale

5.1 Samples

As seen in Sec. 4.1 the ATLAS collaboration uses a multistaged approach to calibrate jets, where the final step corrects for any measured response differences observed between selected data and simulated samples. The results presented in this thesis are primarily derived using 34.7 fb^{-1} of 13 TeV data taken between April 22nd and October 26th 2016. Some results using 3.9 fb^{-1} of 13 TeV data taken between June 3rd and November 3rd 2015 are also presented. The measured response in data is compared to results derived using simulated samples. In γ+jet the nominal simulated sample has been generated using the leading order event generator PYTHIA 8 [31] and the NNPDF2.3LO Parton Distribution Function (PDF) set [32]. The PDF describes how the momentum of the proton is shared between its various parton constituents. For the Z+jet nominal sample the hard scattering is simulated as a $2\rightarrow3$ scattering event using the next-to-leading-order generator POWHEG [33–35] and the CTEQ6L1 PDF set [36]. PYTHIA 8 provides the fragmentation for both of these samples using p_{T}-ordered parton showers and the Lund String Model [37]. These generated events are propagated through a simulation of the ATLAS detector based on GEANT4 [38]. The interactions of the propagating particles are modeled using the Bertini Cascade model up to 5 GeV, with a smooth transition to the FTFP model for higher energies [39]. In the Bertini Cascade model the incident hadron enters the target nucleus (modeled as a set of spherical shells) and creates secondary particles based on the free space nucleon-nucleon cross sections for that collision. These secondaries move in straight lines about the nucleus, reflecting from or transmitting through the shells and producing secondary and tertiary collisions. The cascade ends when all particles, which are kinematically able to, have left the shells. The FTFP model simulates the inelastic scattering of hadrons using the FRITIOF model, where one or two QCD strings connect partons in the two nuclei. These strings are excited by momentum exchange, and the masses of the strings are chosen randomly. These strings then decay into secondary particles using the Precompound model. This default ATLAS nuclear interaction model (called a physics list) is known as FTFP_BERT.

5.2 Event and Physics Object Selection Criteria

5.2.1 Reference Selection

In-situ jet calibration techniques require that the jet to be measured is balanced back-to-back with a well measured reference object. Criteria are applied to select events with the correct topology, as well as to ensure that the required objects are well measured.

Photons

The first requirement used to select γ+jet events is that the event must have satisfied a fully efficient single photon trigger. In each event that passes this trigger requirement the leading photon (the photon with the highest energy) is considered to be a reference object candidate. The photon must be in the central region of the detector ($|\eta|<1.37$) and have a transverse momentum greater than 25 GeV.

Each reconstructed photon has a tag associated with it indicating how the photon was reconstructed. For this study the tag is required to be either AuthorPhoton or AuthorAmbiguous. AuthorPhoton means that no tracks with more than 4 Si hits have been associated with the electromagnetic calorimeter cluster, or that any associated track has no hits in the pixel layers and is associated with a two track vertex in the silicon detector. This leads to either unconverted or converted photons, where converted photons refer to photons which have interacted with material in the calorimeter and have been 'converted' into an electron/positron pair. It should be noted that these converted photons can have one or two tracks associated with them with one track conversions being the result of a lost track, with the lost track either being a low energy track which is missed or a high energy track which is on top of the first track. AuthorAmbiguous is a tag for all electromagnetic objects (electrons, positrons, photons) that by reconstruction alone cannot be identified as either a photon or an electron.

In addition to this reconstruction-level identification there is a second, more thorough set of criteria used in this analysis to ensure that the object in question is in fact a photon [40]. This identification puts requirements on how the energy is distributed within the calorimeter. Included are cuts on the fraction of the total energy in the hadronic calorimeter to help eliminate hadrons that fluctuate to have large EM content (through the production of π^0s), and on the energy in any secondary maximum in the preshower layer to remove neutral pions, which would manifest as two photons in the preshower/calorimeter. Differences in the distributions of these shower shape variables have been observed between data and Monte Carlo samples. This mismodeling is compensated by applying additional corrections to shower shape variables in the Monte Carlo samples before performing the photon selection.

To further reduce the number of jets faking photons an additional p_{T} dependent isolation criterion is applied to the photon, capitalizing on the fact that energy deposits from jets

are more diffuse than those from photons. This cut requires that the sum of the energy in topo-clusters within a distance $\Delta R = \sqrt{\eta^2 + \phi^2} = 0.4$ of the photon, but excluding the photon itself, must be less than $0.022\ p_{\mathrm{T}} + 2.45$ GeV. There is also a requirement that the sum of the momentum of tracks within $\Delta R = 0.2$ of the candidate photon, excluding those identified as conversion electrons/photons, is less than 5% of the momentum of the photon. Finally it has been found that the purity of the converted photons can be further enhanced by applying a requirement that the amount of energy of the reconstructed cluster roughly matches the energy of the track. In this study, for a two-track converted photon the energy of the cluster divided by the momentum of the track must be between 0.5 and 1.5, with the requirement loosened to be less than 2.0 for single-track converted photons.

Z Bosons

To create a Z boson candidate this study requires exactly two "good" leptons which are both the same flavour (electrons or muons) with opposite charge (one particle, one anti-particle). These two leptons must reconstruct to have a mass between 66 GeV and 116 GeV, an interval loosely centered around the Z-boson mass (91.19 GeV). The requirements for being a "good" electron or muon are described below.

Electrons

The trigger used for the Z+jet analysis searches for events with two loose (see below) electrons with energy above 15 GeV. Electrons are required to be within the range of the tracking detectors ($|\ \eta\ |<2.47$) but excluding the transition region between the barrel and the endcap ($1.37 <|\ \eta\ |< 1.52$). A minimum p_{T} requirement of 20 GeV is also applied to the electrons. In ATLAS, electrons are identified by applying a cut on the output of a multivariate likelihood function, where the inputs are many of the same variables that are used in photon identification [41]. ATLAS has a number of predefined selection levels (tight, medium, loose, loose+b layer, very loose [41]) providing a range of signal acceptance/background rejection levels. For this study the loose electron selection criteria are used to maximize statistics. Finally there is also an isolation cut applied to electrons, where the loose isolation working point is used. This loose working point is set to keep 99% of all electrons and includes cuts on both the relative energy in the calorimeter and the momentum in the tracker within $\Delta R = 0.2$ of the electron.

Muons

$\mathrm{Z} \rightarrow \mu\mu$ events are triggered using the lowest unprescaled dimuon trigger, which required two 10 GeV or 14 GeV muons depending on the data-taking period. Muons are required to be within $|\ \eta\ |< 2.4$ and have a transverse momentum greater than 20 GeV. Muons also have predefined identification levels [42]; this study uses the loose identification. A loose

isolation cut is also used for muons, where the isolation area is within $\Delta R = 0.2$ for the calorimeter and $\Delta R = 0.3$ for the tracking detector.

5.2.2 Jet Selection

The jets used in this study are reconstructed with the anti-k_t algorithm, using 4-2-0 topo-clusters as input at both the EM and LC scale, and with size parameter R=0.4. As jets are found by searching for large concentrated deposits of energy in the calorimeter, without further conditions imposed, photons and electrons are also expected to appear in the collection of reconstructed jets and must therefore be removed. Jets within $\Delta R = 0.2$ of a photon identified by a separate algorithm (see Sec. 5.2.1) are removed from the jet collection, as are jets within $\Delta R = 0.35$ of a lepton.

Clusters, and therefore jets, can be affected by calorimeter noise bursts, cosmic ray showers, pathological cells in the calorimeter, and other backgrounds. The ATLAS collaboration has predefined levels of data cleaning to identify these types of events [43]. These cleaning levels make use of a pulse quality variable Q which is a quantitative measure of the difference between the measured and expected shape of the electronic signal in the LAr calorimeter cells. Both the average of this value for cells within a jet (which is then normalized to the range [0,1]) and the fraction of cells in the jet in the EM/hadronic calorimeter which are 'bad' (defined as $Q > 4000$) are used in jet cleaning. As this study uses MET, any events with a jet above 20 GeV which fail to pass the "BadLoose" requirement will be vetoed. "BadLoose" requires that there is not a large amount of negative energy in the jet (no more than 60 GeV resulting from background/noise subtraction), which removes jets strictly from noise. It also requires that the most energetic layer of the jet not contain more than 99% of the total energy of the jet, therefore eliminating electronic noise bursts. The normalized measure of the pulse shape quality must be less than 0.8. If a significant portion of the jet energy (defined as more than 95% and 50% respectively) is in either the EM or hadronic calorimeter most of the energy in that calorimeter must originate from a well described pulse (80% or 50% respectively). Lastly the total track momentum within a jet is compared to the energy in the calorimeter. If the energy in the tracks represents less than 5% of the total energy in the jet there is likely a large fraction of neutral pions in the jet, so it is required that more than 5% of the total energy of the jet is collected by the EM calorimeter. The "BadLoose" criterion has been found to provide a 99.5% efficiency at selecting good jets above 20 GeV [43].

In 2016 the average number of interactions per bunch crossing in the LHC in a single lumiblock (a period of time of about 1 minute) reached as high as 52.2 (a quantity known as μ) on Oct. 14th, 2016. With such a high luminosity the probability of misidentifying a pileup jet as being part of the hard scattering interaction of interest becomes quite high. ATLAS uses ghost association of a very large number of artificially added tracks, where the track momentum is set infinitesimally small and jets are reclustered (similar to using

ghosts to define area as seen in Sec. 4) [44]), to match tracks to jets and then uses the vertex information for these tracks and the calibrated jet energy as input to the Jet Vertex Tagger (JVT) [45]. The output is a single continuous variable, where 1 corresponds to a perfect match to the primary vertex and 0 corresponds to a pileup jet. The recommended JVT cut of 0.59 is used in this study, which corresponds to an average signal efficiency rate of 92%. Events are required to have at least one jet passing this criterion. The jet with the largest p_{T} is called the leading jet, while the second highest p_{T} jet (if it exists) is known as the subleading jet (J2).

5.2.3 Event Topology Requirements

As the goal of this study is to measure the JES in the central region of the calorimeter the leading jet is required to have $|\eta|<0.8$. The MPF derivation assumes that the system in question consists solely of the reference object back-to-back with the jet to be calibrated. Considering only the selection criteria outlined above this will not always be the case. The assumption can be spoiled by any hard radiation emitted by the incoming particles before the hard scattering known as Initial State Radiation (ISR), or by radiation emitted by the outgoing parton known as Final State Radiation (FSR). These effects can be significantly minimized by explicitly requiring that the leading jet is back-to-back with the reference object in the transverse plane. The troublesome topologies can be further removed by requiring that the subleading jet, if present, contains only a small fraction of the total momentum in the system. These two cuts have been found to be uncorrelated in the past by varying the cuts simultaneously [46].

In this study the back-to-back requirement used is $\Delta\phi\,(\text{leading jet, ref}) > \pi - 0.25$. The subleading jet, if present, is required to have $p_{\mathrm{T}} < \max(12\text{ GeV}, 0.3\times p_{\mathrm{T}}^{\mathrm{ref}})$ at JES+GSC scale.

5.3 MET Selection

As mentioned in Sec. 4.3, the appropriate MET at the same energy scale as the jets to be calibrated must be used in the MPF method. This thesis uses EM and LC scale cluster-based MET to calibrate EM and LC scale jets, respectively. In addition to this correct MET scale requirement the MPF derivation presented in this thesis assumes that all reference objects are well measured at the scales used to construct the MET. In reality this is not necessarily the case and therefore corrections have been applied to the base MET collections to correct for this fact. Electromagnetic objects (electrons, photons) are not perfectly calibrated after reconstruction (despite being reconstructed at EM scale). This means that any subsequent calibrations of their energy must be propagated through to the MET. As muons are not stopped in the calorimeter a larger correction is needed for them. This correction involves removing any potential energy deposits in the calorimeter that have been left by the muons

determined by comparing the muon spectrometer and the ID measurements and then adding in the full p_{T} of the muon into the MET.

One additional complication arises for the GSC calibration (explained in Sec. 4.1). The MPF as presented has no built-in mechanism for testing how well the Monte Carlo simulation models the variables used in the GSC correction. A number of methods for incorporating some test of the GSC were explored, including scaling the measured MPF response in each event by the GSC scale factor for the leading jet, propagating the GSC scale factor for the leading jet to the MET before measuring the response, and propagating the GSC scale factor for each individual jet above 20 GeV through to the MET before making the measurement. In the end all three methods agreed well with each other, and showed that the GSC has very little to no effect on the residual MPF calibration measurement. The decision was made by the jet/EtMiss group to continue to test the GSC using the second of these methods (propagating the GSC of the leading jet to the MET). This correction is used throughout this thesis and the measured response is labeled as either EM+GSC or LC+GSC, depending on the scale of the clusters used to build the MET.

5.4 Measuring the Jet Energy Scale

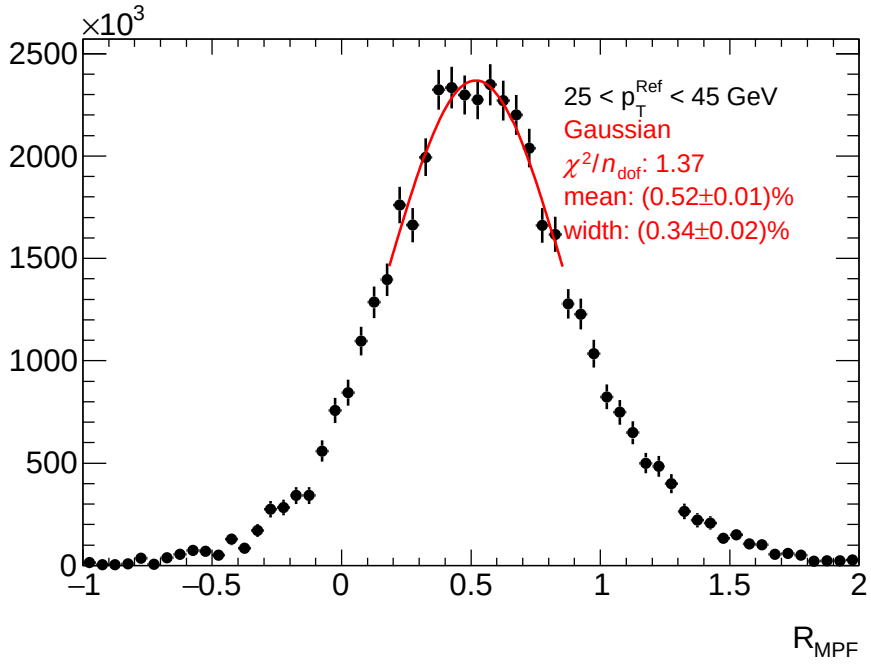

Figure 5.1: The distribution of the measured response in ATLAS using γ+jet events in the 2016 dataset. The response shown here is at EM scale and for events where the photon has a transverse momentum between 25 and 45 GeV.

The average response of a jet is a function of the true energy of that jet (see Sec. 4.2). In order to capture this energy dependence the response must be measured in bins of energy or some other quantity that follows energy. The steeply falling cross section for both the γ and Z+jets processes and the large jet-by-jet fluctuations in visible energy deposited in the calorimeter would conspire to bias the response high if the most obvious choice was used to simply bin in measured jet energy. Instead the p_{T} of the reference object is used, which is a sensible choice as it is already being used in the response measurement itself as a measure of the truth jet's p_{T}. To avoid bias from pathological events with very small or unrealistically large response, the MPF response distribution is fit to a Gaussian function rather than taking a simple mean. In practice the distribution is fit once with a Gaussian over the full range followed by two additional stages where each subsequent fit is performed within a window centred on the mean of the previous fit and a width of 1.6 times the sigma of the previous fit. An example of the response distribution in the γ+jet channel at EM scale for photons with transverse momentum between 25 and 45 GeV in the 2016 dataset is shown in Fig. 5.1, with additional examples being found in appendix B.

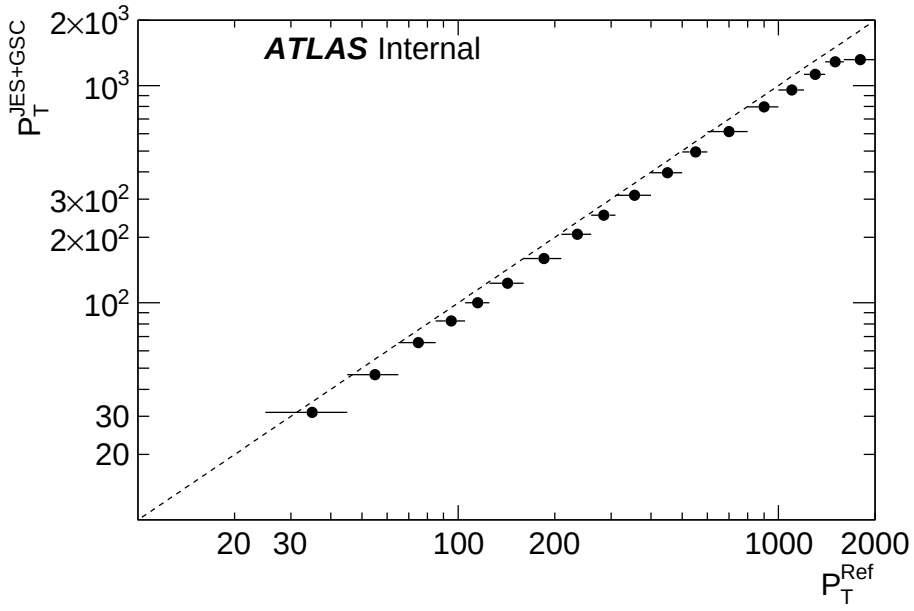

Figure 5.2: The average transverse momentum of the leading jet after the JES and GSC is applied as a function of the energy of the leading photon. The jets are initially reconstructed using EM scale clusters. The dotted line is included along the line $p_{\mathrm{T}}^{\mathrm{ref}} = p_{\mathrm{T}}^{\mathrm{JES+GSC}}$ to help guide the eye.

Finally as jets have a predetermined size it is likely that the jet does not contain the full hadronic recoil in the 2→2 type events used in this study. This is especially true at lower energies where jets tend to be wider, and on average ∼20% of the energy is deposited outside of an anti-k_{t} R=0.4 jet [47]. To remove the effect this imperfect match in p_{T} has on

the binning, the average jet p_{T} after the JES and GSC are applied is measured in each bin. After the response in each reference p_{T} bin is fit and measured the result is then scaled down to the average measured jet p_{T} in that bin. The average jet p_{T} as a function of reference p_{T} can be seen in Fig. 5.2.

Due to data storage constraints during event reconstruction only jets above a predetermined transverse momentum threshold are kept. During the 2015 and 2016 runs at the LHC this threshold for ATLAS was 6 GeV before any calibration. For low p_{T} Z or γ+jet events this threshold has the effect of removing all events where the jet response happened to have fluctuated low. This biases the measured response to be higher than it is in reality leading to an unphysical rise in the response at low energies as can be seen in Fig. 5.3 and Fig. 5.4. This effect is more visible for Z+jet as this channel is used to measure the response at lower jet energies (see Fig. 5.22). While this rise is not the result of some detector behaviour it is a feature in the data to be calibrated, and as such is the correct shape of the calibration curve for this dataset. This rise in the measured response at low p_{T}, combined with the higher response in Monte Carlo and the fact that the reconstruction threshold is at the uncalibrated scale, lead to the dip in the relative data/MC response at low p_{T} as well.

5.5 Systematic Uncertainties

While *in-situ* techniques are used to measure the difference in response between data and MC a number of other factors unrelated to the absolute response difference may also affect this measurement. These factors include mismodelling of any ISR/FSR, mismodelling of the response of any reference objects, background processes contaminating the measurement in data and so on. The potential effect of many of these sources of uncertainty is measured by varying some selection criteria and measuring how these variations affect the central value of the data-to-MC ratio. The effects of these individual cut variations are explored in the following sections.

When using this technique to estimate uncertainties with statistically limited samples one risks inflated systematics caused by statistical fluctuations appearing in multiple measurements. Dynamic rebinning of the results is used to reduce the effects of these fluctuations. This rebinning starts by determining the statistical significance of the shift in the response in a given bin using pseudo-experiments. For the nominal response and each variation, N copies of the response are made, where for each event and each copy a weight chosen from a Poisson distribution with a mean of one is applied. The bin-by-bin statistical uncertainty on each variation is then taken as the RMS of the arithmetic means of the nominal/varied ratios of these N copies. Bin merging is then done by beginning with the first bin and determining if $(data/MC)_{nominal} \,/\, (data/MC)_{varied}$ differs from 1 by more than 1.5 times the statistical uncertainty. If this is not true the bin is combined one by one with subsequent bins until this criterion is true, at which point the process moves on to the

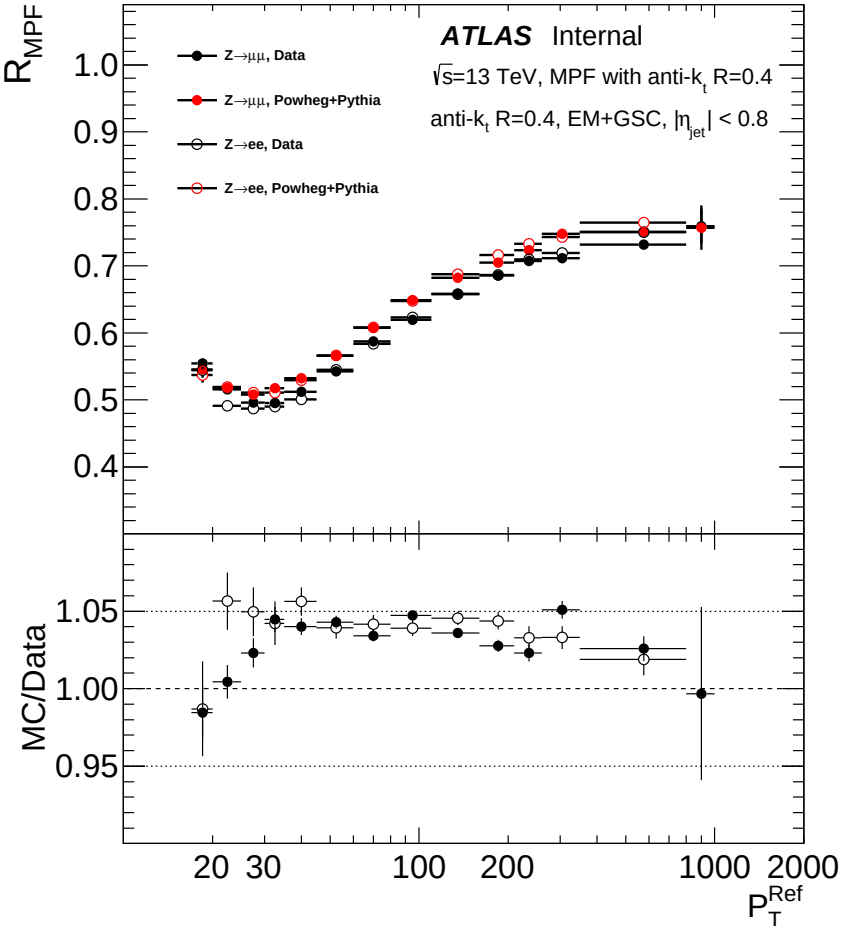

Figure 5.3: The MPF response as measured using both Z→ee and Z→ $\mu\mu$+jet events. Red points indicate Monte Carlo, black points are data, hollow points are Z→ee and filled points are Z→ $\mu\mu$. Measured at EM+GSC scale using 2016 data.

next bin. This procedure is done starting from both the highest and lowest p_{T} bins, where in the end the direction yielding the largest number of merged bins is used. An example of these pseudo-experiments is shown in Fig. 5.5 while an example of the effect of the entire rebinning process can be seen in Fig. 5.6.

5.5.1 Initial- and Final-state Radiation

As mentioned in Sec. 5.2.3 cuts restricting the maximum transverse momentum of any secondary jets and the opening angle between the jet and the reference object are very good at reducing the effects of FSR and ISR. However the amount by which these requirements suppress additional radiation is not guaranteed to be well modeled. Any radiation mismodelling has the possibility of affecting the relative response between data and Monte Carlo, and this effect is measured by varying the associated selection cuts. Studies have been pre-

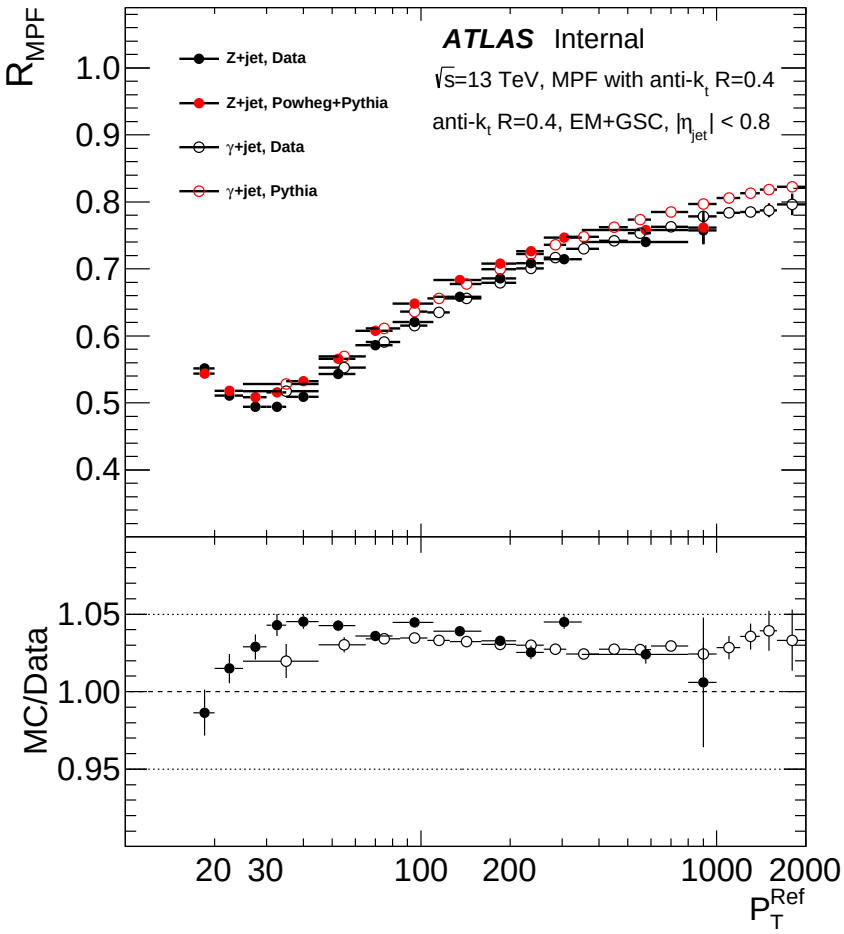

Figure 5.4: The MPF response as measured using both Z+jet (with the Z→ee and Z→ $\mu\mu$ channels combined) and γ+jet events. Red points indicate Monte Carlo, black points are data, hollow points are γ+jet and filled points are Z+jet. Measured at EM+GSC scale using 2016 data.

formed in the past which have determined that these cuts essentially are independent and their associated systematics should be treated as such [48].

Variation of the Sub-leading Jet Cut

The effect of the subleading jet p_{T} cut is mostly to remove FSR. This cut is varied from the nominal value ($p_{\mathrm{T}} < \max(12\ \mathrm{GeV}, 0.3\times p_{\mathrm{T}}^{\mathrm{ref}})$) to both a looser value of $p_{\mathrm{T}} < \max(12$ GeV, $0.4\times p_{\mathrm{T}}^{\mathrm{ref}})$ and a tighter one of $p_{\mathrm{T}} < \max(10$ GeV, $0.2\times p_{\mathrm{T}}^{\mathrm{ref}})$. The effect of this cut variation on the ratio of the measured response in data and MC is found to be quite small (less than 0.2%) as can be seen in Fig. 5.6. Further insight into the effects of varying the amount of FSR allowed by the selection criteria can be gained by observing how well the MC models the response in data as a function of the ratio of the energy in the subleading jet to the energy in the reference object. As seen in Fig. 5.7 the absolute value of the measured

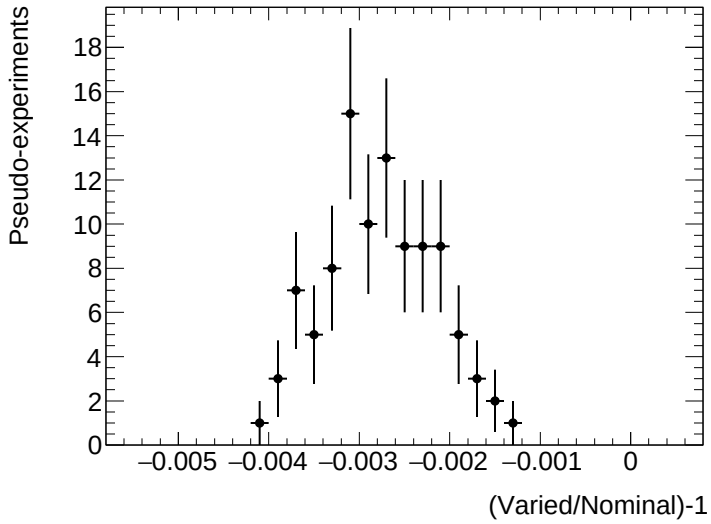

Figure 5.5: Distribution of 100 pseudo-experiments used to estimate the statistical uncertainty on the effect of loosening the subleading jet cut. This particular distribution is used to determine the uncertainty at EM+GSC scale in 2016 data for γ+jet events with a photon p_{T} between 105 and 125 GeV.

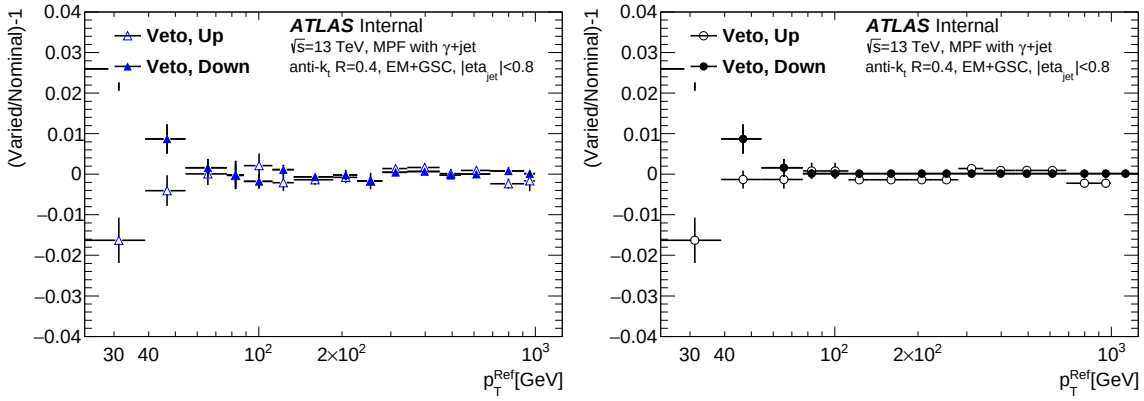

(a) No rebinning

(b) With rebinning

Figure 5.6: Effect of varying the subleading jet p_{T} cut up and down on the EM scale MPF response using γ+jet events in 2016 before and after rebinning.

response does in fact vary as a function of the energy in the subleading jet. However, this effect is well modeled by the Monte Carlo, with the data/MC response ratio varying only by a percent or so between events with no subleading jets and events with subleading jets containing 45% of the energy of the photon. This percent level effect is suppressed because the rest of the selection criteria even without the subleading jet or the $\Delta\phi$ cuts favour a $2\rightarrow2$ event topology, causing the majority of events to have a soft subleading jet if one exists at all. This dependence of the measured response on the subleading jet cut is smaller when

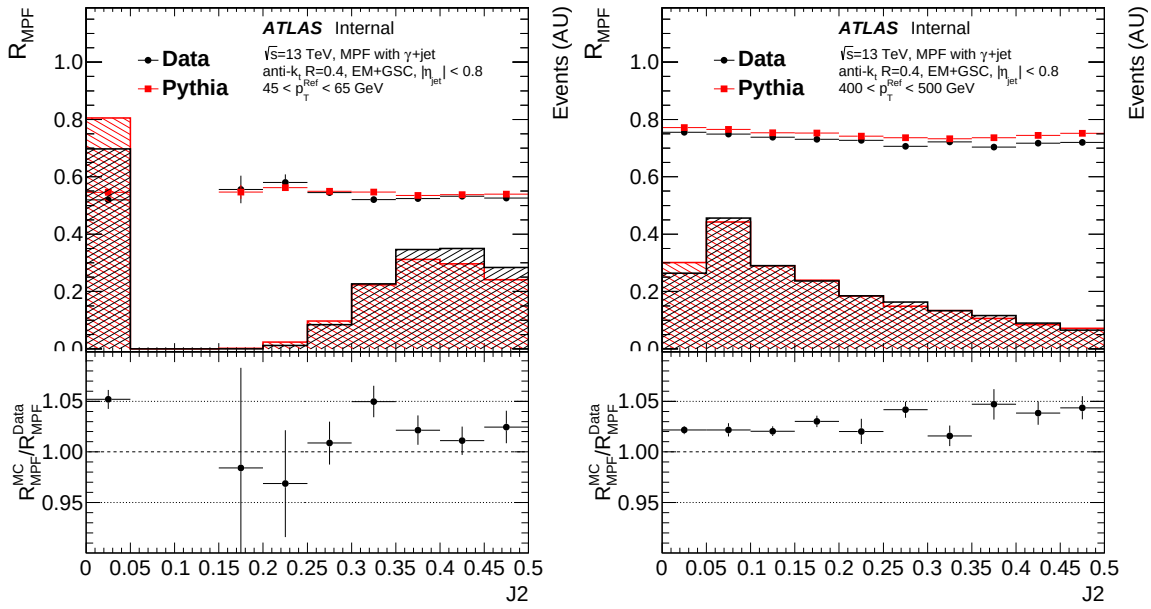

(a) 45-65 GeV (b) 400-500 GeV

Figure 5.7: Response as a function of the fraction of the photon energy contained in the subleading jet (J2) in two different p_{T} bins along with the distribution of events plotted against the same variable. At lower reference p_{T} a jet with a small fraction of the reference objects p_{T} falls below the reconstruction threshold. This leads to a large number of events that appear to have no subleading jet. All selection cuts listed in Sec. 5.2 have been applied except for the subleading jet cut and the $\Delta\phi$ cut.

using the MPF compared to a p_{T}-balance based calibration, and is therefore a strength of the MPF.

Variation of the Delta Phi Cut

The effect of the $\Delta\phi$ cut is mostly to remove ISR. Just like the subleading jet case, this cut is varied from its nominal value ($\Delta\phi\,(\text{leading jet, ref}) > \pi - 0.25$) to both a looser ($\Delta\phi > \pi - 0.35$) and a tighter ($\Delta\phi > \pi - 0.15$) requirement. Once again insight can be gained into the effects of this variation by measuring the response as a function of $\Delta\phi$ and observing how well the MC models this behaviour (see Fig.5.8).

The MPF has a smaller but still present dependence on the $\Delta\phi$ cut compared to the subleading jet cut. This dependence is well modeled for events where $\Delta\phi > \pi - 0.15$. As mentioned in the context of the subleading jet cut simply requiring a "good" photon and a jet in the event tends to force them to be back-to-back, even without any explicit cuts forcing this configuration. This can be seen in Fig. 5.8, where even without applying any cuts to J2 or $\Delta\phi$ a large number of events have $\Delta\phi > \pi - 0.15$. This is especially true at higher p_{T}^{γ}, reducing the importance of the $\Delta\phi$ cut and therefore the impact of the cut variation as seen in Fig. 5.9.

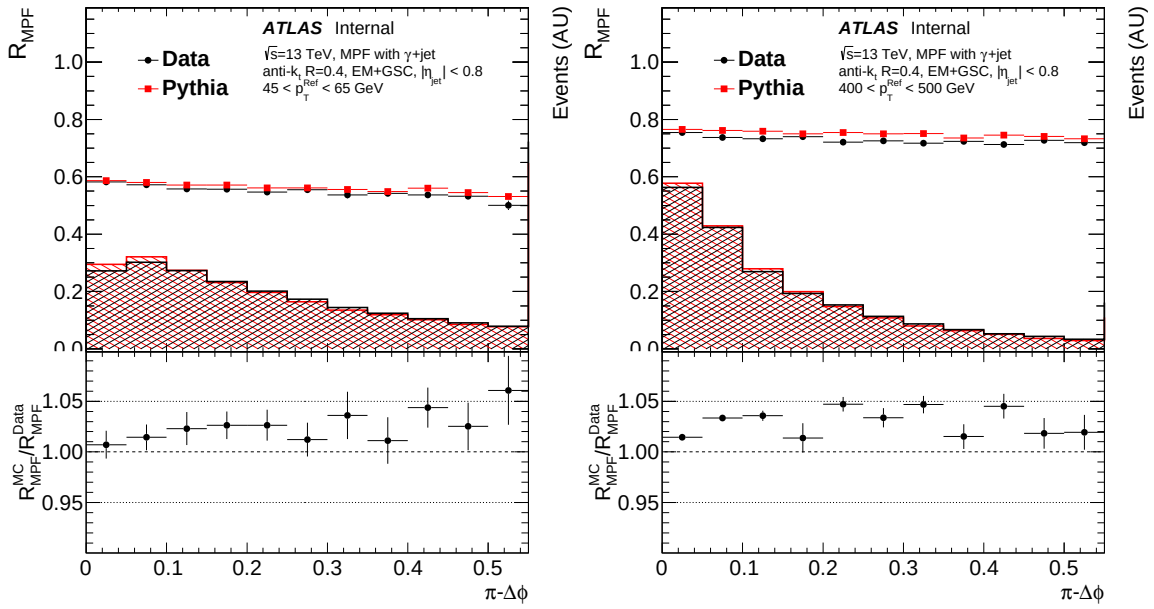

(a) 45-65 GeV (b) 400-500 GeV

Figure 5.8: Response as a function of the opening angle in azimuth between the reference object and the leading jet ($\Delta\phi$) in two different p_{T} bins along with the distribution of events plotted against the same variable. All selection cuts listed in Sec. 5.2 have been applied except for the subleading jet cut and the $\Delta\phi$ cut.

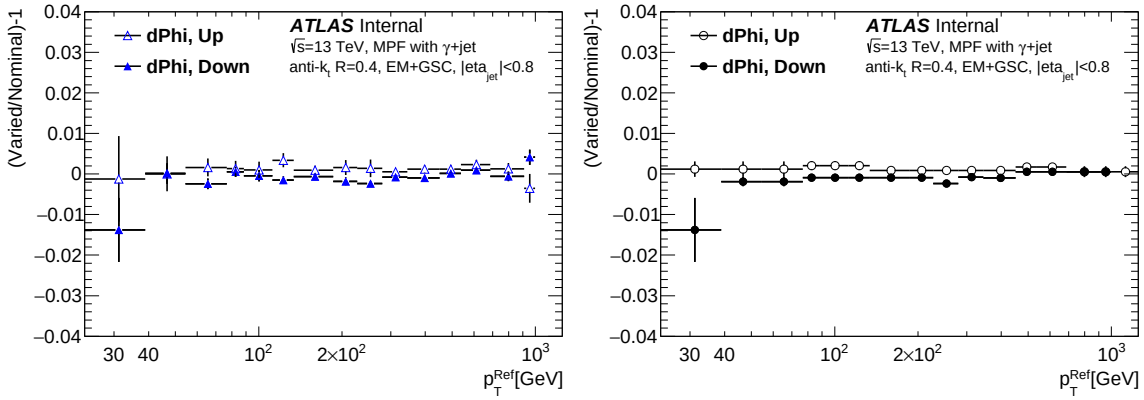

(a) No rebinning (b) With rebinning

Figure 5.9: Effect of varying the $\Delta\phi$ cut up and down on the EM scale MPF response using γ+jet events in 2016 before and after rebinning.

5.5.2 Uncertainties Related to the Reference Object

With *in-situ* jet calibration techniques making use of a well measured reference object to estimate the energy of the particle jet it is easy to see how strongly the quality of the calibration depends on the accuracy of the reference calibration. Any mismodeling of the energy of the reference object(s) will therefore directly affect the measured MPF. This section

first describes both scale and resolution uncertainties associated with electromagnetically interacting objects (both electrons and photons). This is followed by a description of these uncertainties for the muons used in the (Z$\rightarrow \mu\mu$)+jet channel.

E/Gamma Energy Scale and Resolution

Beginning at the EM scale does not guarantee that EM objects will be properly calibrated after reconstruction. It also does not guarantee that the distribution of the energy deposited in the calorimeter will be well modeled in simulated samples. As is the case for jets, the ATLAS collaboration uses a number of steps to fully calibrate both electrons and photons. These calibrations include a simulation based multivariate regression that corrects for both energy missed by the reconstruction as well as accounting for where the energy was deposited in the calorimeter [49]. Also included is an *in-situ* based calibration that corrects for the difference in response between data and simulation. This is derived using the known mass peak of the Z boson in Z$\rightarrow$ee decays.

The uncertainties from these corrections are propagated through to the jet calibration by measuring the effect of varying the correction up and down by one sigma. The effect of this variation is shown in Fig. 5.10 for γ+jet events, and is found to be approximately 1% over the full p_{T} range considered. This is much smaller for Z+jet events. This is due to a combination of the uncertainties for electrons being smaller than for photons, the electrons being produced back-to-back cancelling a portion of the scale variations, and because in events where the Z decays into a pair of muons the variation has no effect (see Fig. 5.11).

In addition to the calibration factors used to bring both electrons and photons back to their truth level energy, the electron/photon performance group also measures the energy resolution. These studies have shown that the resolution is better in the simulation than it is for data. To account for this discrepancy a Gaussian smearing factor is applied to the energy in the simulated pseudo-data. The uncertainty on the relative difference in resolution is propagated to the measured JES by varying this smearing up and down by one sigma. The effect of this smearing on the EM+GSC response as measured in γ+jet is shown in Fig. 5.12.

Muon Scale and Resolution

As for electrons and photons, the energy of muons is smeared to improve the agreement between the measured resolution in data and Monte Carlo. Muons also have uncertainties associated with both the momentum scale and the smearing applied to the momentum in MC samples [50]. The momentum smearing is done independently for both the inner detector and the muon spectrometer. The impact of each of these three variations on the ratio of the MPF in data and Monte Carlo is at most on the order of 0.1% over the full p_{T} range measured, with the exception of one large fluctuation in the lowest p_{T} bin for the muon spectrometer smearing (see Figs. 5.13, 5.14, and 5.15).

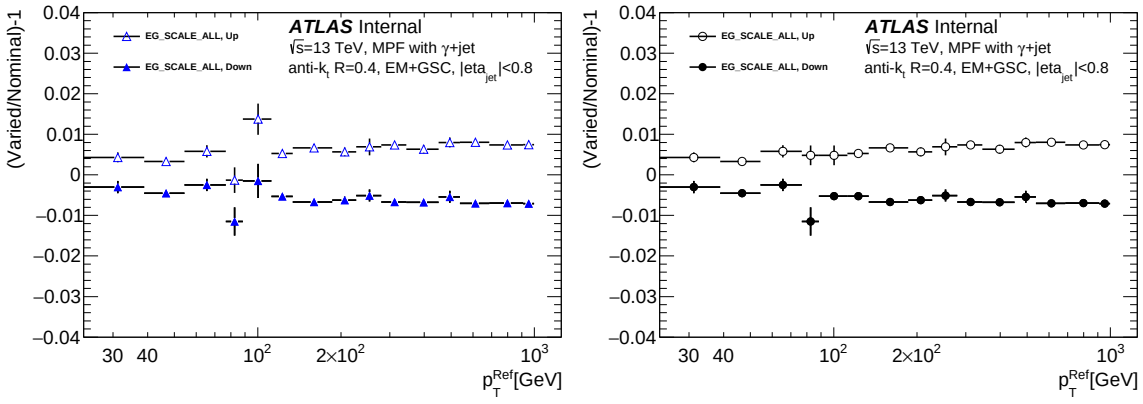

(a) No rebinning (b) With rebinning

Figure 5.10: Effect of varying the photon energy scale up and down on the EM+GSC scale MPF response using γ+jet events in 2016 before and after rebinning.

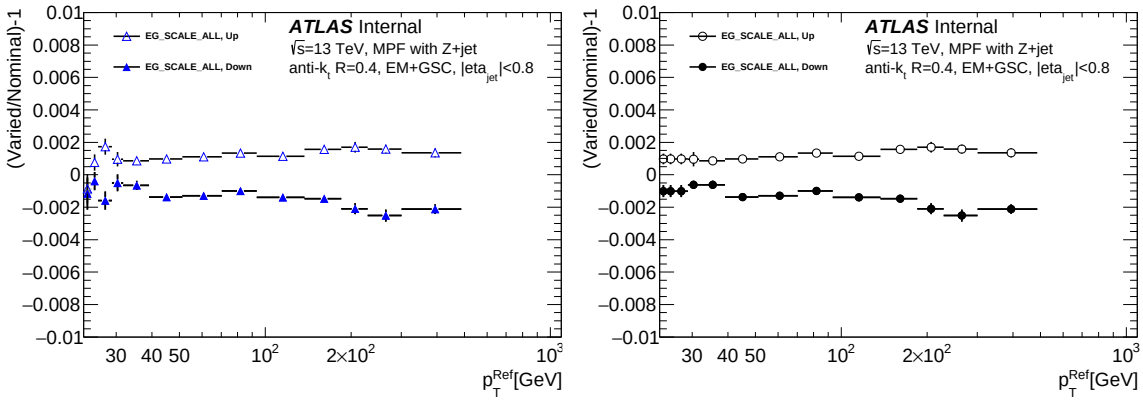

(a) No rebinning (b) With rebinning

Figure 5.11: Effect of varying the electron energy scale up and down on the EM+GSC scale MPF response using Z+jet events in 2016 before and after rebinning. Note that the y-axis scale is different from Fig. 5.10.

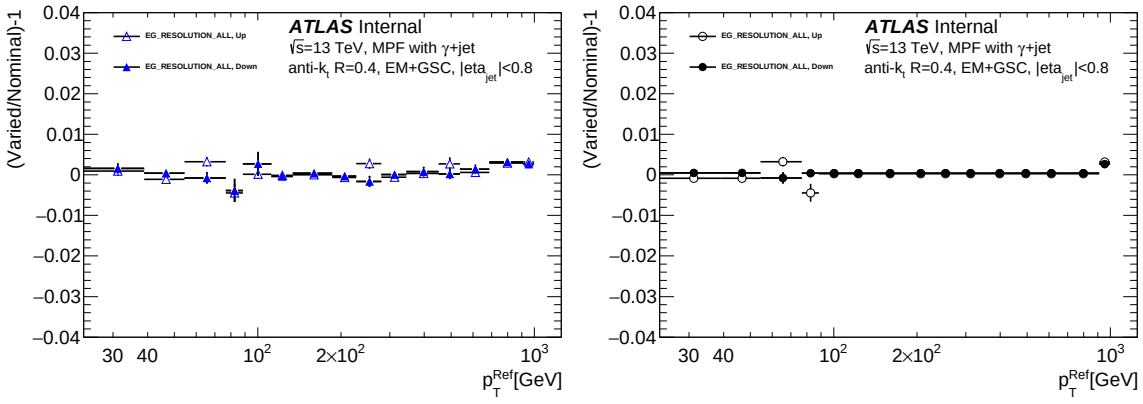

(a) No rebinning (b) With rebinning

Figure 5.12: Effect of varying the photon energy smearing up and down on the EM+GSC scale MPF response using γ+jet events in 2016 before and after rebinning.

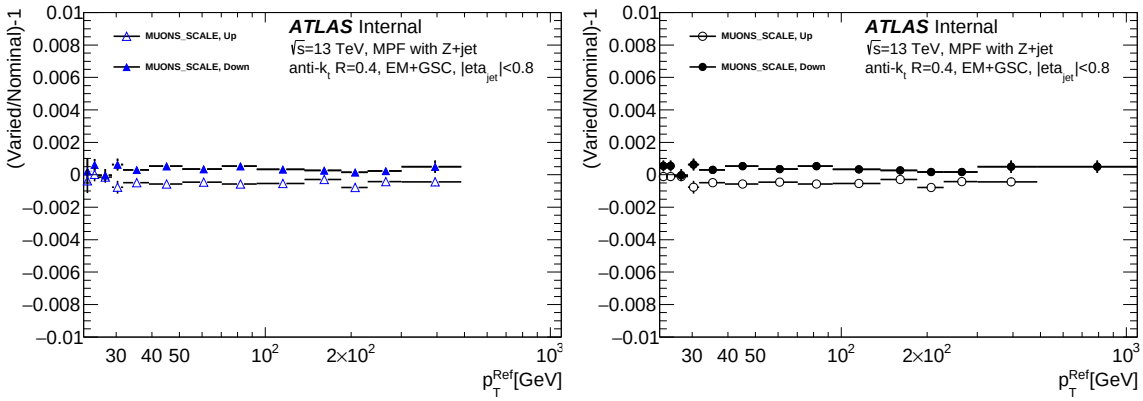

(a) No rebinning (b) With rebinning

Figure 5.13: Effect of varying the muon momentum scale up and down on the EM+GSC scale MPF response using Z+jet events in 2016 before and after rebinning. Note that the y-axis scale is different from Fig. 5.10.

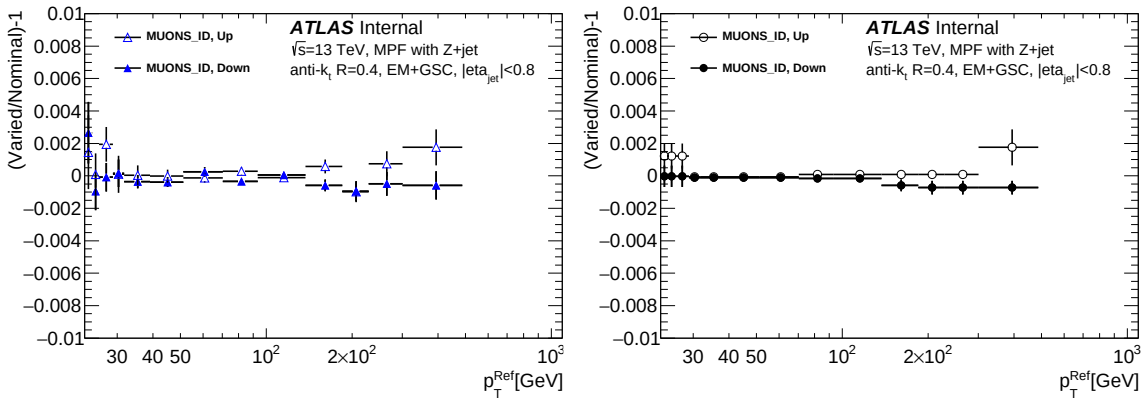

(a) No rebinning (b) With rebinning

Figure 5.14: Effect of varying the momentum smearing in the ID up and down on the EM+GSC scale MPF response using Z+jet events in 2016 before and after rebinning. Note that the y-axis scale is different from Fig. 5.10.

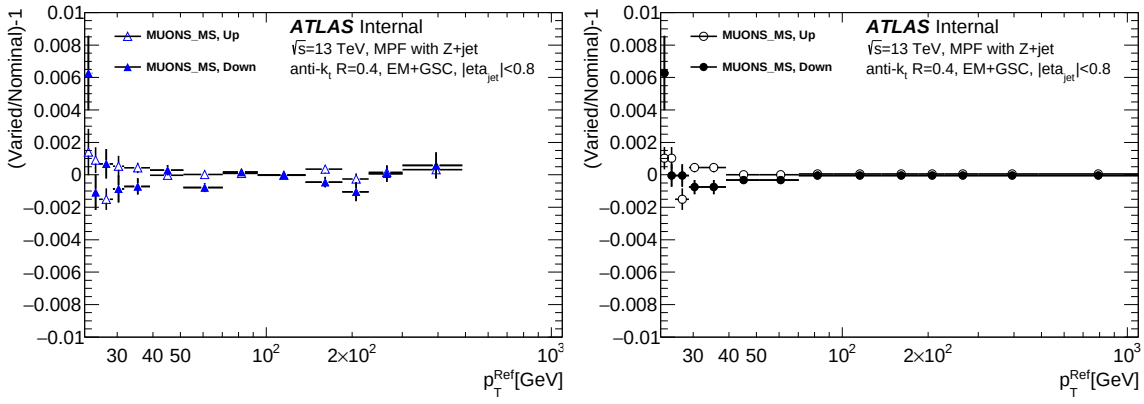

(a) No rebinning (b) With rebinning

Figure 5.15: Effect of varying the momentum smearing in the MS up and down on the EM+GSC scale MPF response using Z+jet events in 2016 before and after rebinning. Note that the y-axis scale is different from Fig. 5.10.

5.5.3 JVT

The effect of misidentifying pileup jets as part of the hard scattering is measured by varying the JVT requirement from its nominal value of 0.59 to both a more restrictive (0.91) and a less restrictive (0.11) value. These values have average signal acceptance rates of 85% and 97%, respectively. The choice of a JVT working point has very little effect on the data/Monte Carlo agreement for the MPF, changing by less than 0.02% over most of the p_{T} range considered. This illustrates the relative immunity of the MPF technique to pileup in general. There is a small potential effect at low p_{T} where the numerous low energy pileup jets could have a larger effect, but even in this region the agreement never changes by more than a third of a percent. The small dependence of the MPF on pileup can be further seen in Figs. 5.17 and 5.18, which shows the dependence of the measured response on the average number of collisions per lumiblock (μ) and the number of reconstructed vertices (NPV) respectively. This built-in pileup resiliency is another strength of the MPF method.

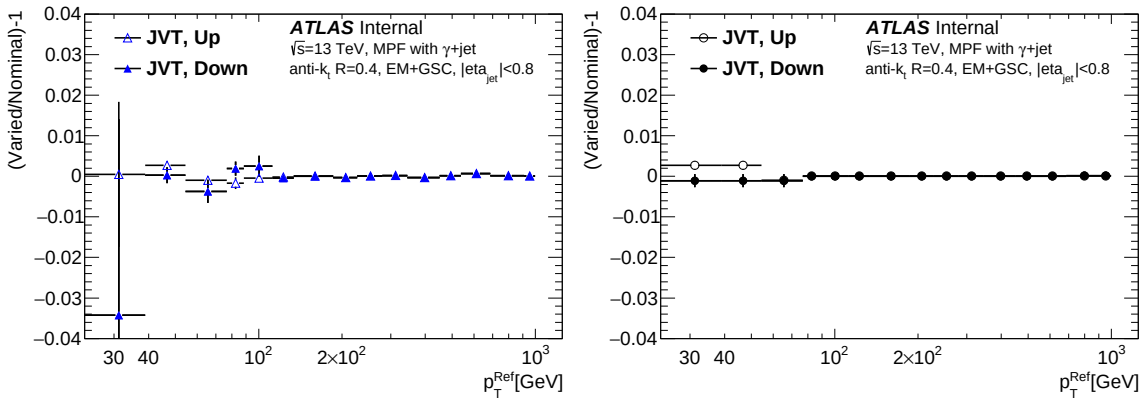

(a) No rebinning

(b) With rebinning

Figure 5.16: Effect of varying the JVT requirement to be more/less strict in rejecting pileup jets on the EM+GSC scale MPF response using γ+jet events in 2016 before and after rebinning.

5.5.4 Photon Purity

In Sec. 4.2 a simplified model of jet calorimeter showering was presented where after each interaction new pions are created, and on average 1/3 of the pions are π^0's which rapidly decay into a photon pair. While it is true that on average each pion flavour is produced in roughly equal proportions, this is not necessarily true for any given jet. From time to time a jet will fluctuate to have a very large number of neutral pions at some early stage of its development, either during the parton shower or its interaction with the material of the calorimeter, leading to a dense deposit of EM energy. This is exactly what the photon/electron reconstruction algorithms look for, and removing this jet is the reason for the strict identification requirements. Even with all of the strict identification criteria

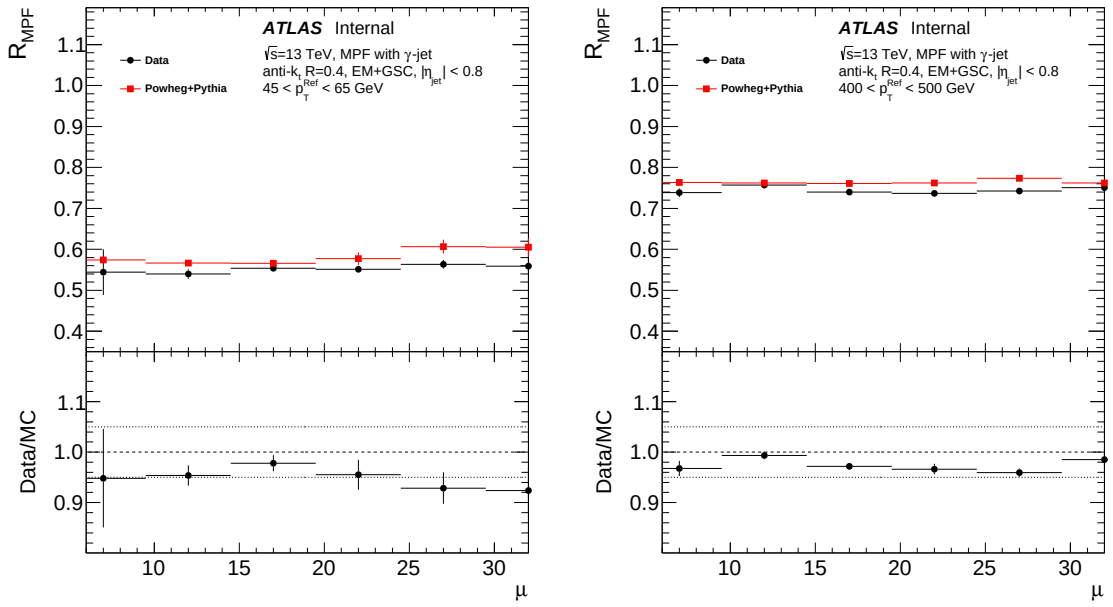

(a) 45-65 GeV (b) 400-500 GeV

Figure 5.17: Response as a function of the average number of collisions per bunch crossing for a given lumiblock (μ) in two different p_{T} bins. This quantity is a measure of both the amount of in-time and out-of-time pileup present in the event.

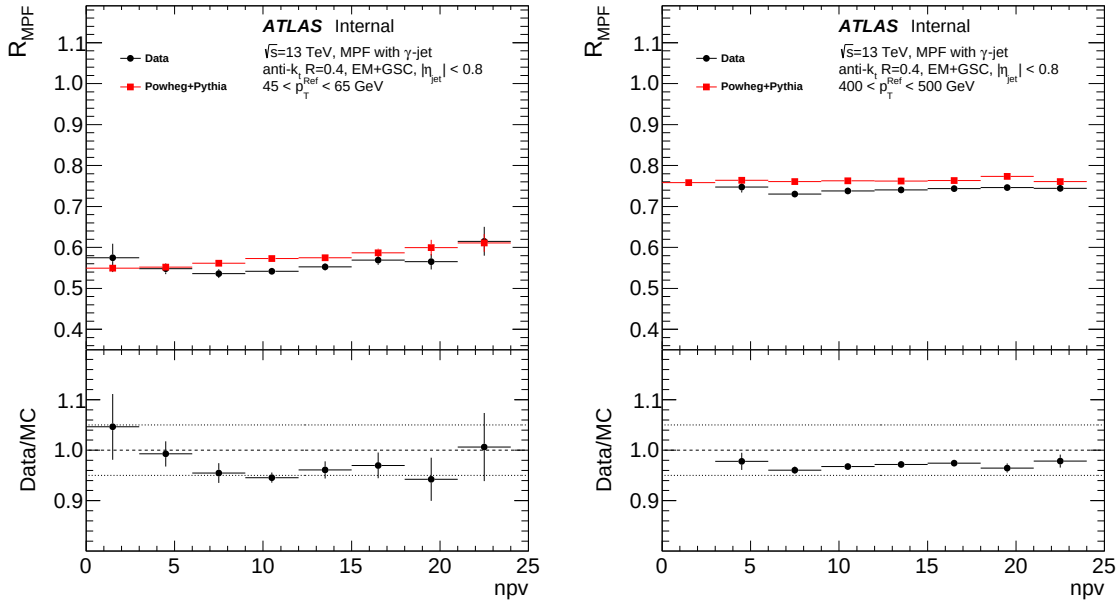

(a) 45-65 GeV (b) 400-500 GeV

Figure 5.18: Response as a function of the number of reconstructed primary vertices in the event (npv) in two different p_{T} bins. This quantity is used as a measure of the amount of in-time pileup present in the event.

described earlier in this chapter, the sheer number of dijet events compared to γ+jet events means that a non-negligible number of dijet events will be misidentified as γ+jet events. The misidentified reference jets in dijet events have a lower response than photons, meaning these events will lead to a higher jet response being derived than in true γ+jet events (the denominator in Eq. 4.9 is too small). An uncertainty is added to the γ+jet response measurement to account for this.

The size of this effect, and therefore the size of the uncertainty that should be assigned to cover it, depends on how large the jet contamination of the photon sample is. The purity of the photon sample must therefore be quantified. To estimate the background (dijet fakes where one jet fakes a photon) that satisfies the selection criteria used in this study, sideband regions, which are dominated by dijet fakes, are used. Two cuts are chosen which ideally have a large impact on the signal acceptance while being uncorrelated. In this study the relative energy/momentum isolation cut and the photon identification cut are used (see Fig. 5.19).

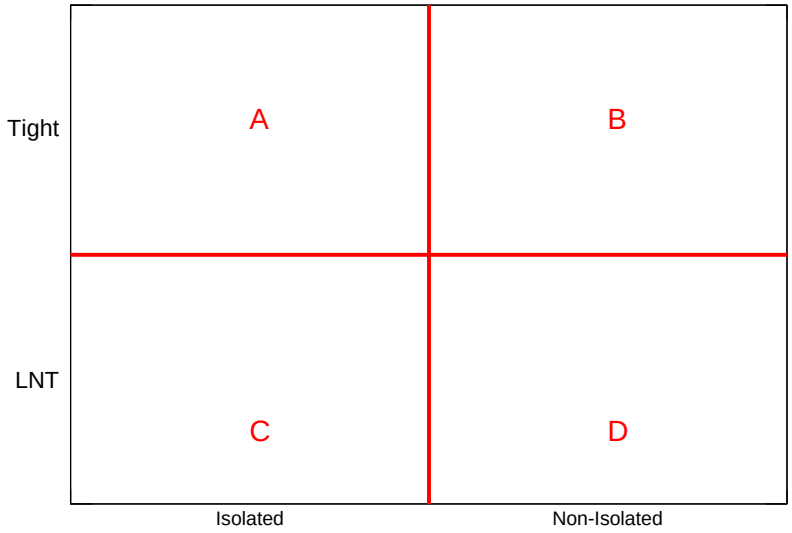

Figure 5.19: Diagram showing the signal region (A) and sidebands that are used in the photon signal purity measurement. LNT is "Loose-Not-Tight".

Unfortunately the photon ID cut does have an impact on the fraction of background events that pass the isolation cut. In order to resolve this issue a looser photon ID selection criterion is applied before beginning the process. This means that in this section events that fail the tight criteria will have passed a loose one, and these events will be labelled as "loose-not-tight", or LNT.

The events that pass both of these cuts are located in region A, which has both signal and background events. Events that fail both cuts fall into region D, with regions B and C corresponding to events that pass one cut and fail the other (see Fig. 5.19) . Using this labeling and the fact that the background distribution is independent of these cuts, the following equations hold

$$\frac{A_{\text{data}}^{\text{background}}}{B_{\text{data}}^{\text{background}}} = \frac{C_{\text{data}}^{\text{background}}}{D_{\text{data}}^{\text{background}}}, \tag{5.1}$$

$$A_{\text{data}}^{\text{background}} = \frac{C_{\text{data}}^{\text{background}} B_{\text{data}}^{\text{background}}}{D_{\text{data}}^{\text{background}}}. \tag{5.2}$$

Now if regions B, C, and D are assumed to contain only background events, then $X_{\text{data}}^{\text{background}} = X_{\text{data}}$ for $X = B$, C, and D, and:

$$\text{Purity} = \frac{A_{\text{data}}^{\text{signal}}}{A_{\text{data}}} = 1 - \frac{A_{\text{data}}^{\text{background}}}{A_{\text{data}}} = 1 - \frac{C_{\text{data}} B_{\text{data}}}{D_{\text{data}} A_{\text{data}}} \tag{5.3}$$

This very simple derivation assumes that regions B, C, and D contain only background, which is not necessarily true. This potential "signal leakage" is accounted using a signal only MC sample and measuring the amount of signal in each background region relative to the amount in the signal region. That is to say for each region X a correction $\lambda_X \equiv \frac{X_{\text{signal}}^{\text{MC}}}{A_{\text{signal}}^{\text{MC}}}$ can be defined. Assuming that the distribution of signal events is the same in data as it is in MC

$$X_{\text{data}}^{\text{background}} = X_{\text{data}} - \lambda_X A_{\text{data}}^{\text{signal}} \tag{5.4}$$

Using this definition Eq. 5.3 becomes

$$\text{Purity} = \frac{A_{\text{data}}^{\text{signal}}}{A_{\text{data}}} = 1 - \frac{\left(C_{\text{data}} - \lambda_C A_{\text{data}}^{\text{signal}}\right)\left(B_{\text{data}} - \lambda_B A_{\text{data}}^{\text{signal}}\right)}{\left(D_{\text{data}} - \lambda_D A_{\text{data}}^{\text{signal}}\right) A_{\text{data}}}. \tag{5.5}$$

Rearranging leads to an expression that is quadratic in $A_{\text{data}}^{\text{signal}}$ with the solutions being

$$a = \lambda_B \lambda_C - \lambda_D \tag{5.6}$$

$$b = D_{\text{data}} + \lambda_D A_{\text{data}} - \lambda_C B_{\text{data}} - \lambda_B C_{\text{data}} \tag{5.7}$$

$$c = C_{\text{data}} B_{\text{data}} - A_{\text{data}} D_{\text{data}} \tag{5.8}$$

$$A_{\text{data}}^{\text{signal}} = \frac{-b \pm \sqrt{b^2 - 4ac}}{2a}, \tag{5.9}$$

where the smaller of the two solutions is chosen.

Another potential issue is that even when requiring that photons must pass the loose requirement before being included in the analysis sample, the background shape is still

affected by the two cuts. The size of this correlation is measured using background only MC and looking at

$$R^{\mathrm{MC}}_{\mathrm{background}} = \left(A^{\mathrm{background}}_{\mathrm{MC}} D^{\mathrm{background}}_{\mathrm{MC}}\right) / \left(B^{\mathrm{background}}_{\mathrm{MC}} C^{\mathrm{background}}_{\mathrm{MC}}\right) \tag{5.10}$$

which would modify Eq.5.5 to read as

$$\mathrm{Purity} = \frac{A^{\mathrm{signal}}_{\mathrm{data}}}{A_{\mathrm{data}}} = 1 - R^{\mathrm{MC}}_{\mathrm{background}} \frac{\left(C_{\mathrm{data}} - \lambda_C A^{\mathrm{signal}}_{\mathrm{data}}\right)\left(B_{\mathrm{data}} - \lambda_B A^{\mathrm{signal}}_{\mathrm{data}}\right)}{\left(D_{\mathrm{data}} - \lambda_D A^{\mathrm{signal}}_{\mathrm{data}}\right) A_{\mathrm{data}}}. \tag{5.11}$$

With the loose photon ID criteria used in this thesis $R^{\mathrm{MC}}_{\mathrm{background}}$ was found to be 1.45. This once again gives an expression that is quadratic in $A^{\mathrm{signal}}_{\mathrm{data}}$ and can be solved the same way. The base line purity measurement (labeled as "simple") as well as the purity with the two corrections (signal leakage and signal leakage+background correlation) are shown in Fig. 5.20.

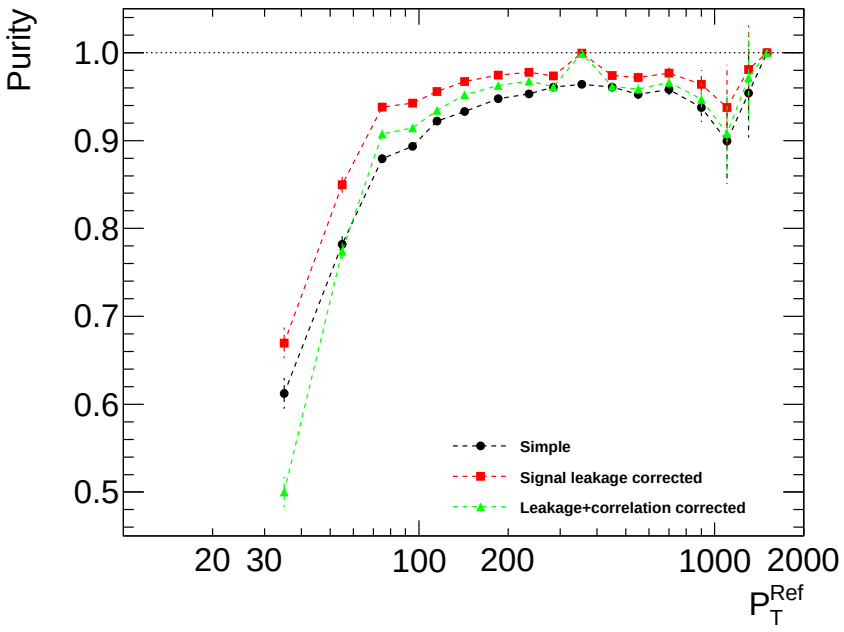

Figure 5.20: Measured photon purity in the γ+jet channel. The baseline purity is shown in black, the red points include the signal leakage correction, and the green points include both the signal leakage correction and the background correlation correction.

If the measured response in dijet events is identical to the one measured in γ+jet events it does not matter how much dijet contamination there is in the signal region. This difference in measured response is the second factor contributing to the effect of dijet contamination on the MPF ratio. It has been studied in the past using background-only MC samples,

where it was found that the relative response difference between signal and background could conservatively be covered by assuming a flat 5% response difference across all p_{T} [51]. This conservative estimate is still used. It can be helpful to study the difference in response between the tight photon selection and the loose-not-tight selection as well (see Fig. 5.21), which shows that a 5% absolute difference in response would be a large overestimate over the majority of the p_{T} range considered. Note that by their very nature the response of dijet fakes is closer to the response of photons than most jets because they have a large EM component.

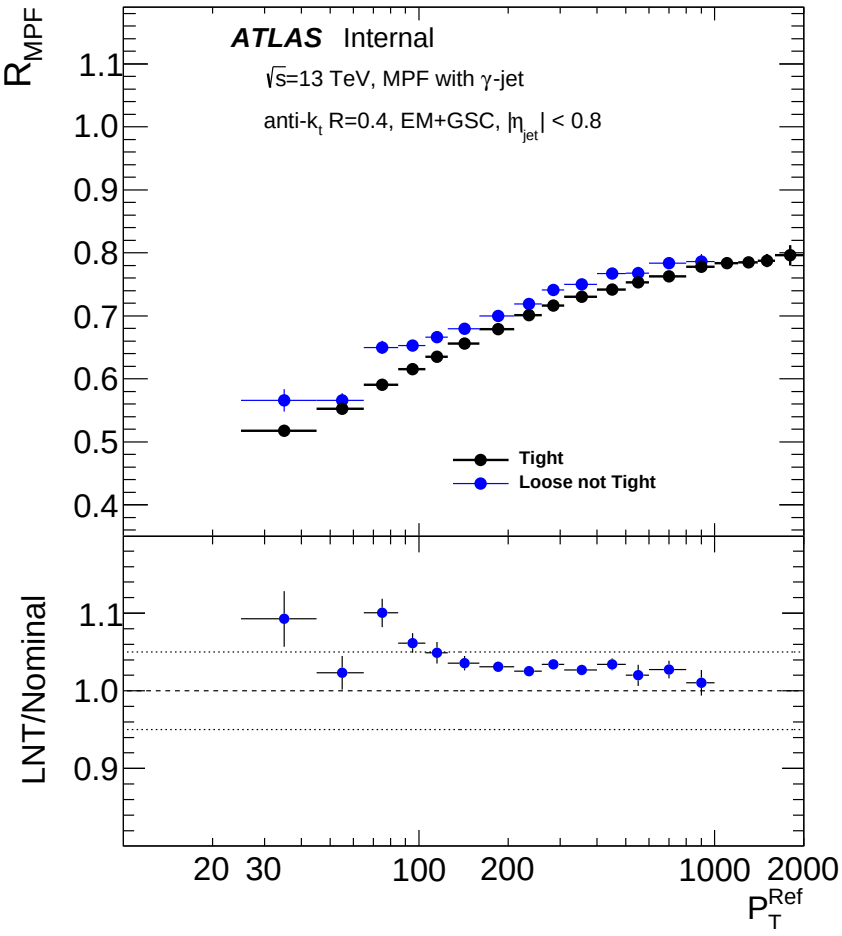

Figure 5.21: Comparison of the EM+GSC scale MPF response using the tight photons selection compared to using the loose-not-tight (LNT) selection.

5.5.5 Monte Carlo Generator

Within the ATLAS collaboration a large variety of Monte Carlo generators are used. An additional uncertainty is included to cover any potential differences in the jet response between

samples produced with different generators. It is derived by comparing the nominal results to a set of results calculated using a second, different, Monte Carlo sample. The second samples used in this study have both been generated and showered using SHERPA [52], which uses the cluster fragmentation model as described in [53]. For the γ+jet sample the CT10 PDF set [54] is used while NNPDF3.0 NNLO [55] is used for Z+jet. The detector simulation is still the default ATLAS setup, which uses GEANT4 with the Bertini Cascade Model transitioning to the Fritiof Model combined with the Precompound model (called FTFP) at higher energy. The EM+GSC scale response measured using γ+jet in the SHERPA sample can be seen in Fig. 5.22, while the response in SHERPA using Z+jet can be seen in Fig. 5.23.

5.5.6 Results

The various systematic uncertainties discussed in this chapter are added in quadrature (along with the statistical uncertainty on the central values) to obtain the total uncertainty on the residual data/MC correction. The uncertainties on the EM+GSC scale response using γ+jet events are shown in Fig. 5.26. Above 60 GeV the total uncertainty is approximately flat at 1%, with the single largest component over the majority of that range being the photon energy scale uncertainty. Below 60 GeV the uncertainty grows to about 6% with increasing contributions from the MC-based the photon purity uncertainties. The uncertainty on the JES for the EM+GSC scale using Z+jet events is shown in Fig. 5.27; it is on the order of 0.5% between $\sim$ 30 GeV and 500 GeV. In this range the largest component to the uncertainty varies between the MC generator uncertainty and the statistical uncertainty. Above 500 GeV the Z+jet calibration becomes statistically limited while for lower energies (below 30 GeV) the MC generator uncertainty sets the scale (up to 4%).

The response for LC+GSC scale jets for γ+jet and Z+jet are shown in Figs. 5.24 and 5.25, with the uncertainties shown in Figs. 5.28 and 5.29, respectively. The uncertainties using γ+jet are once again approximately flat at around 1% above 60 GeV, with the largest component being the photon energy scale. Below 60 GeV the largest components are photon purity and the generator uncertainty, which is slightly larger at LC scale leading to a larger overall uncertainty (up to $\sim$ 7%). The LC+GSC scale uncertainty for Z+jet events is similar to the EM+GSC scale uncertainty, dropping as low as $\sim$ 0.5% between 30 GeV and 500 GeV and growing to slightly more than 5% at the lowest energies due to a slightly larger disagreement between the two generators at LC scale.

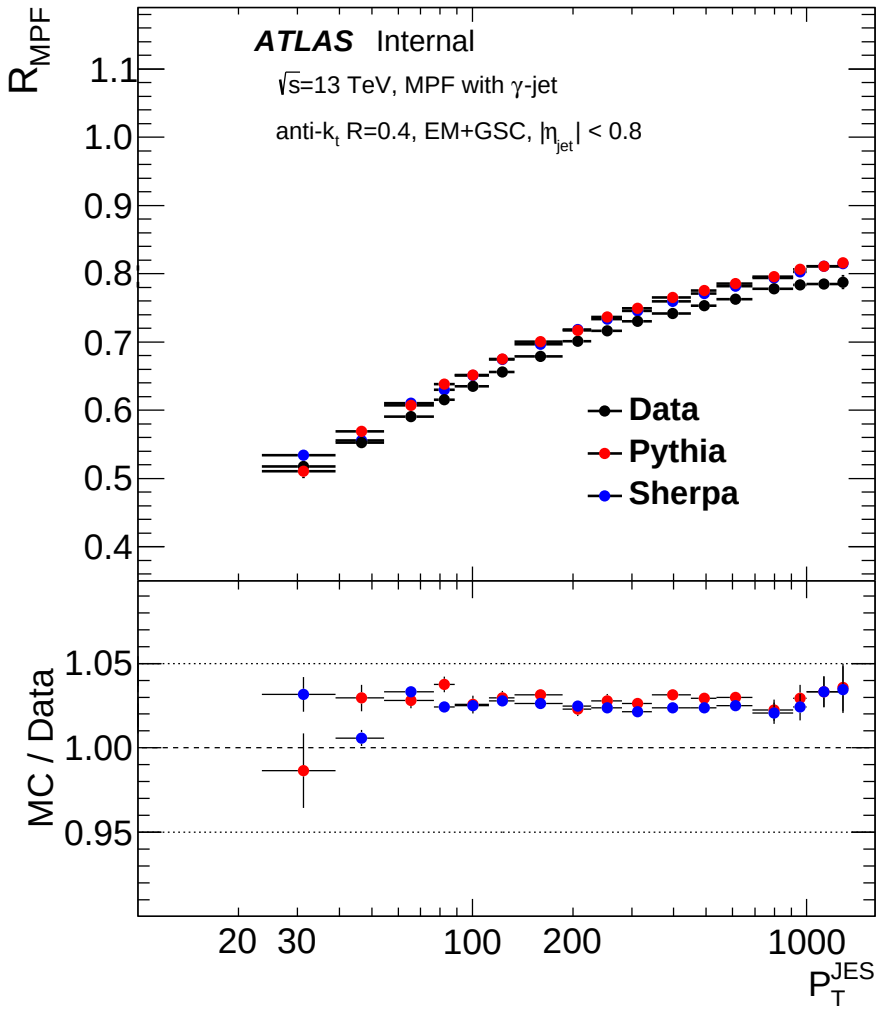

Figure 5.22: The EM+GSC scale response measured using the MPF technique in γ+jet events. Shown in black is the response measured using data from the 2016 dataset, in red is the nominal Monte Carlo sample and in blue is an additional Monte Carlo sample for comparison. See text for details on the Monte Carlo models. The lower inset shows the data to Monte Carlo ratio, with the colour of the points corresponding to the simulated sample used in the ratio.

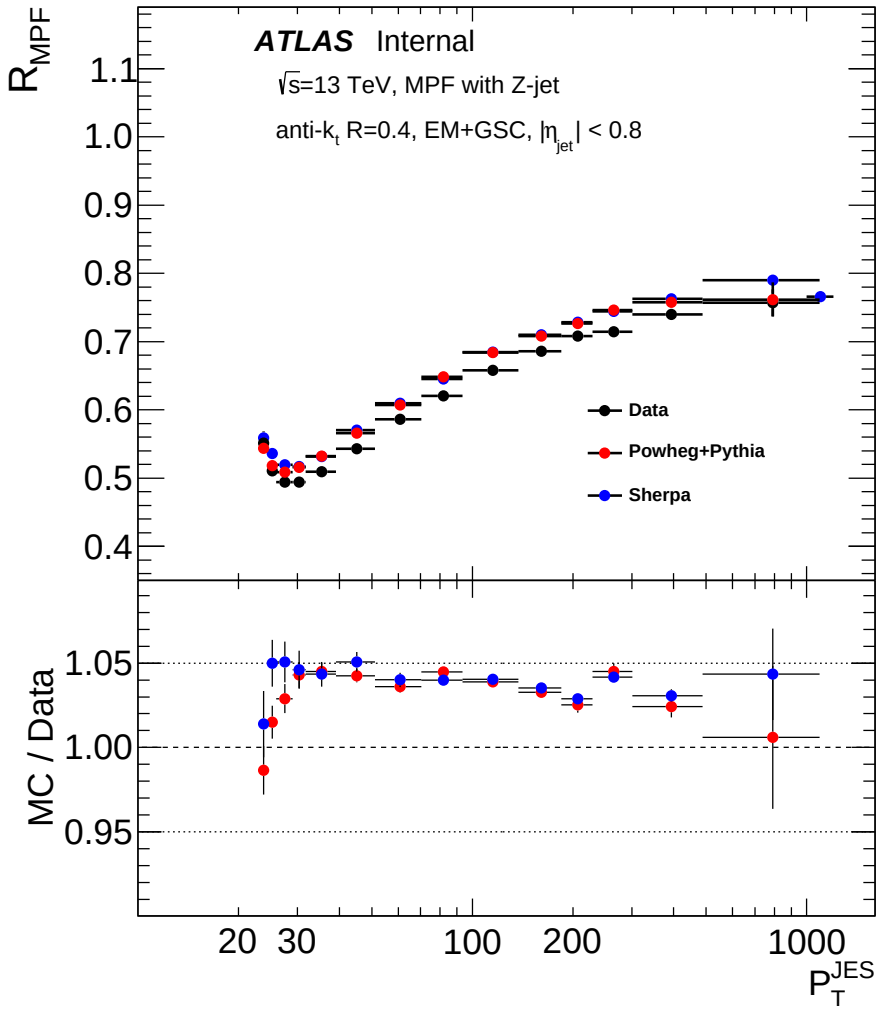

Figure 5.23: The EM+GSC scale response measured using the MPF in Z+jet events. Shown in black is the response measured using data from the 2016 dataset, in red is the nominal Monte Carlo sample and in blue is an additional Monte Carlo sample for comparison. The lower inset shows the data to Monte Carlo ratio, with the colour of the points corresponding to the simulated sample used in the ratio.

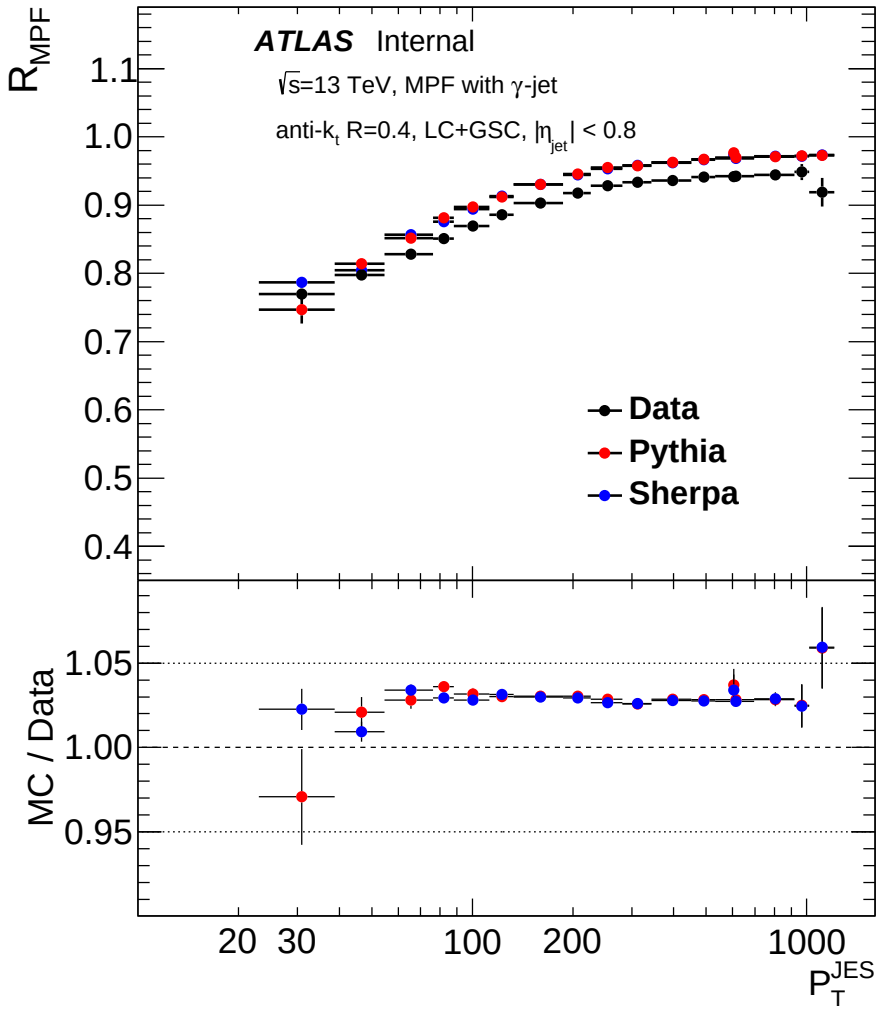

Figure 5.24: The LC+GSC scale response measured using the MPF technique in γ+jet events. Shown in black is the response measured using data from the 2016 dataset, in red is the nominal Monte Carlo sample (Powheg+Pythia) and in clue is an additional Monte Carlo sample for comparison. The lower inset shows the data to Monte Carlo ratio, with the colour of the points corresponding to the simulated sample used in the ratio.

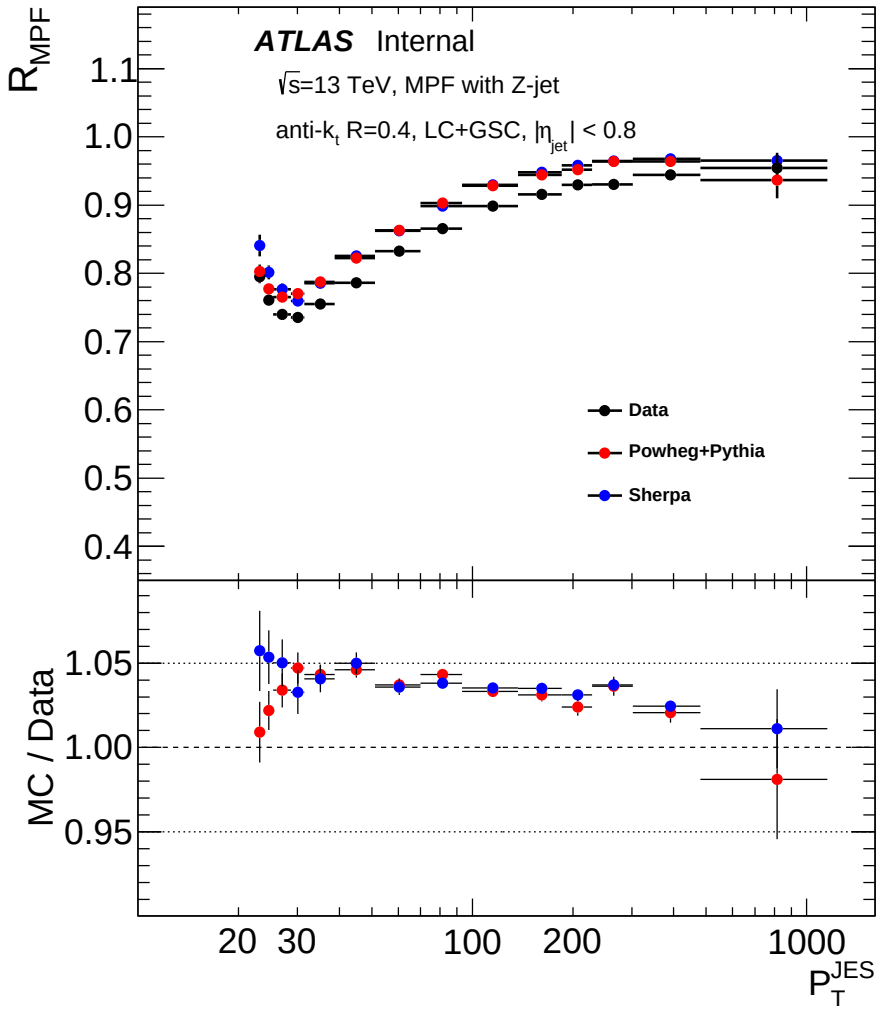

Figure 5.25: The LC+GSC scale response measured using the MPF technique in Z+jet events. Shown in black is the response measured using data from the 2016 dataset, in red is the nominal Monte Carlo sample (Powheg+Pythia) and in clue is an additional Monte Carlo sample for comparison. The lower inset shows the data to Monte Carlo ratio, with the colour of the points corresponding to the simulated sample used in the ratio.

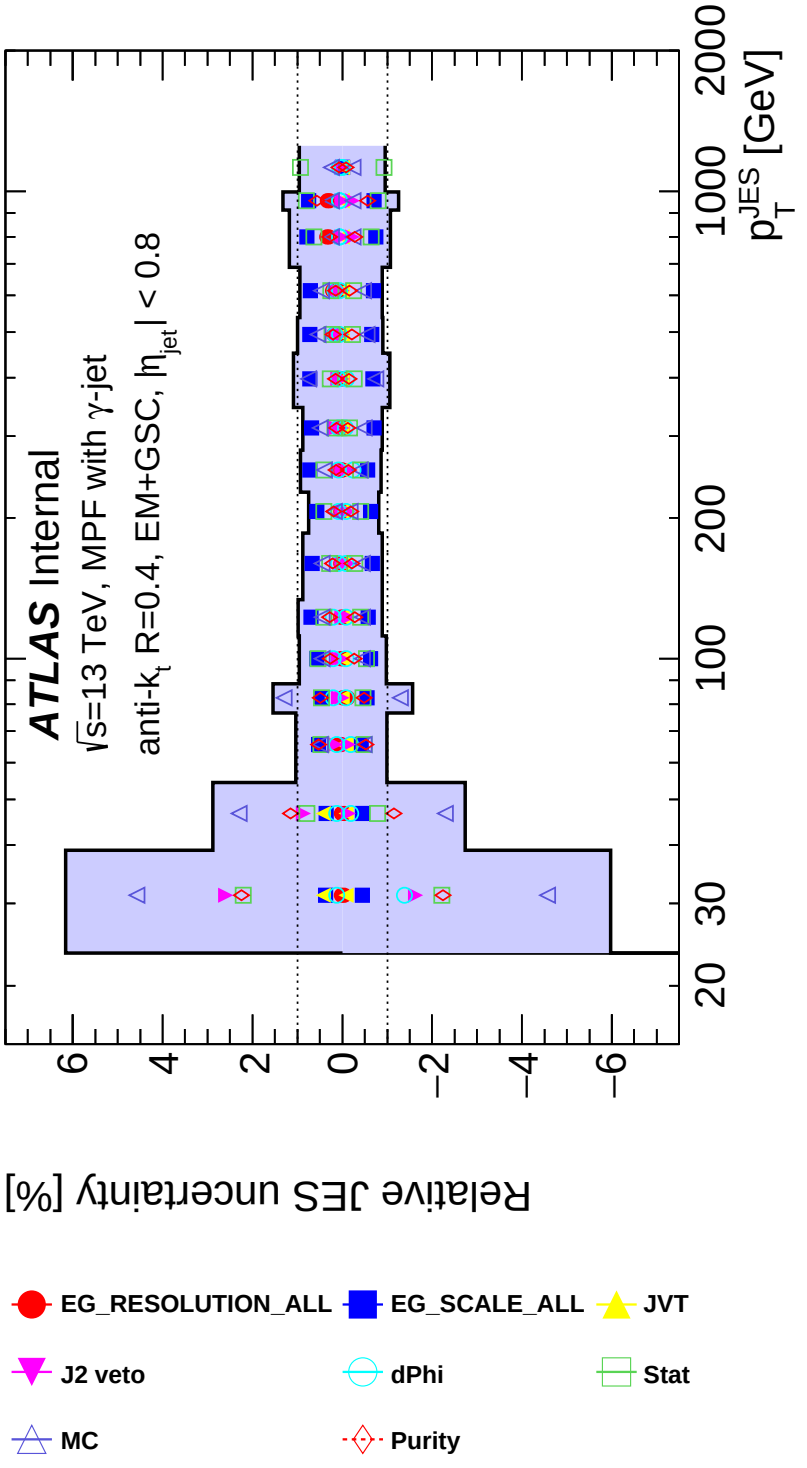

Figure 5.26: The total uncertainty (both statistical and systematic) on the measurement of the relative EM+GSC scale response between data and MC using γ+jet events. It is broken down into the various uncertainty sources that go into the total uncertainty.

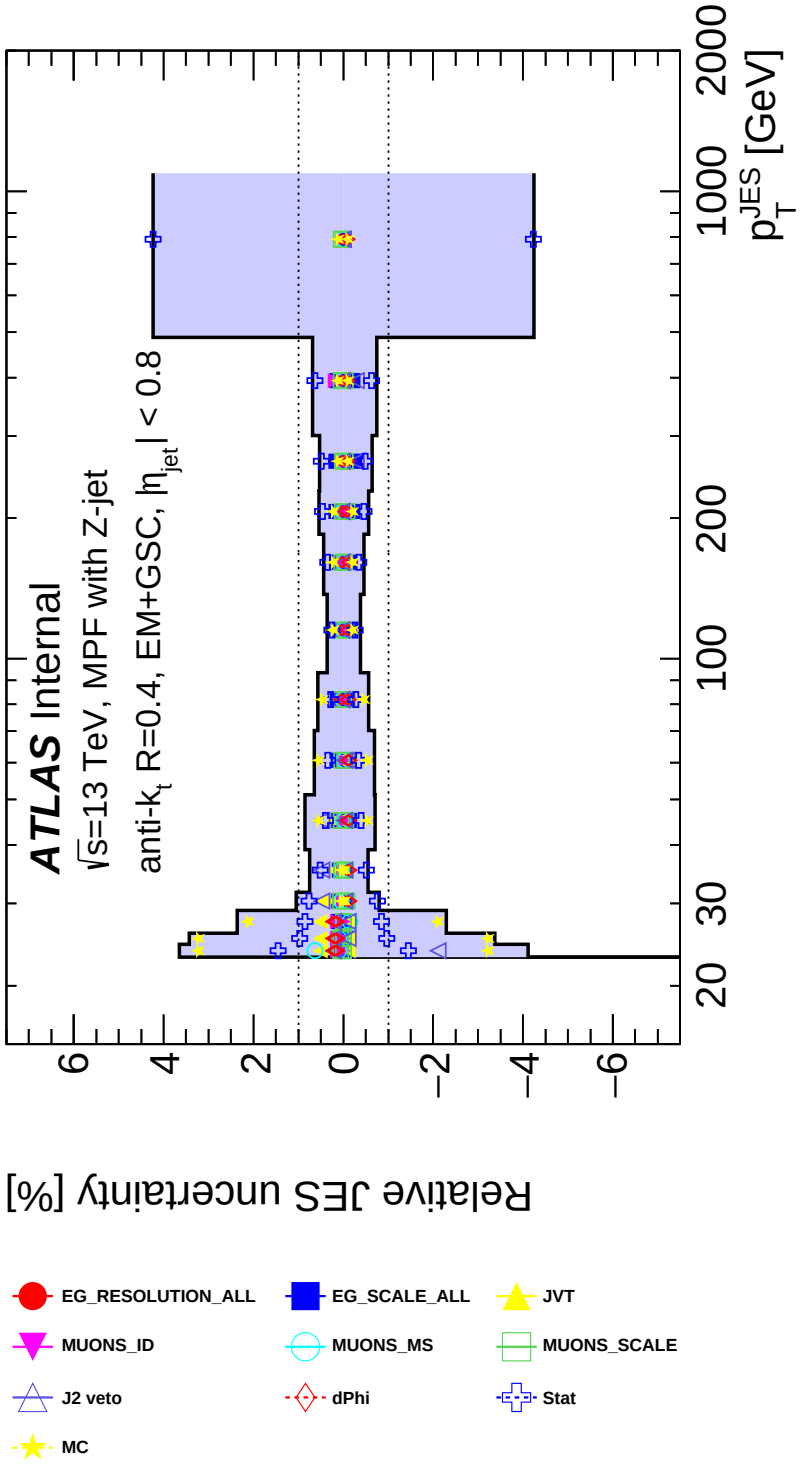

Figure 5.27: The total uncertainty (both statistical and systematic) on the measurement of the relative EM+GSC scale response between data and MC using Z+jet events. It is broken down into the various uncertainty sources that go into the total uncertainty.

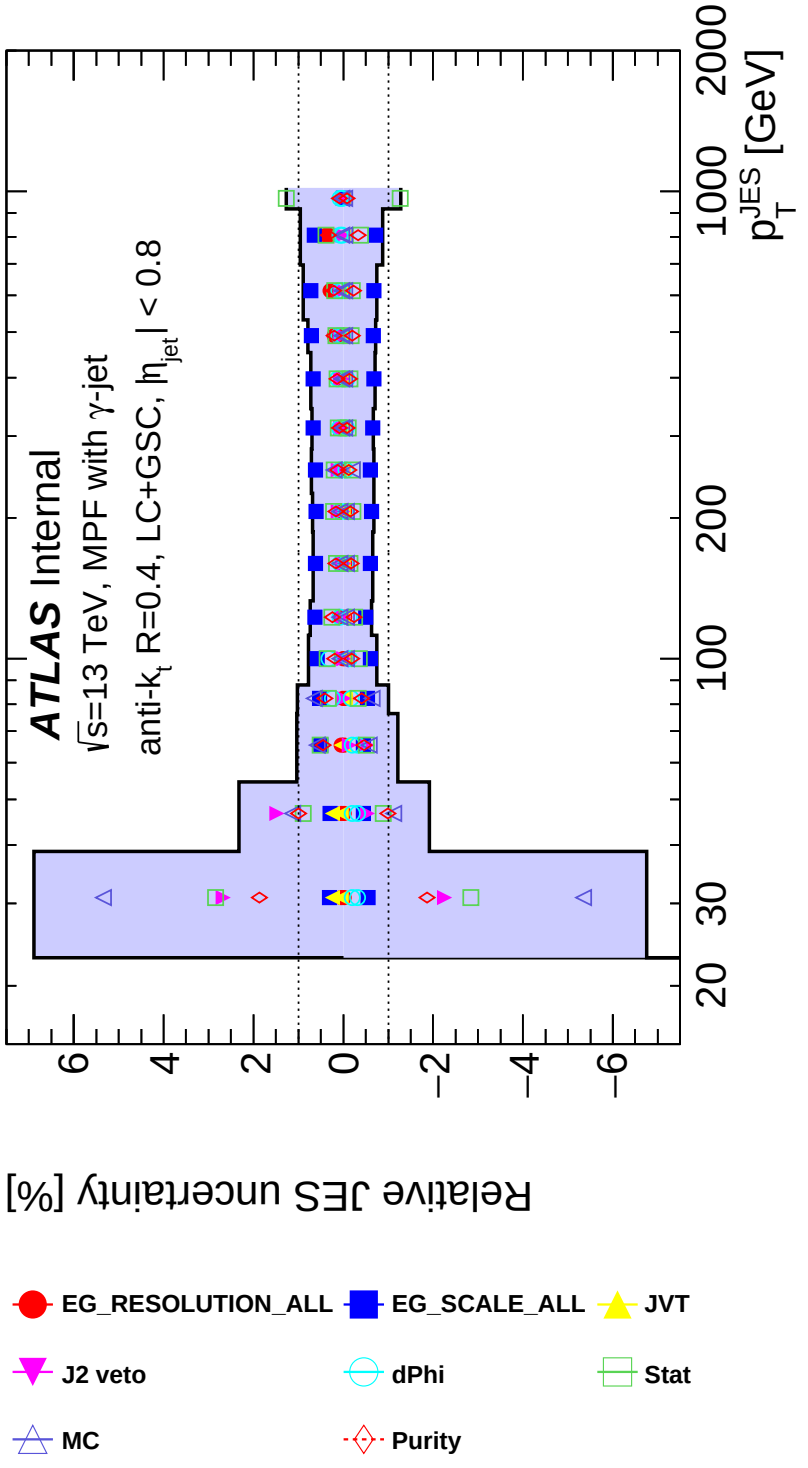

Figure 5.28: The total uncertainty (both statistical and systematic) on the measurement of the relative LC+GSC scale response between data and MC using γ+jet events. It is broken down into the various uncertainty sources that go into the total uncertainty.

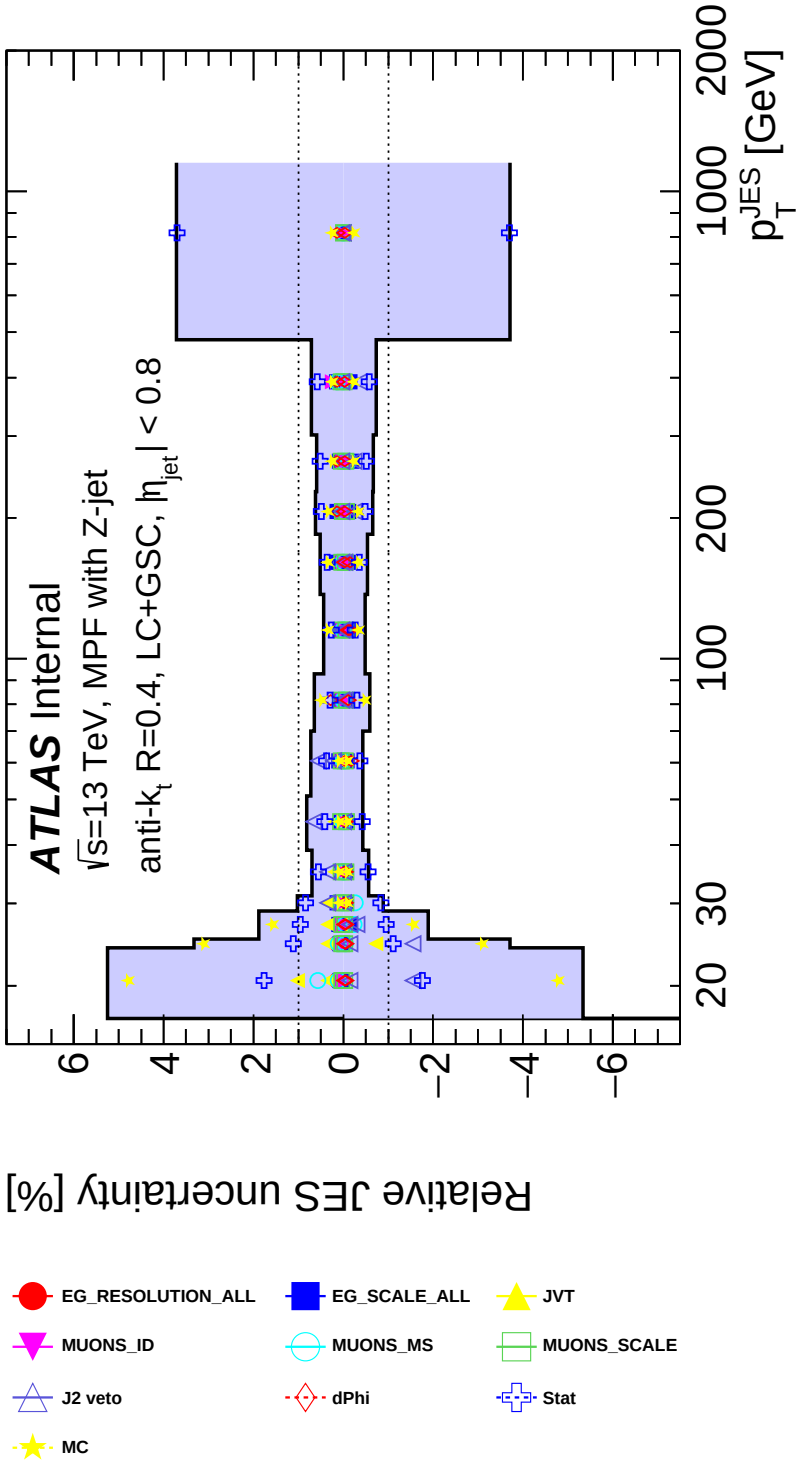

Figure 5.29: The total uncertainty (both statistical and systematic) on the measurement of the relative LC+GSC scale response between data and MC using Z+jet events. It is broken down into the various uncertainty sources that go into the total uncertainty.

Chapter 6

Additional Jet Studies

Even with a jet calibration firmly in hand additional studies on jet phenomenology can go a long way towards advancing our knowledge of the jet response and potentially moving towards better calibrations in the future. In this chapter the question is explored of how the energy from the hadronic recoil in the 2→2 systems used in *in-situ* calibration schemes is distributed around the jet axis. The flow of energy across the boundary of the jet definition is also studied (see the showering correction in Sec. 4.4). Finally some key assumptions used in the derivation of the MPF are examined, including the relationship between the response of the recoil and the response of the jet, as well as the effect of the underlying event on the derivation of the MPF.

6.1 Distribution of Hadronic Recoil Energy

As mentioned in Sec. 4.4 the majority of the energy from the hadronic recoil resides within a narrow energy core that has a large energy density (the core of the reconstructed the jet). In this section this statement is explored by measuring how the energy from the recoil is distributed around the calorimeter. This is done by measuring the average energy density in an annulus with an inner radius of $r-\Delta r$ and an outer radius of $r+\Delta r$, which is defined as

$$\rho\left(r\right)=\left(\frac{E\left(r-\Delta r,r+\Delta r\right)}{\pi\left[\left(r+\Delta r\right)^{2}-\left(r-\Delta r\right)^{2}\right]E^{\mathrm{jet}}}\right), \tag{6.1}$$

where $E\left(r-\Delta r,r+\Delta r\right)$ is the sum of the energy of all clusters with a distance R from the jet between $r-\Delta r$ and $r+\Delta r$. As this thesis aims to measure this energy density profile in the context of an MPF based calibration, results are obtained using the same selection used in the main analysis (see Sec. 5.2), and are also binned in $p_{\mathrm{T}}^{\mathrm{ref}}$. The energy distributions using EM-scale clusters at three different reference energies with Z+jet events are shown in Figs. 6.1, 6.2, and 6.3. One feature that should be understood is a dip in energy density at the boundary of the jet (in this case at $\Delta R=0.4$). This dip is not a feature of the recoil or the calorimeter, but of the jet reconstruction algorithm, which creates an object

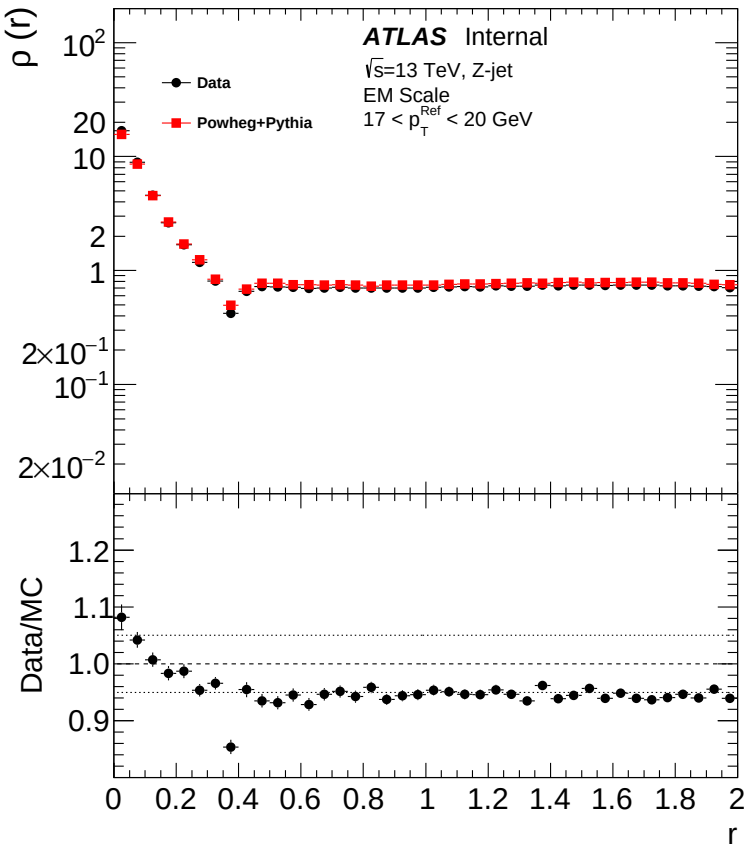

Figure 6.1: Average distribution of energy surrounding the leading jet in Z+jet events with p_{T}^{Z} between 17 and 20 GeV.

which is centered on the most energetic clusters it contains [56]. The location of the jet axis can be affected by significant energy clusters near the jet reconstruction boundary, which effectively moves these clusters closer to the axis, depleting the region just inside of the jet boundary. For example, consider a jet growing from $R = 0.35$ to $R = 0.4$. If this jet growth only adds clusters with energies which are small with respect to the energy of the growing proto-jet the centre of the jet (the four-momentum sum of its constituents) does not move very much. If there is a cluster with a relatively high energy compared to the energy of the proto-jet the centre of the jet will move closer to this new addition. This process moves high energy clusters away from the jet boundary towards the centre of the jet. This effect is especially evident for lower energy jets where even very small energy clusters represent a relatively large fraction of the total jet energy. This dip is therefore more pronounced in Fig. 6.1 than in Fig. 6.2 or Fig 6.3. The jet reconstruction threshold also affects the energy density distribution for the region with low reference object energy. With these topologies events with more energy distributed outside of the jet definition (beyond R=0.4 in this

case) do not have enough energy in the core to pass the threshold. This means that in Fig. 6.1 the energy density flattens out more quickly as a function of R than it would if the reconstruction threshold were removed.

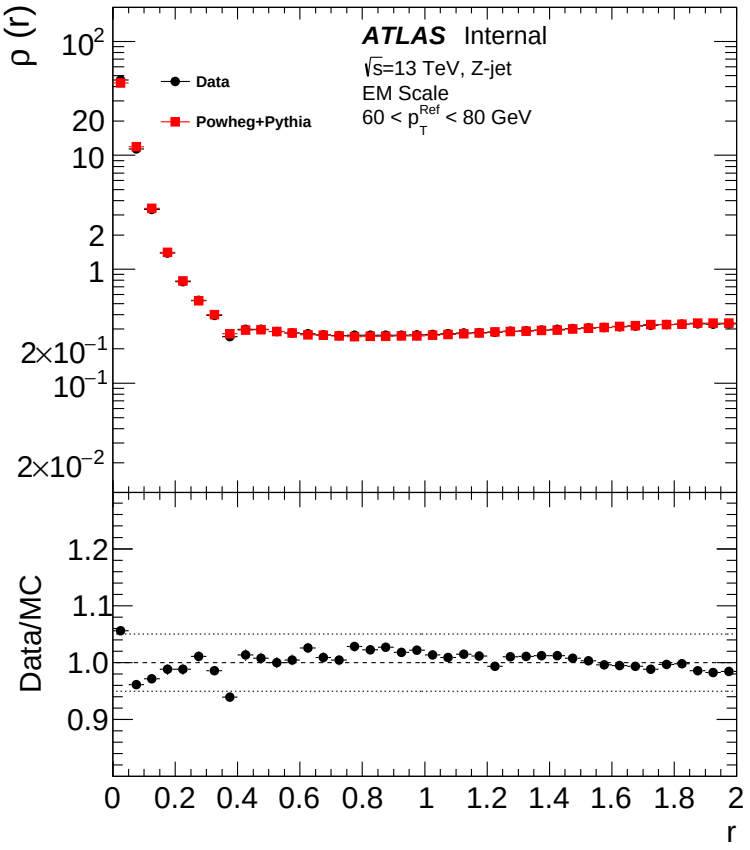

Figure 6.2: Average distribution of energy surrounding the leading jet in Z+jet events with p_{T}^{Z} between 60 and 80 GeV.

At larger distances from the jet's core the energy density is relatively flat, which corresponds to the average pileup energy density. There is also a slight increase in the energy density with growing distance from the leading jet. This is caused by the presence of the subleading jet, which tends to be produced in the same hemisphere of the calorimeter as the reference object.

6.2 Expanded MPF Derivation

In Sec. 4.3 a derivation of the MPF was presented which considered only the hard scattering part of the event, ignoring any potential effects of the underlying event and pileup (see Fig. 6.4). This potential deficiency in the derivation was justified by arguing that the under-

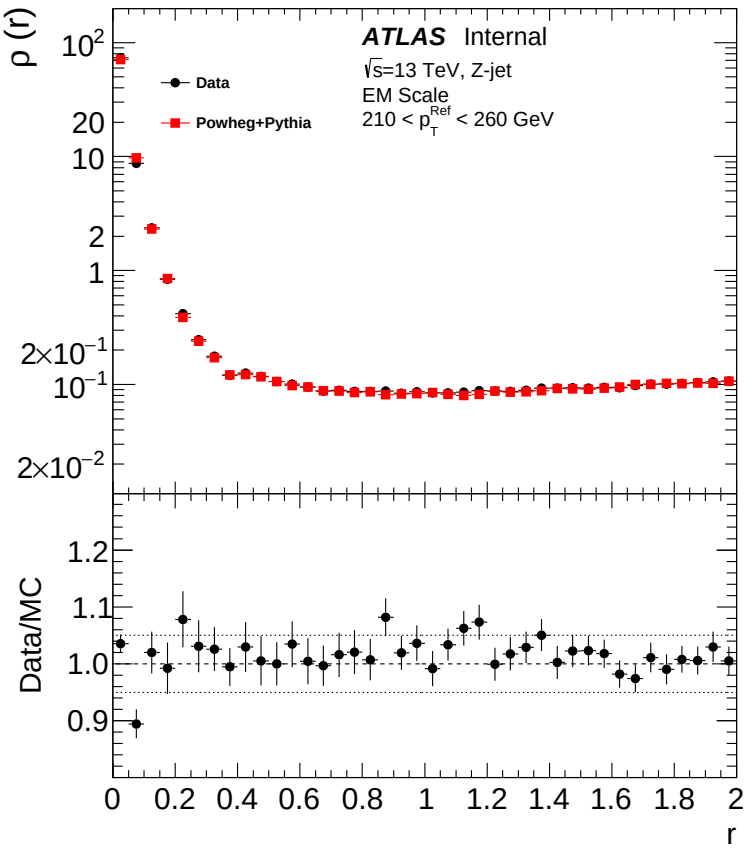

Figure 6.3: Average distribution of energy surrounding the leading jet in Z+jet events with p_{T}^{Z} between 210 and 260 GeV.

lying event and pileup are symmetric in ϕ when averaged over many events and therefore do not contribute to the measured MPF response. This assumption is tested in this section.

The definition of the MPF in Eq. 4.9, is modified by a term Δ^{OA} that accounts for the effect of other activity in the event on measured R_{recoil},

$$R_{\mathrm{recoil}} = 1 + \frac{\vec{E}_{\mathrm{T}}^{\mathrm{miss,recoil}} \cdot \hat{p}_{\mathrm{T}}^{\mathrm{ref}}}{E_{\mathrm{T}}^{\mathrm{ref}}} + \Delta^{\mathrm{OA}}, \tag{6.2}$$

where it is explicitly shown that the original derivation assumed that the MET originated completely from the mismeasurement of the energy of the recoil. In an effort to obtain an expression in terms of measurable quantities $\vec{E}_{\mathrm{T}}^{\mathrm{miss,recoil}}$ is now expressed as

$$\vec{E}_{\mathrm{T}}^{\mathrm{miss,recoil}} = \vec{E}_{\mathrm{T}}^{\mathrm{recoil}} - \vec{E}_{\mathrm{T}}^{\mathrm{meas,recoil}}, \tag{6.3}$$

which is to say the amount of energy that isn't measured is simply equal to the total energy minus the energy that has been measured. Using the response R_{recoil} of the calorimeter for

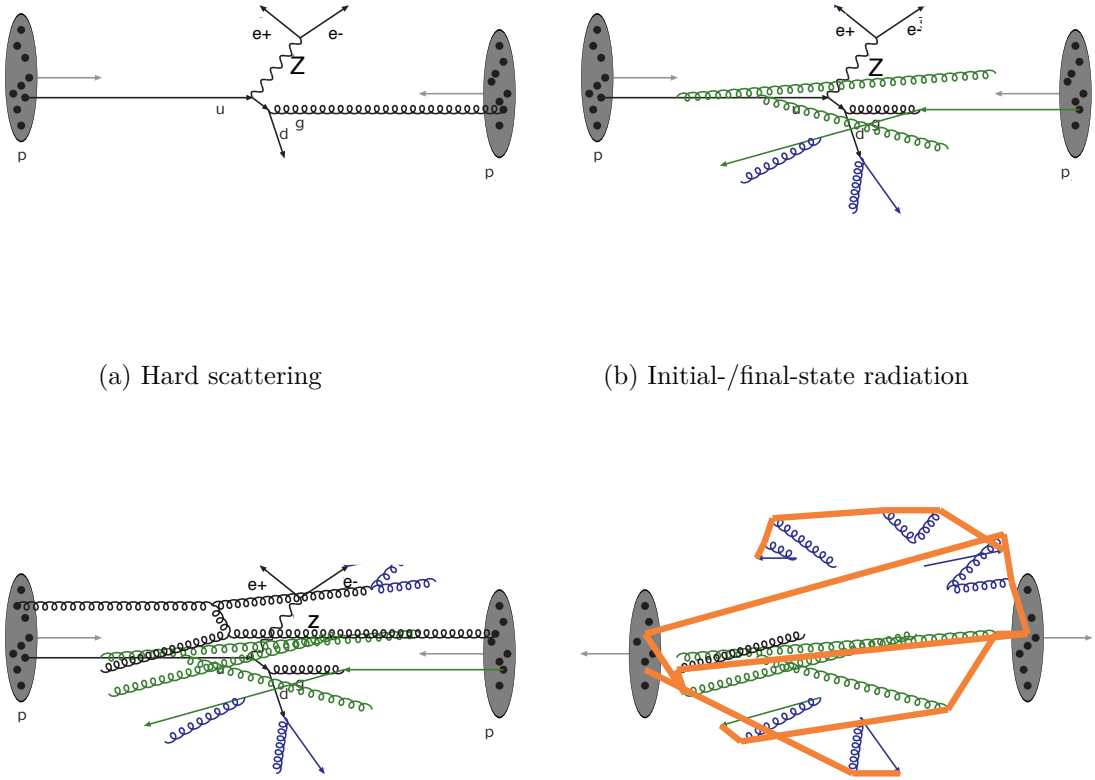

(a) Hard scattering

(b) Initial-/final-state radiation

(c) Multiple collisions

(d) Colour connection to spectator partons

Figure 6.4: Illustration showing the various processes that contribute to the underlying event. Panel *a*) shows the initial hard scattering of interest, in this case a Z boson is produced back-to-back with a quark with the boson subsequently decaying into an electron/positron pair. This is the idealized scenario assumed in the original derivation of the MPF in Sec. 4.3. In panel *b*) both the incoming and outgoing partons are shown to radiate, which spoils the balance between the Z boson and the hard scattered quark and adds additional particles to the final state. Panel *c*) shows that multiple parton-parton interactions can occur within a single proton-proton collision, and that these additional interactions are also affected by initial- and final-state radiation. Panel *d*) illustrates the colour connection between all of the partons generated during the collision and the spectator partons which were not directly involved. As these particles travel further apart these colour connections will create additional particles. Finally all of these created particles can also decay, creating an even greater number of particles in the final state. Images from [57].

the recoil,

$$R_{\text{recoil}}\vec{E}_{\text{T}}^{\text{recoil}} = \vec{E}_{\text{T}}^{\text{meas,recoil}}, \tag{6.4}$$

which leads to

$$\vec{E}_{\text{T}}^{\text{miss,recoil}} = \vec{E}_{\text{T}}^{\text{meas,recoil}} \left(\frac{1 - R_{\text{recoil}}}{R_{\text{recoil}}} \right). \tag{6.5}$$

Using this definition of $\vec{E}_{\text{T}}^{\text{miss,recoil}}$ in Eq. 6.2 and rearranging to solve for Δ^{OA}, the following expression is obtained for the contribution of the other activity to the MPF

$$\Delta^{\text{OA}} = (R_{\text{recoil}} - 1) \left(1 + \frac{\hat{n}_{\text{ref}} \cdot \vec{E}_{\text{T}}^{\text{meas,recoil}}}{R_{\text{recoil}} E_{\text{T}}^{\text{ref}}} \right). \tag{6.6}$$

To use this expression both the response of the recoil and the measured recoil energy must be known, neither of which is true. To first order the other activity can be treated as being ϕ symmetric and therefore the effect of the other activity on the MPF can be assumed to be small (note the MPF has been successfully used in jet calibration schemes in the past). This allows the use of the MPF itself as a measure of the response of the recoil. Obtaining a measurement of the full energy of the hadronic recoil at the detector level with the underlying event removed (and without including pileup) is also a difficult issue. As the MPF technique already intimately connects the energy of the recoil to the energy of the jet this strategy will be used again. A range of jet cone sizes will be used ranging from a jet size parameter of R=0.1, which contains only the highest energy most central components of a jet, to R=1.0 which contains essential all of the hard scattering along with a significant amount of underlying event. As these are non-standard jet collections in ATLAS the residual pileup correction is not available for all sizes considered, however it is still possible to remove the majority of the pileup from each jet using the jet area subtraction as described in Sec. 4.1.

It is worth noting a few limitations of this technique before moving further. Just like in the derivation of the MPF, substituting the energy of the leading jet for the energy of the recoil is a sensible substitution only when the leading jet makes up the majority of the recoil (when the balance is not spoiled by ISR/FSR). This is ensured once again by applying both a $\Delta\phi$ and subleading jet (J2) requirement. In the case of this analysis $\Delta\phi$ (leading jet, ref)>2.9 and the p_{T} of the subleading jet without calibration must be less than 5% of the p_{T} of the reference object ($p_{\text{T}}^{J2} < 0.05\ p_{\text{T}}^{\text{ref}}$). These very tight selection criteria remove nearly all events in the lowest $p_{\text{T}}^{\text{ref}}$ bins. At low energies pileup becomes a larger issue, first by pileup jets being misidentified as the subleading jet which changes how strict the previously applied requirement is, and then by pileup jets being misidentified as the leading jet causing the event to fail the $\Delta\phi$ requirement. Examples of Δ^{OA} distributions can be seen in Fig. 6.5.

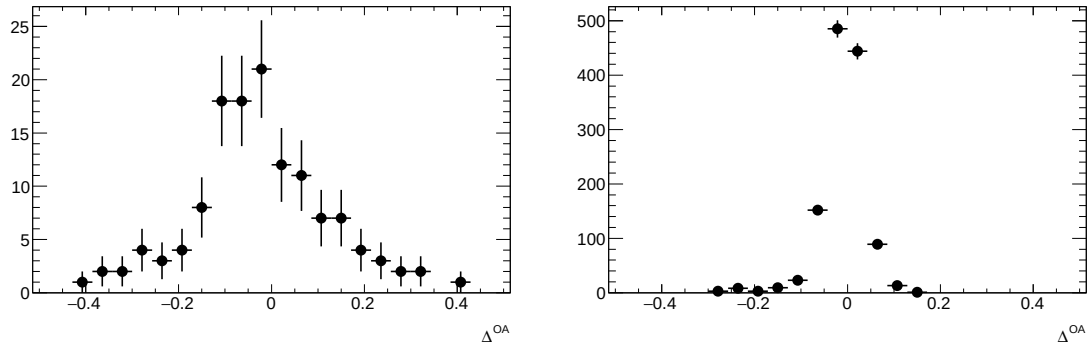

(a) 45 GeV $< p_{\mathrm{T}}^{\mathrm{ref}} <$ 60 GeV (b) 260 GeV $< p_{\mathrm{T}}^{\mathrm{ref}} <$ 350 GeV

Figure 6.5: Distributions of Δ^{OA} in 2016 data at EM scale using Z+jet events for two different p_{T}^{Z} bins. Made using anti-k_{t} r=0.4 jets as an estimate for the hadronic recoil energy.

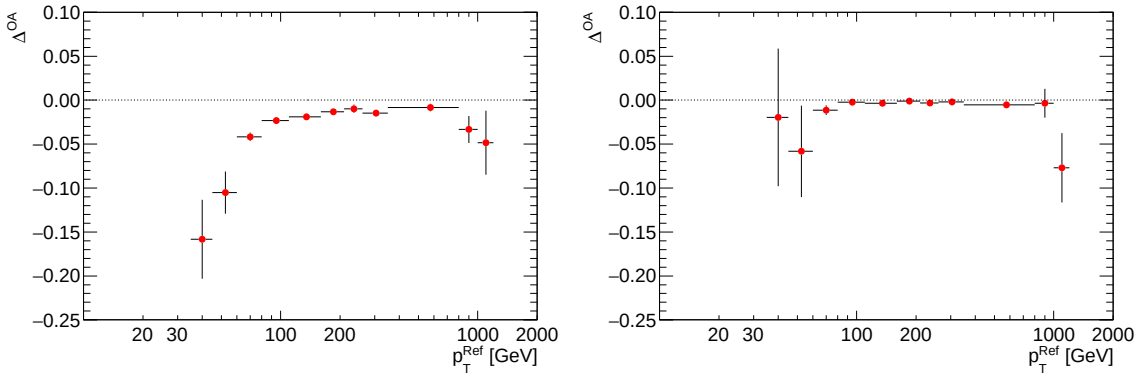

(a) Anti-k_{t} R=0.1 (b) Anti-k_{t} R=0.4

Figure 6.6: The effect of the other activity in the event on the measured recoil response, as determined using Eq. 6.6. The leading anti-k_{t} R=0.1/0.4 jet reconstructed using EM scale clusters is used as an estimate for the energy of the full recoil. Using data collected in 2016.

This measure of the effect of the other activity on the MPF is shown as a function of $p_{\mathrm{T}}^{\mathrm{ref}}$ using various jet sizes as a substitute for the energy of the recoil in Figs. 6.6 and 6.7. As seen in Sec. 6.1 the energy density of jets in the energy range considered remains large compared to that of pileup/underlying activity out to at least a distance of $\Delta\mathrm{R} = 0.4$ away from the jet axis. For this reason the use of jets reconstructed using size parameters smaller than this value as a stand-in for the energy of the recoil is known to be a bad approximation, and therefore these plots are included only for illustrative purposes. It is also worth noting that in the lowest $p_{\mathrm{T}}^{\mathrm{ref}}$ bins the effect of the reconstruction threshold is to remove all events with a low $\vec{E}_{\mathrm{T}}^{\mathrm{meas,recoil}}$, biasing the quantity high. This effect is seen in Fig. 6.7 for anti-k_{t} R=1.0 jets where Δ^{OA} becomes positive at low energies.

As shown in Fig. 6.8 Δ^{OA} can be quite sensitive to the choice of cone size at small values of p_{T} but it tends to show that the MPF is not affected by the other activity in the event

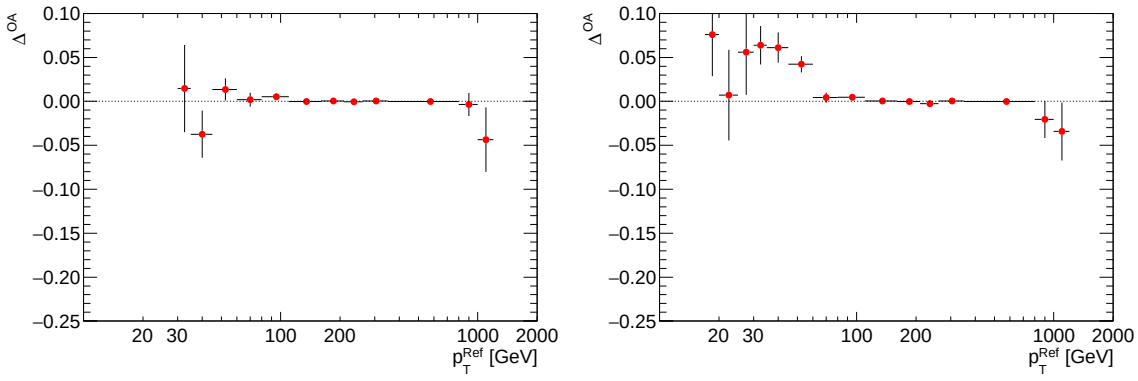

(a) Anti-k_t R=0.7 (b) Anti-k_t R=1.0

Figure 6.7: The effect of the other activity in the event on the measured recoil response, as determined using Eq. 6.6. The leading anti-k_t R=0.7/1.0 jet reconstructed using EM scale clusters is used as an estimate for the energy of the full recoil. Using data collected in 2016.

when using a suitably large radius jet which includes the full recoil. This means that the previously used assumption that the other activity is ϕ symmetric when averaged over a large number of events is correct and therefore does not affect the MPF's ability to measure the response of the recoil.

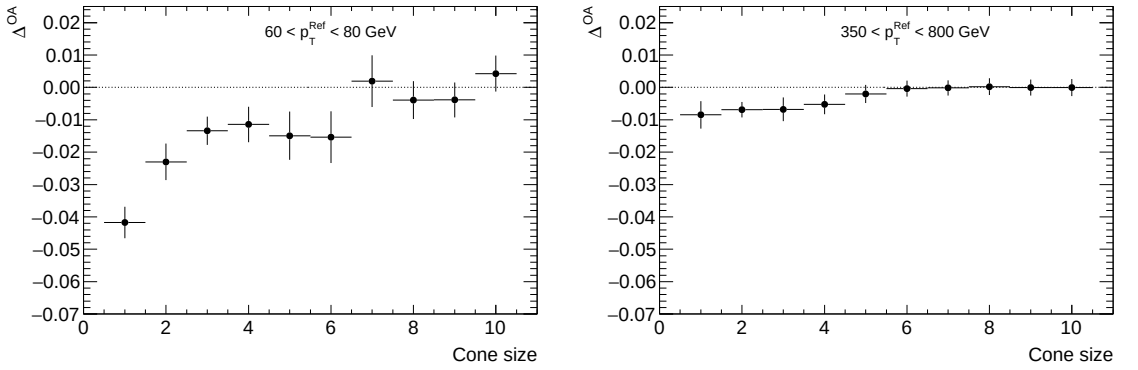

(a) 60 GeV $< p_T^{ref} <$ 80 GeV (b) 350 GeV $< p_T^{ref} <$ 800 GeV

Figure 6.8: The effect of the other activity in the event on the measured recoil response, as determined using Eq. 6.6. The dependence of this quantity on the size of the jet used as a stand in for the total recoil is shown for two p_T^{ref} bins. Results shown have been measured using EM scale jets from the 2016 ATLAS dataset.

6.3 Showering Studies

In Sec. 4.4 the so-called showering and topology corrections were briefly introduced as being factors which, when applied together, correct for the difference between the response of the

hadronic recoil (as measured by the MPF) and the response of the jet which is needed for calibration. In previous JES versions in ATLAS the assumption has been that these corrections are well modeled by the Monte Carlo simulation, and an additional conservative uncertainty was added to cover any potential differences [47]. In this thesis these corrections are calculated using a purely simulation based technique to both reduce the systematic uncertainty assigned to the *in-situ* JES and further explore how the calorimeter responds to energy deposits and how that energy flows within the calorimeter.

Sec. 4.4 also introduced the true calorimeter response, which is the sum of the visible energy in the calorimeter deposited by particles originally in the particle jet divided by the total energy of the particle jet, and was used to define both the showering and topology corrections.

$$R_{\text{true}} = \frac{\sum_{i \in \text{particle jet}} E_i^{\text{measured}}}{\sum_{i \in \text{particle jet}} E_i^{\text{true}}} \tag{6.7}$$

$$S = \frac{R_{\text{true}}}{R_{\text{jet}}}. \tag{6.8}$$

To measure this response the 'calibration hits' recorded by the GEANT4 simulation are used. Calibration hits are a history of the idealized interactions between the final state particles and the detector used by GEANT4 to model the deposition of energy by these particles in the detector and the production of secondary particles created in the shower. Each hit corresponds to a single stable particle which initialized the hit, and is characterized by a position (which can be associated with a calorimeter cell) and an energy. The energy of each hit is subdivided into energy deposited by EM interactions (EM energy) or nuclear interactions (non-EM energy), non-visible energy used to excite nuclei (called 'invisible energy') and energy which escapes the calorimeter via neutrinos or muons (called 'escaped energy'). Furthermore every calibration hit is also labeled as being in an active or inactive region of a sampling calorimeter cell, or in dead material (material outside of the calorimeter). Using this information the true calorimeter response can be calculated by summing both the EM and non-EM energy deposited by all particles in the particle jet in the active regions of cells which have been included in a reconstructed topo-cluster and scaling the total energy of each of these cells by their sampling fraction.

As the energy density inside of a jet decreases with increasing distance from the core, it is more likely for energy which was inside of the jet definition at the particle level to move out at the reconstructed level than it is for particles originally outside of the jet to migrate in. That is to say on average the true calorimeter response should be larger than the measured response, meaning the showering correction should be expected to be greater than one. The rate that this energy density is changing near the edge of the jet (and therefore the size of this effect) should be expected to decrease with increasing energy (as the recoil becomes more collimated) and with increasing jet size (as the jet boundary moves further into the tails of the recoil distribution). An example of the distribution of

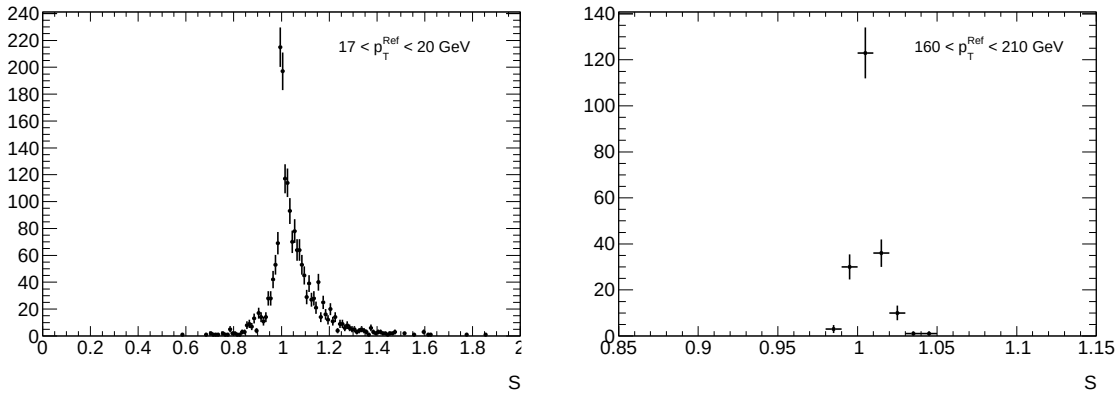

(a) 17 GeV $< p_{\mathrm{T}}^{\mathrm{ref}} <$ 20 GeV (b) 160 GeV $< p_{\mathrm{T}}^{\mathrm{ref}} <$ 210 GeV

Figure 6.9: Showering correction distributions for anti-k_{t} R=0.4 jets at EM scale using Z+jet events in two p_{T}^{Z} bins (note the different x axis scales). Sample generated using POWHEG, showered with PYTHIA and the nuclear interactions modeled using FTFP_BERT (see Sec. 5.1).

measured showering corrections for a single reference p_{T} bin can be seen in Fig. 6.9. As the asymmetry of this distribution is a result of real effects (the slope of the energy density as a function of distance) and not the result of a few pathological events it should be included in the factor S. For this reason the mean of these distributions is taken as a measure of the average showering correction, as opposed to fitting the distribution and using the most probable value.

As this is a Monte Carlo only study an uncertainty on these corrections is obtained by exploring different models for the generation of the calorimeter shower which have been found to cover a range of showering scenarios. As the showering correction is largely affected by the flow of energy inside of the calorimeter, this study will explore the effects of changing the nuclear interaction models used by GEANT4. As a alternative to the default ATLAS model (FTFP_BERT, introduced in Sec. 5.1) a second model named QGSP_BIC is used. This model is used as it differs from FTFP_BERT for a large number of variables related to calorimeter showering [58]. One important notable difference between these two models is the width of the showers produced. This difference in width is necessary to gauge the sensitivity of the showering correction to the jet structure near its boundary. At low energies (below 9.9 GeV) QGSP_BIC uses the Binary Cascade Model (BIC), which propagates the incident particles through 3D models of nuclei that have been created using the expected density and nucleon momentum. Energy is lost by individual hadron/nucleon resonance formation and decay as the incident hadron travels in curved trajectories in a smooth nuclear potential. This differs from the Bertini Cascade model used by FTFP_BERT below 5 GeV which models each nucleus as a continuous medium with new particles being created based on the free space nucleon-nucleon cross sections for that collision.

At higher energies (above 12 GeV) QGSP_BIC uses the Quark Gluon String Model (QGSM) combined with the same Precompound model used in combination with the Fritiof model in FTFP. Both QGSP and FTFP construct 3D models of nuclei from individual nucleons which are subsequently flattened because the incoming hadrons are Lorentz-boosted, and both models make use of QCD strings to model the interactions between the incident hadrons and the atomic nuclei which subsequently decay resulting in secondary particles. The difference is that FTFP can only exchange momentum and create excited nuclei/hadrons, while QGSP can exchange partons and momentum. Diffractive excitations are modeled using a random transverse momentum component sampled from a parameterized Gaussian and the longitudinal component calculated using light cone constraints [38] [39]. The gap between BIC and the QGSM (9.9 GeV - 12 GeV) is covered using the Low Energy Parameterization (LEP) model which has its origins in GHEISHA[59].

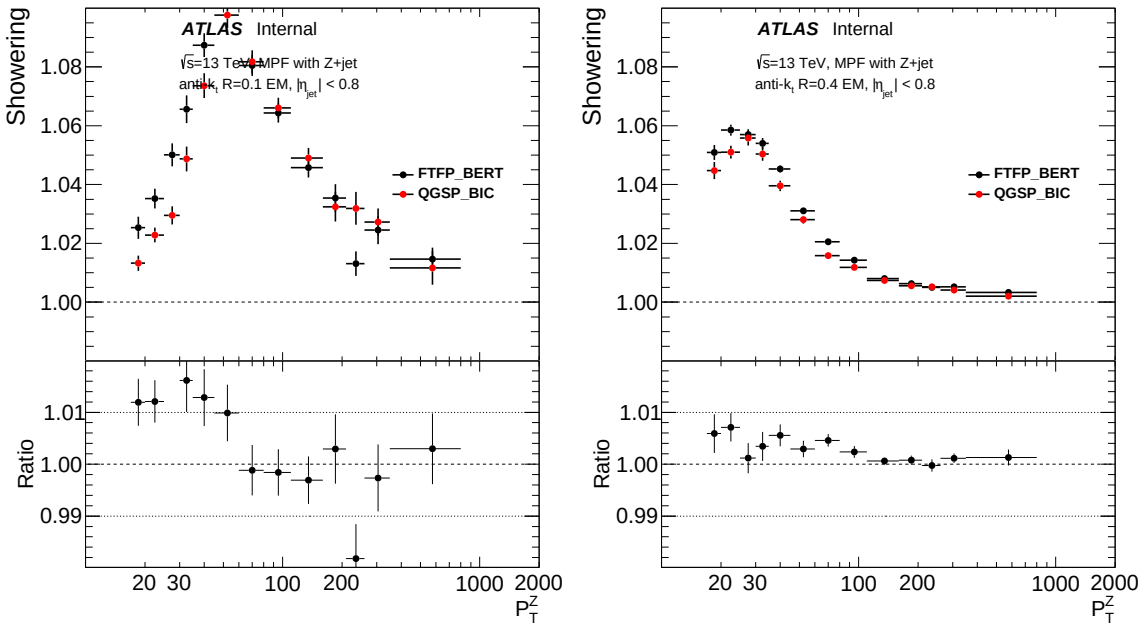

(a) Anti-k_t R=0.1 (b) Anti-k_t R=0.4

Figure 6.10: The showering correction S as defined in Sec. 4.4 for anti-k_t R=0.1/0.4 jets at EM scale.

The showering correction using anti-k_t jets in a range of sizes is shown in Figs. 6.10 and 6.11. As expected the showering correction decreases with energy for all jet sizes, and at higher energies the showering correction decreases with increasing jet size. Once again at low energies the jet reconstruction threshold removes jets with a low R_{jet}, biasing the measured mean to be high and therefore lowering the measured showering correction. This effect is especially evident for low energy small jets (anti-k_t R=0.1) as determining the leading jet with this size can be problematic. It is also worth noting that there is very little difference in the showering correction between the different physics lists used, with

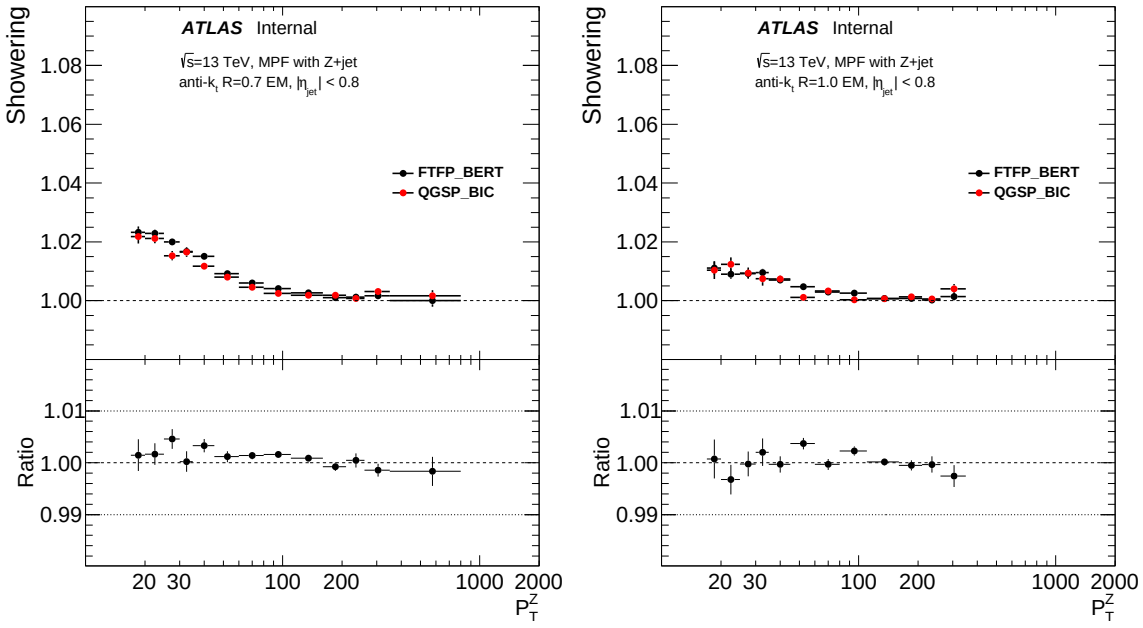

(a) Anti-k_t R=0.7 (b) Anti-k_t R=1.0

Figure 6.11: The showering correction S as defined in Sec. 4.4 for anti-k_t R=0.7/1.0 jets at EM scale.

the largest differences being on the order of 0.5% between 30-80 GeV for anti-k_t R=0.4 jets. The observed differences may be caused by a combination of the higher response to charged pions in QGSP_BIC [58] along with the overall narrower shower profiles observed using QGSP_BIC[60].

Using Monte Carlo truth information it is possible to identify each jet as having originated from a light quark or a gluon. This distinction is more than just academic, as gluon initiated jets tend to have a larger number of lower energy particles and tend to be wider than jets initiated by light quarks. These differences mean that the average jet response for a predominantly gluon-initiated jet sample (dijet for example) can be significantly different than the response in a primarily quark-initiated jet sample (both Z+jet and γ+jet), a fact which is accounted for in the JES uncertainty by both a flavour response and flavour composition uncertainty [61]. With these facts as motivation the showering correction has also been measured individually for both quark and gluon jets.

The showering correction for both quark and gluon initiated jets can be seen in Fig. 6.12. As gluon jets do tend to be wider the showering correction for them tends to be larger as well. Fig. 6.12 does appear to show that the choice of physics list has a larger effect on the showering correction for gluon jets than it does for quark jets. Unfortunately the fraction of jets in Z+jet samples which are initiated by gluons is very small (∼15%), leaving the comparison between the two physics lists statistically limited.

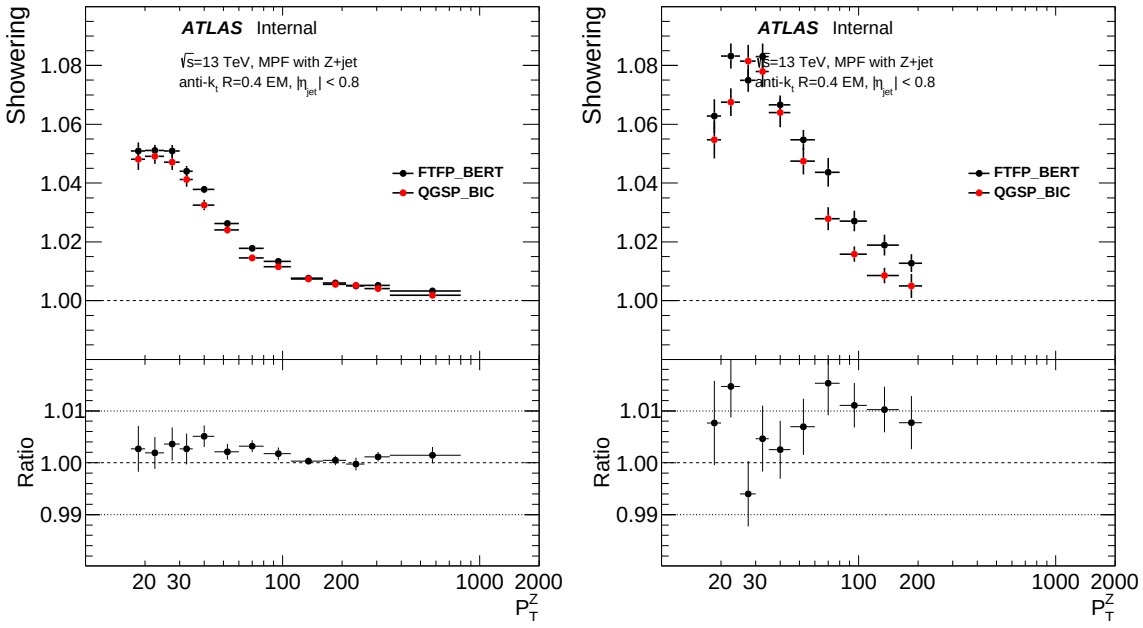

(a) Quark initiated jets

(b) Gluon initiated jets

Figure 6.12: The showering correction S as defined in Sec. 4.4 for anti-k_t R=0.4 jets at EM scale for quark/gluon initiated jets.

6.4 Topology Correction

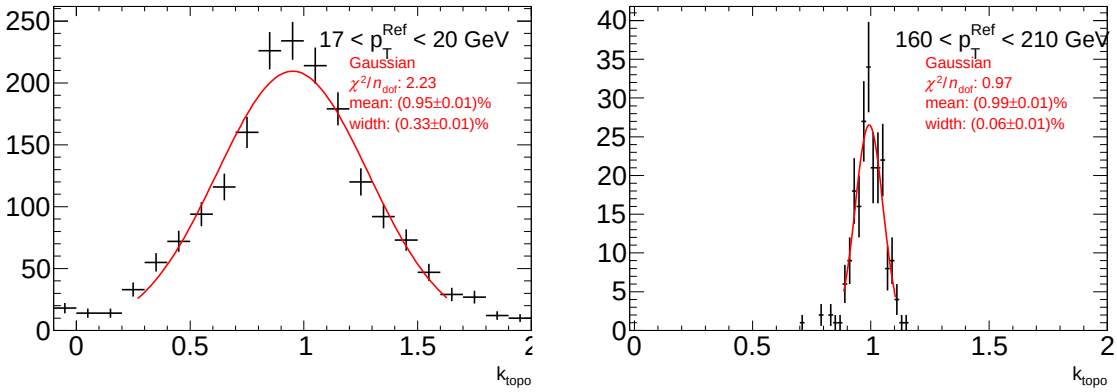

(a) 17 GeV $< p_{\mathrm{T}}^{\mathrm{ref}} <$ 20 GeV

(b) 160 GeV $< p_{\mathrm{T}}^{\mathrm{ref}} <$ 210 GeV

Figure 6.13: Topology correction distributions for anti-k_t R=0.4 jets at EM scale using Z+jet events in two p_{T}^{Z} bins. Sample generated using POWHEG, showered with PYTHIA and the nuclear interactions modeled using FTFP_BERT (see Sec. 5.1).

Along with the showering correction Sec. 4.4 introduced the topology correction, a second factor which accounts for the difference in response between the full hadronic recoil and the response of the more densely packed and higher energy particles in the jet core. The

correction is defined as the ratio

$$k_{\text{topo}} = \frac{R_{\text{MPF}}}{R_{\text{true}}} \tag{6.9}$$

of the MPF response to the true calorimeter response, once again defined as

$$R_{\text{true}} = \frac{\sum_{i \in \text{particle jet}} E_i^{\text{measured}}}{\sum_{i \in \text{particle jet}} E_i^{\text{true}}}. \tag{6.10}$$

As the MPF response makes use of the missing transverse energy the response distributions tend to be quite wide and symmetric. The same Gaussian fitting procedure used in the nominal MPF response measurement is therefore used to extract the mean of these distributions (see Fig. 6.13). The observed topology corrections using samples generated with the same two physics lists used to explore the showering correction (FTFP_BERT and QGSP_BIC) can be seen for a number of cone sizes in Figs. 6.14 and 6.15.

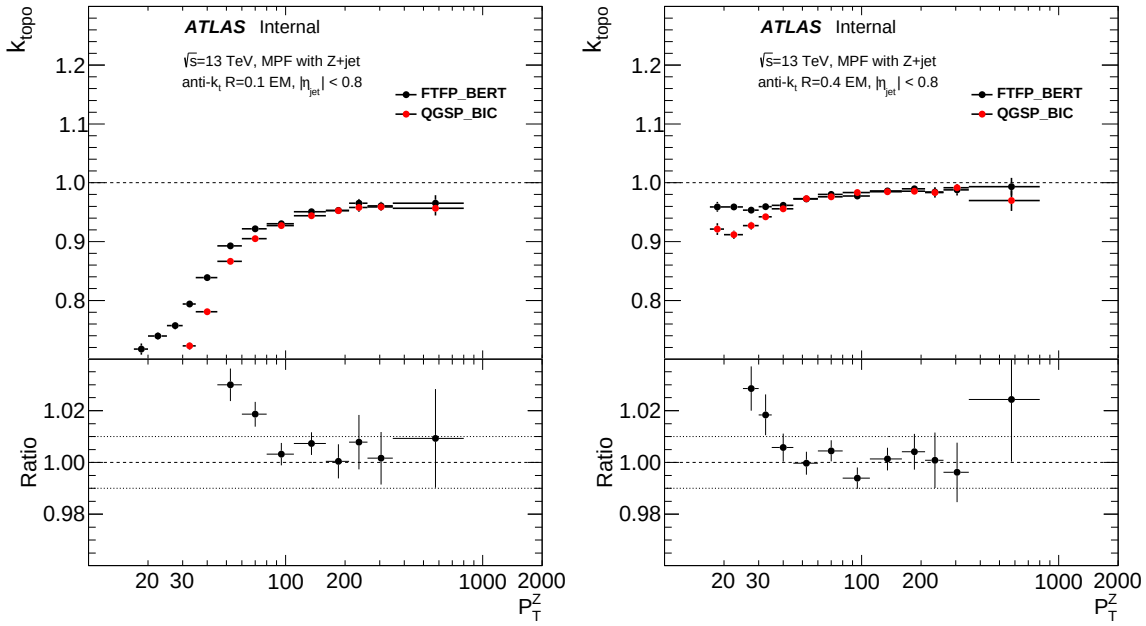

(a) Anti-k_t R=0.1 (b) Anti-k_t R=0.4

Figure 6.14: The topology correction k_{topo} as defined in Sec. 4.4 for anti-k_t R=0.1/0.4 jets at EM scale.

For jets smaller than the size of the recoil (∼0.6) the topology correction is less than one as the response of the high energy particles in a very narrow jet is larger than the average response of the entire recoil. For jets between R=0.4 and R=0.7 the topology correction is small (<5%) over the energy range considered, showing that the effects of the low energy/low response particles at the fringes of the recoil have very little effect on the total response of the recoil. For jets with size parameters which extend beyond the range of the recoil a large amount of underlying event directed in the same direction as the jet is

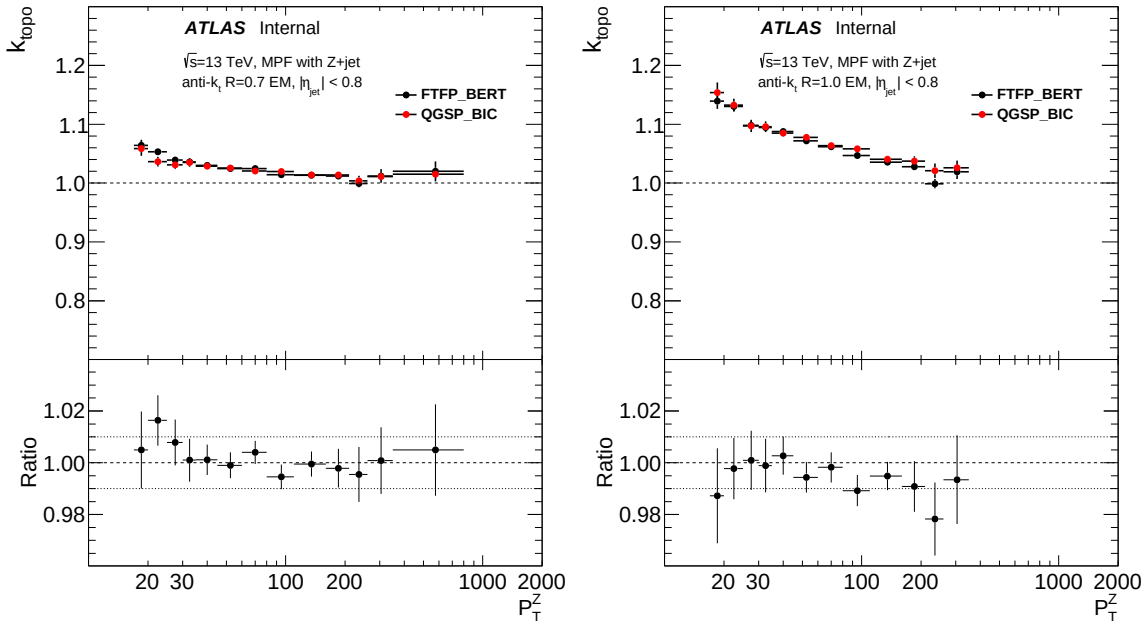

(a) Anti-k_t R=0.7 (b) Anti-k_t R=1.0

Figure 6.15: The topology correction k_{topo} as defined in Sec. 4.4 for anti-k_t R=0.7/1.0 jets at EM scale.

included in the jet. This means that a large number of low energy particles are included in the truth jet, and as the true calorimeter response does not include the underlying event in the opposite direction of the jet to partially cancel this effect (which the MPF does) these low energy/low response particles lower the true calorimeter response and therefore raise the topology correction to be greater than one. The choice of physics list has very little effect on the topology correction, with variations being on average less than 0.5% for all cone sizes above 80 GeV (above 40 GeV for cone sizes greater than 0.2). Below this energy the variations become larger, growing to between 1-3% for jet sizes larger than R=0.1. This large variation at low energy appears to be caused by a combination of the higher response to charged pions seen in QGSP_BIC [58] and the reconstruction threshold. With a lower response FTFP_BERT will be more affected by the reconstruction threshold at low energies and will continue to be affected up to higher energies compared to QGSP_BIC. In the past it has been shown that while R_{MPF} is biased by the reconstruction threshold the effect of this bias is smaller than that observed when measuring R_{jet}, and therefore R_{true}. This larger bias would cause the measured k_{topo} to be low, which is consistent with the idea that the growing difference between physics lists is at least partially caused by this difference in response.

For larger jets (greater than $\sim$ R=0.6) the topology correction becomes positive. This is a result of the truth jet growing large enough that it begins to include more low energy/low response particles from the underlying event. This means that the true calorimeter response

of these jets begins to decrease beyond the response of the recoil. While these low energy/low response particles are also present and contribute to the measured response in the MPF they are canceled out by additional low energy particles which are directed towards the same hemisphere of the detector as the reference object which are not taken into account for the true response.

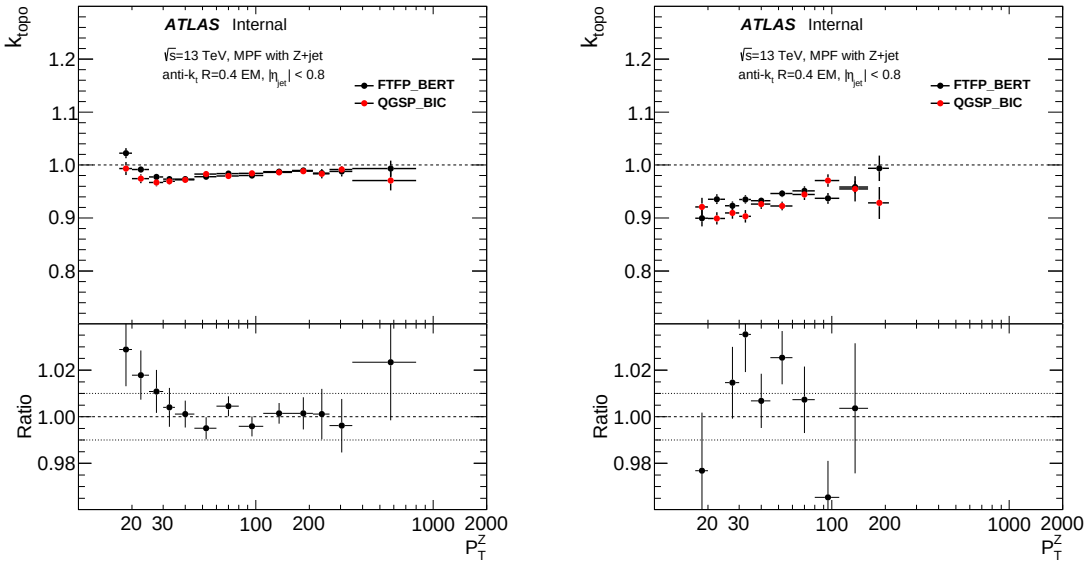

(a) Quark initiated jets

(b) Gluon initiated jets

Figure 6.16: The topology correction k_{topo} as defined in Sec. 4.4 for anti-k_{t} R=0.4 jets at EM scale for quark/gluon initiated jets.

The topology correction has also been studied individually for both quark and gluon initiated jets. As quark initiated jets on average have a lower number of particles with a higher energy per particle than gluon jets the same fraction of the total recoil energy is able to be reconstructed using a smaller jet size. This can be seen in Fig. 6.16 which shows the anti-k_{t} R=0.4 jet topology correction for both quark and gluon initiated jets, where the correction is larger for gluon initiated jets as a larger fraction of the recoil energy is made up of low energy particles far away from the jet axis. Another approach to understanding the difference can be seen in Fig. 6.17, which shows that the average true calorimeter response for anti-k_{t} R=0.5 quark jets is approximately equal to the total response of the recoil using the MPF. This is only true for gluon initiated jets when using larger anti-k_{t} R=0.7 jets.

6.5 Combination

$$R_{\text{jet}} = R_{\text{MPF}} \left(\frac{R_{\text{true}}}{R_{\text{MPF}}} \right) \left(\frac{R_{\text{jet}}}{R_{\text{true}}} \right) = \frac{R_{\text{MPF}}}{k_{\text{topo}} S} \tag{6.11}$$

Both the topology and showering corrections give insight into jet related physics, with the showering correction measuring the flow of energy across the jet reconstruction bound-

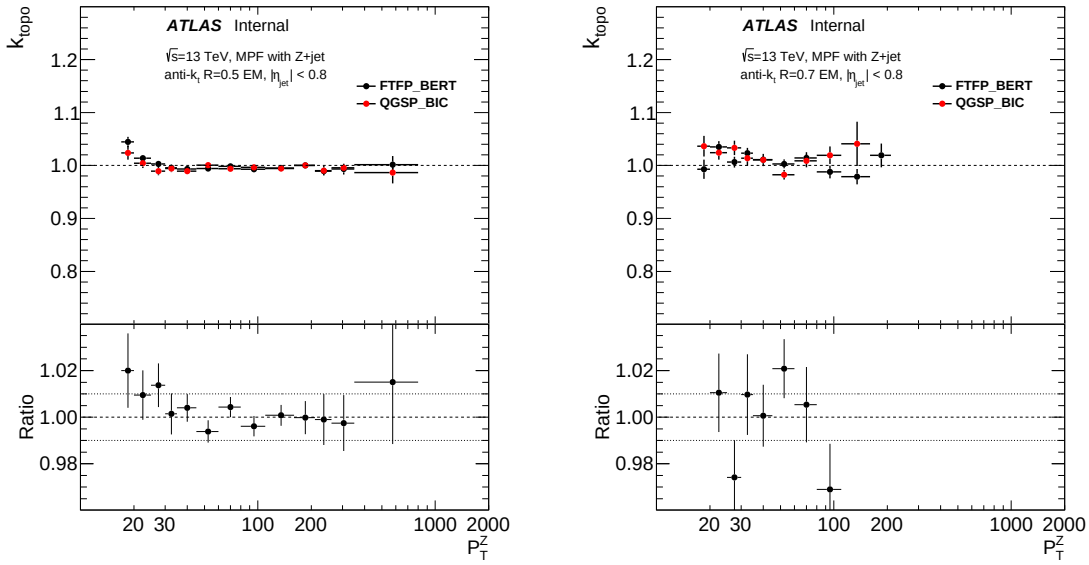

(a) Quark initiated jets, anti-k_t R=0.5 (b) Gluon initiated jets, anti-k_t R=0.7

Figure 6.17: The topology correction is defined in Sec. 4.4 as the ratio of the true calorimeter response to the MPF. Shown above is the topology correction for quark jets using anti-k_t R=0.5 jets and for gluon jets using anti-k_t R=0.7. In both cases the topology correction ≈ 1, showing that a larger jet size is required to capture the same fraction of a gluon initiated recoil when compared to a quark initiated recoil.

ary and the topology correction measuring the effect that jet energy density has on the response. These two corrections can be applied to the MPF to measure an absolute jet energy scale, and practically to provide sensitivity to the choice of physics lists as an additional uncertainty on using the MPF for an *in-situ* measurement. The two corrections depend on R_{true} and can therefore be combined to eliminate the sensitivity of the final correction to this part of the MC simulation. For that reason a single correction C is defined:

$$C = \frac{1}{k_{\text{topo}} S} = \frac{R_{\text{jet}}}{R_{\text{MPF}}} \tag{6.12}$$

As previously mentioned the smaller charged pion response in FTFP_BERT (along with a narrow showering width) causes both the showering correction S and the topology correction k_{topo} to be larger at low energies as a result of the reconstruction threshold bias. It is therefore not surprising that the inverse of the product of these two quantities is smaller for FTFP_BERT at low energies. The variation between the two physics lists grows steadily as the energy is decreased, with the differences getting as large as 5% in at 20 GeV for anti-k_t R=0.4 jets, as seen in Fig. 6.18. The correction C has also been measured event by event, with the distributions of these measurements being fit using the same procedure used in the nominal MPF analysis. The means of these fits as a function of reference energy are shown in Fig. 6.19. The size of the discrepancy between the two physics lists shrinks

when calculating C directly, with differences never being larger than 1% as compared to the up to 5% differences observed when using a combination of the two individual calculations, although the absolute size of the correction remains comparable. This difference originates from the use of the arithmetic means used as the centroid of the showering correction.

It is also worth noting that for jet sizes larger than anti-k_t R=0.4 increasing the jet size increases the size of the correction C. This is a result of extending the jet cone size beyond the boundaries of the recoil, which increases the number of low energy/low response particles included in the jet definition. This effect is compensated for in the MPF by the presence of additional low energy/low response particles which deposit energy in the same hemisphere of the calorimeter as the reference object (i.e $\Delta R\,(\text{jet}, \text{particle}) > \pi/2$), the same reason that the topology correction becomes greater than one for large jet sizes.

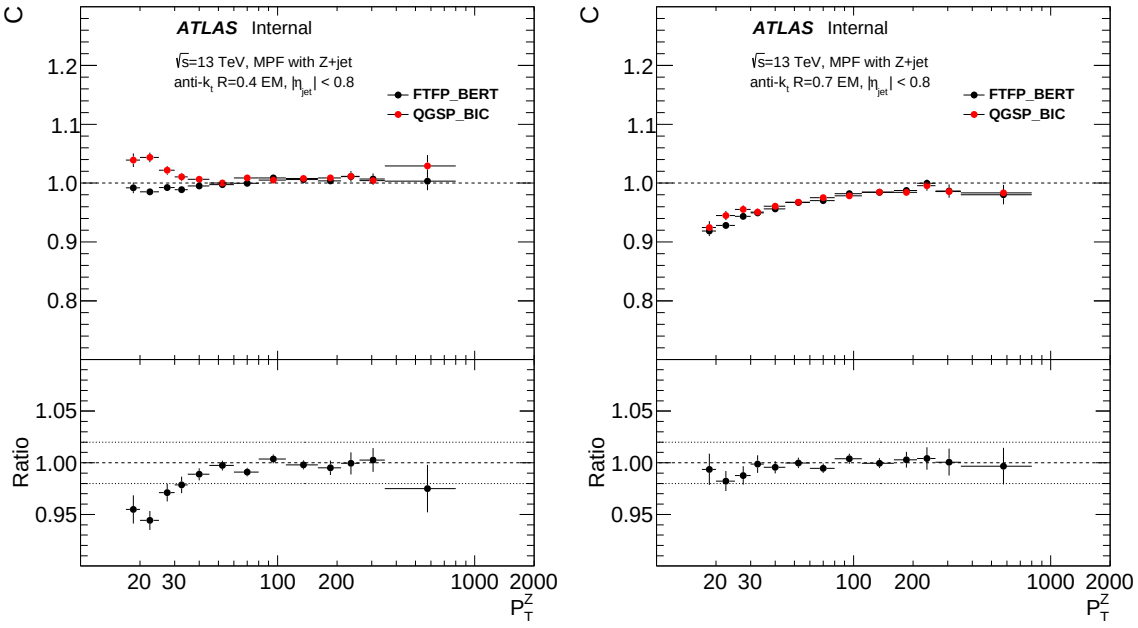

(a) Anti-k_t R=0.4 (b) Anti-k_t R=0.7

Figure 6.18: MPF correction C as defined in Eq. 6.12 for anti-k_t R=0.4/0.7 jets at EM scale, calculated as the inverse of the product of the showering and topology corrections calculated in the previous section.

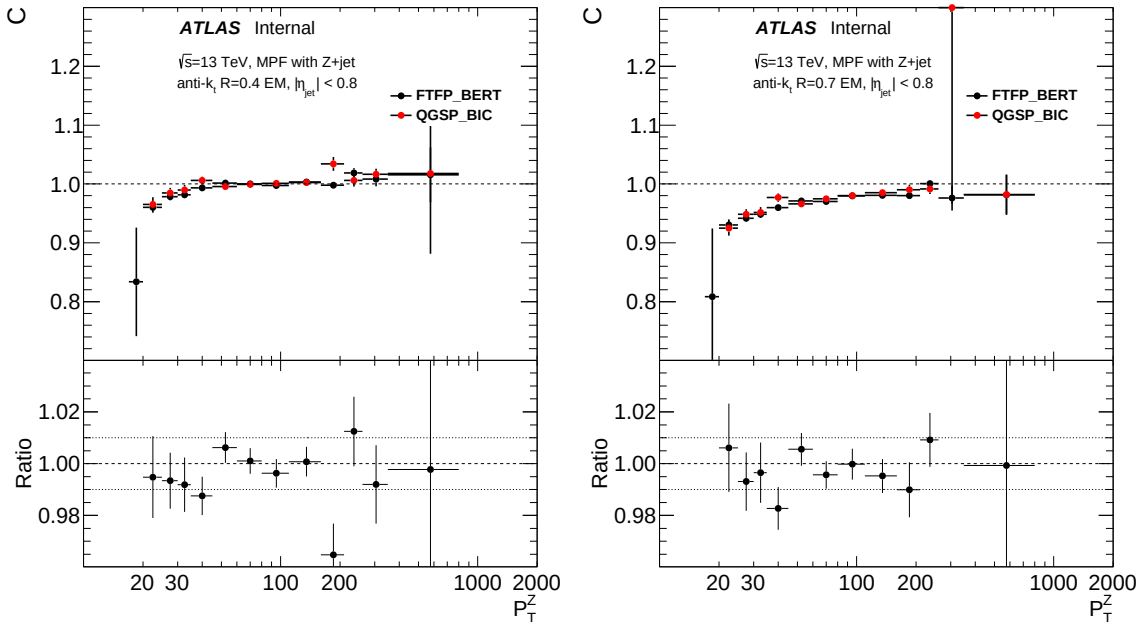

(a) Anti-k_t R=0.4 (b) Anti-k_t R=0.7

Figure 6.19: MPF correction C as defined in Eq. 6.12 for anti-k_t R=0.4/0.7 jets at EM scale. Here the total correction is calculated event by event and the mean of a Gaussian fit to the distribution of this correction is used as the central value.

Chapter 7

Conclusion

As the LHC collides protons, every collision results in some hadronic activity in the final state. This means that a precise knowledge of the jet energy scale is an important factor to the success of the ATLAS physics program. This thesis measures the jet energy scale in ATLAS using the missing transverse energy projection fraction method (MPF) applied to both Z+jet and γ+jet events. In both channels the response of both EM and LC scale jets has been measured. In moving from the $\sim$ 4 fb^{-1} collected in 2015 to the $\sim$ 35 fb^{-1} collected in 2016 the uncertainties with the Z+jet channel for both scales was reduced from $\sim$ 1.2% to $\sim$ 0.8% between 30 GeV and 500 GeV. The uncertainty on the γ+jet channel was also reduced, remaining slightly below 1%, while extending the range of validity of the calibration from 700 GeV to 1.2 TeV. Moving forward these studies will be expanded to include a third scale of jet inputs known as particle flow objects which combine both calorimeter and tracking information. In addition to producing the jet calibration required for the ATLAS physics program, several studies were done to understand better and validate the MPF technique. Many of the assumptions previously made were tested and validated.

The energy density of the hadronic recoil as a function of distance from the reconstructed jet axis has been studied. The excess in energy density caused by the hadronic recoil above the underlying event is found to be mostly contained within a distance of R=0.7, with the majority of this excess being comfortably contained within a cone of R=0.5 for jets with energy above 60 GeV. Studies of the effect of pileup and other activity on the MPF's ability to measure the response of the calorimeter to the hadronic recoil are also presented. These studies use a number of different size parameters when reconstructing jets, using large jet sizes as a proxy for the full hadronic recoil. These studies show that the assumption that this additional energy in the event does not affect the measurement is in fact valid.

Studies on the effect of the flow of energy across the jet reconstruction boundary have also been performed by way of the so-called showering correction. The showering correction shows that the amount of energy leaving the jet is larger than the amount entering from other activity, and that on average a low energy ($\sim$ 30 GeV) anti-k_t R=0.4 jets would have a response 6% higher if this effect was removed. The size of this effect becomes smaller both

with increasing jet energy and increasing jet size. The showering correction was shown to vary by less than 0.5% with the choice of physics list, which, among other things, models the development of the calorimeter shower.

Finally the importance of the low energy/low response particles near the fringe of the hadronic recoil to the response of the total recoil is studied by way of the topology correction. These low energy particles are found to bring the response of the recoil down approximately 5% compared to the response of the core, for the case of an anti-k_{t} R=0.4 jet. This difference once again decreases with increasing jet size. This quantity is unaffected by the choice of physics list above 30-40 GeV. However, the choice of the physics list changes the impact of the jet reconstruction threshold at low pt.

The dependence on the choice of physics list for these two quantities can be added as a uncertainty on the MPF method for in-situ calibration. The uncertainty on these effects have previously been covered by adding the uncertainty from the so-called out-of-cone (OOC) correction for the p_{T} balance method, an unrelated quantity which was believed to be a conservative estimate on the uncertainty. Using the dependence of the measured total correction on the choice of physics list as a measure of the uncertainty on this quantity in place of the OOC uncertainty leads to a reduction from 3% to 0.5% uncertainty in the lowest energy bin for the Z+jet analysis, with the uncertainty remaining approximately unchanged above 35 GeV. In the γ+jet channel after the rebinning described in Sec. 5.5 there is no depence of this total correction on the choice of physics list. This is a reduction from the OOC uncertainty which in 2016 was approximately 1% below 50 GeV and 0.5% in the 50-100 GeV range. These more precise uncertainties reduce the overall uncertainty on the JES for jets below 100 GeV. Since the JES uncertainty is the largest contribution to the total uncertainty in many ATLAS analyses, the work described in this thesis will noticeably improve ATLAS results at low energy.

Appendix A

Personal Contributions

With ATLAS being an international collaboration with thousands of individuals contributing, it may not be clear which work was performed by a single individual. I therefore include a list of my contributions over the course of my thesis.

- Produced both γ and Z+jet results for the final 2012 calibration using preexisting code from Masters degree [47].
- Preliminary 14 TeV expected limits for exotic dijet searches [62].
- Investigations into using γ+jet to improve η intercalibration at low energies.
- Rewrote MPF analysis code to be compatible with move to a new data format (xAODs). This code has since been adopted as the default for both MPF and p_{T} balance based calibrations.
- Final *in-situ* results for γ and Z+jet for 2015 and 2016 [61].
- The studies into the effect of other activity on the MPF technique presented in this thesis, along with additional studies measuring the effect pileup and radiation on Δ^{OA}. Validation of the MPF technique in a high-pileup environment.
- The full showering/topology correction studies presented in this thesis. Reduction of systematic uncertainty on the Jet Energy Scale, especially at low p_{T}.

Appendix B

2016 JES Results

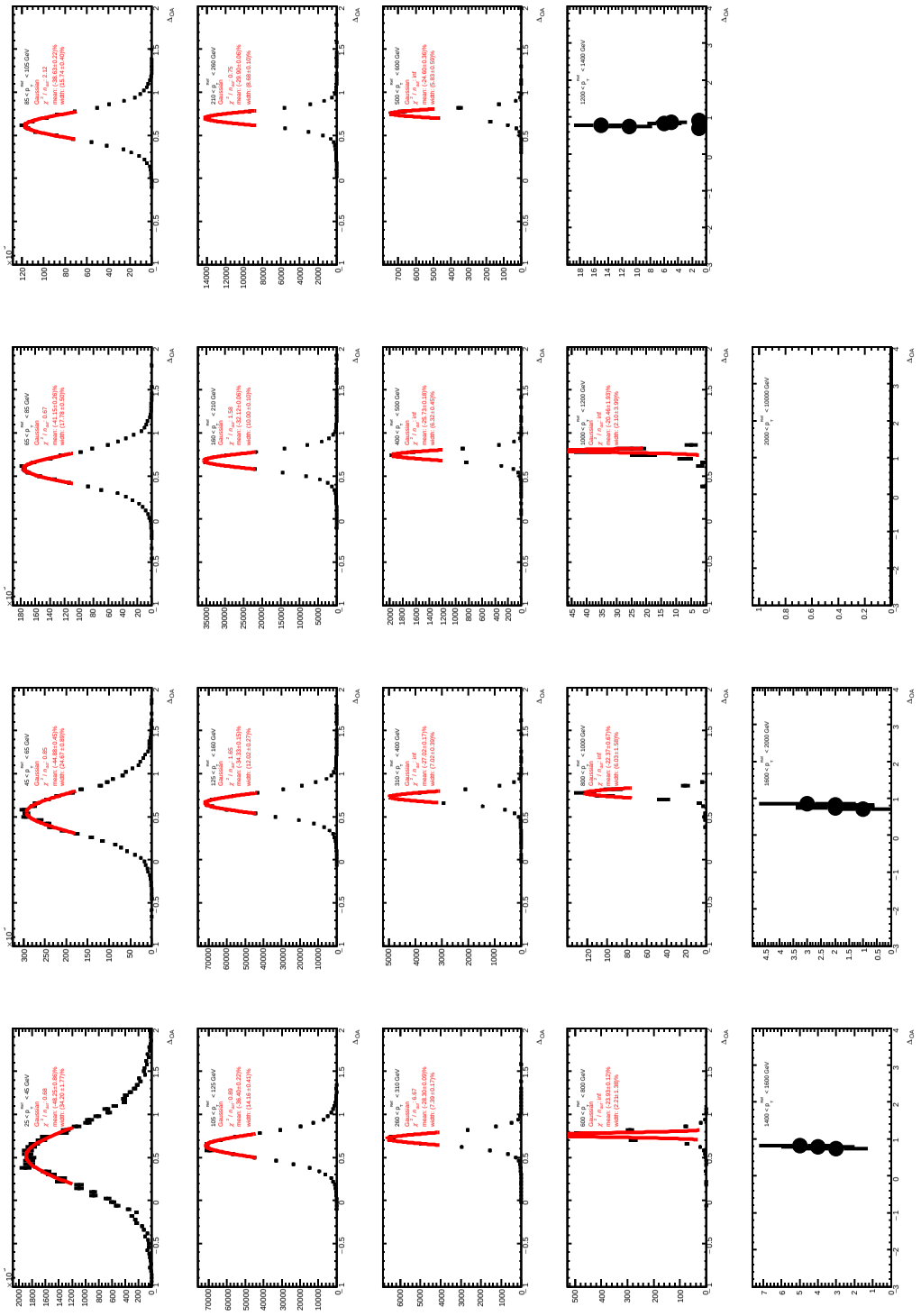

Figure B.1: EM+GSC scale response distributions using γ+jet events in 2016 data. Also shown in red is a Gaussian curve which has been sit using the procedure described in Sec. 5.4.

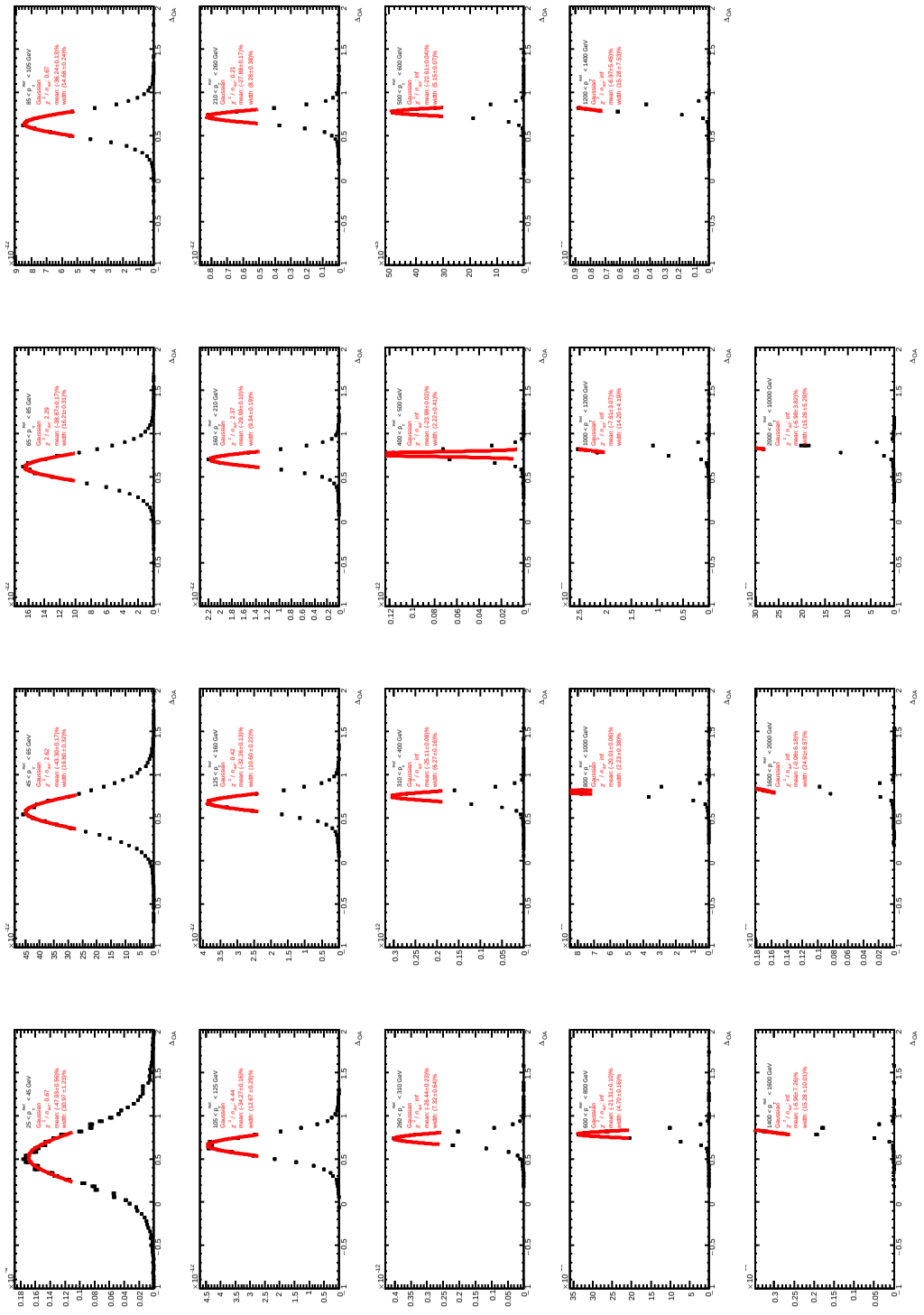

Figure B.2: EM+GSC scale response distributions using γ+jet events using Pythia. Also shown in red is a Gaussian curve which has been sit using the procedure described in Sec. 5.4.

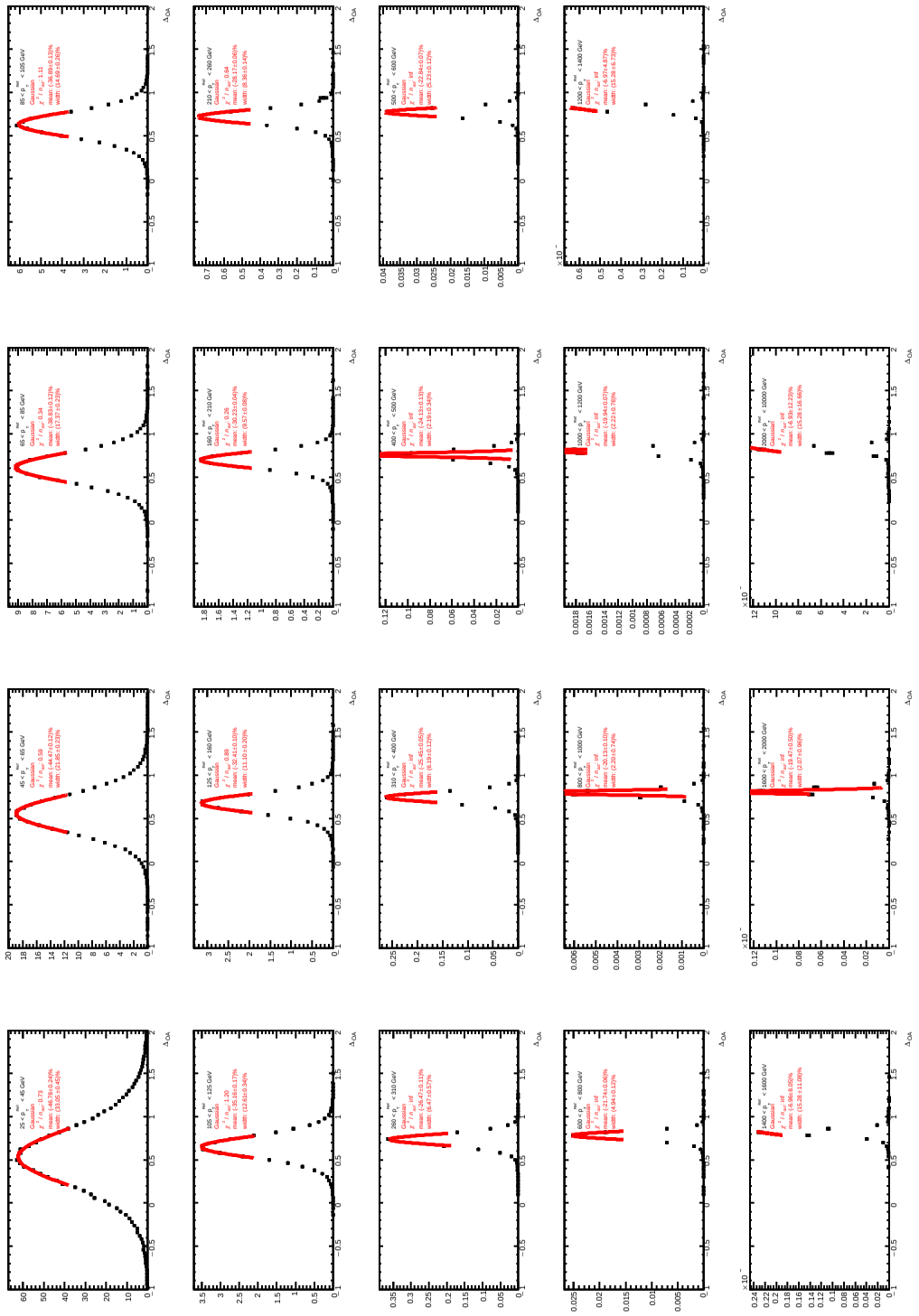

Figure B.3: EM+GSC scale response distributions using γ+jet events in using Sherpa. Also shown in red is a Gaussian curve which has been sit using the procedure described in Sec. 5.4.

Appendix C

2015 JES Results

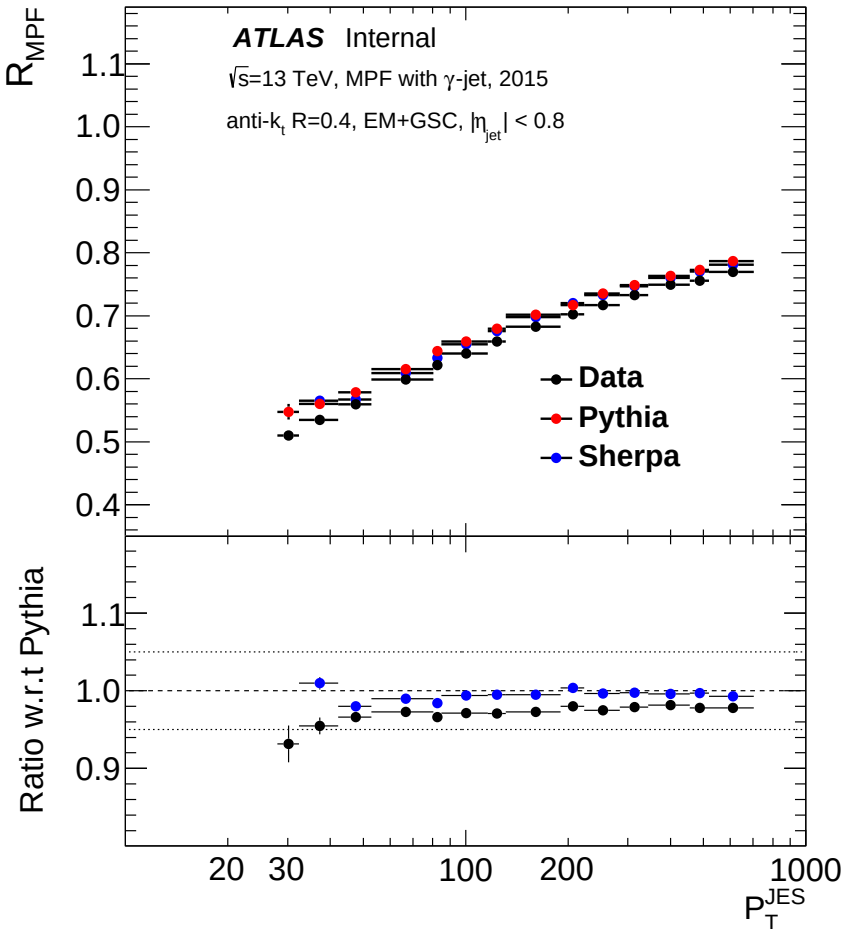

Figure C.1: The EM+GSC scale response measured using the MPF technique in γ+jet events. Shown in black is the response measured using data from the 2015 dataset, in red is the nominal Monte Carlo sample (Powheg+Pythia) and in clue is an additional Monte Carlo sample for comparison. The lower inset shows the data to Monte Carlo ratio, with the colour of the points corresponding to the simulated sample used in the ratio.

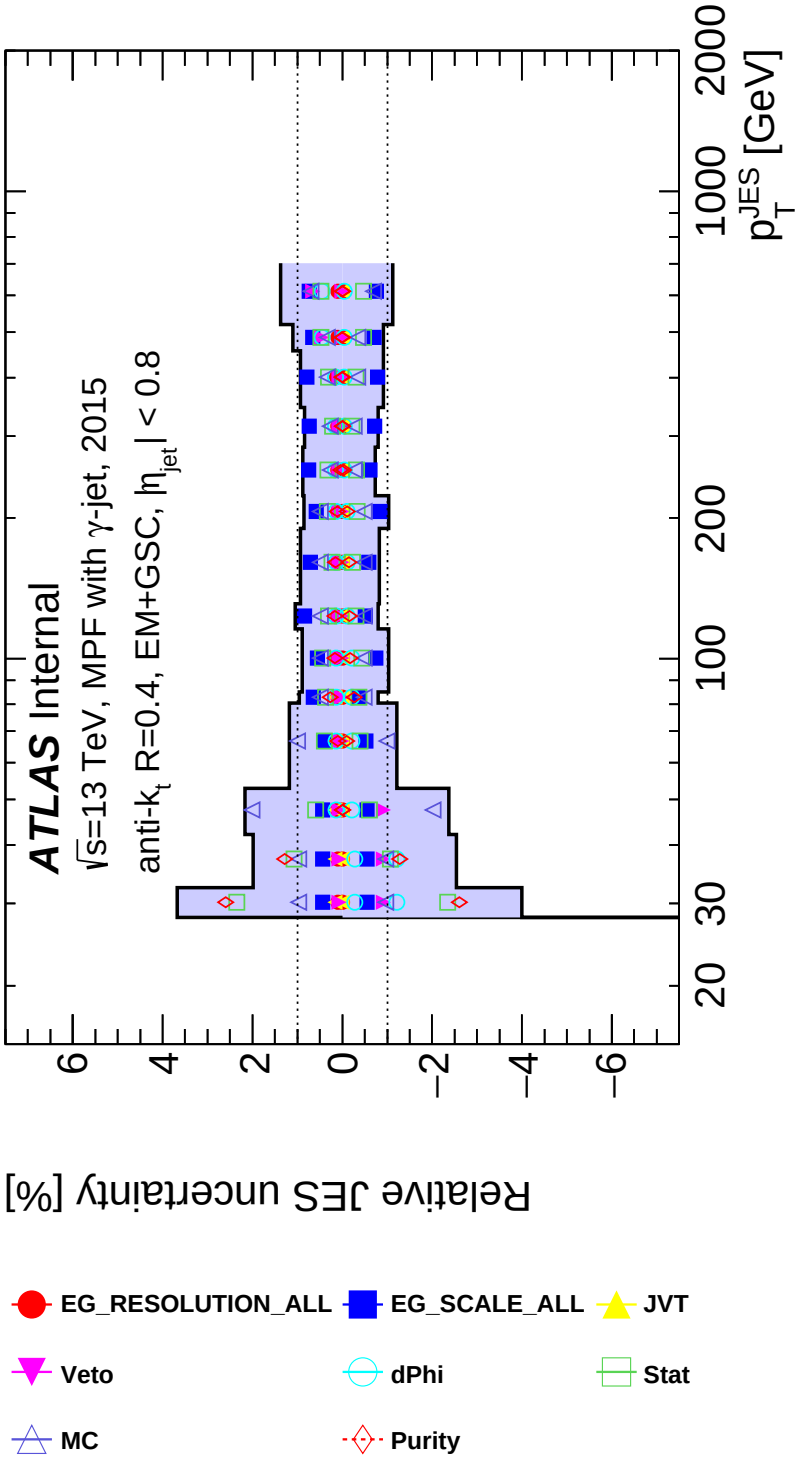

Figure C.2: The total uncertainty (both statistical and systematic) on the measurement of the relative EM+GSC scale response between data and MC using γ+jet events from 2015. It is broken down into the various uncertainty sources that go into the total uncertainty.

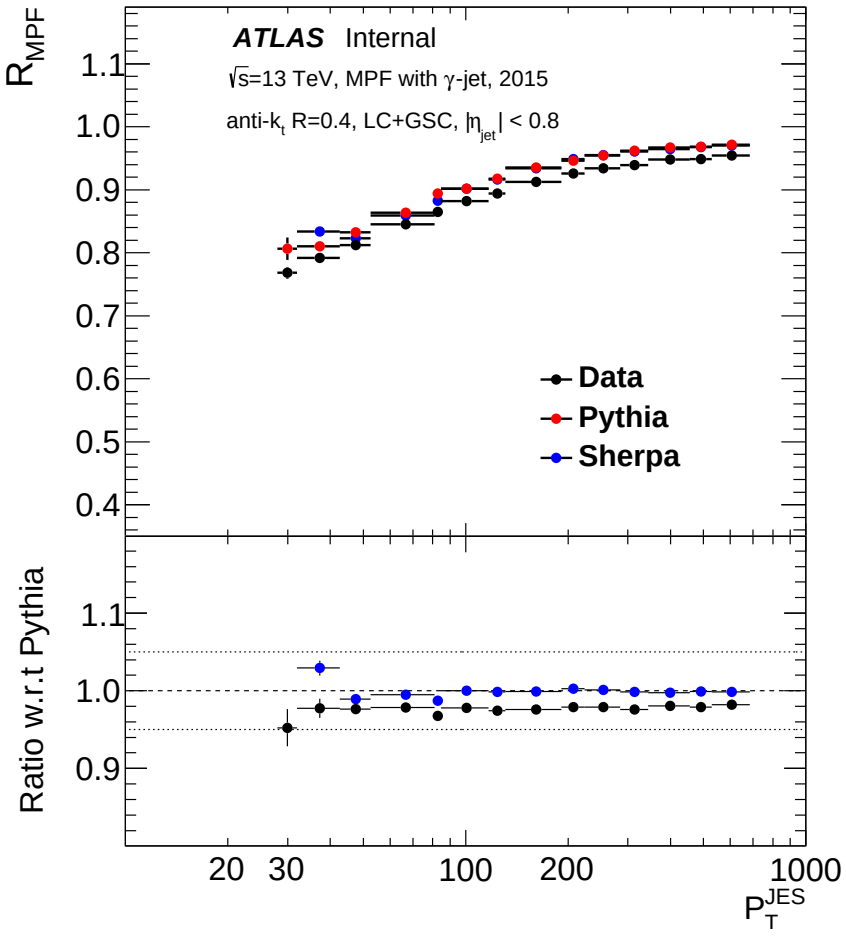

Figure C.3: The LC+GSC scale response measured using the MPF technique in γ+jet events. Shown in black is the response measured using data from the 2015 dataset, in red is the nominal Monte Carlo sample (Powheg+Pythia) and in clue is an additional Monte Carlo sample for comparison. The lower inset shows the data to Monte Carlo ratio, with the colour of the points corresponding to the simulated sample used in the ratio.

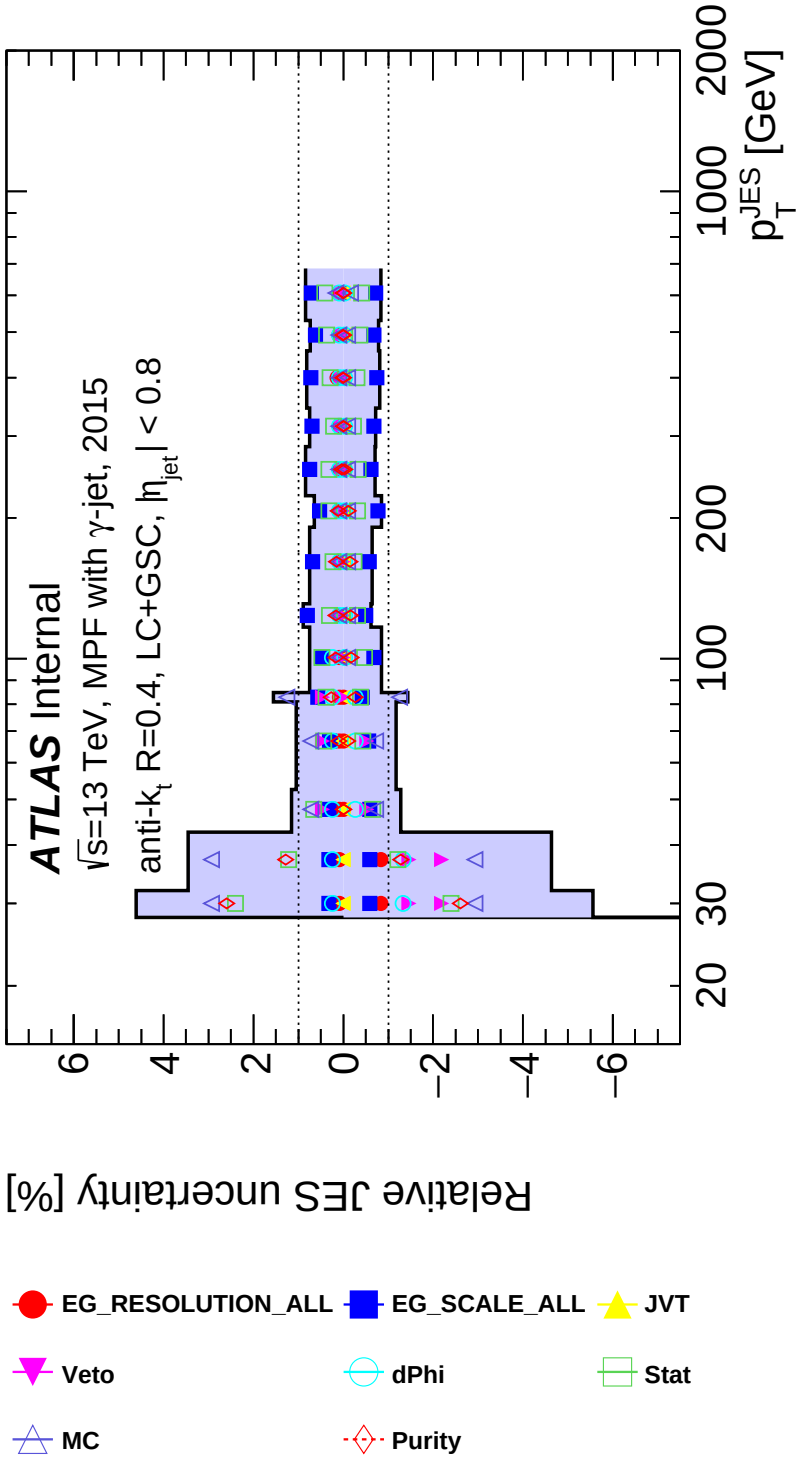

Figure C.4: The total uncertainty (both statistical and systematic) on the measurement of the relative LC+GSC scale response between data and MC using γ+jet events from 2015. It is broken down into the various uncertainty sources that go into the total uncertainty.

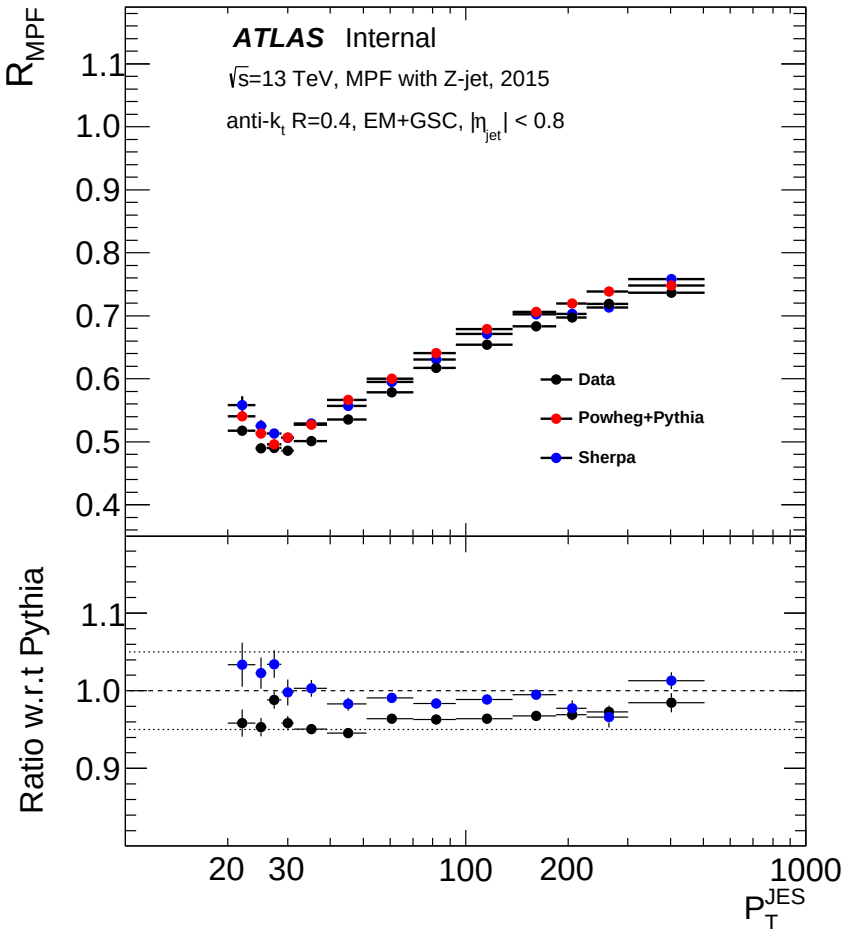

Figure C.5: The EM+GSC scale response measured using the MPF technique in Z+jet events. Shown in black is the response measured using data from the 2015 dataset, in red is the nominal Monte Carlo sample (Powheg+Pythia) and in clue is an additional Monte Carlo sample for comparison. The lower inset shows the data to Monte Carlo ratio, with the colour of the points corresponding to the simulated sample used in the ratio.

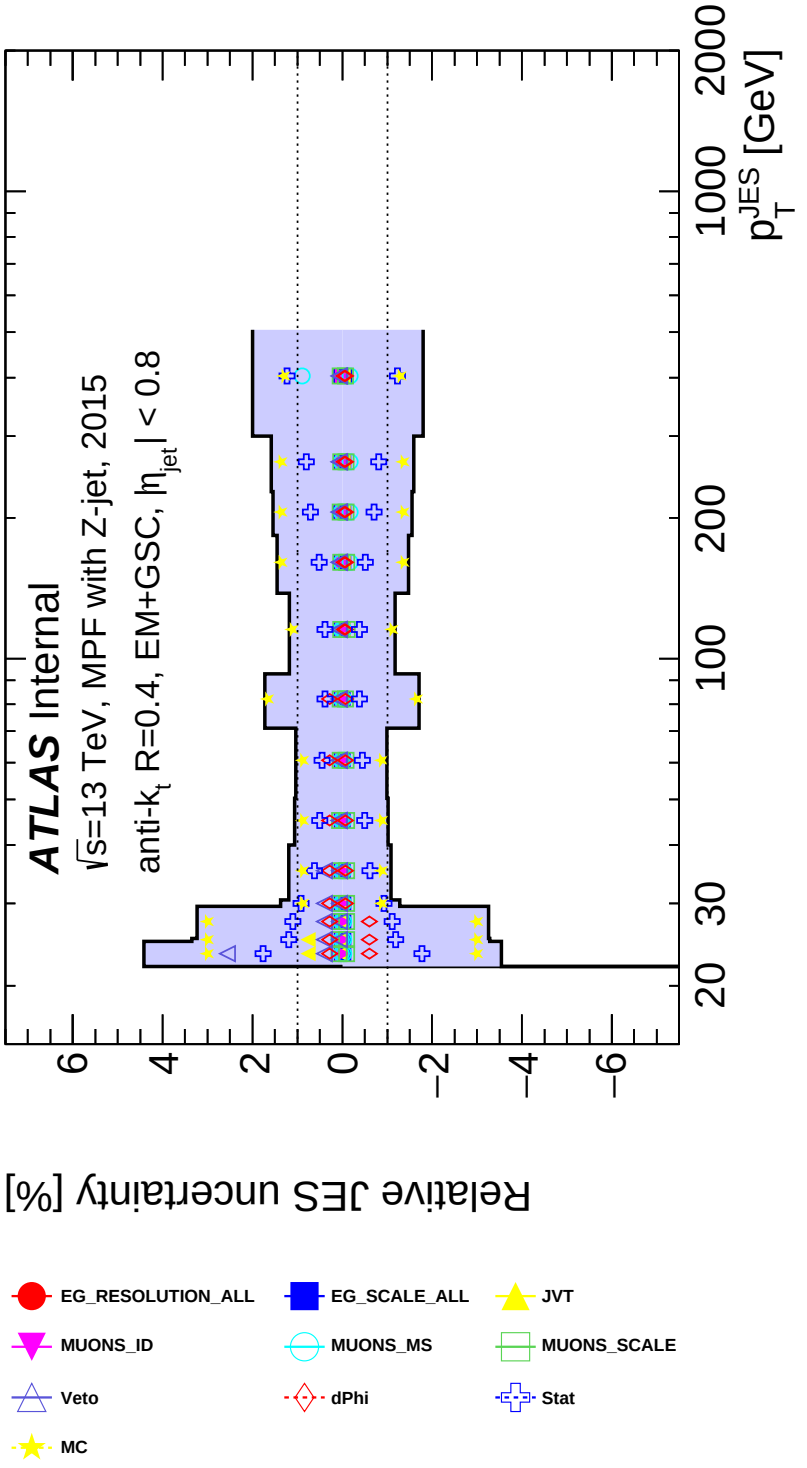

Figure C.6: The total uncertainty (both statistical and systematic) on the measurement of the relative EM+GSC scale response between data and MC using Z+jet events from 2015. I t is broken down into the various uncertainty sources that go into the total uncertainty.

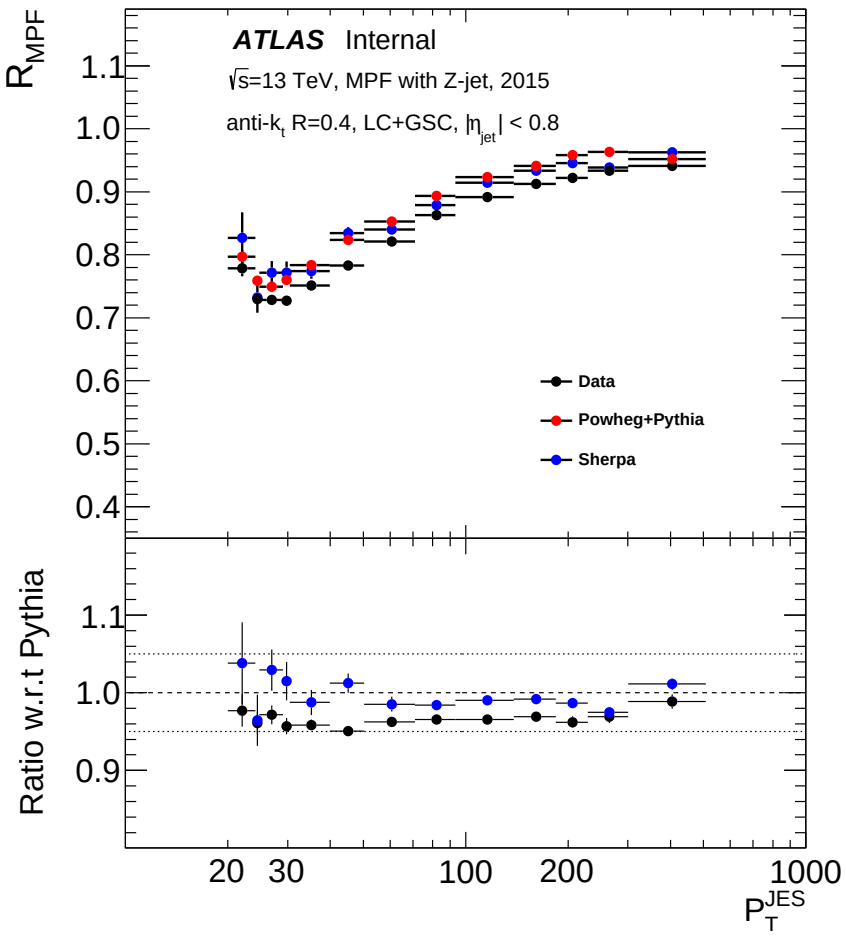

Figure C.7: The LC+GSC scale response measured using the MPF technique in Z+jet events. Shown in black is the response measured using data from the 2015 dataset, in red is the nominal Monte Carlo sample (Powheg+Pythia) and in clue is an additional Monte Carlo sample for comparison. The lower inset shows the data to Monte Carlo ratio, with the colour of the points corresponding to the simulated sample used in the ratio.

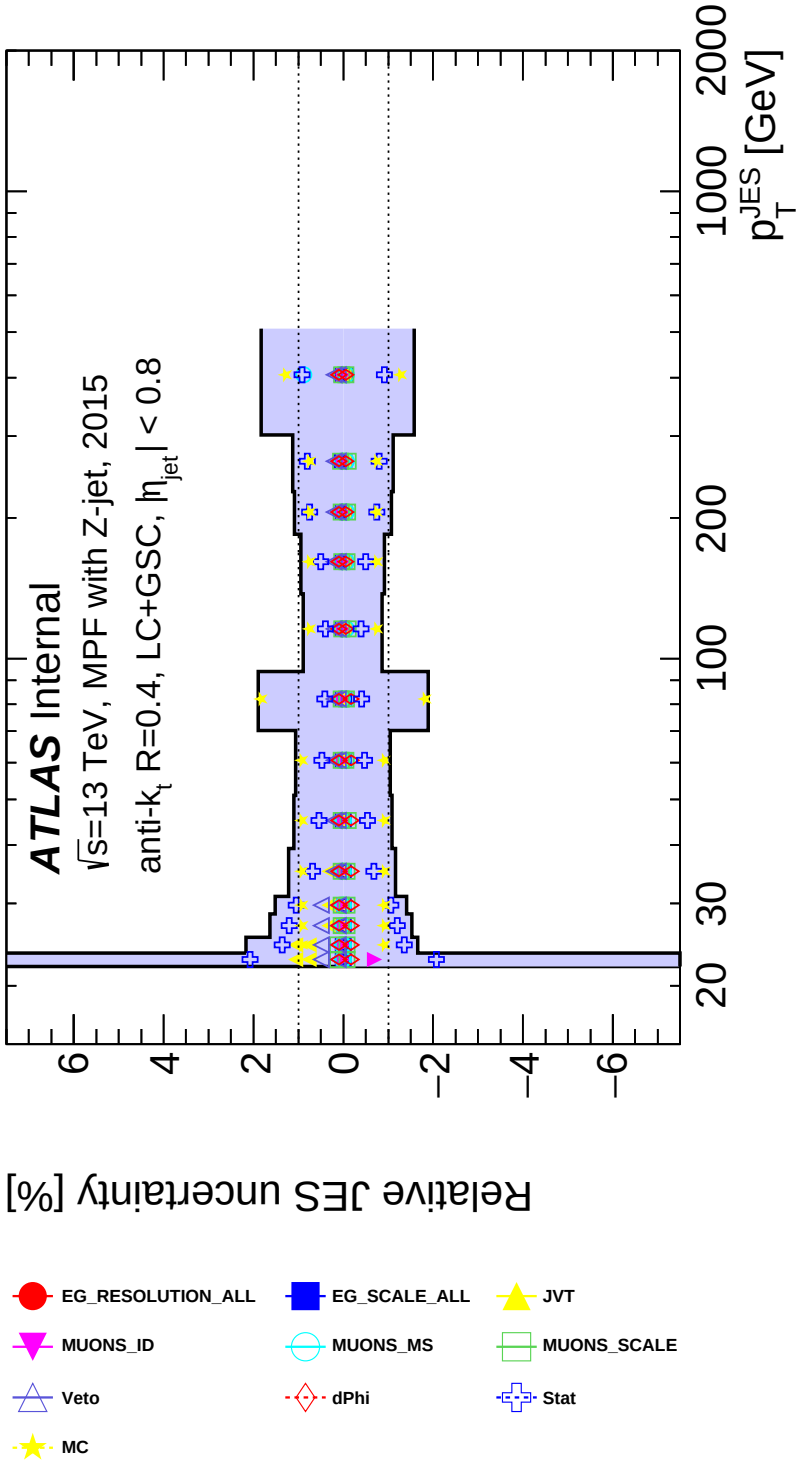

Figure C.8: The total uncertainty (both statistical and systematic) on the measurement of the relative LC+GSC scale response between data and MC using Z+jet events from 2015. I t is broken down into the various uncertainty sources that go into the total uncertainty.

Appendix D

Response vs. the subleading jet cut at EM+GSC using γ+jet events in 2016

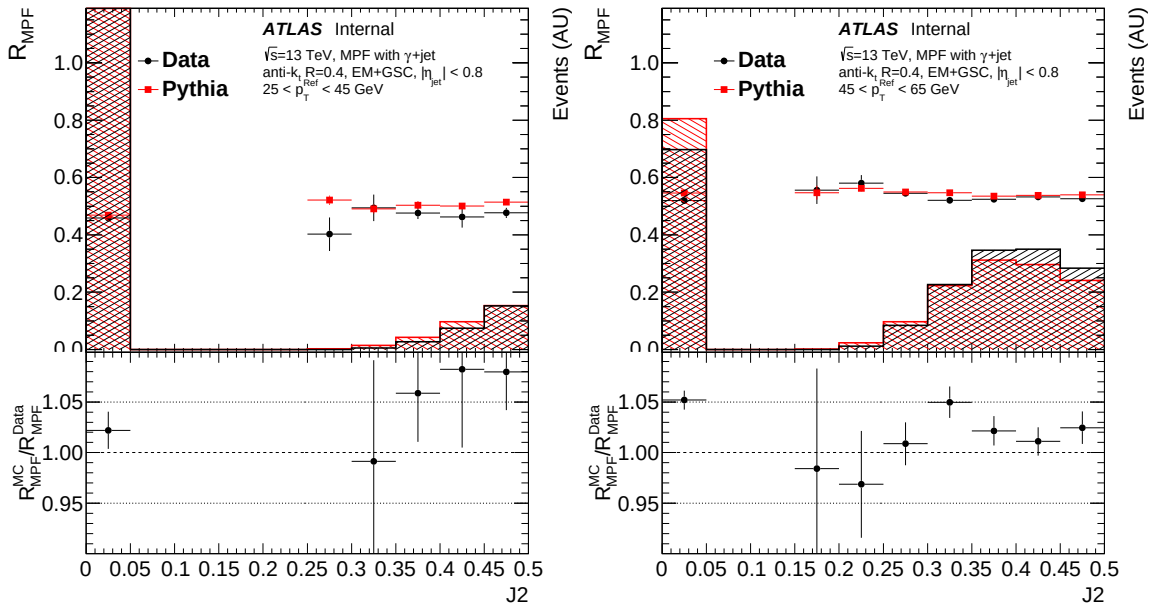

(a) 25-45 GeV

(b) 45-65 GeV

Figure D.1: Response as a function of the fraction of the photon energy contained in the subleading jet (J2) in two different p_{T} bins along with the distribution of events plotted against the same variable. The excess of events with a recorded subleading jet p_{T} being 0% of the reference p_{T} is caused by the subleading jet being below the jet reconstruction threshold. All selection cuts listed in Sec. 5.2 have been applied except for the subleading jet cut and the $\Delta\phi$ cut.

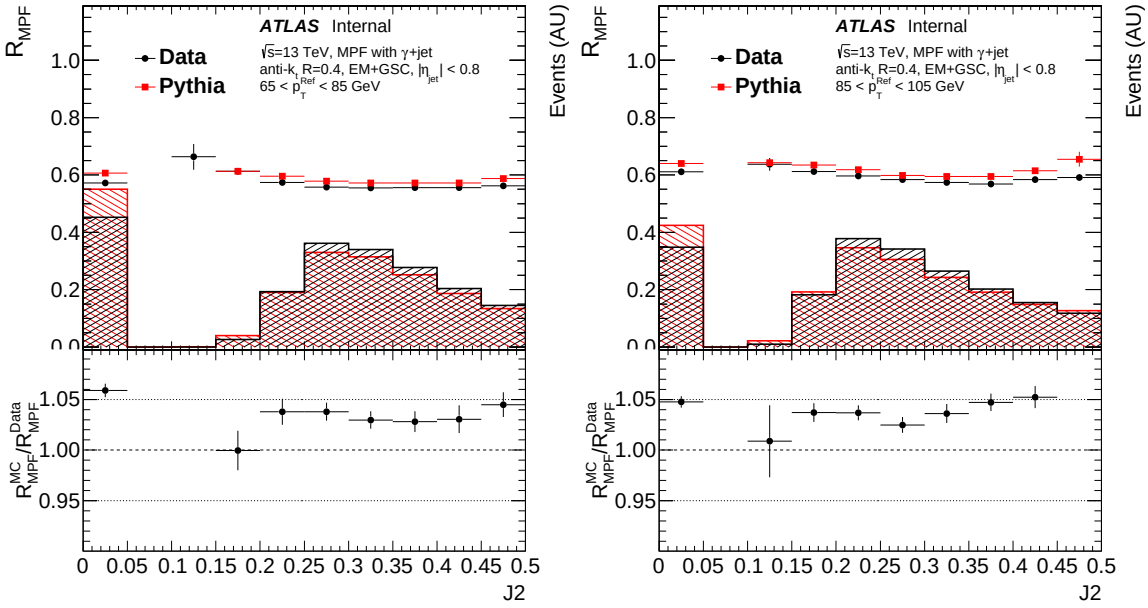

(a) 65-85 GeV (b) 85-105 GeV

Figure D.2: Response as a function of the fraction of the photon energy contained in the subleading jet (J2) in two different p_{T} bins along with the distribution of events plotted against the same variable. The excess of events with a recorded subleading jet p_{T} being 0% of the reference p_{T} is caused by the subleading jet being below the jet reconstruction threshold. All selection cuts listed in Sec. 5.2 have been applied except for the subleading jet cut and the $\Delta\phi$ cut.

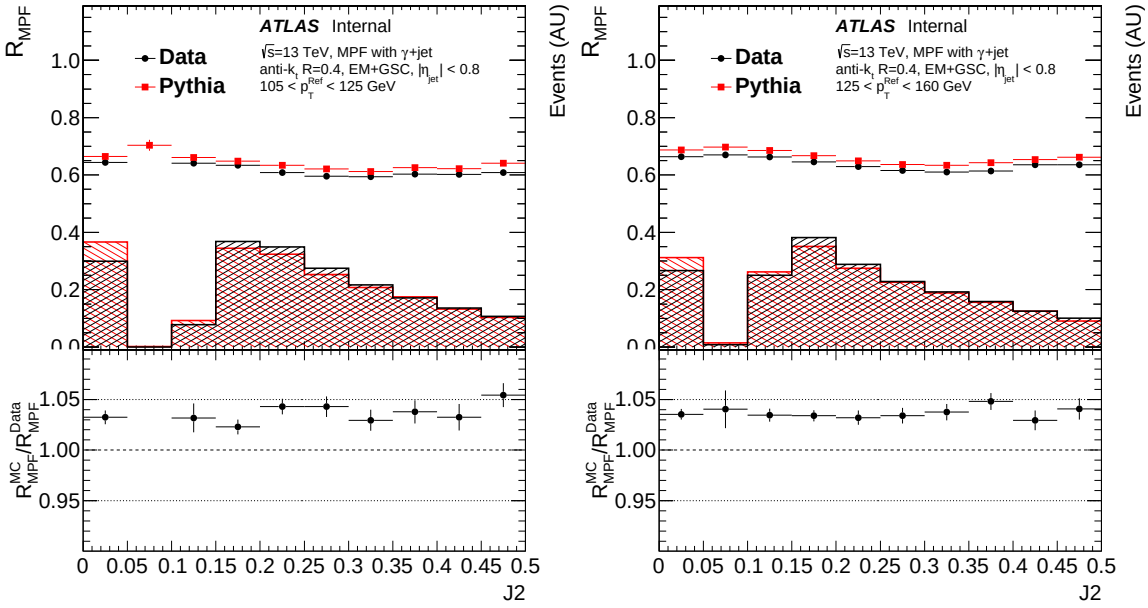

(a) 105-125 GeV

(b) 125-160 GeV

Figure D.3: Response as a function of the fraction of the photon energy contained in the subleading jet (J2) in two different p_{T} bins along with the distribution of events plotted against the same variable. The excess of events with a recorded subleading jet p_{T} being 0% of the reference p_{T} is caused by the subleading jet being below the jet reconstruction threshold. All selection cuts listed in Sec. 5.2 have been applied except for the subleading jet cut and the $\Delta\phi$ cut.

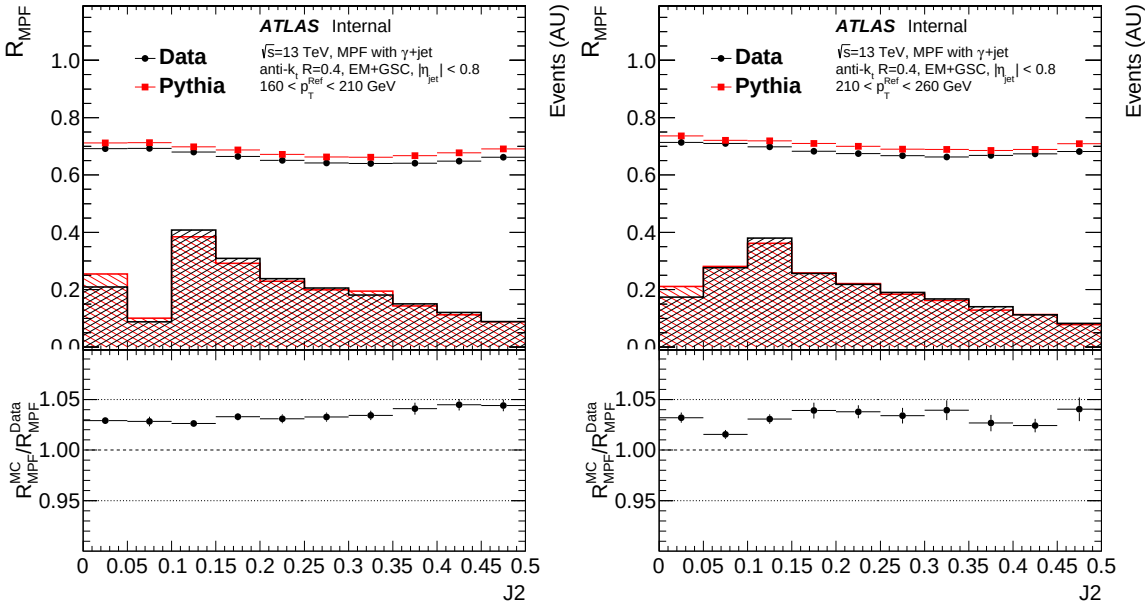

(a) 160-210 GeV

(b) 210-260 GeV

Figure D.4: Response as a function of the fraction of the photon energy contained in the subleading jet (J2) in two different p_{T} bins along with the distribution of events plotted against the same variable. The excess of events with a recorded subleading jet p_{T} being 0% of the reference p_{T} is caused by the subleading jet being below the jet reconstruction threshold. All selection cuts listed in Sec. 5.2 have been applied except for the subleading jet cut and the $\Delta\phi$ cut.

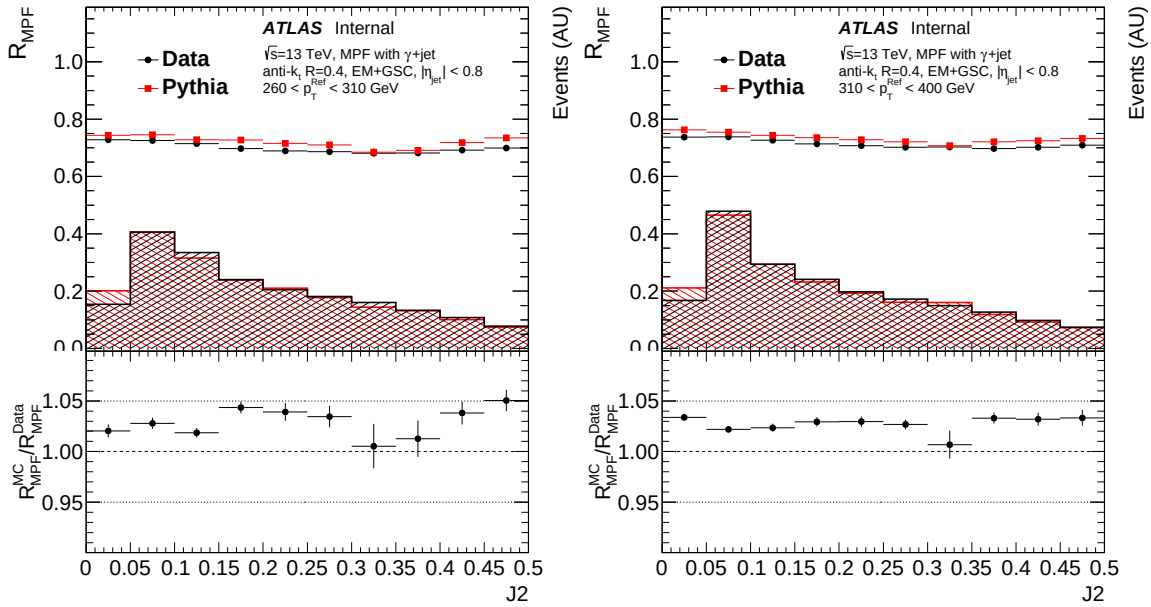

(a) 260-310 GeV (b) 310-400 GeV

Figure D.5: Response as a function of the fraction of the photon energy contained in the subleading jet (J2) in two different p_{T} bins along with the distribution of events plotted against the same variable. All selection cuts listed in Sec. 5.2 have been applied except for the subleading jet cut and the $\Delta\phi$ cut.

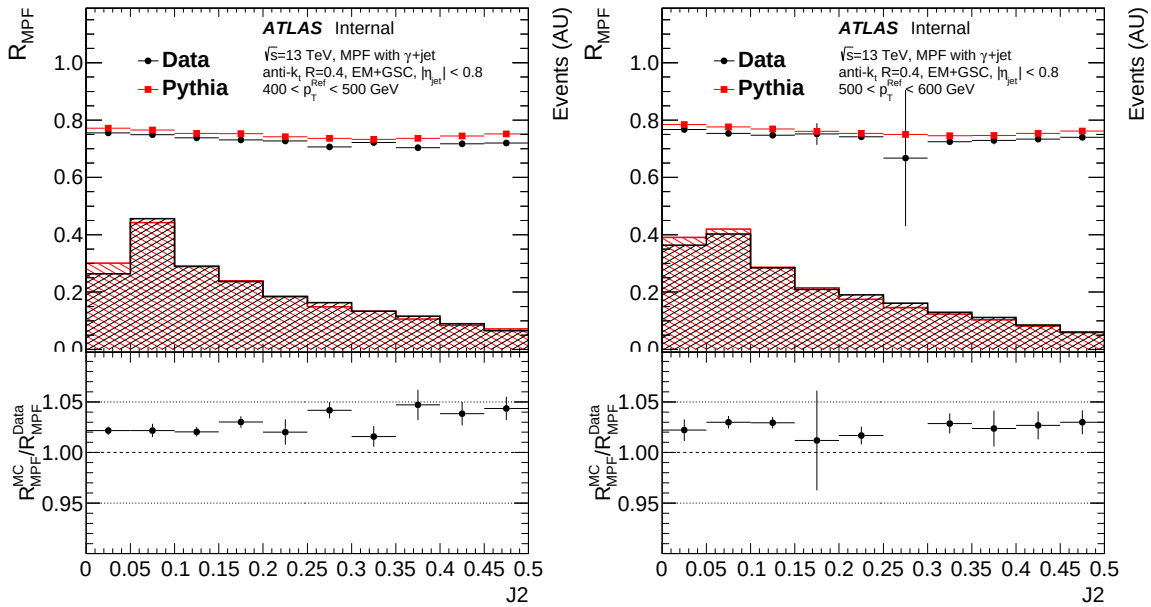

(a) 400-500 GeV (b) 500-600 GeV

Figure D.6: Response as a function of the fraction of the photon energy contained in the subleading jet (J2) in two different p_{T} bins along with the distribution of events plotted against the same variable. All selection cuts listed in Sec. 5.2 have been applied except for the subleading jet cut and the $\Delta\phi$ cut.

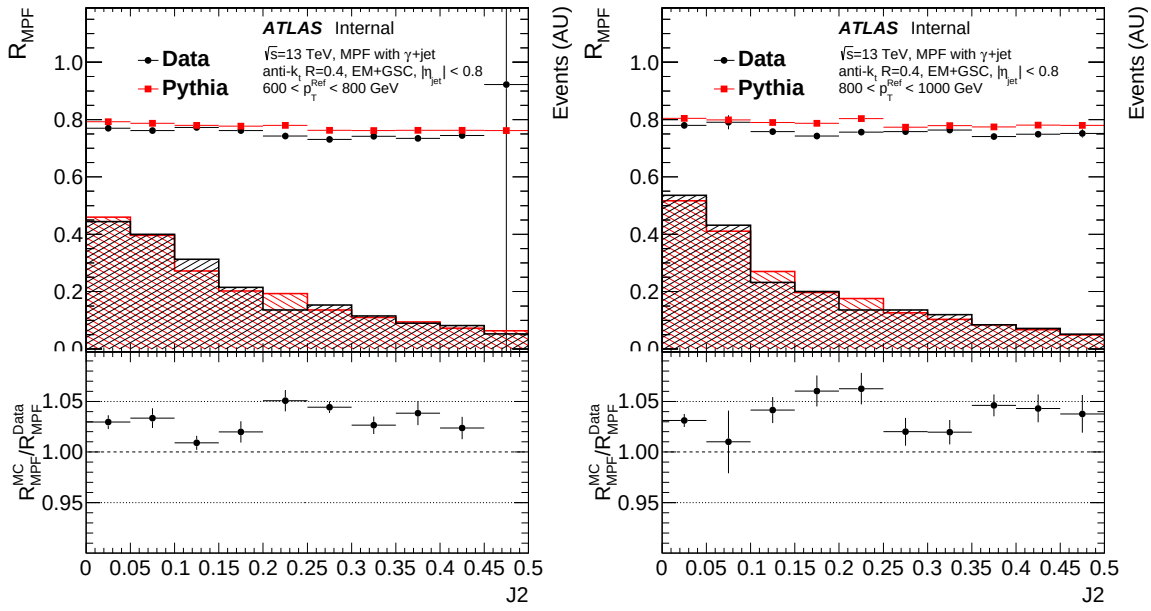

(a) 600-800 GeV

(b) 800-1000 GeV

Figure D.7: Response as a function of the fraction of the photon energy contained in the subleading jet (J2) in two different p_{T} bins along with the distribution of event s plotted against the same variable. All selection cuts listed in Sec. 5.2 have been applied except for the subleading jet cut and the $\Delta\phi$ cut.

Appendix E

Response vs. the $\Delta\phi$ cut at EM+GSC using γ+jet events in 2016

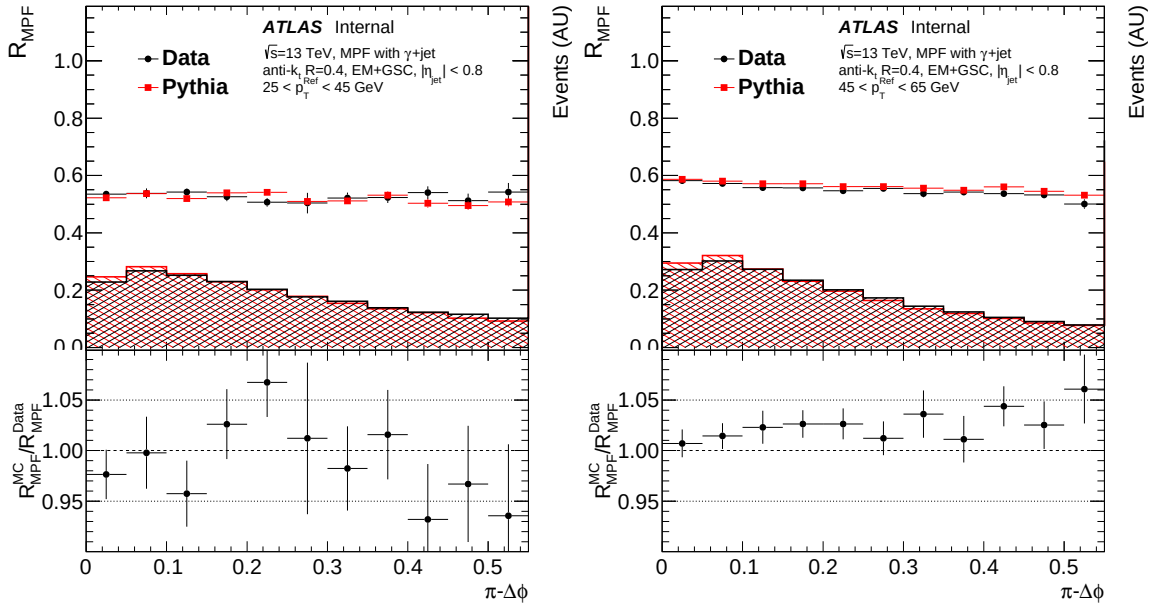

(a) 25-45 GeV (b) 45-65 GeV

Figure E.1: Response as a function of the opening angle in azimuth between the reference object and the leading jet ($\Delta\phi$) in two different p_{T} bins along with the distribution of events plotted against the same variable. All selection cuts listed in Sec. 5.2 have been applied except for the subleading jet cut and the $\Delta\phi$ cut.

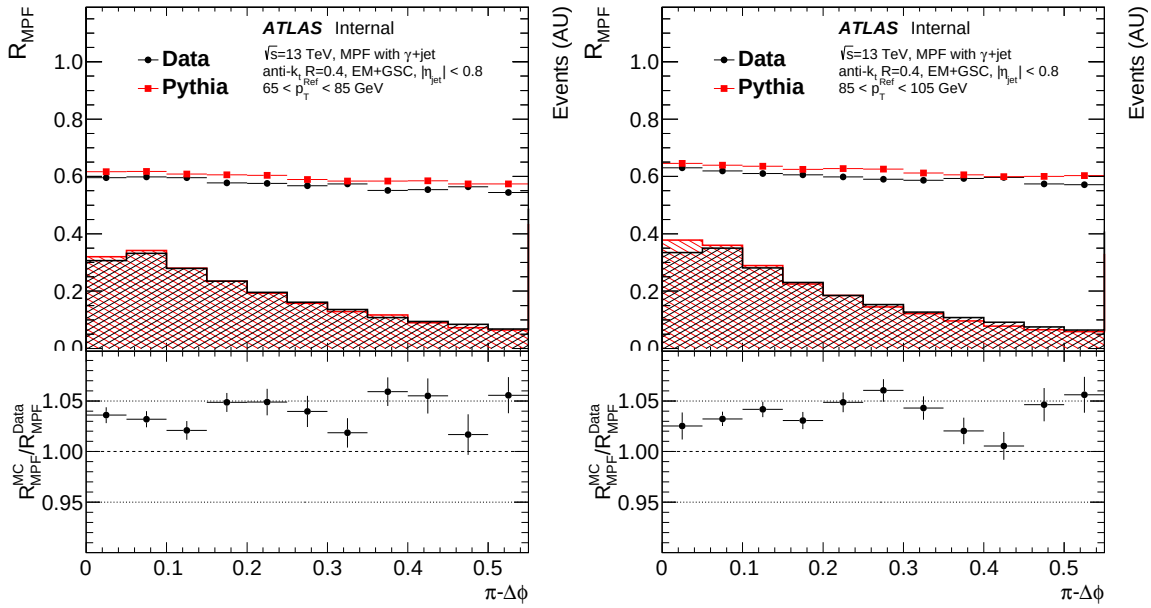

(a) 65-85 GeV (b) 85-105 GeV

Figure E.2: Response as a function of the opening angle in azimuth between the reference object and the leading jet ($\Delta\phi$) in two different p_{T} bins along with the distribution of events plotted against the same variable. All selection cuts listed in Sec. 5.2 have been applied except for the subleading jet cut and the $\Delta\phi$ cut.

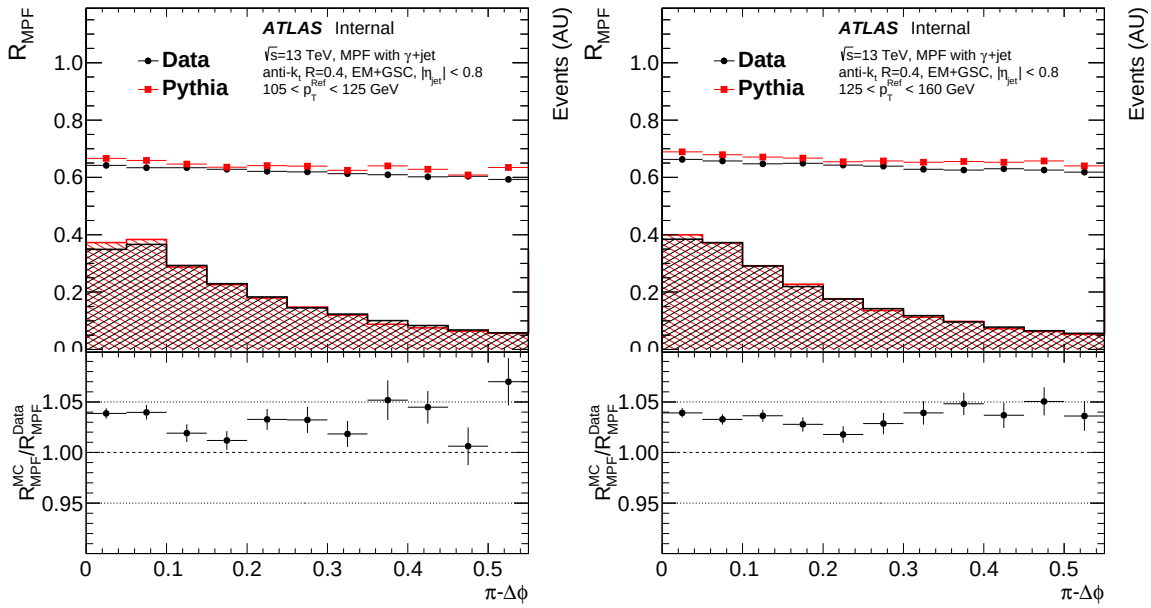

(a) 105-125 GeV (b) 125-160 GeV

Figure E.3: Response as a function of the opening angle in azimuth between the reference object and the leading jet ($\Delta\phi$) in two different p_{T} bins along with the distribution of events plotted against the same variable. All selection cuts listed in Sec. 5.2 have been applied except for the subleading jet cut and the $\Delta\phi$ cut.

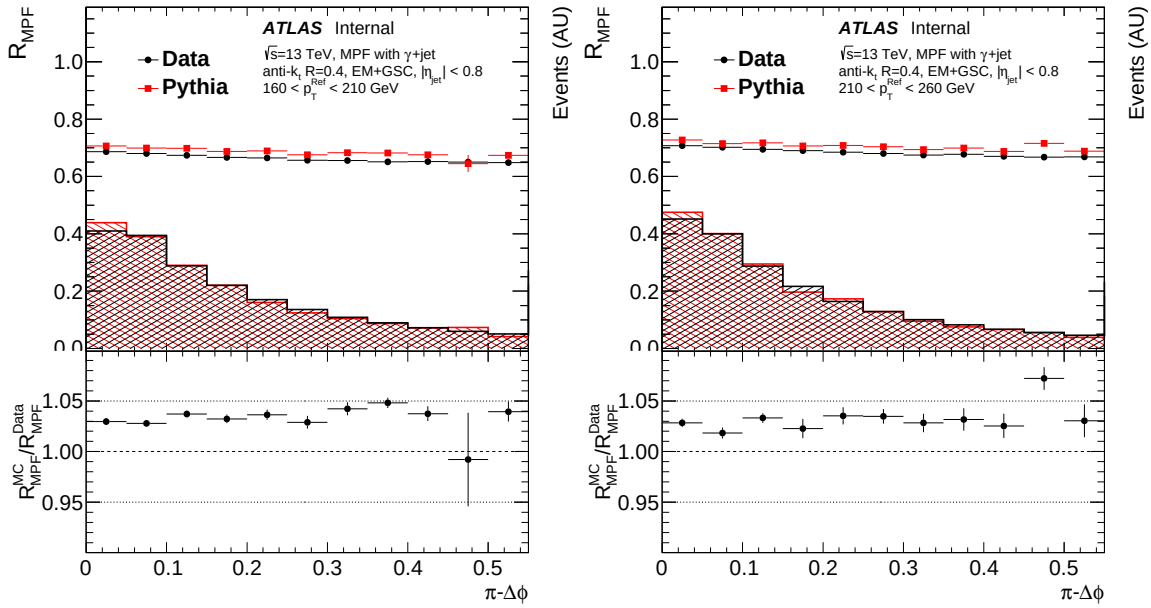

(a) 160-210 GeV (b) 210-260 GeV

Figure E.4: Response as a function of the opening angle in azimuth between the reference object and the leading jet ($\Delta\phi$) in two different p_{T} bins along with the distribution of events plotted against the same variable. All selection cuts listed in Sec. 5.2 have been applied except for the subleading jet cut and the $\Delta\phi$ cut.

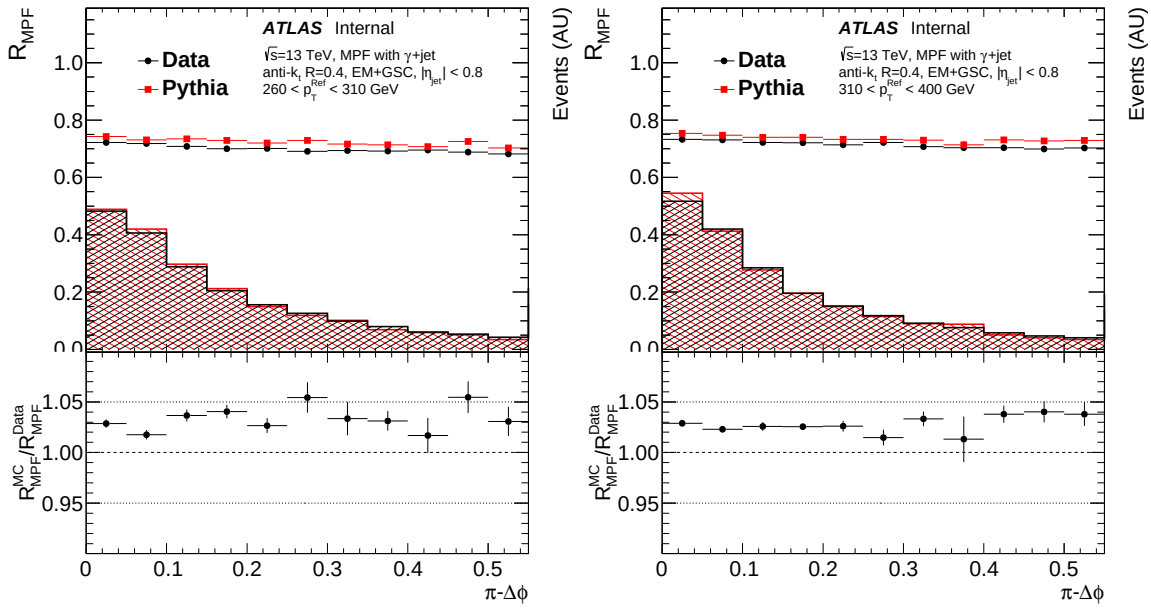

(a) 260-310 GeV (b) 310-400 GeV

Figure E.5: Response as a function of the opening angle in azimuth between the reference object and the leading jet ($\Delta\phi$) in two different p_{T} bins along with the distribution of events plotted against the same variable. All selection cuts listed in Sec. 5.2 have been applied except for the subleading jet cut and the $\Delta\phi$ cut.

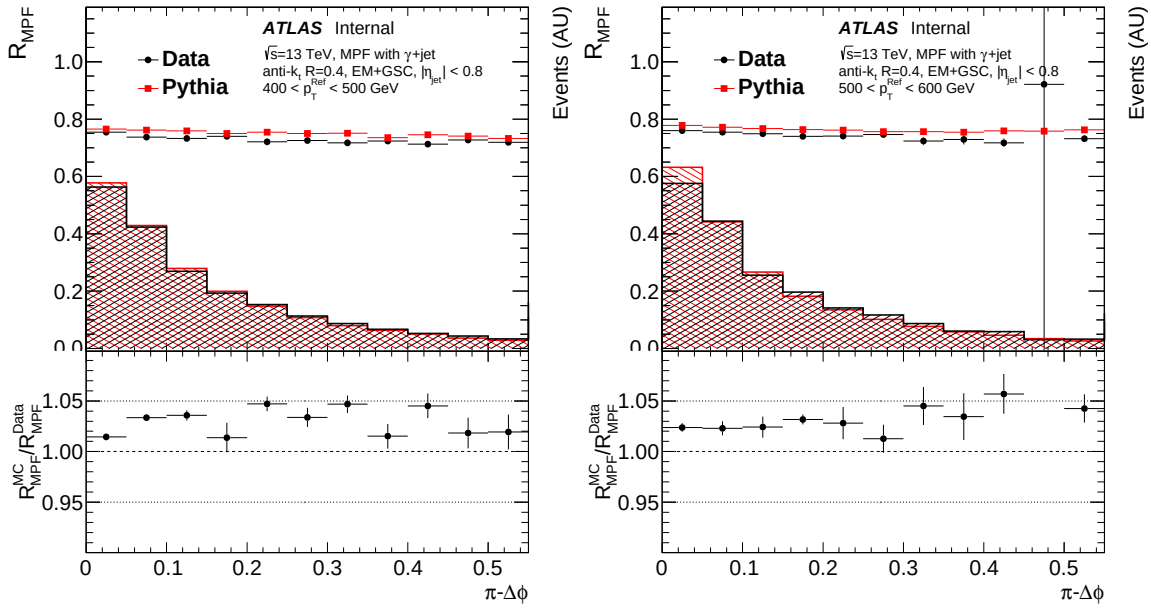

(a) 400-500 GeV (b) 500-600 GeV

Figure E.6: Response as a function of the opening angle in azimuth between the reference object and the leading jet ($\Delta\phi$) in two different p_{T} bins along with the distribution of events plotted against the same variable. All selection cuts listed in Sec. 5.2 have been applied except for the subleading jet cut and the $\Delta\phi$ cut.

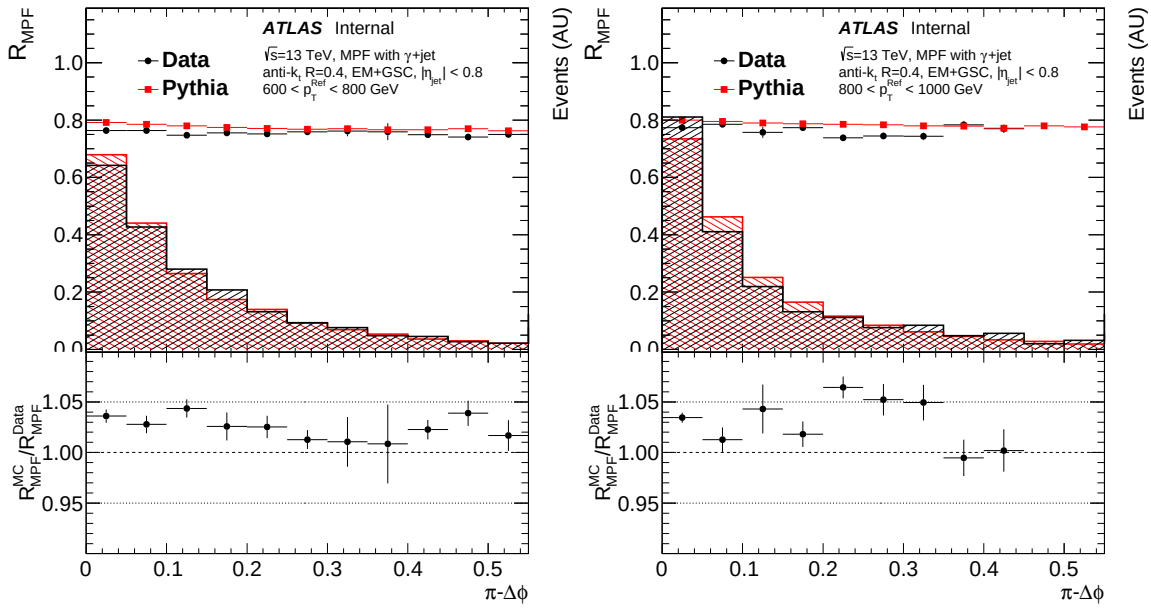

(a) 600-800 GeV (b) 800-1000 GeV

Figure E.7: Response as a function of the opening angle in azimuth between the reference object and the leading jet ($\Delta\phi$) in two different p_{T} bins along with the distribution of events plotted against the same variable. All selection cuts listed in Sec. 5.2 have been applied except for the subleading jet cut and the $\Delta\phi$ cut.

Appendix F

Showering correction for Z+jet events

Fig. F.1 shows the showering correction distributions for all p_{T} bins for anti-k_{t} R=0.4 jets in Z+jet using FTFP_BERT. The remainder of this appendix will show the energy dependence of the showering correction for both FTFP_BERT and QGSP_BIC for standard Z+jet as well as Z+jet separated into light quark and gluon only samples using a number of jet sizes. The showering correction is intended to measure the flow of energy in jets. Very small jets tend to have only a small number of constituents, and therefore will tend to give non-useful results. With that in mind, the results for anti-k_{t} R=0.1 (and R=0.2 to some extend) are included in this thesis more to satisfy the readers curiosity than to be something potentially useful.

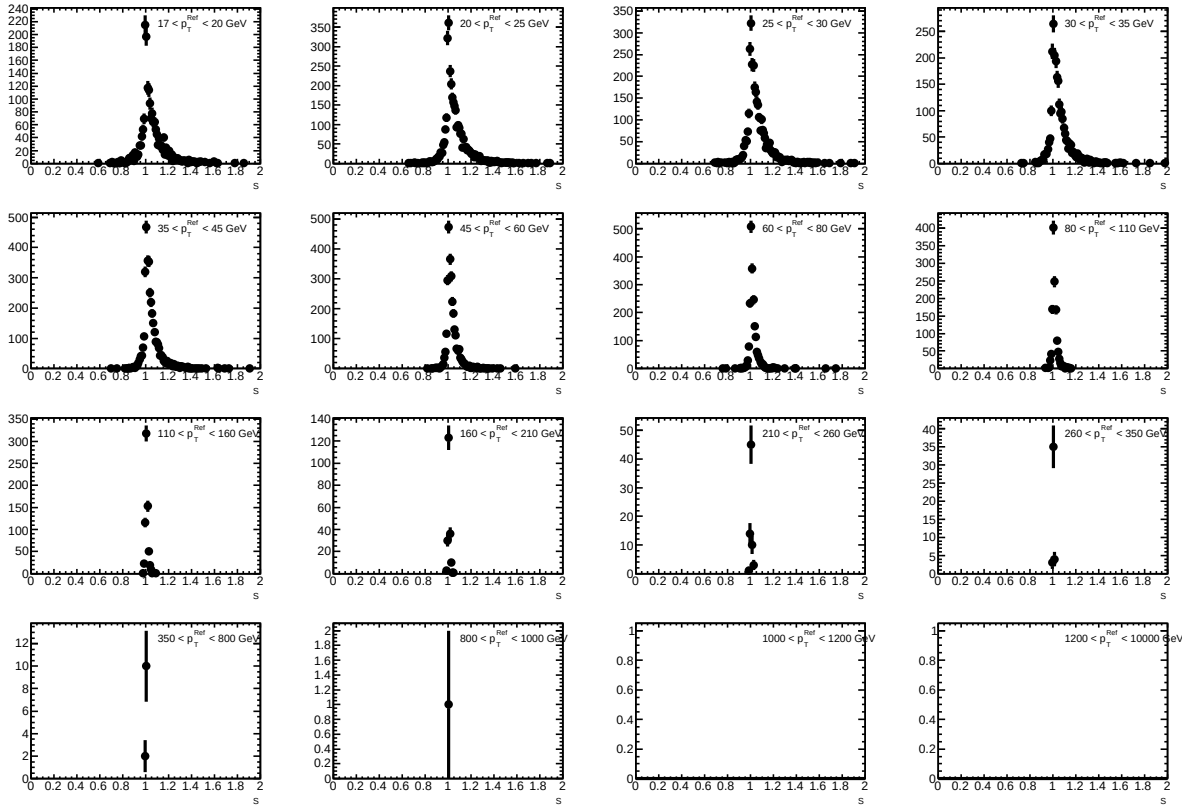

Figure F.1: Showering correction distributions for all p_{T} bins considered using FTFP_BERT in Z+jet for anti-k_{t} R=0.4 jets.

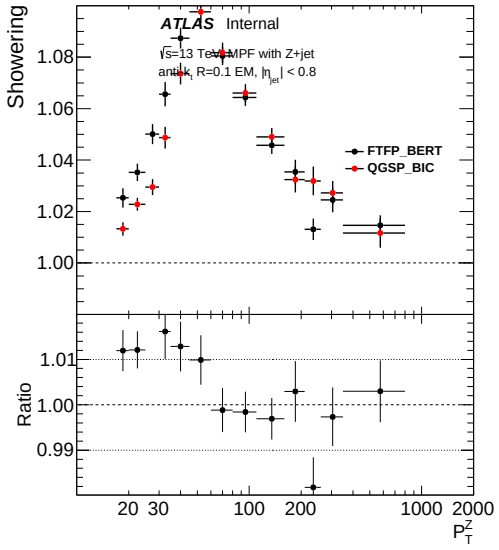

Figure F.2: Showering correction for anti-k_t R=0.1 jets with Z+jet events

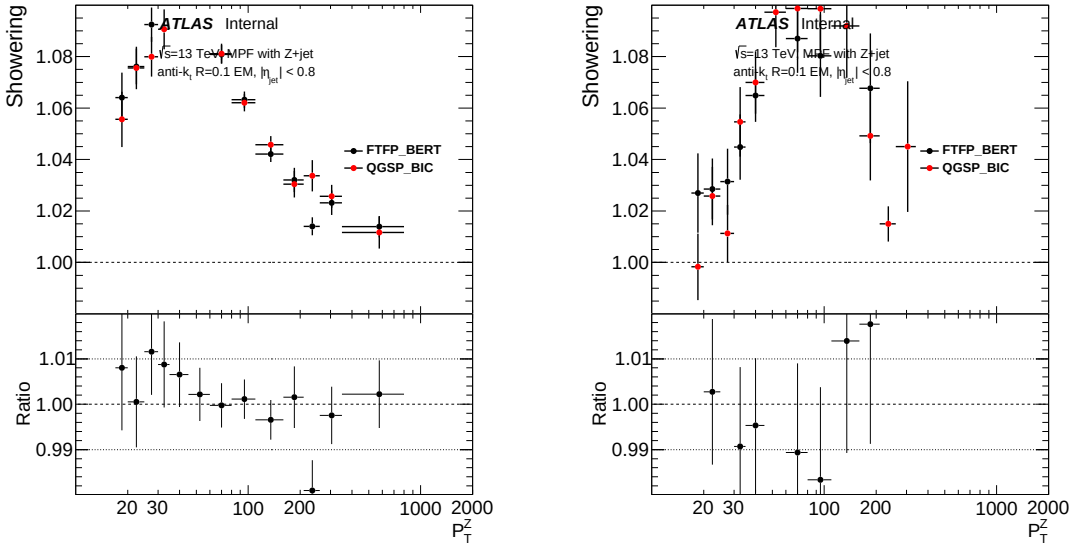

(a) Quark jets

(b) Gluon jets

Figure F.3: Showering correction for both quark and gluon initiated jets, as measured using Z+jet events with anti-k_t R=0.1 jets

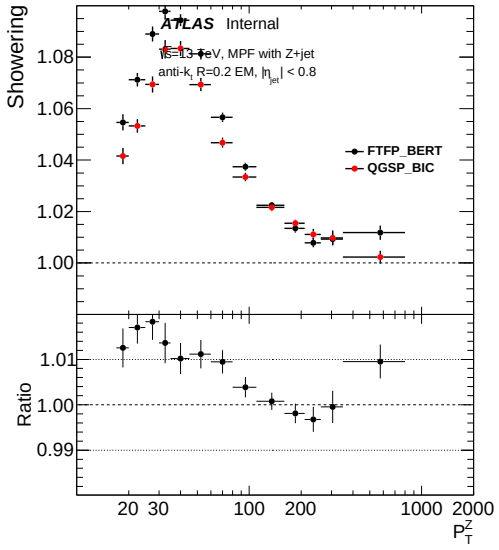

Figure F.4: Showering correction for anti-k_t R=0.2 jets with Z+jet events

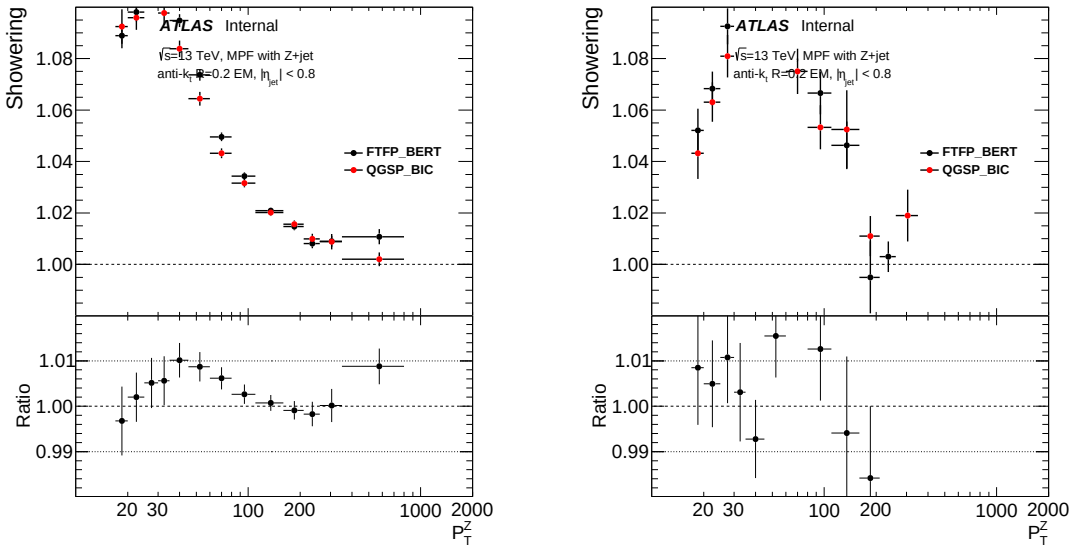

(a) Quark jets

(b) Gluon jets

Figure F.5: Showering correction for both quark and gluon initiated jets, as measured using Z+jet events with anti-k_t R=0.2 jets

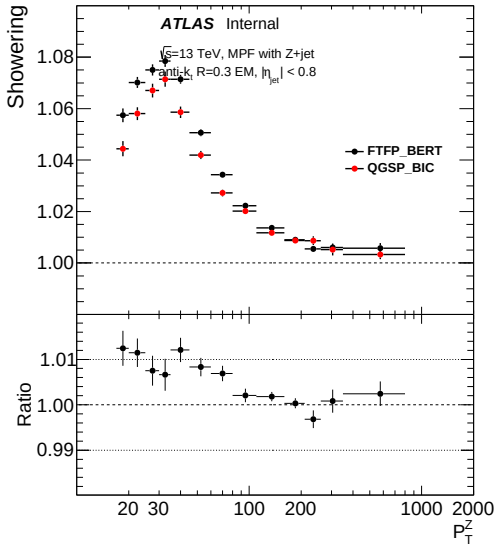

Figure F.6: Showering correction for anti-k_t R=0.3 jets with Z+jet events

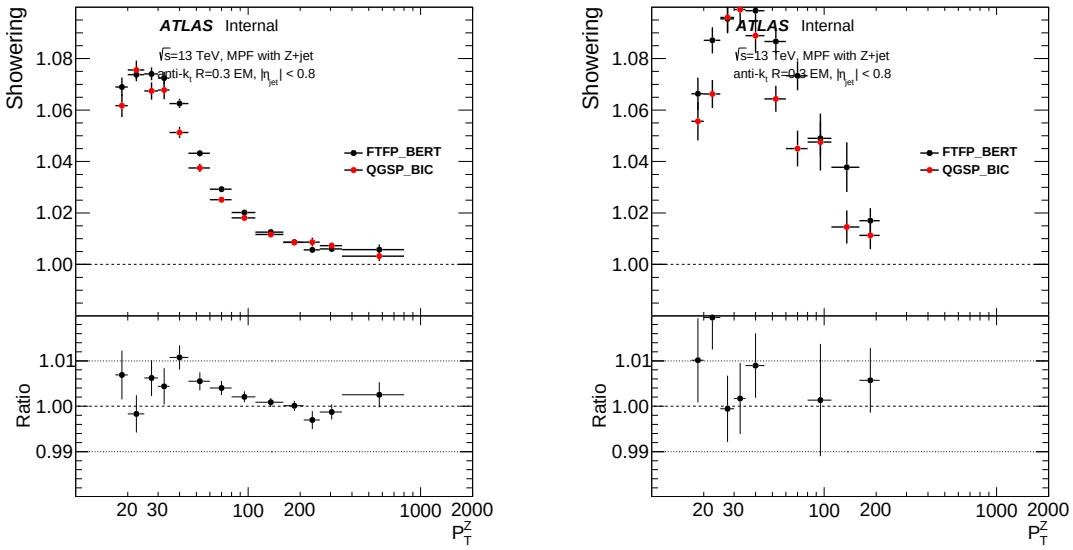

(a) Quark jets

(b) Gluon jets

Figure F.7: Showering correction for both quark and gluon initiated jets, as measured using Z+jet events with anti-k_t R=0.3 jets

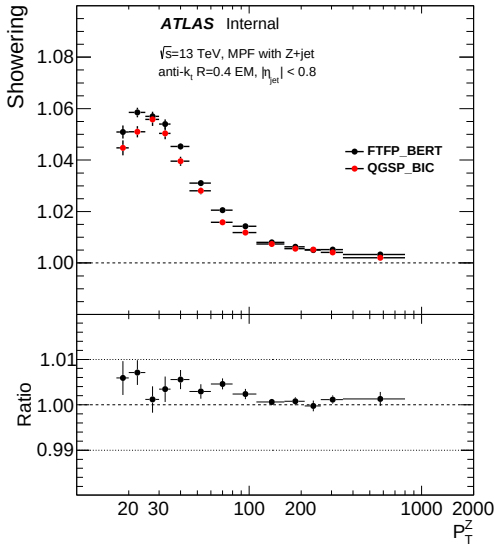

Figure F.8: Showering correction for anti-k_t R=0.4 jets with Z+jet events

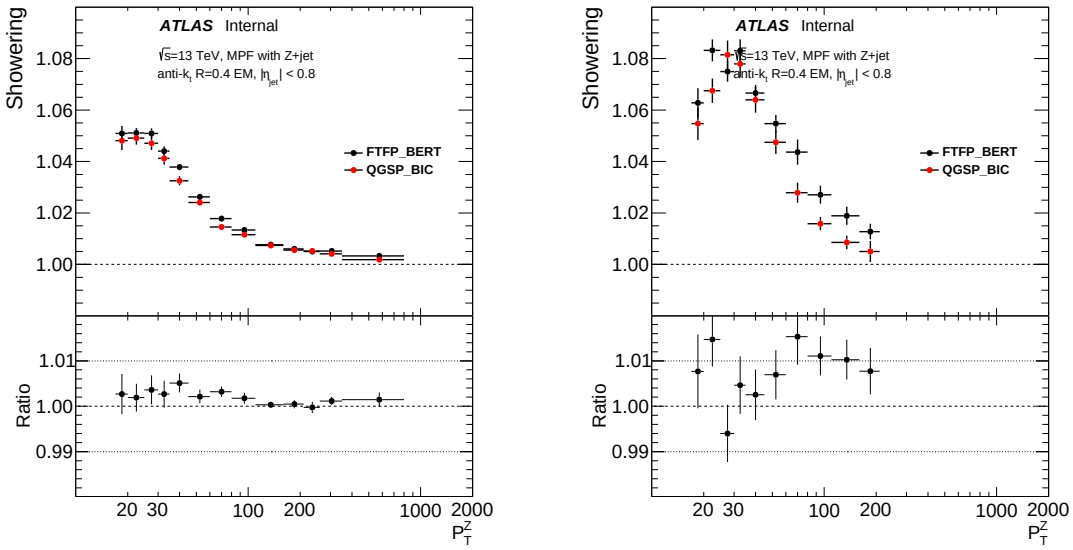

(a) Quark jets

(b) Gluon jets

Figure F.9: Showering correction for both quark and gluon initiated jets, as measured using Z+jet events with anti-k_t R=0.4 jets

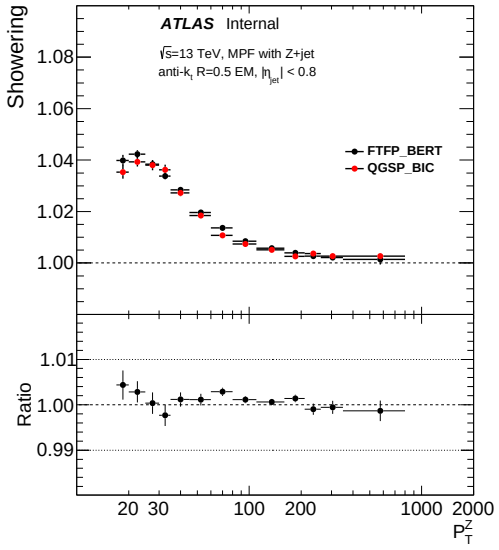

Figure F.10: Showering correction for anti-k_t R=0.5 jets with Z+jet events

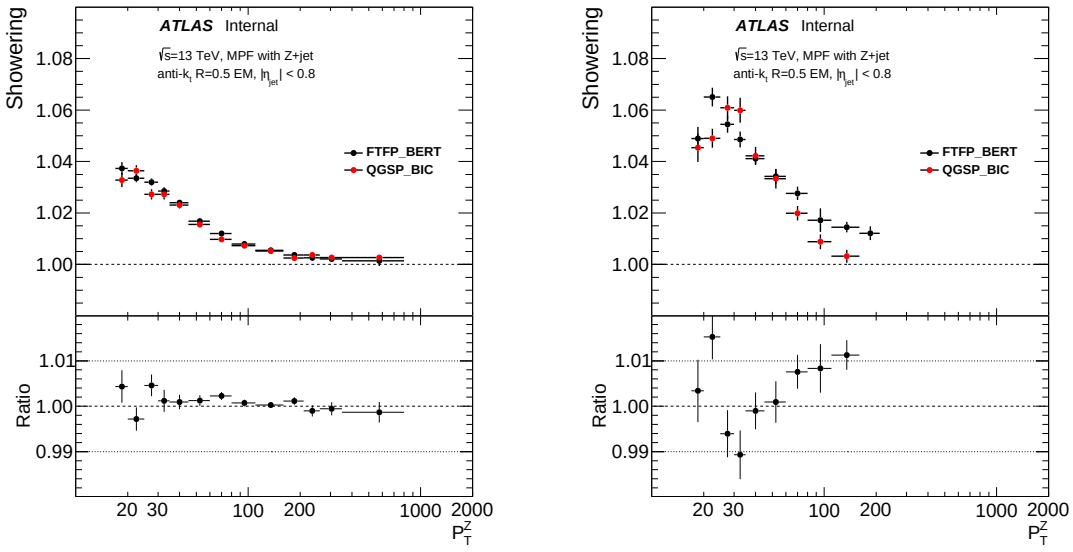

(a) Quark jets

(b) Gluon jets

Figure F.11: Showering correction for both quark and gluon initiated jets, as measured using Z+jet events with anti-k_t R=0.5 jets

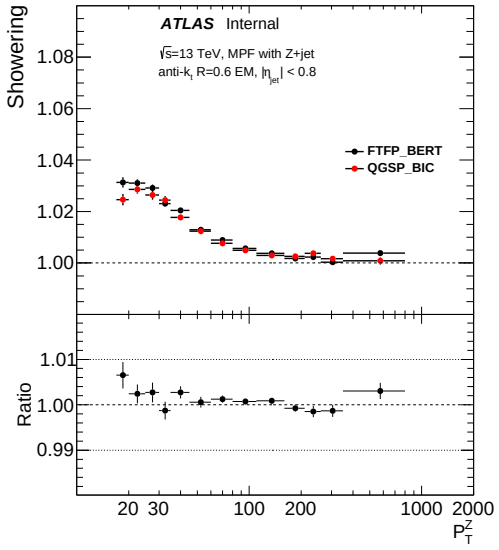

Figure F.12: Showering correction for anti-k_{t} R=0.6 jets with Z+jet events

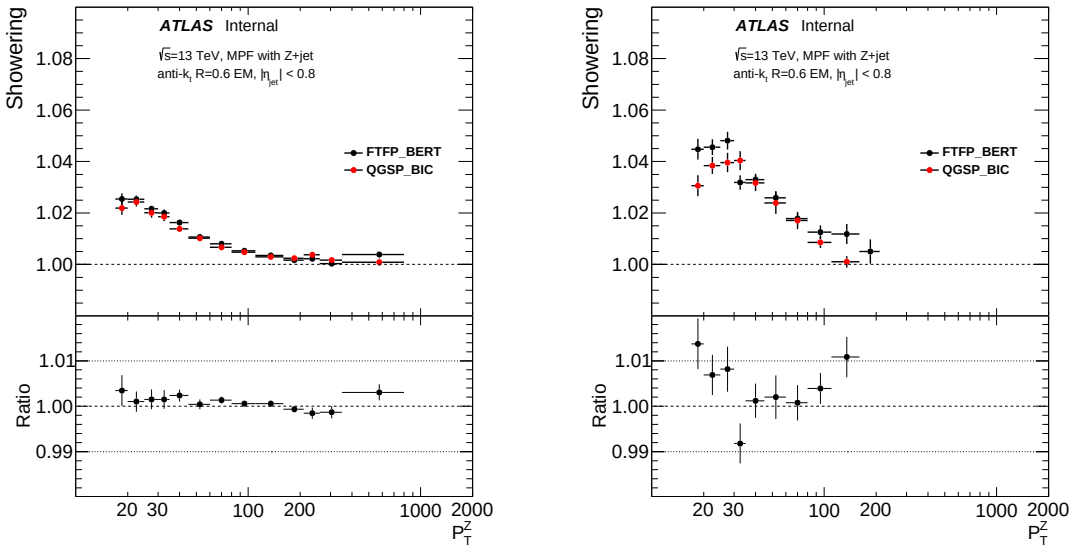

(a) Quark jets

(b) Gluon jets

Figure F.13: Showering correction for both quark and gluon initiated jets, as measured using Z+jet events with anti-k_{t} R=0.6 jets

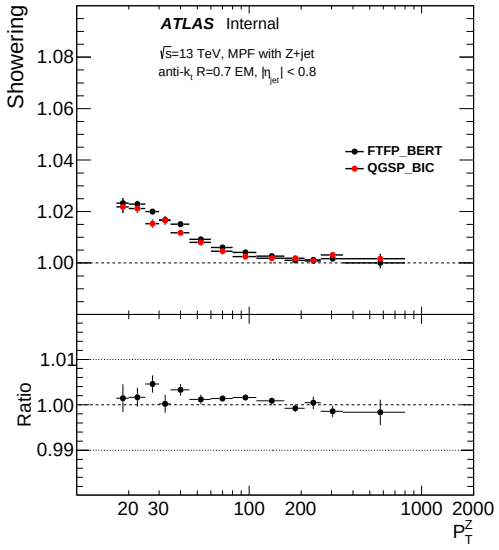

Figure F.14: Showering correction for anti-k_t R=0.7 jets with Z+jet events

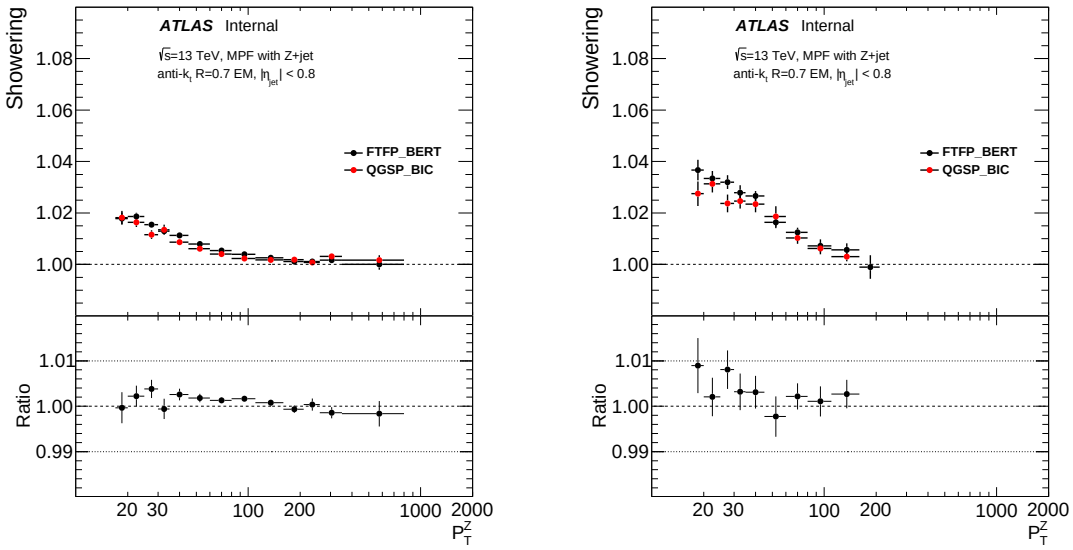

(a) Quark jets (b) Gluon jets

Figure F.15: Showering correction for both quark and gluon initiated jets, as measured using Z+jet events with anti-k_t R=0.7 jets

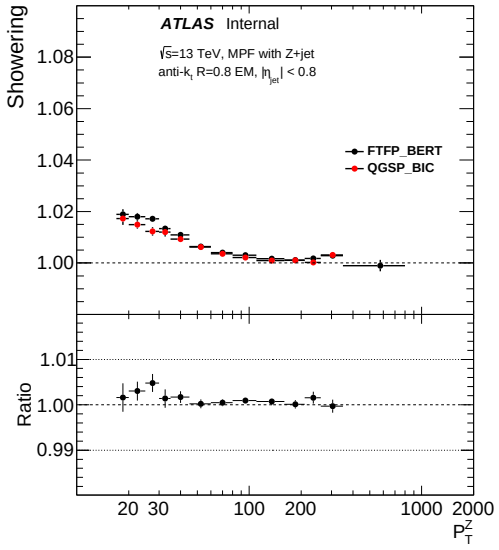

Figure F.16: Showering correction for anti-k_{t} R=0.8 jets with Z+jet events

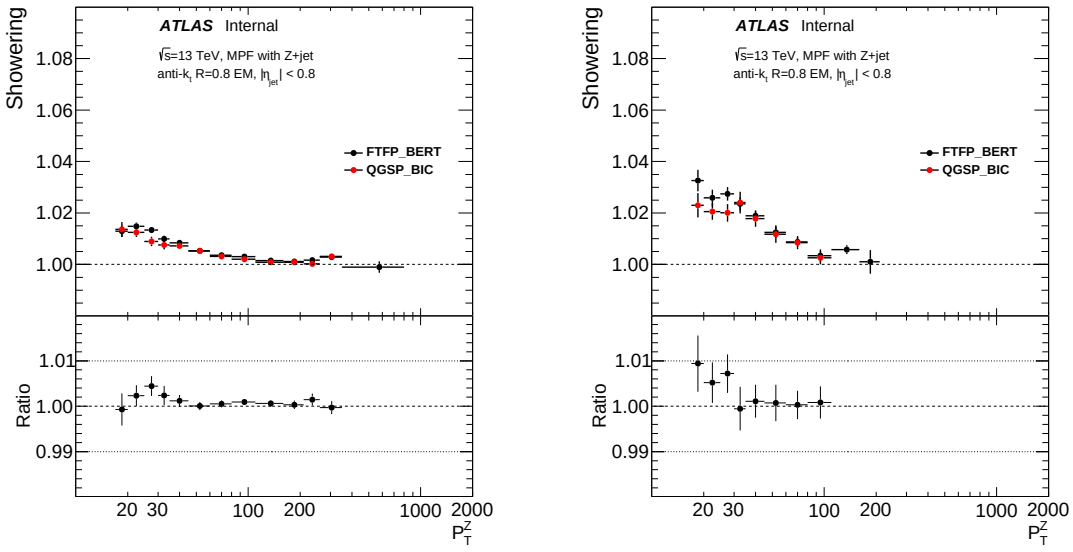

(a) Quark jets

(b) Gluon jets

Figure F.17: Showering correction for both quark and gluon initiated jets, as measured using Z+jet events with anti-k_{t} R=0.8 jets

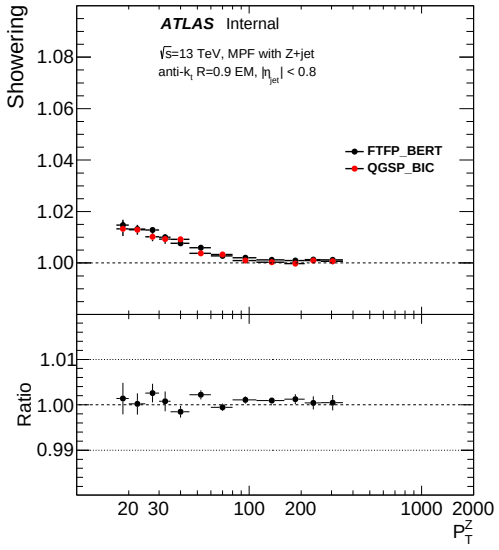

Figure F.18: Showering correction for anti-k_t R=0.9 jets with Z+jet events

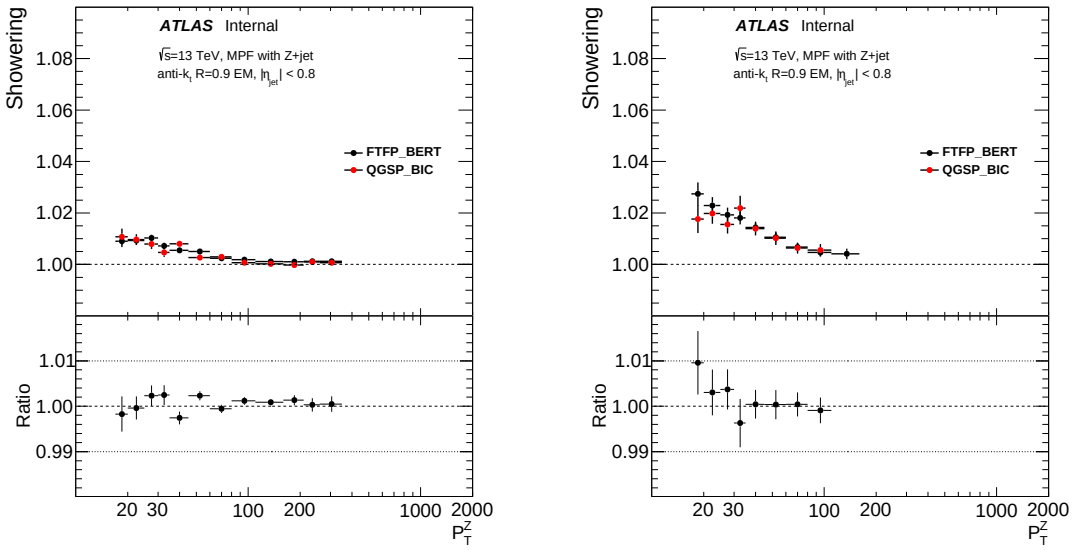

(a) Quark jets

(b) Gluon jets

Figure F.19: Showering correction for both quark and gluon initiated jets, as measured using Z+jet events with anti-k_t R=0.9 jets

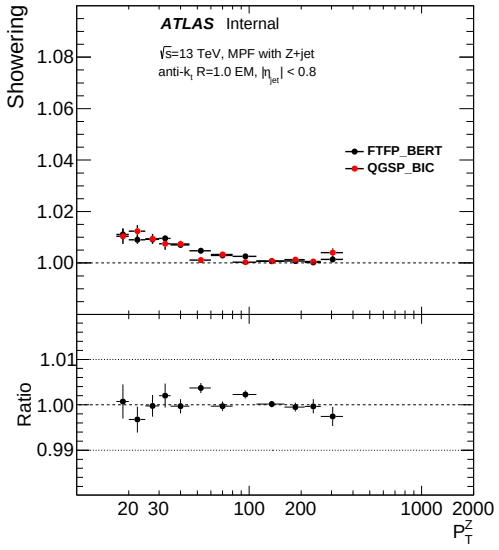

Figure F.20: Showering correction for anti-k_{t} R=1.0 jets with Z+jet events

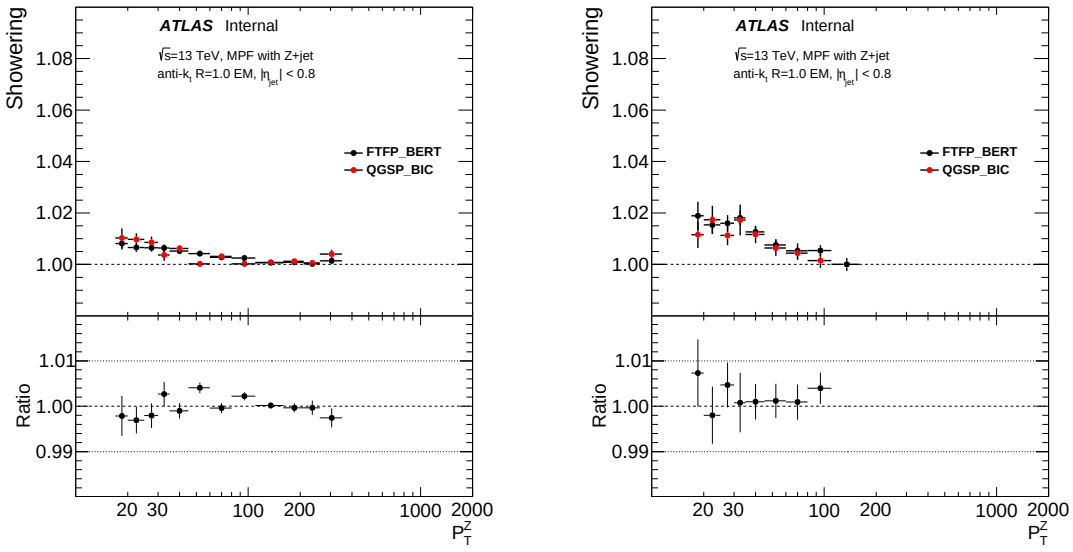

(a) Quark jets

(b) Gluon jets

Figure F.21: Showering correction for both quark and gluon initiated jets, as measured using Z+jet events with anti-k_{t} R=1.0 jets

Appendix G

Showering correction for γ+jet events

Fig. G.1 shows the showering correction distributions for all p_{T} bins for anti-k_{t} R=0.4 jets in γ+jet using FTFP_BERT. The remainder of this appendix will show the energy dependence of the showering correction for both FTFP_BERT and QGSP_BIC for standard γ+jet as well as γ+jet separated into light quark and gluon only samples using a number of jet sizes. The showering correction is intended to measure the flow of energy in jets. Very small jets tend to have only a small number of constituents, and therefore will tend to give non-useful results. With that in mind, the results for anti-k_{t} R=0.1 (and R=0.2 to some extend) are included in this thesis more to satisfy the readers curiosity than to be something potentially useful.

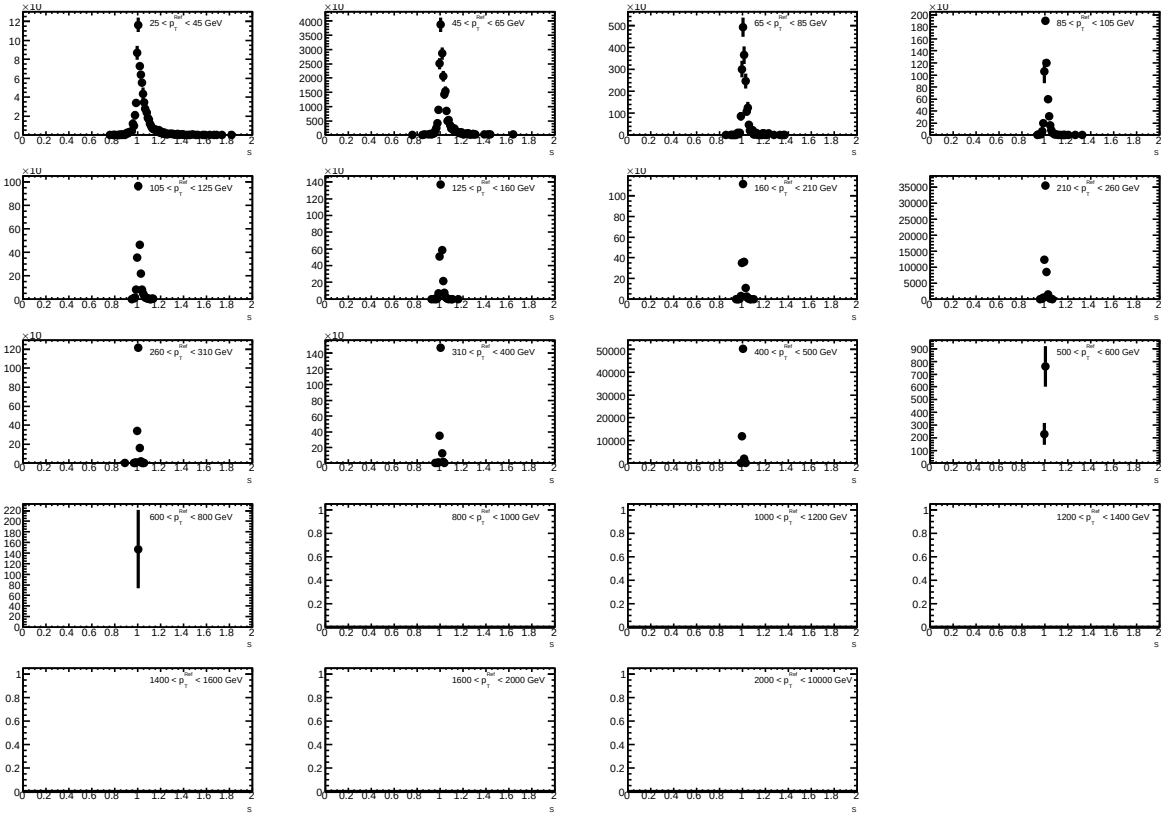

Figure G.1: Showering correction distributions for all p_{T} bins considered using FTFP_BERT in γ+jet for anti-k_{t} R=0.4 jets.

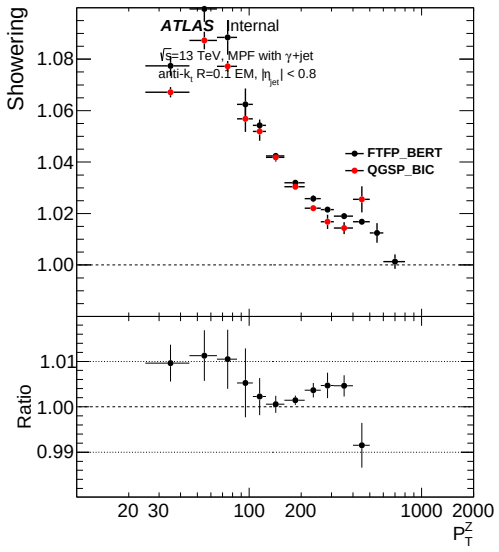

Figure G.2: Showering correction for anti-k_t R=0.1 jets with γ+jet events

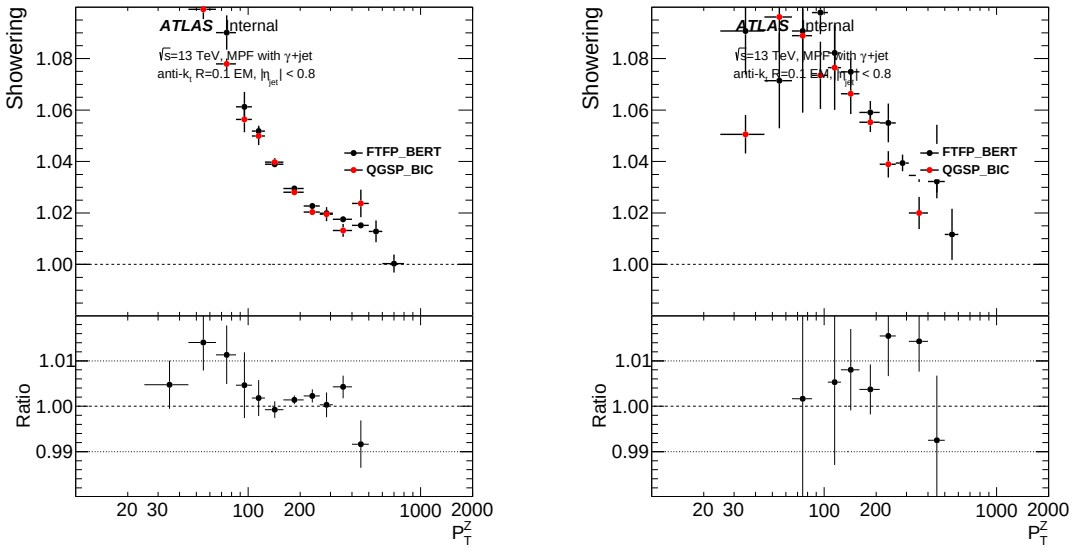

(a) Quark jets

(b) Gluon jets

Figure G.3: Showering correction for both quark and gluon initiated jets, as measured using γ+jet events with anti-k_t R=0.1 jets

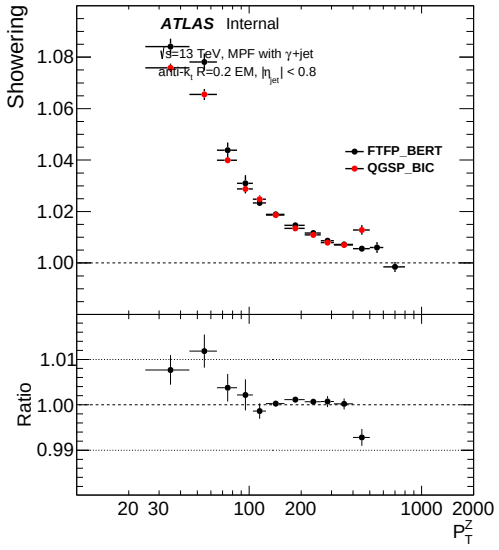

Figure G.4: Showering correction for anti-k_t R=0.2 jets with γ+jet events

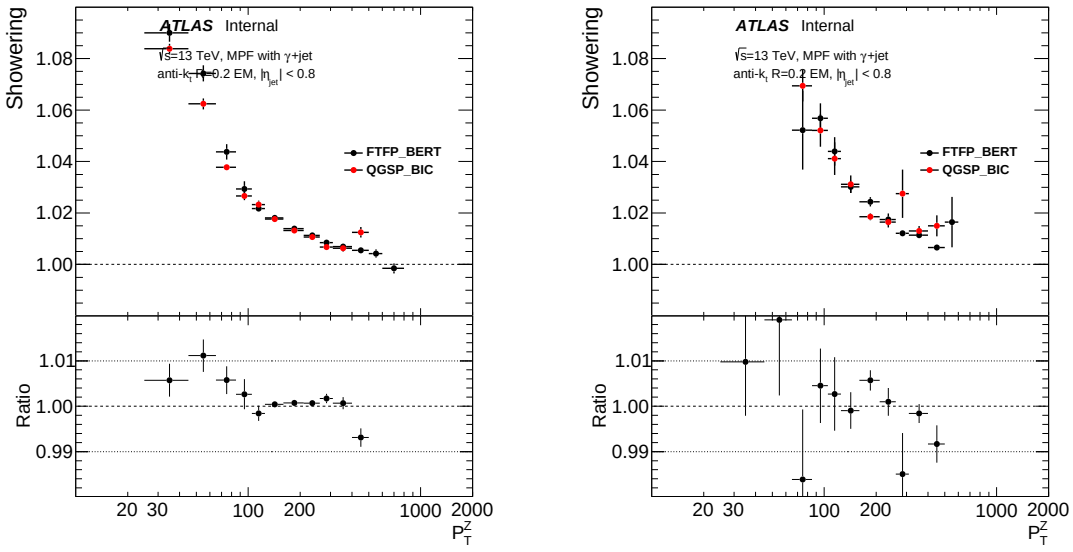

(a) Quark jets

(b) Gluon jets

Figure G.5: Showering correction for both quark and gluon initiated jets, as measured using γ+jet events with anti-k_t R=0.2 jets

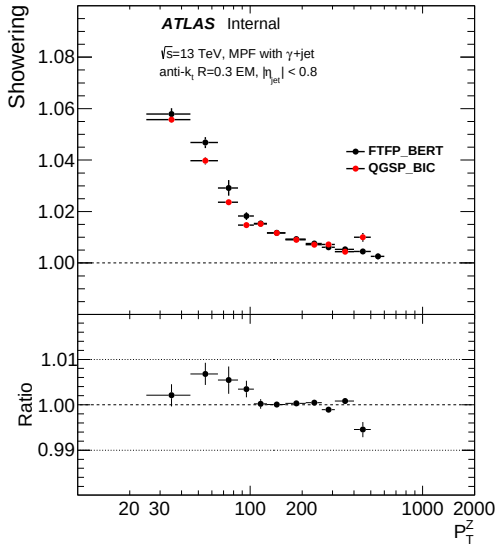

Figure G.6: Showering correction for anti-k_t R=0.3 jets with γ+jet events

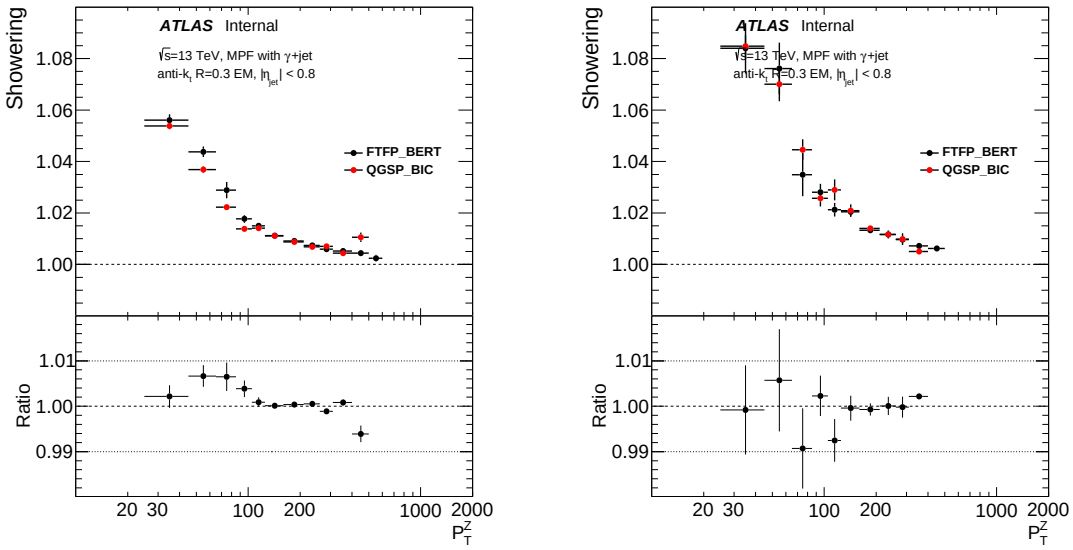

(a) Quark jets

(b) Gluon jets

Figure G.7: Showering correction for both quark and gluon initiated jets, as measured using γ+jet events with anti-k_t R=0.3 jets

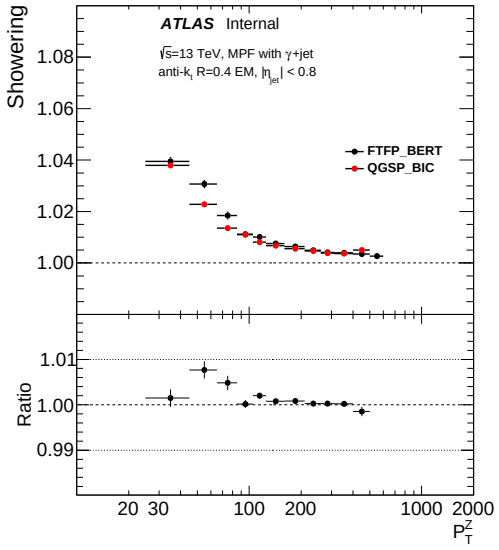

Figure G.8: Showering correction for anti-k_t R=0.4 jets with γ+jet events

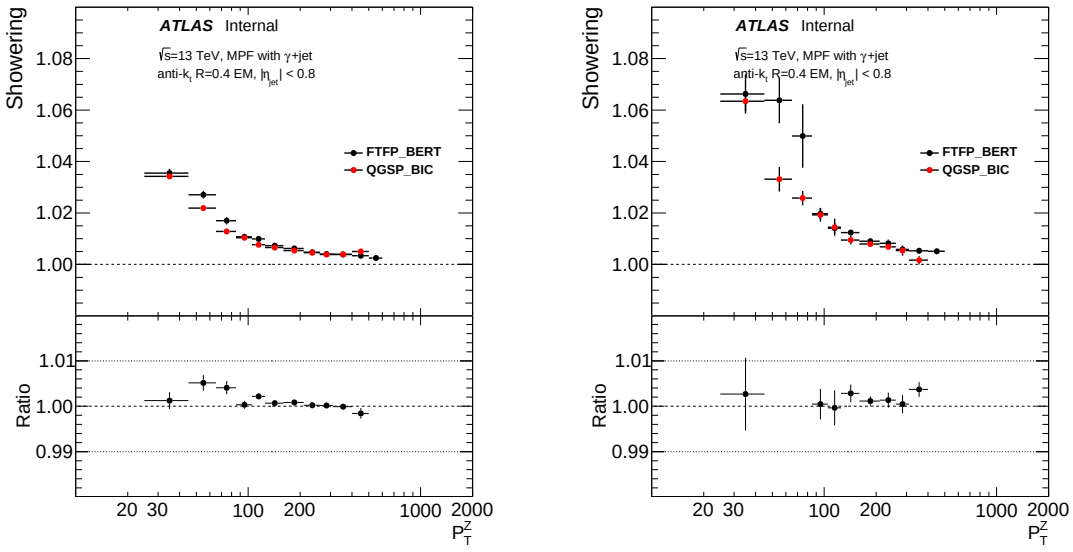

(a) Quark jets

(b) Gluon jets

Figure G.9: Showering correction for both quark and gluon initiated jets, as measured using γ+jet events with anti-k_t R=0.4 jets

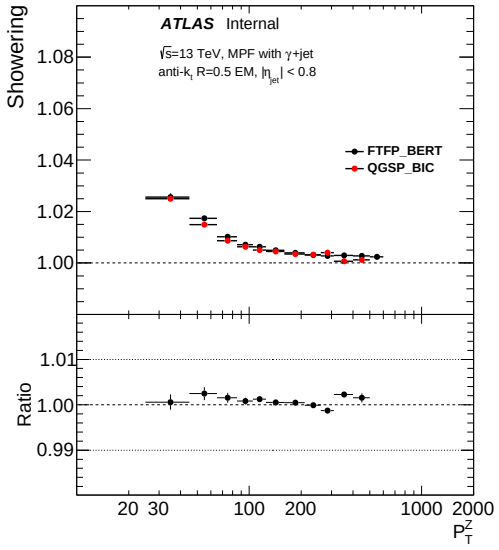

Figure G.10: Showering correction for anti-k_t R=0.5 jets with γ+jet events

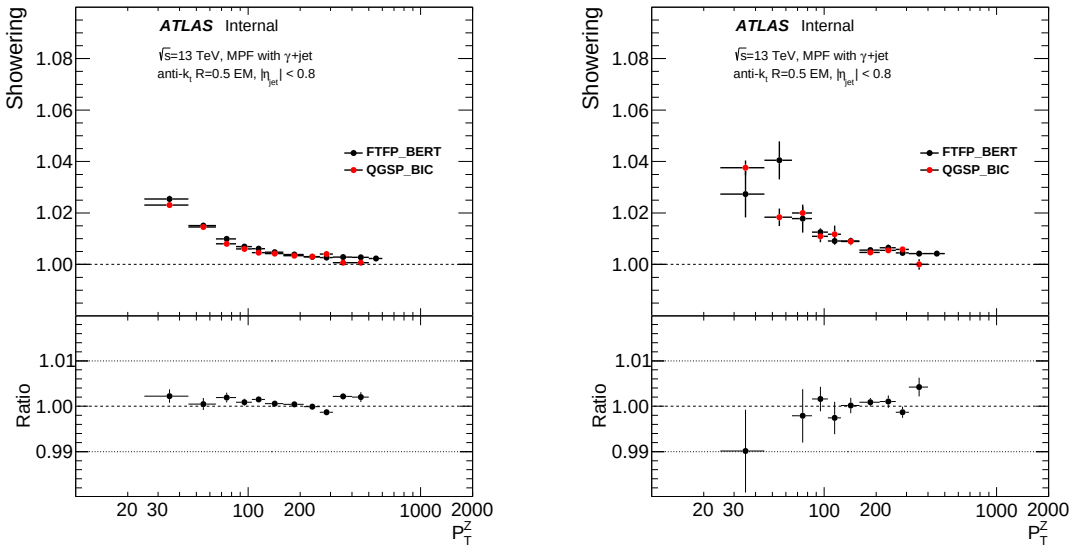

(a) Quark jets

(b) Gluon jets

Figure G.11: Showering correction for both quark and gluon initiated jets, as measured using γ+jet events with anti-k_t R=0.5 jets

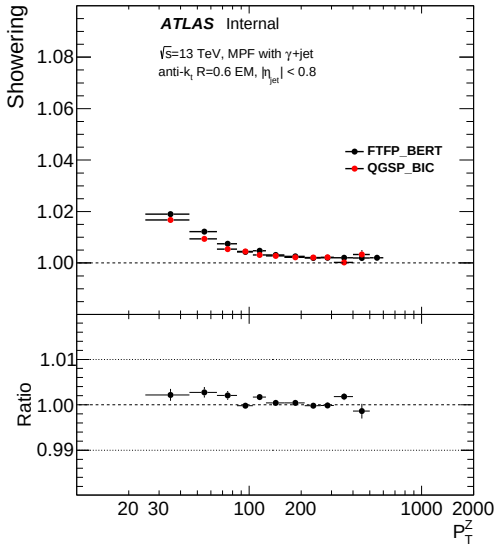

Figure G.12: Showering correction for anti-k_t R=0.6 jets with γ+jet events

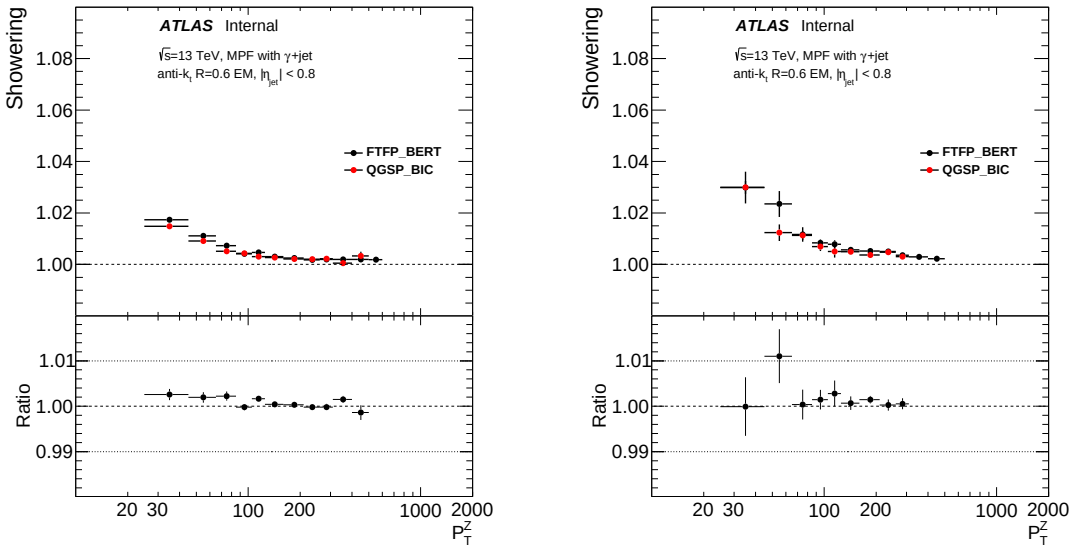

(a) Quark jets

(b) Gluon jets

Figure G.13: Showering correction for both quark and gluon initiated jets, as measured using γ+jet events with anti-k_t R=0.6 jets

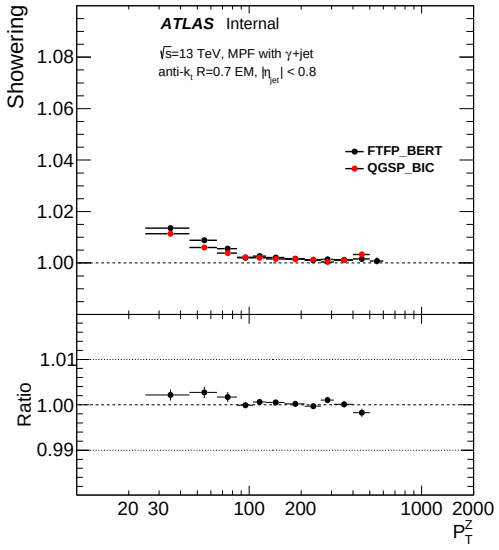

Figure G.14: Showering correction for anti-k_{t} R=0.7 jets with γ+jet events

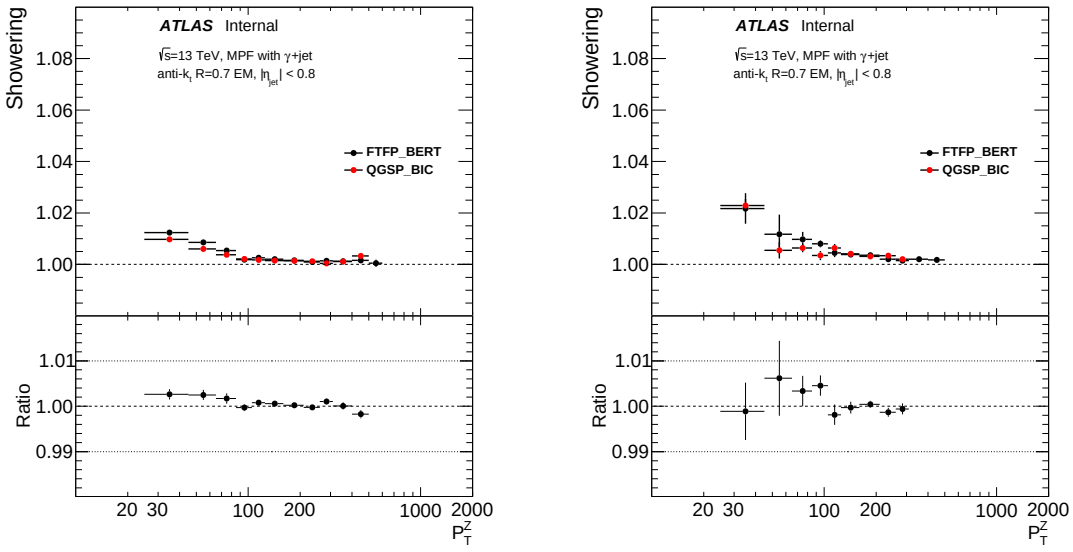

(a) Quark jets

(b) Gluon jets

Figure G.15: Showering correction for both quark and gluon initiated jets, as measured using γ+jet events with anti-k_{t} R=0.7 jets

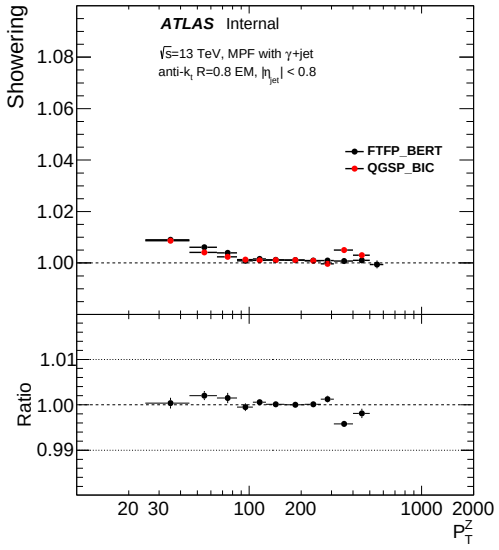

Figure G.16: Showering correction for anti-k_t R=0.8 jets with γ+jet events

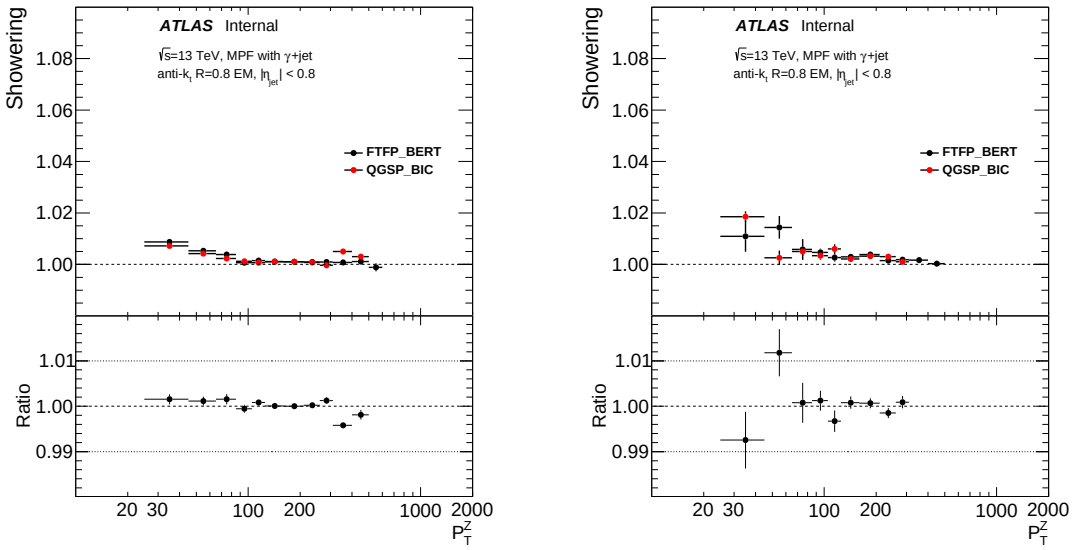

(a) Quark jets

(b) Gluon jets

Figure G.17: Showering correction for both quark and gluon initiated jets, as measured using γ+jet events with anti-k_t R=0.8 jets

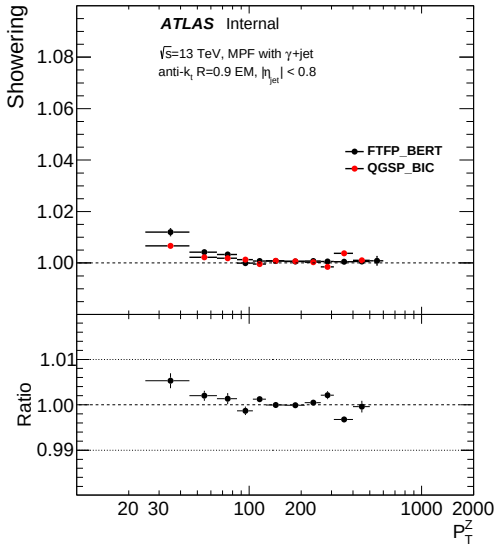

Figure G.18: Showering correction for anti-k_{t} R=0.9 jets with γ+jet events

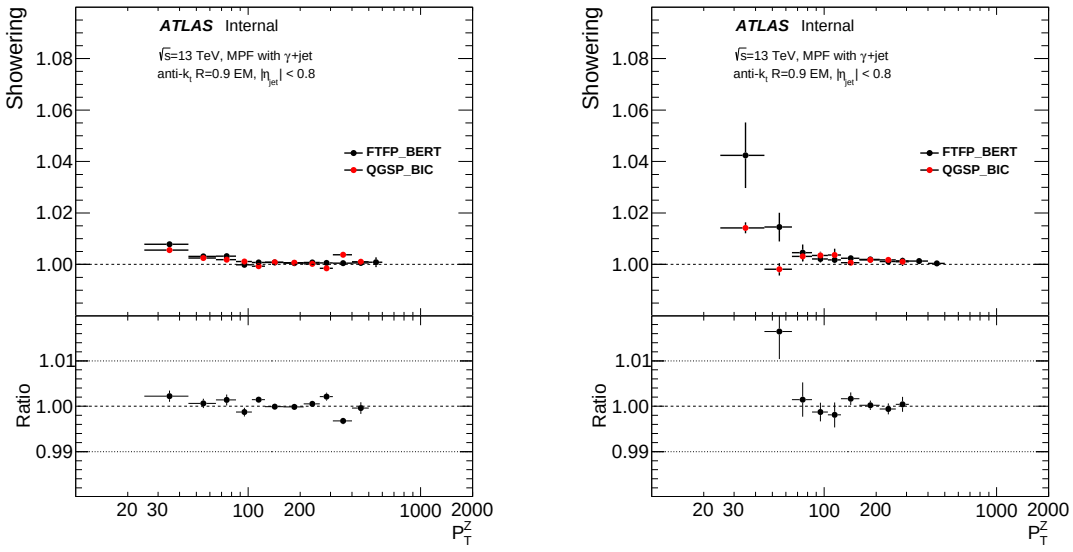

(a) Quark jets

(b) Gluon jets

Figure G.19: Showering correction for both quark and gluon initiated jets, as measured using γ+jet events with anti-k_{t} R=0.9 jets

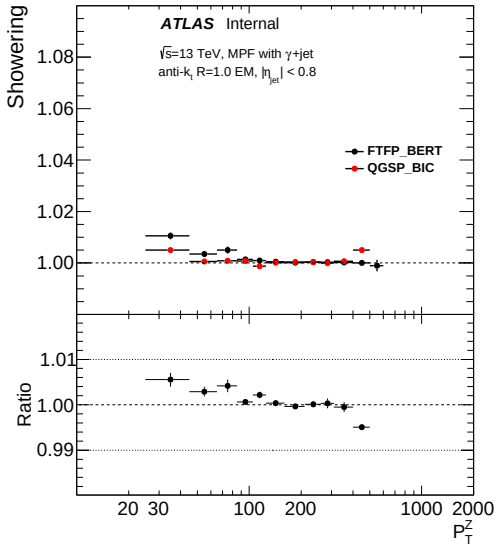

Figure G.20: Showering correction for anti-k_{t} R=1.0 jets with γ+jet events

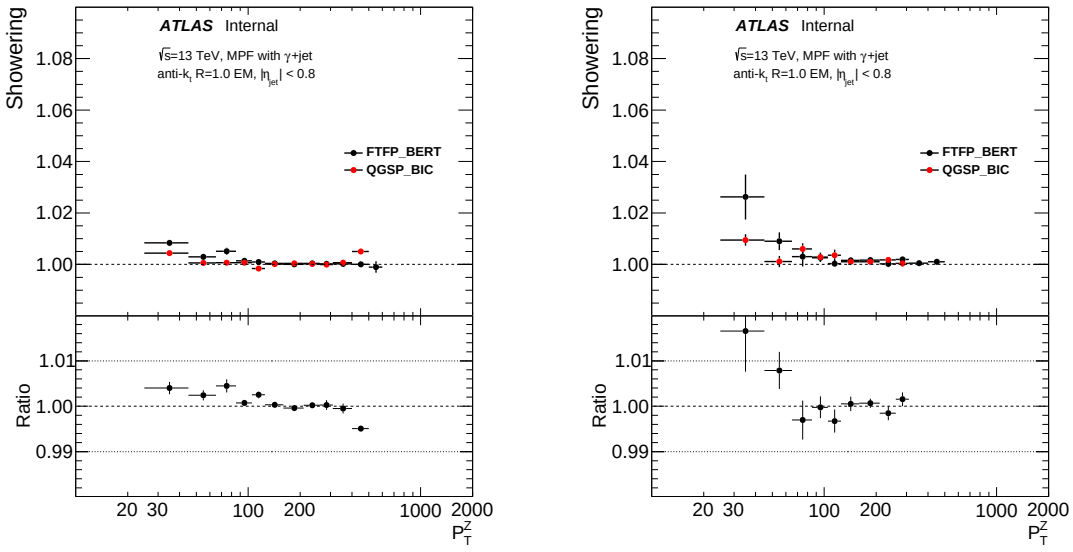

(a) Quark jets

(b) Gluon jets

Figure G.21: Showering correction for both quark and gluon initiated jets, as measured using γ+jet events with anti-k_{t} R=1.0 jets

Appendix H

Topology correction for Z+jet events

Fig. H.1 shows the topology correction distributions for all p_{T} bins for anti-k_{t} R=0.4 jets in Z+jet using FTFP_BERT. The remainder of this appendix will show the energy dependence of the topology correction for both FTFP_BERT and QGSP_BIC for standard Z+jet as well as Z+jet separated into light quark and gluon only samples using a number of jet sizes. The topology correction is intended to measure the flow of energy in jets. Very small jets tend to have only a small number of constituents, and therefore will tend to give non-useful results. With that in mind, the results for anti-k_{t} R=0.1 (and R=0.2 to some extend) are included in this thesis more to satisfy the readers curiosity than to be something potentially useful.

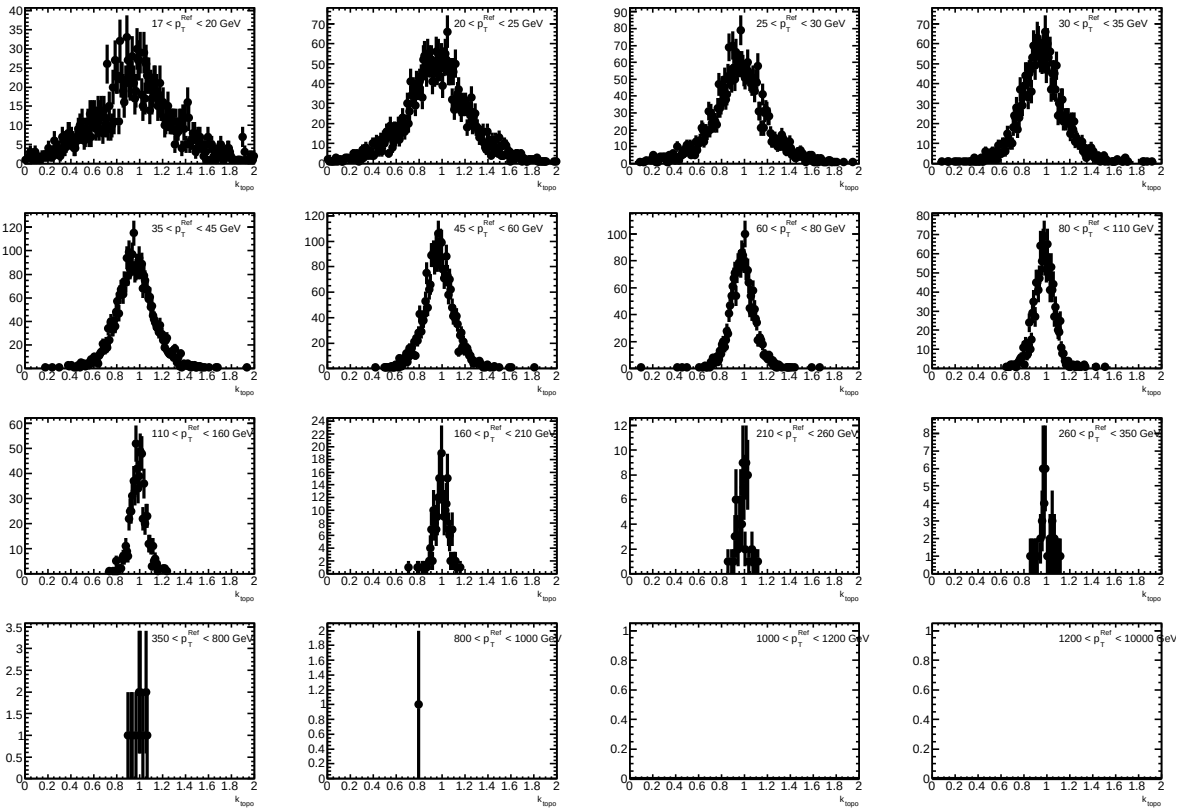

Figure H.1: Topology correction distributions for all p_{T} bins considered using FTFP_BERT in Z+jet for anti-k_{t} R=0.4 jets.

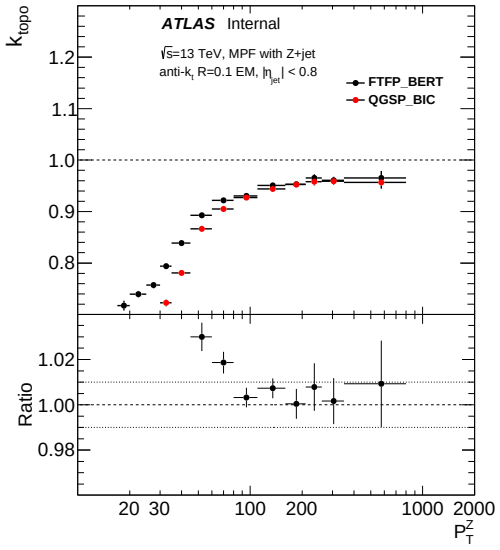

Figure H.2: Topology correction for anti-k_t R=0.1 jets with Z+jet events

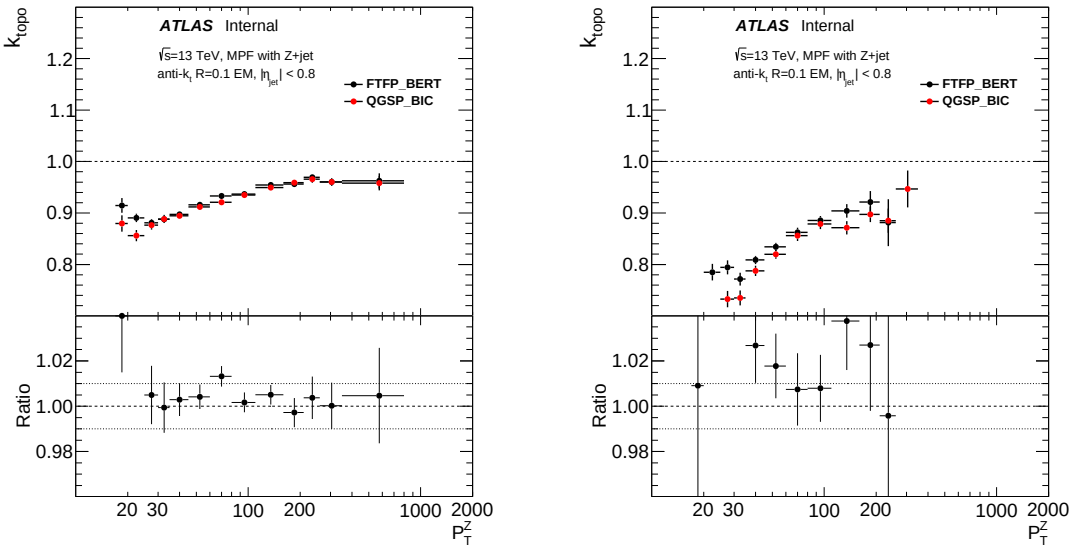

(a) Quark jets

(b) Gluon jets

Figure H.3: Topology correction for both quark and gluon initiated jets, as measured using Z+jet events with anti-k_t R=0.1 jets

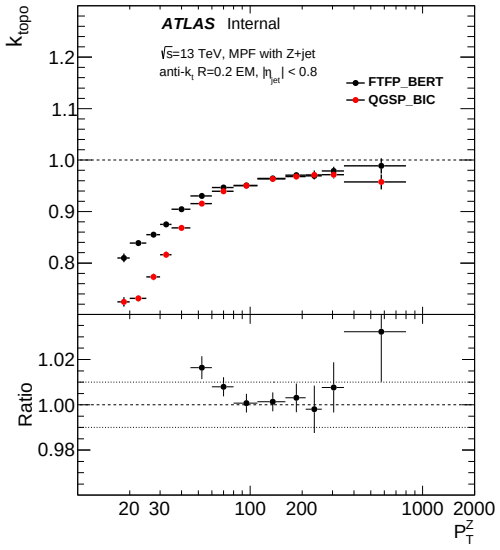

Figure H.4: Topology correction for anti-k_t R=0.2 jets with Z+jet events

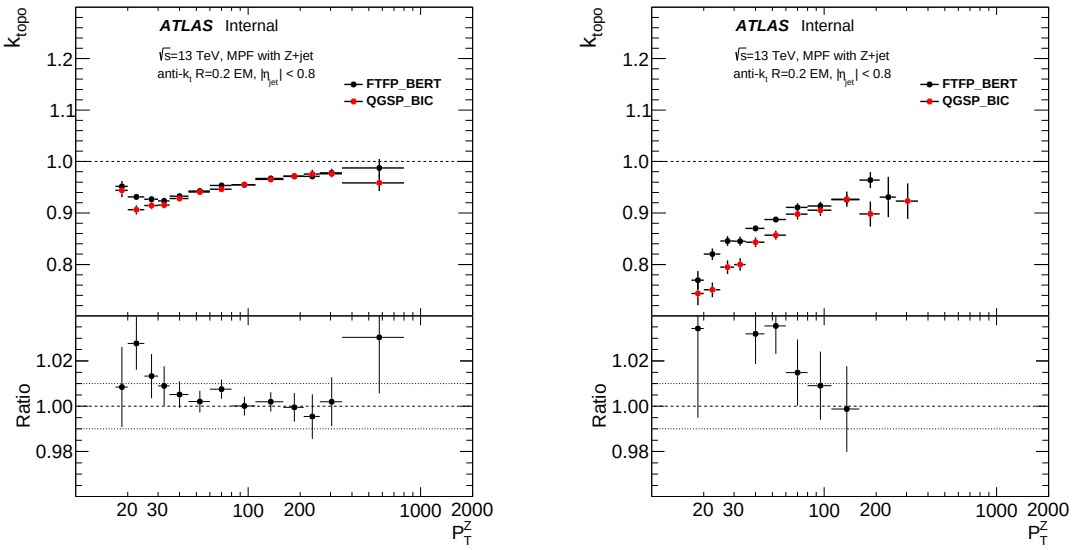

(a) Quark jets

(b) Gluon jets

Figure H.5: Topology correction for both quark and gluon initiated jets, as measured using Z+jet events with anti-k_t R=0.2 jets

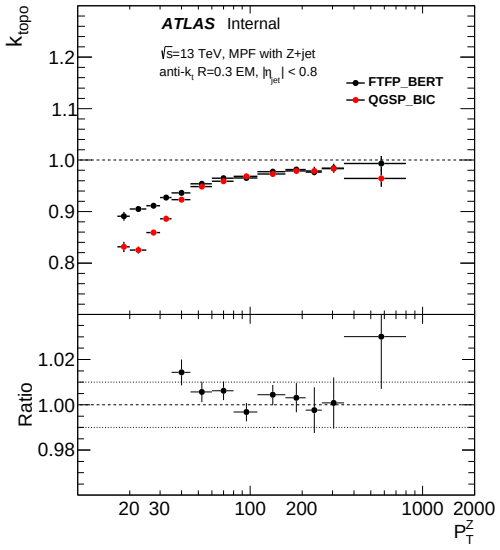

Figure H.6: Topology correction for anti-k_t R=0.3 jets with Z+jet events

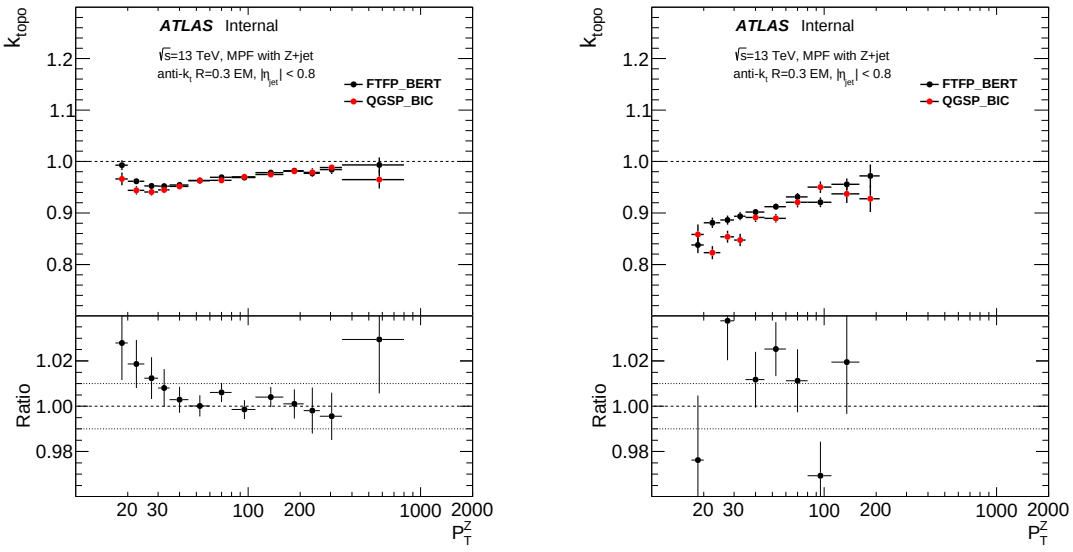

(a) Quark jets

(b) Gluon jets

Figure H.7: Topology correction for both quark and gluon initiated jets, as measured using Z+jet events with anti-k_t R=0.3 jets

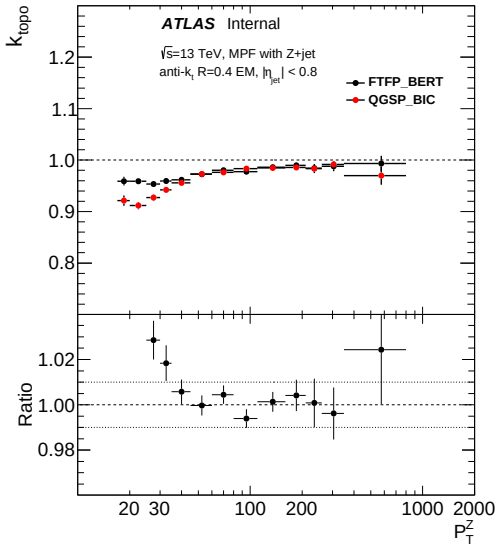

Figure H.8: Topology correction for anti-k_t R=0.4 jets with Z+jet events

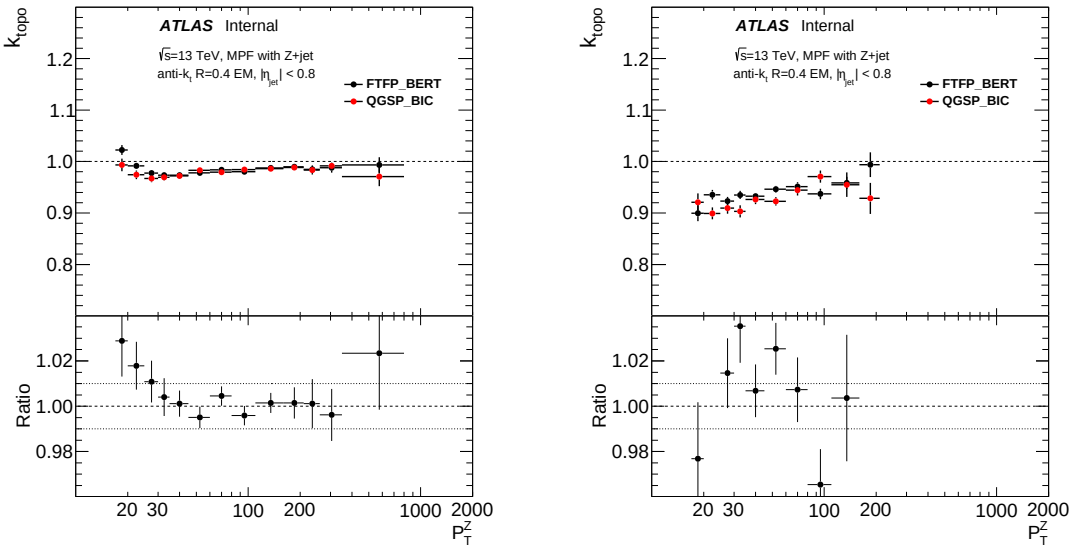

(a) Quark jets

(b) Gluon jets

Figure H.9: Topology correction for both quark and gluon initiated jets, as measured using Z+jet events with anti-k_t R=0.4 jets

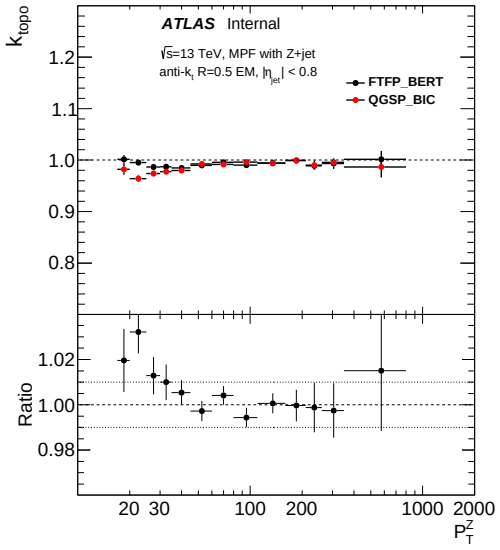

Figure H.10: Topology correction for anti-k_t R=0.5 jets with Z+jet events

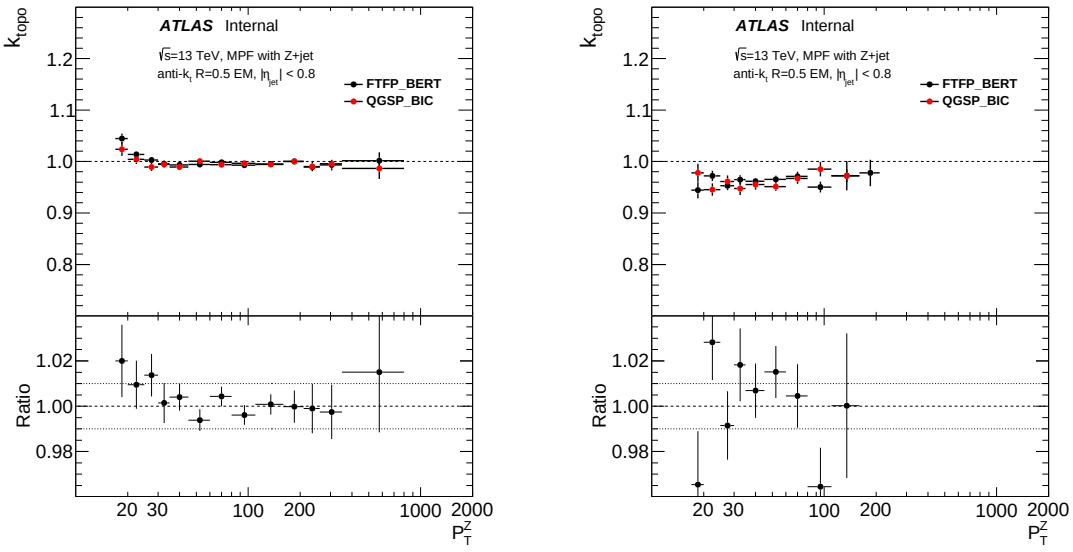

(a) Quark jets

(b) Gluon jets

Figure H.11: Topology correction for both quark and gluon initiated jets, as measured using Z+jet events with anti-k_t R=0.5 jets

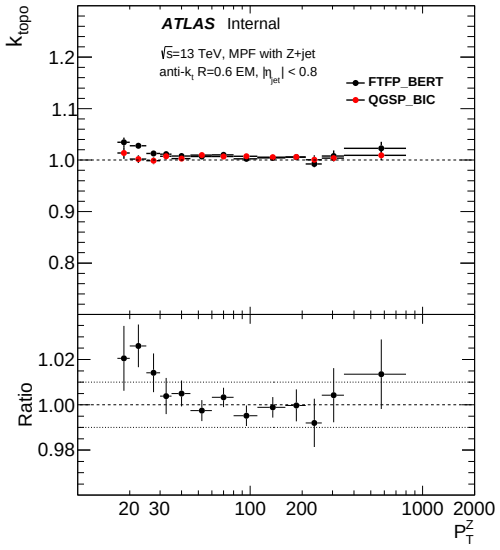

Figure H.12: Topology correction for anti-k_t R=0.6 jets with Z+jet events

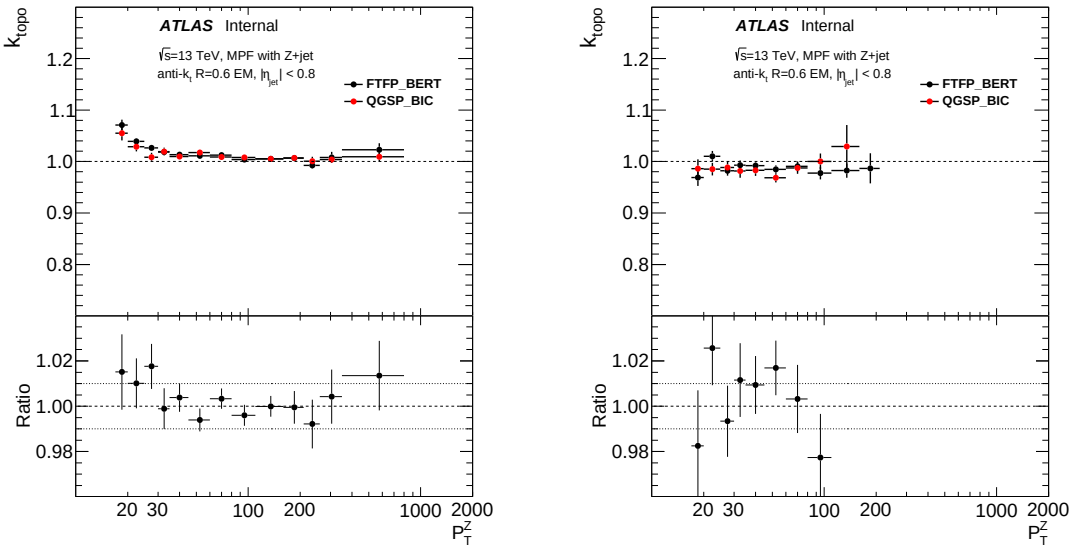

(a) Quark jets

(b) Gluon jets

Figure H.13: Topology correction for both quark and gluon initiated jets, as measured using Z+jet events with anti-k_t R=0.6 jets

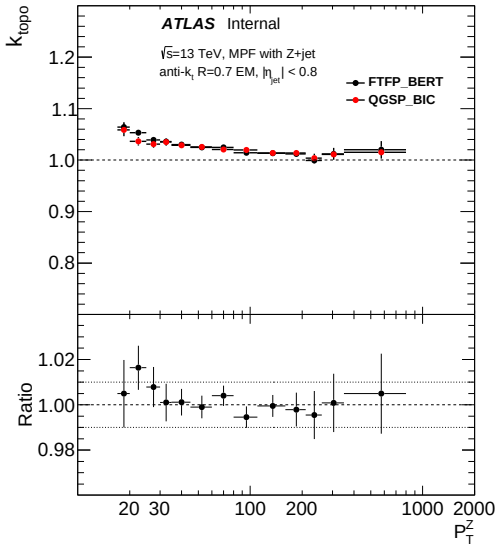

Figure H.14: Topology correction for anti-k_t R=0.7 jets with Z+jet events

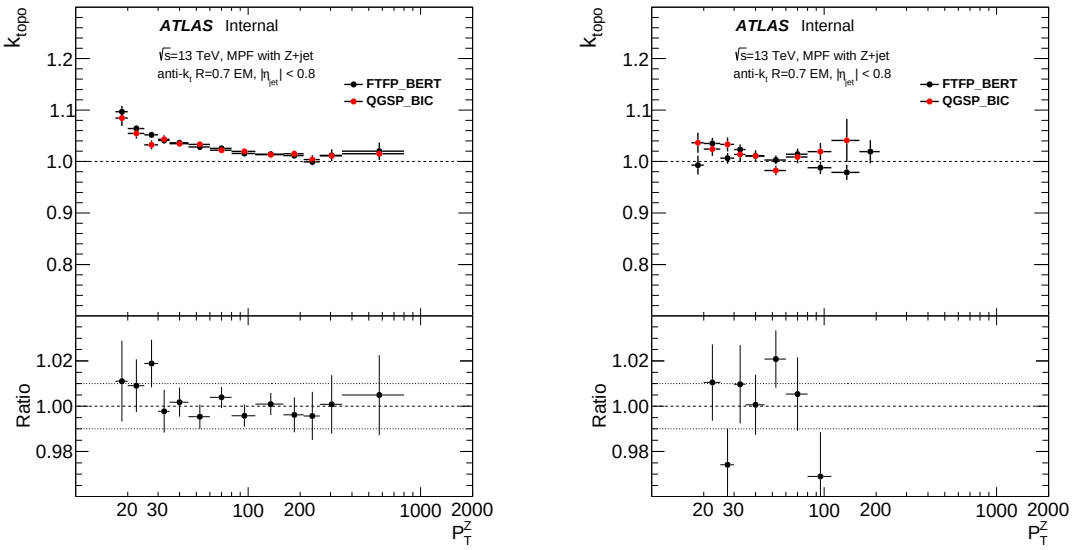

(a) Quark jets

(b) Gluon jets

Figure H.15: Topology correction for both quark and gluon initiated jets, as measured using Z+jet events with anti-k_t R=0.7 jets

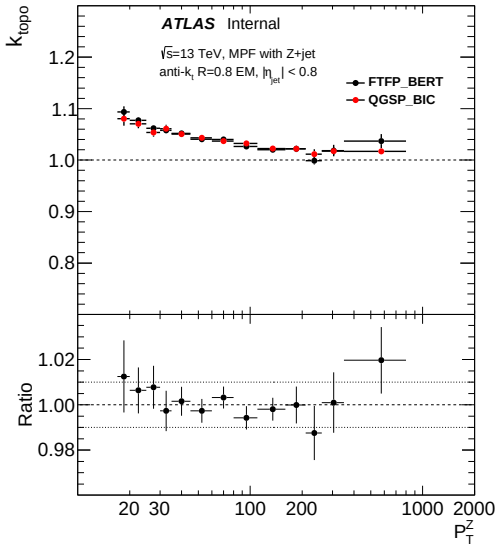

Figure H.16: Topology correction for anti-k_t R=0.8 jets with Z+jet events

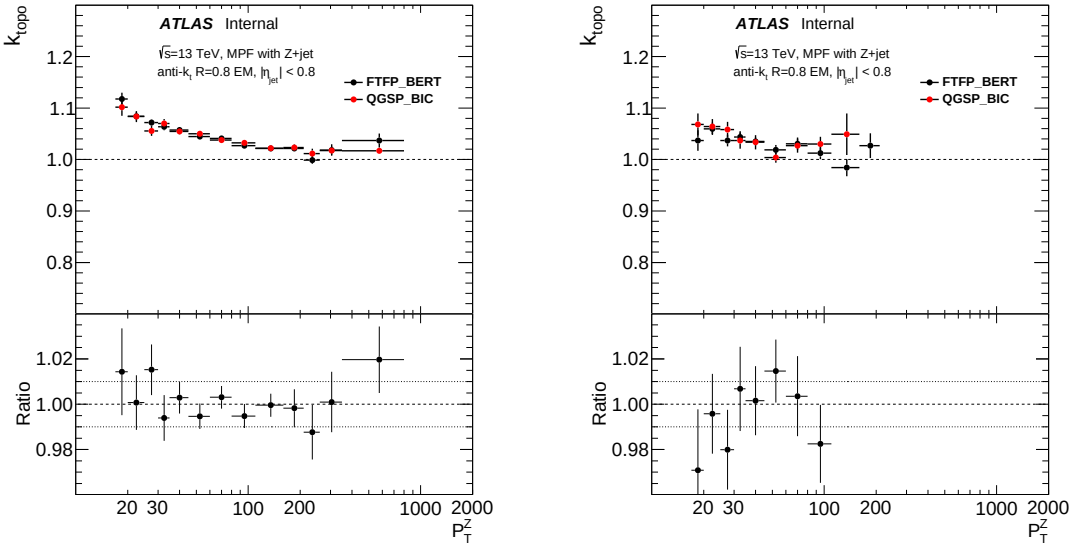

(a) Quark jets

(b) Gluon jets

Figure H.17: Topology correction for both quark and gluon initiated jets, as measured using Z+jet events with anti-k_t R=0.8 jets

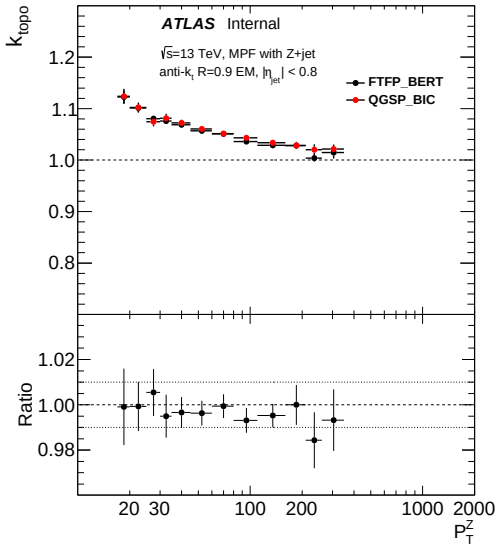

Figure H.18: Topology correction for anti-k_t R=0.9 jets with Z+jet events

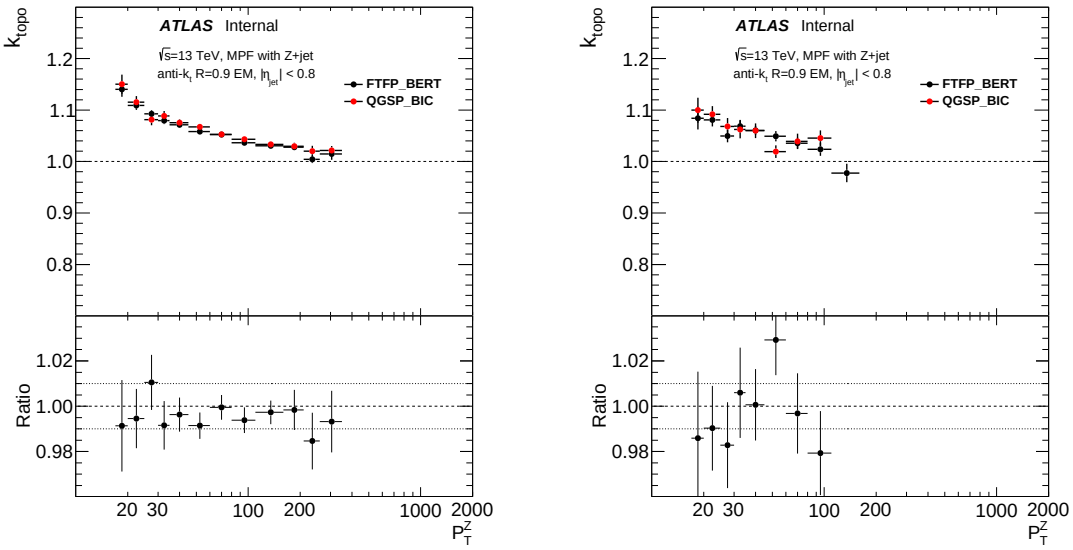

(a) Quark jets

(b) Gluon jets

Figure H.19: Topology correction for both quark and gluon initiated jets, as measured using Z+jet events with anti-k_t R=0.9 jets

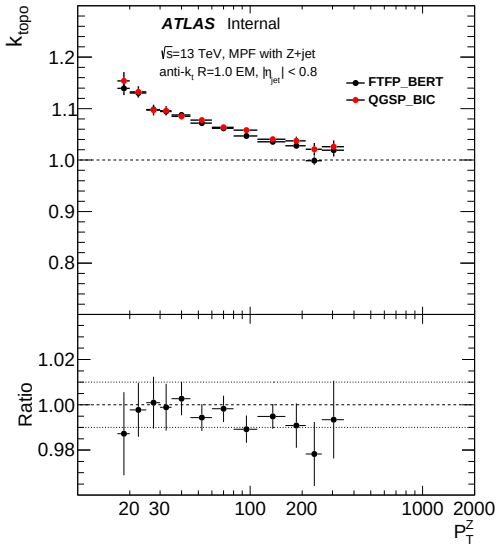

Figure H.20: Topology correction for anti-k_t R=1.0 jets with Z+jet events

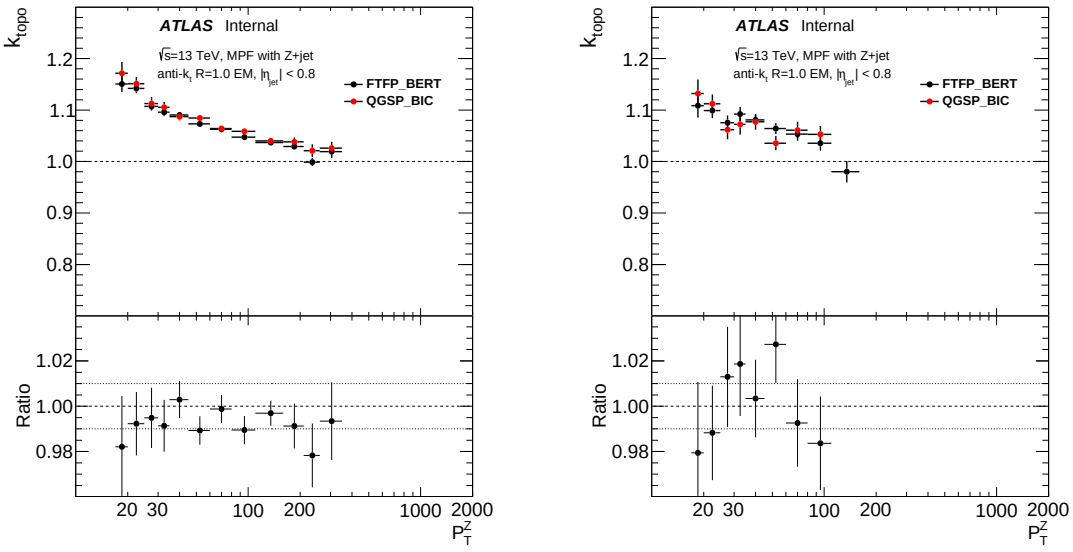

(a) Quark jets

(b) Gluon jets

Figure H.21: Topology correction for both quark and gluon initiated jets, as measured using Z+jet events with anti-k_t R=1.0 jets

Appendix I

Topology correction for γ+jet events

Fig. I.1 shows the topology correction distributions for all p_{T} bins for anti-k_{t} R=0.4 jets in γ+jet using FTFP_BERT. The remainder of this appendix will show the energy dependence of the topology correction for both FTFP_BERT and QGSP_BIC for standard γ+jet as well as γ+jet separated into light quark and gluon only samples using a number of jet sizes. The topology correction is intended to measure the flow of energy in jets. Very small jets tend to have only a small number of constituents, and therefore will tend to give non-useful results. With that in mind, the results for anti-k_{t} R=0.1 (and R=0.2 to some extend) are included in this thesis more to satisfy the readers curiosity than to be something potentially useful.

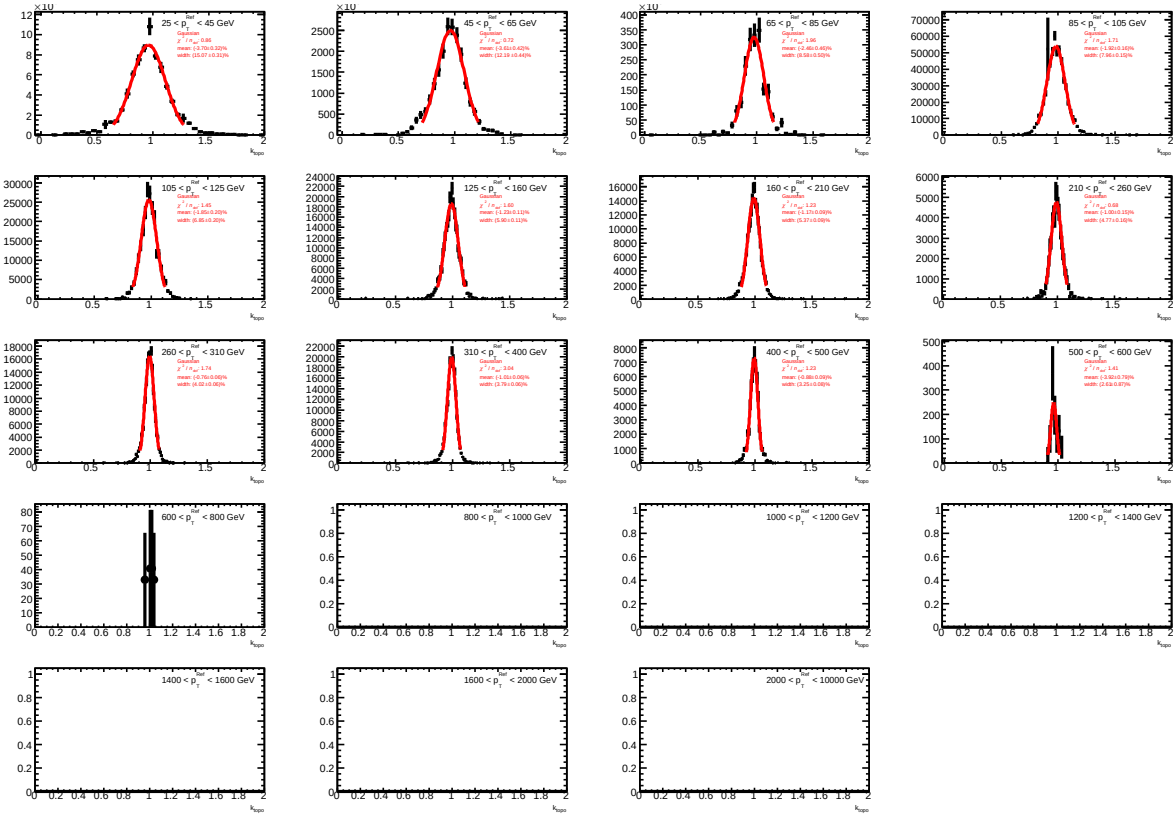

Figure I.1: Topology correction distributions for all p_{T} bins considered using FTFP_BERT in γ+jet for anti-k_{t} R=0.4 jets.

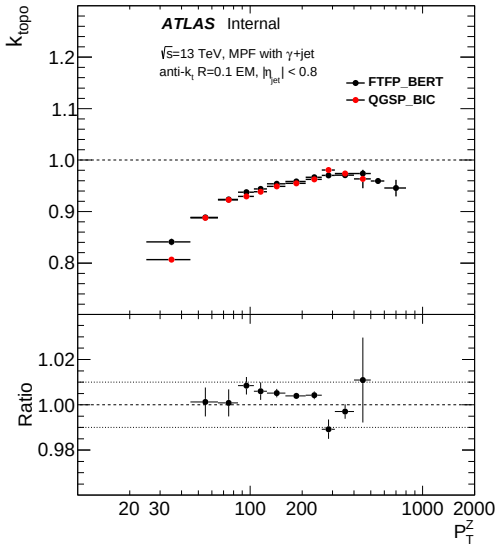

Figure I.2: Topology correction for anti-k_t R=0.1 jets with γ+jet events

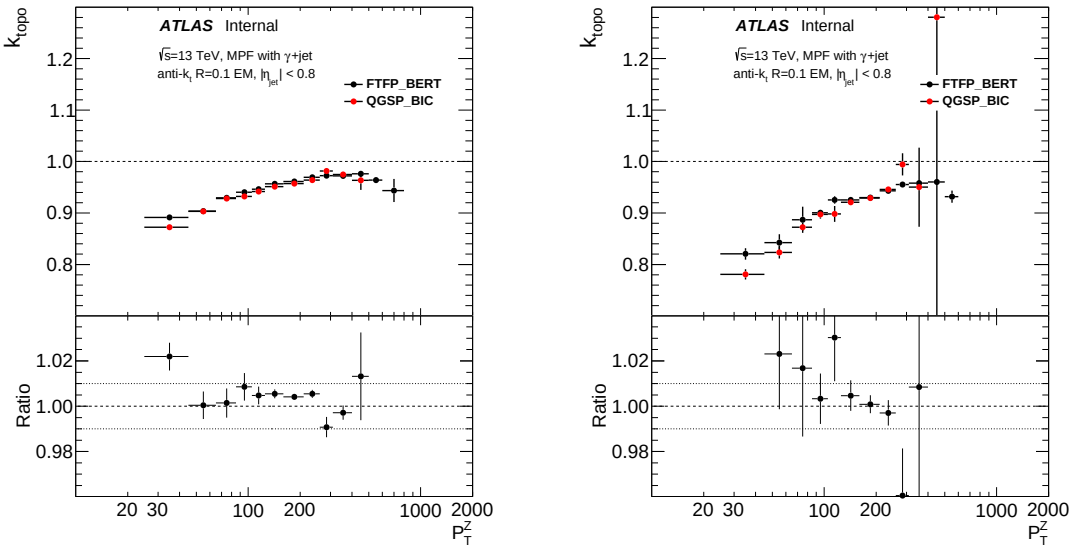

(a) Quark jets

(b) Gluon jets

Figure I.3: Topology correction for both quark and gluon initiated jets, as measured using γ+jet events with anti-k_t R=0.1 jets

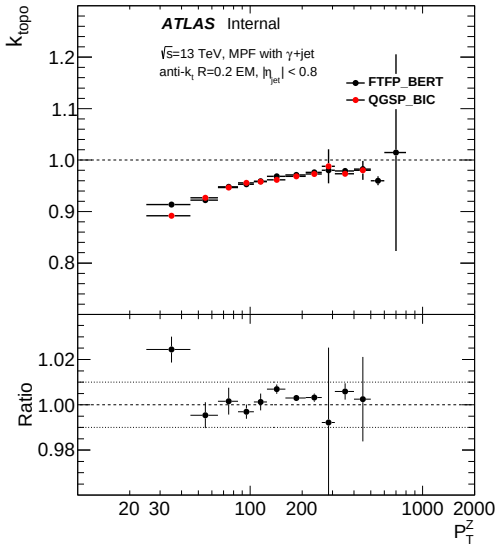

Figure I.4: Topology correction for anti-k_t R=0.2 jets with γ+jet events

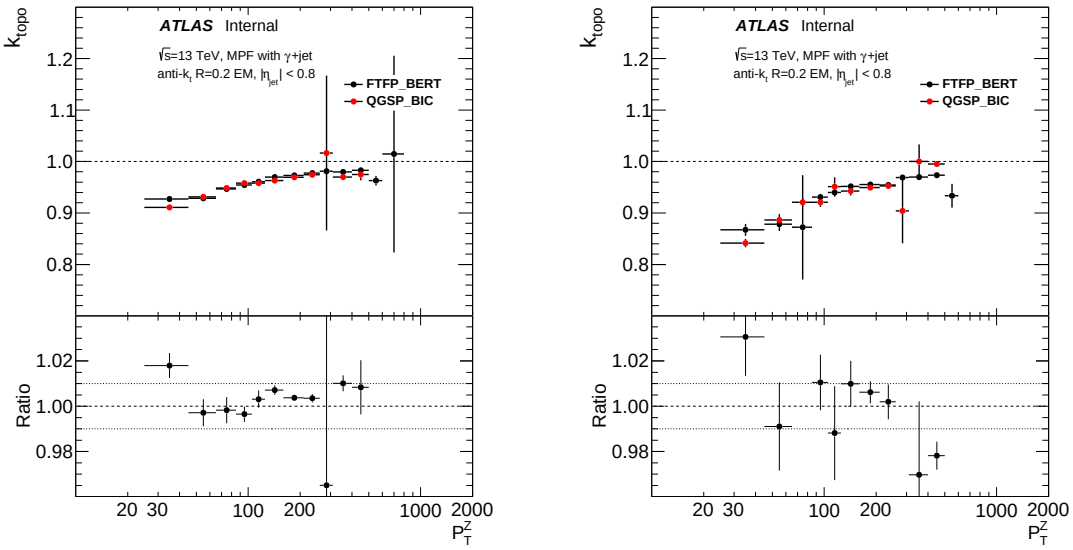

(a) Quark jets

(b) Gluon jets

Figure I.5: Topology correction for both quark and gluon initiated jets, as measured using γ+jet events with anti-k_t R=0.2 jets

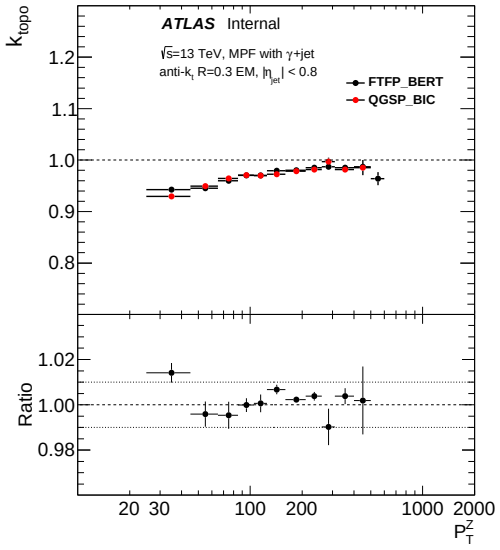

Figure I.6: Topology correction for anti-k_t R=0.3 jets with γ+jet events

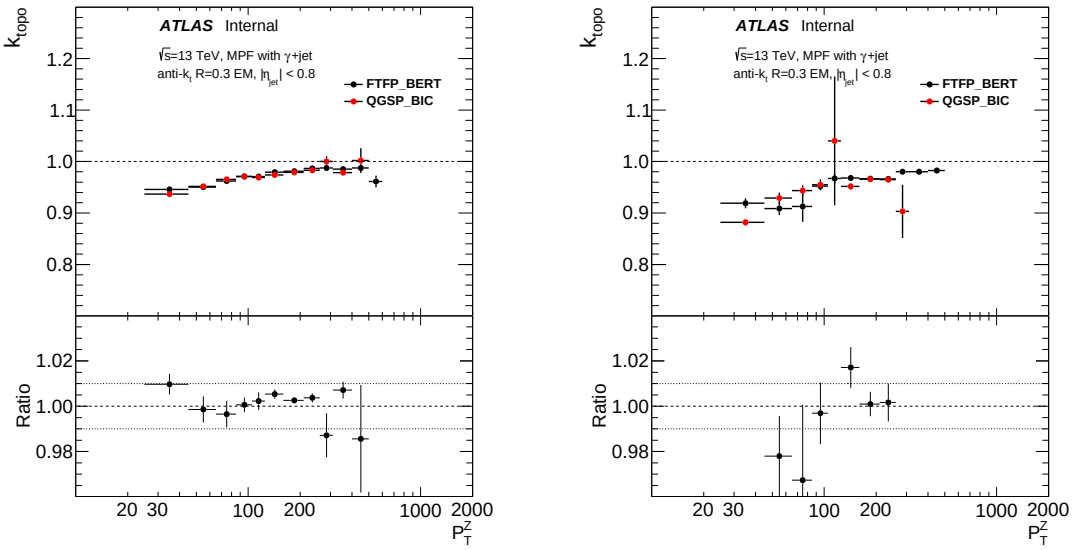

(a) Quark jets

(b) Gluon jets

Figure I.7: Topology correction for both quark and gluon initiated jets, as measured using γ+jet events with anti-k_t R=0.3 jets

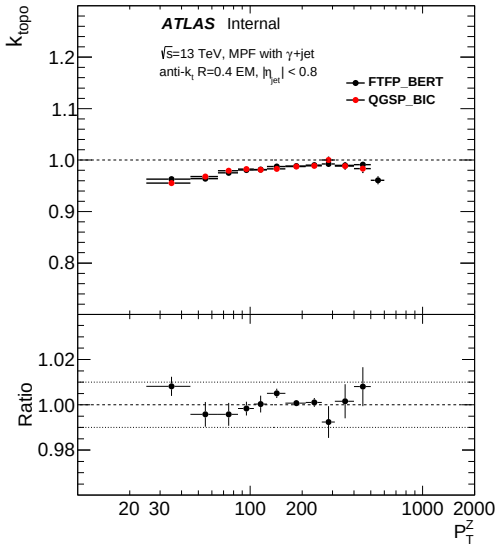

Figure I.8: Topology correction for anti-k_t R=0.4 jets with γ+jet events

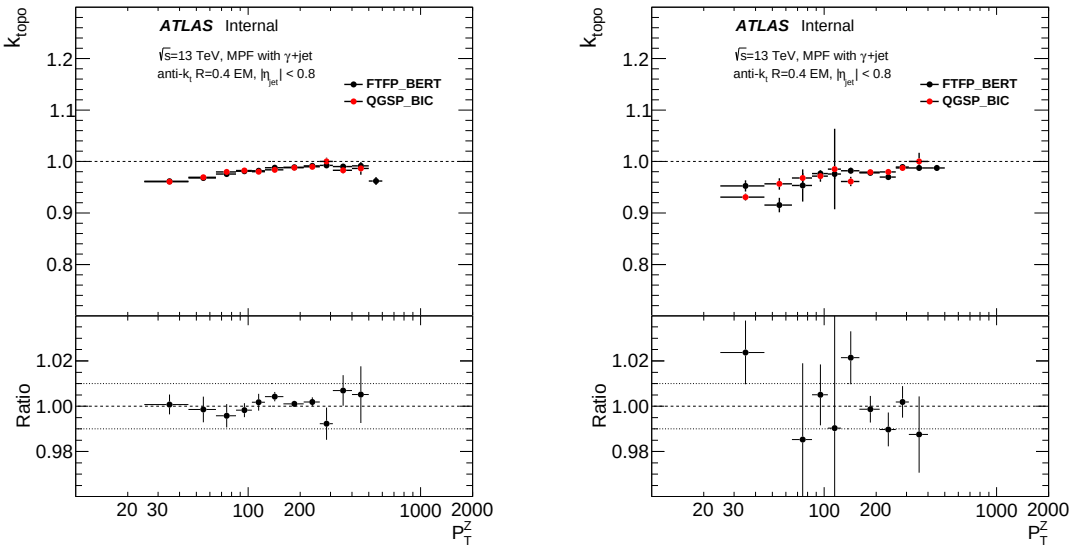

(a) Quark jets

(b) Gluon jets

Figure I.9: Topology correction for both quark and gluon initiated jets, as measured using γ+jet events with anti-k_t R=0.4 jets

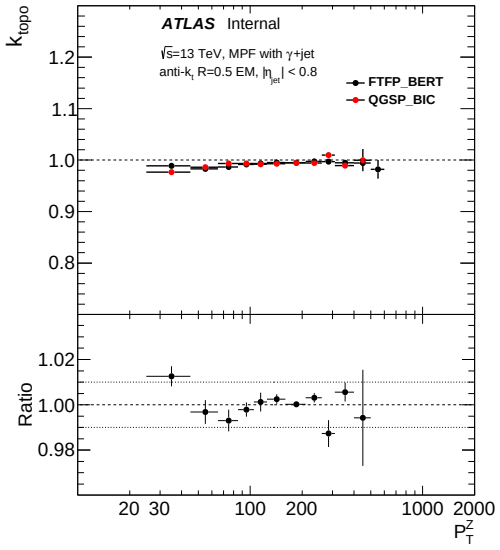

Figure I.10: Topology correction for anti-k_t R=0.5 jets with γ+jet events

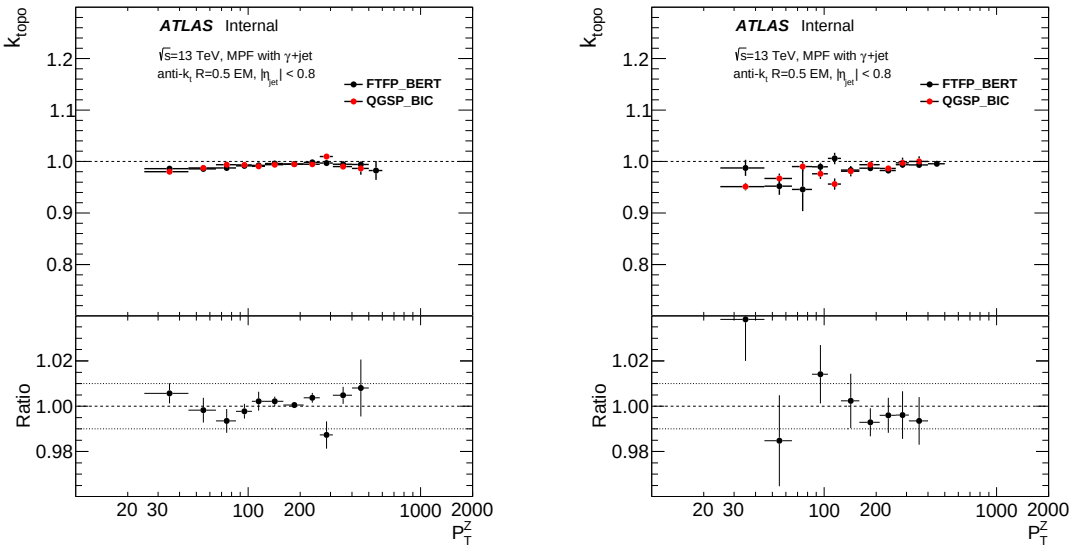

(a) Quark jets

(b) Gluon jets

Figure I.11: Topology correction for both quark and gluon initiated jets, as measured using γ+jet events with anti-k_t R=0.5 jets

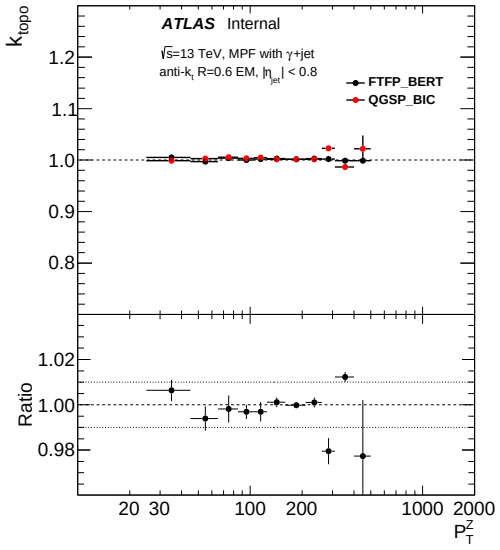

Figure I.12: Topology correction for anti-k_t R=0.6 jets with γ+jet events

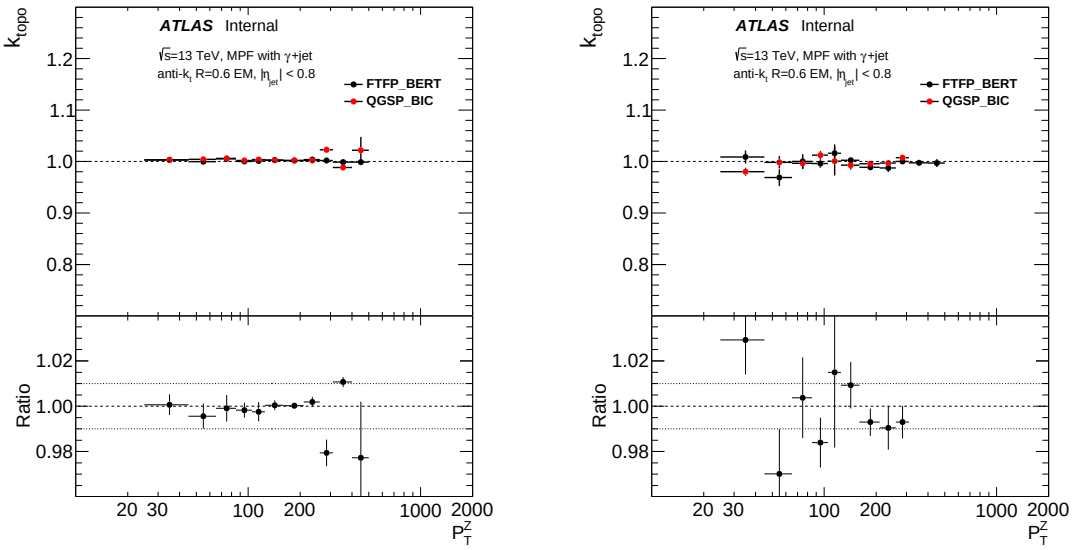

(a) Quark jets

(b) Gluon jets

Figure I.13: Topology correction for both quark and gluon initiated jets, as measured using γ+jet events with anti-k_t R=0.6 jets

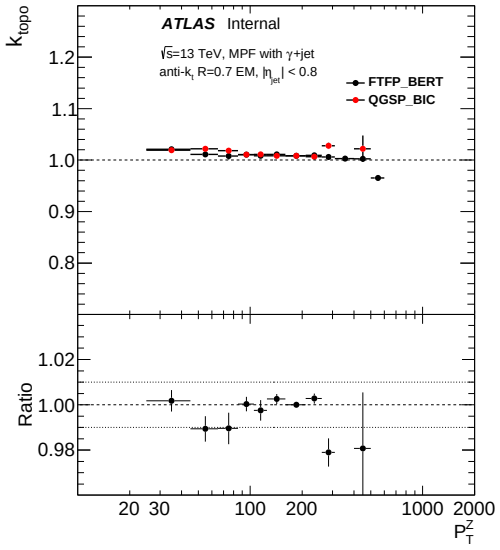

Figure I.14: Topology correction for anti-k_t R=0.7 jets with γ+jet events

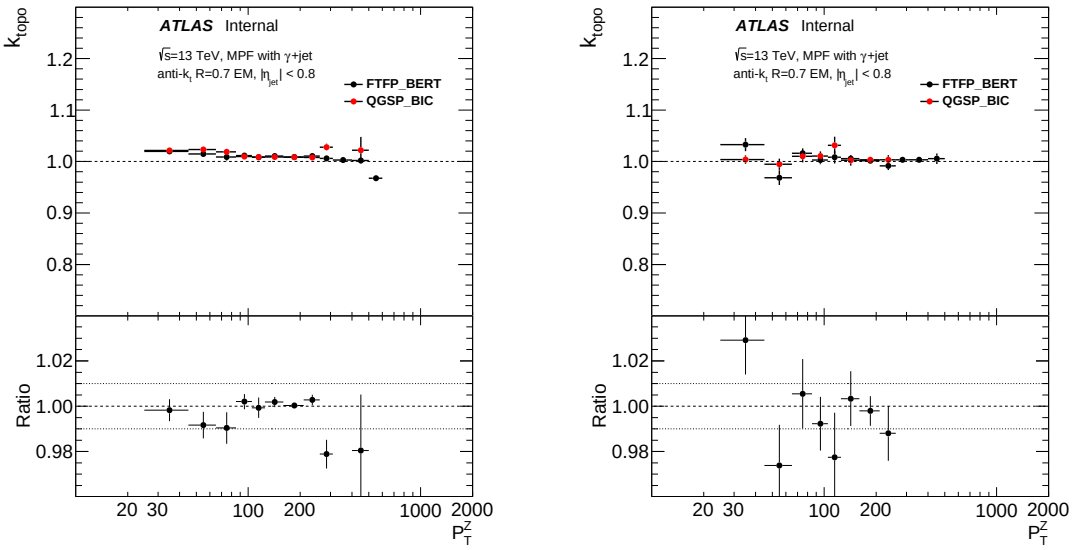

(a) Quark jets

(b) Gluon jets

Figure I.15: Topology correction for both quark and gluon initiated jets, as measured using γ+jet events with anti-k_t R=0.7 jets

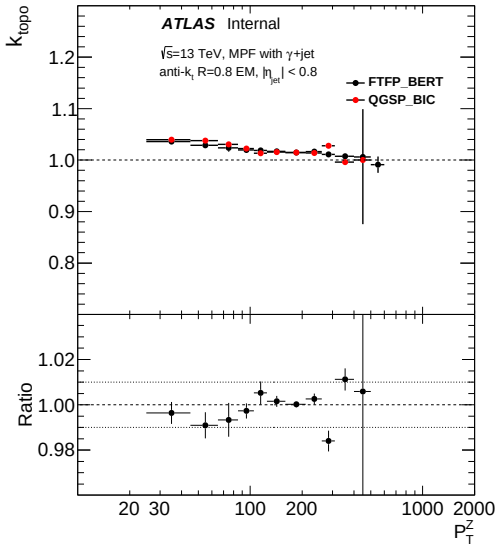

Figure I.16: Topology correction for anti-k_t R=0.8 jets with γ+jet events

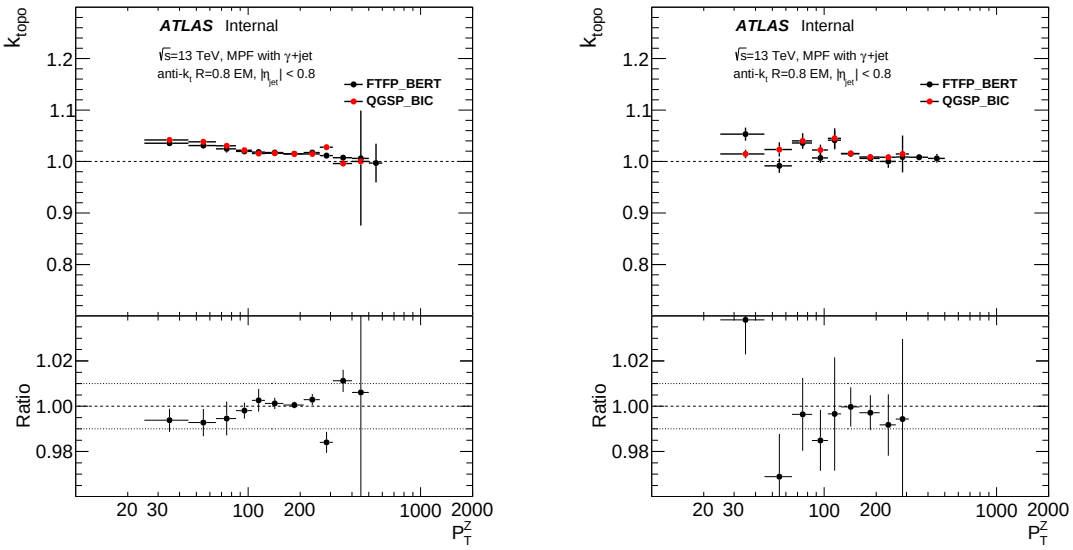

(a) Quark jets

(b) Gluon jets

Figure I.17: Topology correction for both quark and gluon initiated jets, as measured using γ+jet events with anti-k_t R=0.8 jets

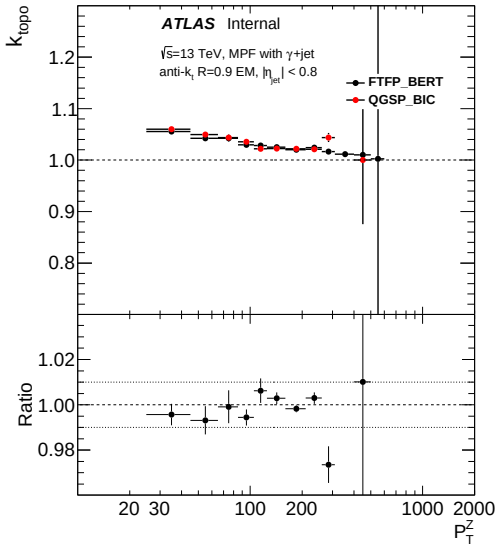

Figure I.18: Topology correction for anti-k_t R=0.9 jets with γ+jet events

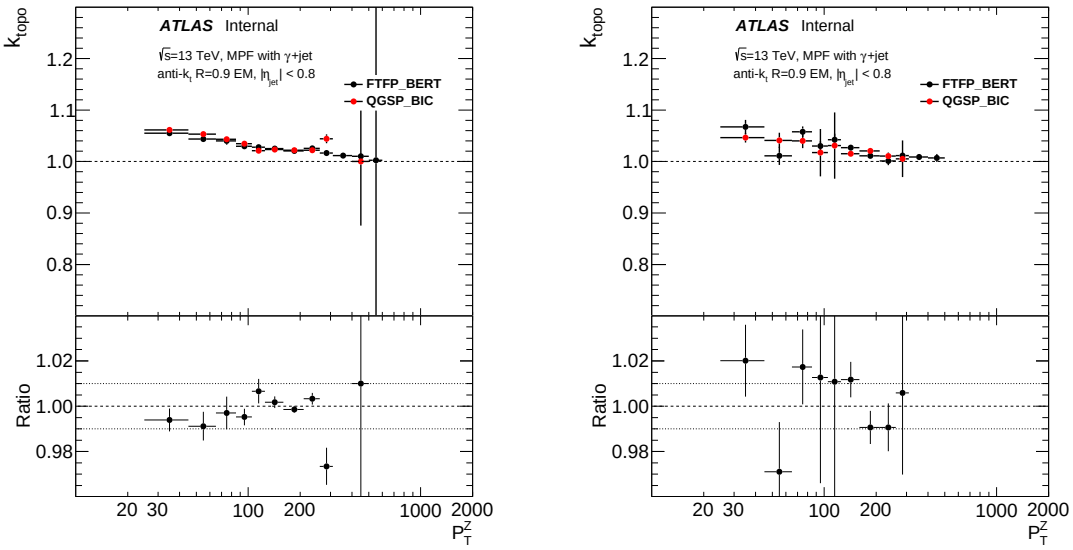

(a) Quark jets

(b) Gluon jets

Figure I.19: Topology correction for both quark and gluon initiated jets, as measured using γ+jet events with anti-k_t R=0.9 jets

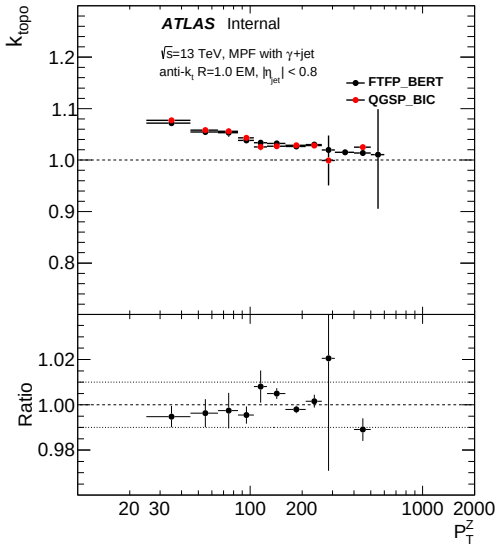

Figure I.20: Topology correction for anti-k_t R=1.0 jets with γ+jet events

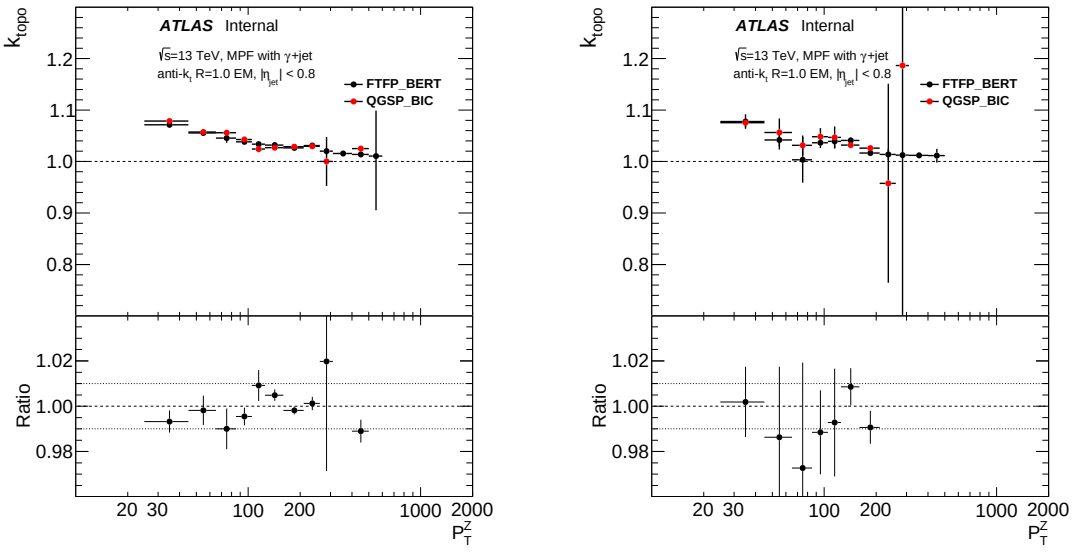

(a) Quark jets

(b) Gluon jets

Figure I.21: Topology correction for both quark and gluon initiated jets, as measured using γ+jet events with anti-k_t R=1.0 jets

Bibliography

[1] K. A. Olive et al. Review of Particle Physics. *Chin. Phys.*, C38:090001, 2014.

[2] Oliver Sim Brüning, Paul Collier, P Lebrun, Stephen Myers, Ranko Ostojic, John Poole, and Paul Proudlock. *LHC Design Report*. CERN, Geneva, 2004.

[3] The ALICE Collaboration. First proton–proton collisions at the LHC as observed with the ALICE detector: measurement of the charged-particle pseudorapidity density at $\sqrt{s} = 900$ GeV. *The European Physical Journal C*, 65(1):111–125, 2009.

[4] Oliver Sim BrÃijning, Paul Collier, P Lebrun, Stephen Myers, Ranko Ostojic, John Poole, and Paul Proudlock. *LHC Design Report*. CERN, Geneva, 2004.

[5] Joao Pequenao. Computer generated image of the whole ATLAS detector. Mar 2008.

[6] Joao Pequenao. Computer generated image of the ATLAS inner detector. Mar 2008.

[7] Alignment of the ATLAS Inner Detector and its Performance in 2012. Technical Report ATLAS-CONF-2014-047, CERN, Geneva, Jul 2014.

[8] Sho Iwamoto. Supersymmetry after the Higgs discovery and its LHC phenomenology. 2013.

[9] A Miucci. The atlas insertable b-layer project. *Journal of Instrumentation*, 9(02):C02018, 2014.

[10] M Capeans, G Darbo, K Einsweiller, M Elsing, T Flick, M Garcia-Sciveres, C Gemme, H Pernegger, O Rohne, and R Vuillermet. ATLAS Insertable B-Layer Technical Design Report. Technical Report CERN-LHCC-2010-013. ATLAS-TDR-19, CERN, Geneva, Sep 2010.

[11] The ATLAS Collaboration. The atlas experiment at the cern large hadron collider. *Journal of Instrumentation*, 3(08):S08003, 2008.

[12] C. Grupen and B. Shwartz. *Particle Detectors*. Cambridge Monographs on Particle Physics, Nuclear Physics and Cosmology. Cambridge University Press, 2008.

[13] R Wigmans. Calorimetry. *Scientifica Acta*, 2(1):18–55, 2008.

[14] J. H. Hubbell, H. A. Gimm, and I. Øverbø. Pair, Triplet, and Total Atomic Cross Sections (and Mass Attenuation Coefficients) for 1 MeV-100 GeV Photons in Elements Z=1 to 100. *Journal of Physical and Chemical Reference Data*, 9(4), 1980.

[15] Joao Pequenao. Computer Generated image of the ATLAS calorimeter. Mar 2008.

[16] *ATLAS muon spectrometer: Technical Design Report*. Technical Design Report ATLAS. CERN, Geneva, 1997.

[17] Yu Nakahama. The atlas trigger system: Ready for run-2. *Journal of Physics: Conference Series*, 664(8):082037, 2015.

[18] Morad Aaboud et al. Performance of the ATLAS Track Reconstruction Algorithms in Dense Environments in LHC run 2. 2017.

[19] Improved electron reconstruction in ATLAS using the Gaussian Sum Filter-based model for bremsstrahlung. Technical Report ATLAS-CONF-2012-047, CERN, Geneva, May 2012.

[20] Proposal for truth particle observable definitions in physics measurements. Technical Report ATL-PHYS-PUB-2015-013, CERN, Geneva, Jun 2015.

[21] Georges Aad et al. Topological cell clustering in the ATLAS calorimeters and its performance in LHC Run 1. 2016.

[22] Gerald C. Blazey et al. Run II jet physics. In *QCD and weak boson physics in Run II. Proceedings, Batavia, USA, March 4-6, June 3-4, November 4-6, 1999*, pages 47–77, 2000.

[23] Matteo Cacciari, Gavin P. Salam, and Gregory Soyez. The Anti-k(t) jet clustering algorithm. *JHEP*, 04:063, 2008.

[24] Matteo Cacciari, Gavin P. Salam, and Gregory Soyez. FastJet User Manual. *Eur. Phys. J.*, C72:1896, 2012.

[25] Gregory Soyez, Gavin P. Salam, Jihun Kim, Souvik Dutta, and Matteo Cacciari. Pileup subtraction for jet shapes. *Phys. Rev. Lett.*, 110(16):162001, 2013.

[26] Jet global sequential corrections with the ATLAS detector in proton-proton collisions at sqrt(s) = 8 TeV. Technical Report ATLAS-CONF-2015-002, CERN, Geneva, Mar 2015.

[27] Jet energy scale and its systematic uncertainty for jets produced in proton-proton collisions at sqrt(s) = 7 TeV and measured with the ATLAS detector. Technical Report ATLAS-CONF-2010-056, CERN, Geneva, Jul 2010.

[28] Jet energy scale and its systematic uncertainty in proton-proton collisions at sqrt(s)=7 TeV in ATLAS 2010 data. Technical Report ATLAS-CONF-2011-032, CERN, Geneva, Mar 2011.

[29] F Abe, D Amidei, C Anway-Weiss, G Apollinari, M Atac, P Auchincloss, AR Baden, N Bacchetta, W Badgett, Mark W Bailey, et al. Dijet angular distribution in pp collisions at $\sqrt{s} = 1.8$ TeV. *Physical review letters*, 69(20):2896, 1992.

[30] Andrew James Milder. Dijet angular distributions at square root of s = 1800 gev using the d0 detector.

[31] Torbjorn Sjostrand, Stephen Mrenna, and Peter Z. Skands. A Brief Introduction to PYTHIA 8.1. *Comput. Phys. Commun.*, 178:852–867, 2008.

[32] Richard D. Ball, Valerio Bertone, Stefano Carrazza, Luigi Del Debbio, Stefano Forte, Alberto Guffanti, Nathan P. Hartland, and Juan Rojo. Parton distributions with QED corrections. *Nucl. Phys.*, B877:290–320, 2013.

[33] Paolo Nason. A New method for combining NLO QCD with shower Monte Carlo algorithms. *JHEP*, 11:040, 2004.

[34] Stefano Frixione, Paolo Nason, and Carlo Oleari. Matching NLO QCD computations with Parton Shower simulations: the POWHEG method. *JHEP*, 11:070, 2007.

[35] Simone Alioli, Paolo Nason, Carlo Oleari, and Emanuele Re. A general framework for implementing NLO calculations in shower Monte Carlo programs: the POWHEG BOX. *JHEP*, 06:043, 2010.

[36] J. Pumplin, D. R. Stump, J. Huston, H. L. Lai, Pavel M. Nadolsky, and W. K. Tung. New generation of parton distributions with uncertainties from global QCD analysis. *JHEP*, 07:012, 2002.

[37] B. Andersson, G. Gustafson, G. Ingelman, and T. Sjostrand. Parton fragmentation and string dynamics. *Physics Reports*, 97(2):31 – 145, 1983.

[38] S. Agostinelli et al. Geant4a simulation toolkit. *Nuclear Instruments and Methods in Physics Research Section A: Accelerators, Spectrometers, Detectors and Associated Equipment*, 506(3):250 – 303, 2003.

[39] GEANT4 : Physics Reference Manual. 2016. CERN Program Library Long Writeups.

[40] Photon identification in 2015 ATLAS data. Technical Report ATL-PHYS-PUB-2016-014, CERN, Geneva, Aug 2016.

[41] Electron identification measurements in ATLAS using $\sqrt{s} = 13$ TeV data with 50 ns bunch spacing. Technical Report ATL-PHYS-PUB-2015-041, CERN, Geneva, Sep 2015.

[42] Muon reconstruction performance in early $\sqrt{s} = 13$ TeV data. Technical Report ATL-PHYS-PUB-2015-037, CERN, Geneva, Aug 2015.

[43] Selection of jets produced in 13TeV proton-proton collisions with the ATLAS detector. Technical Report ATLAS-CONF-2015-029, CERN, Geneva, Jul 2015.

[44] Pile-up subtraction and suppression for jets in ATLAS. Technical Report ATLAS-CONF-2013-083, CERN, Geneva, Aug 2013.

[45] Tagging and suppression of pileup jets with the ATLAS detector. Technical Report ATLAS-CONF-2014-018, CERN, Geneva, May 2014.

[46] Georges Aad et al. Jet energy measurement with the ATLAS detector in proton-proton collisions at $\sqrt{s} = 7$ TeV. *Eur. Phys. J.*, C73(3):2304, 2013.

[47] Determination of the jet energy scale and resolution at ATLAS using Z/γ–jet events in data at $\sqrt{s} = 8$ TeV. Technical Report ATLAS-CONF-2015-057, CERN, Geneva, Oct 2015.

[48] Determination of the ATLAS jet energy measurement uncertainty using photon-jet events in proton-proton collisions at sqrts = 7 TeV. Technical Report ATLAS-CONF-2011-031, CERN, Geneva, Mar 2011.

[49] Electron and photon energy calibration with the ATLAS detector using data collected in 2015 at $\sqrt{s} = 13$ TeV. Technical Report ATL-PHYS-PUB-2016-015, CERN, Geneva, Aug 2016.

[50] Georges Aad et al. Muon reconstruction performance of the ATLAS detector in proton-proton collision data at $\sqrt{s}$ =13 TeV. *Eur. Phys. J.*, C76(5):292, 2016.

[51] Probing the measurement of jet energies with the ATLAS detector using photon+jet events in proton-proton collisions at $\sqrt{s} = 7$ TeV. Technical Report ATLAS-CONF-2012-063, CERN, Geneva, Jul 2012.

[52] T. Gleisberg, Stefan. Hoeche, F. Krauss, M. Schonherr, S. Schumann, F. Siegert, and J. Winter. Event generation with SHERPA 1.1. *JHEP*, 02:007, 2009.

[53] T. D. Gottschalk. A realistic model for e $^{+}$e $^{-}$ annihilation including parton bremsstrahlung effects. *Nuclear Physics B*, 214:201–222, April 1983.

[54] Hung-Liang Lai, Marco Guzzi, Joey Huston, Zhao Li, Pavel M. Nadolsky, Jon Pumplin, and C. P. Yuan. New parton distributions for collider physics. *Phys. Rev.*, D82:074024, 2010.

[55] Richard D. Ball et al. Parton distributions for the LHC Run II. *JHEP*, 04:040, 2015.

[56] G Choudalakis and M Spousta. Characteristic dip in average transverse energy density and multiplicity around the axis of Anti-kT jets. Technical Report ATL-COM-PHYS-2010-139, CERN, Geneva, Mar 2010.

[57] Torbjorn Sjostrand. Monte carlo 1. introduction and parton showers. page http://home.thep.lu.se/t̃orbjorn/talks/van1ho.pdf, 2013. TRIUMF Summer School, 2013.

[58] Dengfeng Zhang. Validation of Geant4 Physics Lists in testbeam Simulation. Technical Report ATL-COM-TILECAL-2017-012, CERN, Geneva, Feb 2017.

[59] H. Fesefeldt. The Simulation of Hadronic Showers: Physics and Applications. 1985.

[60] C. Adloff et al. Shower development of particles with momenta from 1 to 10 GeV in the CALICE Scintillator-Tungsten HCAL. *JINST*, 9(01):P01004, 2014.

[61] M. Aaboud et al. Jet energy scale measurements and their systematic uncertainties in proton-proton collisions at $\sqrt{s} = 13$ TeV with the ATLAS detector. *Phys. Rev.*, D96(7):072002, 2017.

[62] Dijet resonance searches with the ATLAS detector at 14 TeV LHC. Technical Report ATL-PHYS-PUB-2015-004, CERN, Geneva, Mar 2015.